Computational EPR, ENDOR and DFT Studies of Catalytic Transition Metal Systems

James Hugh Pearson Landon

Thesis submitted for the Degree of PhD

Department of Chemistry

Cardiff University

September 2008

ProQuest LLC
789 East Eisenhower Parkway
P.O. Box 1346
Ann Arbor, MI 48106-1346

Declaration

The research in this thesis was carried out between October 2004 and September 2007 in the Department of Chemistry at Cardiff University and is, to the best of my knowledge, original except where due reference is made to other authors.

The study reported here on geometrically selective epoxide binding by a chiral vanadyl salen complex has been published as

"Discrimination of geometrical epoxide isomers by ENDOR Spectroscopy and DFT calculations: The role of hydrogen bonds"

by Damien M. Murphy, Ian A. Fallis, David J. Willock, James Landon, Emma Carter, and Evi Vinck in *Angewandte Chemie, International Edition*, **2008**, *47*, 1414.

The work on stereo-selective epoxide binding by a chiral vanadyl salen complex is currently in preparation as a manuscript entitled

"Enantioselective binding of structural epoxide isomers by a chiral vanadyl salen complex; A pulsed EPR, *cw*-ENDOR and DFT investigation"

by Damien M. Murphy, Ian A. Fallis, David J. Willock, James Landon, Emma Carter, Sabine van Doorslaer and Evi Vinck.

The work on selective binding of a chiral amine molecule by chiral copper salen complexes is currently in preparation as a manuscript entitled

"Stereoselective binding of chiral amines by chiral Cu-Salen type complexes probed by EPR and ENDOR spectroscopy and DFT" by Damien M. Murphy, Ian A. Fallis, David J. Willock, James Landon, Emma Carter, Sabine van Doorslaer and Evi Vinck.

The work on the incorporation of copper in an aluminium phosphate material is currently in preparation as a manuscript entitled

"Direct evidence for framework Cu(II) ions within an $AlPO_4$ structure; An EPR and DFT investigation"

by Damien M. Murphy, Zelimer Gabelica, M. Filipa Ribeiro, A. Fernandes, Joao P. Loureno, Sabine Valange, A. Louati, David J. Willock, James Landon, Ian A. Fallis and Sabine van Doorslaer.

James Hugh Pearson Landon

Form: PGR_Submission_200701

NOTICE OF SUBMISSION OF THESIS FORM: POSTGRADUATE RESEARCH

CARDIFF UNIVERSITY
PRIFYSGOL CAERDYDD

DECLARATION

This work has not previously been accepted in substance for any degree and is not concurrently submitted in candidature for any degree.

Signed ..... (candidate) Date 24-02-09

STATEMENT 1

This thesis is being submitted in partial fulfillment of the requirements for the degree of .....PhD.....(insert MCh, MD, MPhil, PhD etc, as appropriate)

Signed ..... (candidate) Date 24-02-09

STATEMENT 2

This thesis is the result of my own independent work/investigation, except where otherwise stated. Other sources are acknowledged by explicit references.

Signed ..... (candidate) Date 24-02-09

STATEMENT 3

I hereby give consent for my thesis, if accepted, to be available for photocopying and for inter-library loan, and for the title and summary to be made available to outside organisations.

Signed ..... (candidate) Date 24-02-09

Acknowledgements

I would like to offer my thanks to the many people who contributed so much to this thesis. Firstly to my supervisors, Dr. Dave Willock, Dr. Damien Murphy and Dr. Ian Fallis for their help, guidance and endless patience. Secondly to those with whom I worked each day, to Dr. Emma Carter, for her work and for discussions of a technical and trivial nature, to Dr. J. Grant Hill for various explanations and assistance, to Dr. Ed Jeffery, Dr. Rudy Coquet, Dr. Gareth Evans and James Bushell for showing me the ropes, and to Nathan Dedman, Steve Oldfield and Kara Howard for help along the way. To the EPSRC for funding this work, and finally, to my family for all their support throughout.

"Science may set limits to knowledge, but should not set limits to imagination."

Bertrand Russell

Abstract

The following thesis discusses the combined use of electron paramagnetic resonance (EPR) spectroscopy, electron nuclear double resonance (ENDOR) spectroscopy and density functional theory (DFT) calculations to investigate a number of transition metal catalyst systems; the binding of epoxide molecules by a vanadyl analogue of the catalytically important metallosalen class of compounds; the binding of a chiral aryl amine by a copper salen complex; and the incorporation of copper(II) ions in aluminophosphate materials.

Two classes of epoxide selectivity by a vanadyl salen derivative are presented here, the discrimination of the geometric isomers of 2,3-epoxybutane, *cis*-2,3-epoxybutane and *trans*-2,3-epoxybutane by *N,N'*-bis(3,5-di-tert-butylsalicylidene)-1,2-diaminocyclohexane-vanadium(IV) oxide ([VO(**1**)]) [1] and the stereoselectivity of epoxypropane, 1,2-epoxybutane, chloromethyloxirane and fluoromethyloxirane by [VO(**1**)]. In both cases it is shown that hydrogen-bonding interactions, including interactions between the epoxide oxygen atom and a hydrogen atom bonded to a stereocentre carbon atom of the complex are important in determining the binding mode, thus implicating the given stereocentre carbon atom in the transfer of chirality. In the geometric isomerism of 2,3-epoxybutane, steric arguments regarding the obstruction caused by the methyl groups made on the basis of the DFT structures explain the selectivity observed in the EPR/ENDOR spectra. In the chiral selectivity of the other epoxides, more complicated reasoning, based on tripodal weak hydrogen-bonding configurations involving the hydrogen atoms of the epoxide ring and the oxygen atoms of the complex ligand is required to fully explain the selectivity observed, with different selectivity effects in the more electronegative halogenated epoxides compared to the alkyl cases.

The coordination of methyl benzyl amine to a series of analogues of [Cu(**1**)] with various levels of *tert*-butylation, to model the steric effects in this interaction is studied here using DFT methods to explain the coordination preference for heterochiral pairings observed in the EPR spectra. Reasoning based on the preference of each enantiomer of the MBA to

become involved in $\pi - \pi$ interaction with alternate benzene rings of the complex, along with a slightly increased crowding of one ring over the other caused by the same hydrogen atom as implicated in determining selectivity in the epoxide study (above), namely the hydrogen atom bonded to one of the stereocentre C atoms, explains the selectivity observed in terms of $\pi - \pi$ interactions, also identifying the role of the stereocentre C atoms in conferring chirality.

In combination, these studies demonstrate the importance of weak interactions, namely hydrogen-bonding and $\pi - \pi$ interactions, in determining the binding configurations, and by extension the selectivity of these transition metal complexes. They also describe the nature of the involvement of the stereocentres of the complex in directing that selectivity, delineating a link between the chirality of the complex and that of the bound species in each case.

The importance of using both EPR/ENDOR and DFT techniques in such studies, namely of explaining selectivity observed by EPR in terms of ENDOR and DFT derived geometry parameters is further explored in this thesis in the development of genetic algorithm routines to modify DFT-derived structures, by means of the ENDOR spectra simulated with the hyperfine parameters derived from a simple point-dipole model applied to the coordinates. The application of this process to a sample axial system, $VO(acac)_2$, demonstrates the effectiveness of exploiting the complementary nature of the ENDOR and DFT techniques in this manner.

Finally, a second copper study is reported here. This example is of a microporous aluminophosphate material, and concerns the incorporation of Cu^{II} ions into framework *vs.* extra-framework sites, a subject of some controversy. Here, evidence is presented for the ability of copper to distort the tetrahedral lattice into a distorted octahedral and a square-based pyramidal environment in which one or both of the remaining coordination sites is/are occupied by the templating molecules and water molecules, without rendering the lattice unstable, arguing in favour of framework site incorporation.

Contents

Chapter 1

Introduction

1.1 Homogeneous Epoxidation Catalysis

Epoxides play an important role in the synthesis of dialcohols, aminoalcohols, and ethers [2, 3]. These are all important species in natural product synthesis, and in the production of important pharmaceutical ingredients, of agricultural products, and of flavourings and fragrances. There is therefore a great demand for their optically pure production, which in turn necessitates the production of enantiopure epoxides. The epoxidation of alkenes by per-acids, discovered by Prileschajew [4] in 1909 was later shown by Swern [5] to be stereospecific in generating *cis* epoxides from *cis* alkenes, and *trans* epoxides from *trans* alkenes. Much research effort [6–8] has thus gone into developing transition metal catalysts capable of obtaining high enantiomeric excesses in the epoxidation of achiral olefins. A major breakthrough in the use of metal-based catalysts came in 1980 [9], when Sharpless developed a process in which 2,3-epoxyalcohols were synthesised from allylic alcohols using a titanium catalyst, $Ti(OCH(CH_3)_2)_4$. A comprehensive review of this field is given in reference [10].

1.1.1 Metal Salen Complex Catalysts

The discovery by Sharpless of a metal-based epoxidation catalyst prompted further efforts to identify more general asymmetric transition metal olefin epoxidation catalysts. A principal class of catalysts that was found to achieve this comprises a set of chiral transition metal complexes that are capable of carrying out oxo-transfer to olefins. Mechanistic studies of these processes have uncovered similarities to important biological oxidation systems [11], as well as revealing a means of improving catalyst efficiency and selectivity. Many such catalysts display useful enantioselectivities for a number of substrates, unlike most enzyme promoted selective processes, which has led them to be described by Jacobsen as "privileged chiral catalysts" [12]. Amongst these catalysts is a class of complexes based on chiral *N,N'*-bis-salicylidene-ethylenediamine (salen) type complexes [13] (figure 1.1), whose catalytic properties have been studied in great depth [14].

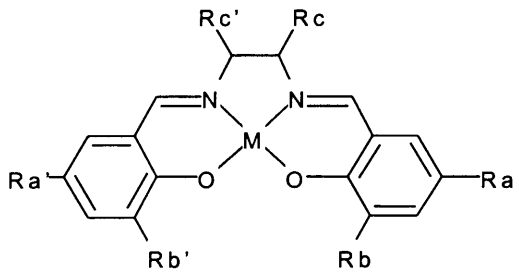

Figure 1.1: *N,N'-bis-salicylidene-ethylenediamine (salen) coordinated to a metal centre [13].*

Epoxidation by salen based complexes requires the transfer of oxygen from the metal centre to the olefin molecule. This involves the reduction of the metal centre, requiring the metal involved to be able to easily alter its oxidation state. Suitable metals include manganese(III), the metal of the original studies by Jacobsen [15, 16], giving rise to the catalyst known as 'Jacobsen's catalyst', figure 1.2, chromium(III) and cobalt(II/III).

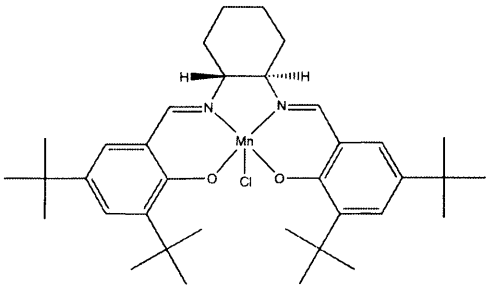

Figure 1.2: *Jacobsen's catalyst [15, 16].*

The metal must receive the oxo group from an oxo source, such as NaOI, then pass it on to the olefin as in figure 1.3.

1.1.2 Oxo-Transfer Mechanism

Various mechanisms have been proposed for the transfer of the oxo group by the metal complex to the olefin. Generally, these mechanisms fall into the categories of proceeding *via* an oxametallacycle intermediate (figure 1.4) [9] or *via* CO bond formation through the

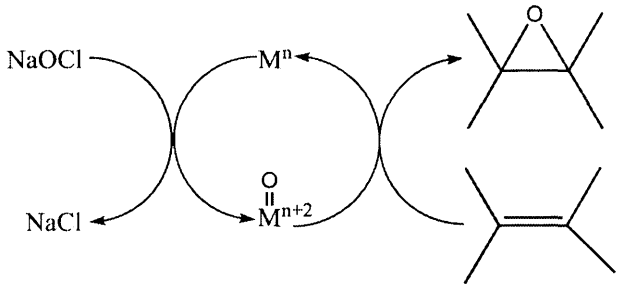

Figure 1.3: *The process of oxidation at the metal centre by an oxidising agent, and the subsequent oxo transfer by the catalyst to the olefin, to generate the epoxide.*

substrate attacking the oxo-group directly (figure 1.5). Studies of salen complexes [17,18] have revealed little or no evidence for the former mechanism, favouring the latter.

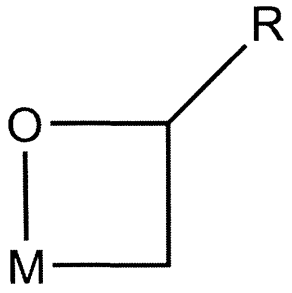

Figure 1.4: *The proposed metallacycle transfer mechanism.*

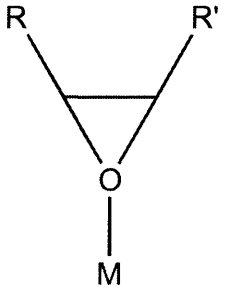

Figure 1.5: *The proposed direct substrate oxo attack mechanism.*

The mechanism by which chiral selection occurs is believed to involve diastereomeric transition states, for achiral substrates, or the diastereomeric discrimination of either enantiomer for chiral substrates. This latter process has only recently been directly observed [19] using bound enantiomers of epoxypropane with a vanadyl analogue of the

catalytically active salen complexes. It was demonstrated using electron nuclear double resonance (ENDOR) spectroscopy that discrimination of homochiral and heterochiral pairings of epoxides and complex took place, with the ENDOR technique able to elucidate structural differences between the adducts. Whilst this study provided evidence for the discrimination of the epoxide enantiomers, it did not supply a mechanism by which this discrimination might occur. Specifically, whilst it was clear that the discrimination was controlled by weak interactions, it was not made clear whether these included electrostatic effects, electronic effects, solvent effects or H-bonding. Also, no connection was made between the selectivity and the stereocentres of the catalyst.

Geometric isomerism studies, in which *cis*-alkenes were found to bind preferentially to *trans*-alkenes, point towards a direct attack by the alkene at an axially coordinated oxo ligand, adopting a side on geometry which is a more restrictive environment for the *trans*-alkenes, as illustrated in figure 1.6.

Figure 1.6: *The differences in side on attack of an axially coordinated oxo ligand between cis- and trans-alkenes. The planar ligand makes the trans binding less favourable.*

This leads to the idea that the stereoselectivity of the salen ligand arises from the equivalence of the two faces of the quasi-planar ligand, with the protons attached to the stereocentre C atoms on opposite sides of the metal centre. From experimental studies [20], summarised in table 1.1, it is also known that the enantioselectivity in such systems is dependent on the presence of bulky substituents such as *tert*-butyl groups on the salicylide benzene rings (at positions Ra, Ra', Rb and Rb' in figure 1.1) and on the substitution at sites Rc and Rc' of further bulky substituents.

Rc,Rc'	Ra,Ra'	Rb,Rb'	ee/%
Ph	H	H	10
Ph	H	Bu^t	84
Cyclohexane	Me	Bu^t	80
Cyclohexane	OMe	Bu^t	86
Cyclohexane	Bu^t	Bu^t	90
Cyclohexane	$OSi(i\text{-}Pr)_3$	Bu^t	92

Table 1.1: *Enantiomeric excesses recorded with a range of substituents on a Mn salen catalyst, in the epoxidation of 1-phenyl-prop-2-ene [20].*

The presence of bulky substituents at positions Rc and Rc' both renders the structure chiral, and also eliminates this position as a direction for olefin attack. This olefin trajectory is important in mechanisms where a selectively bound state of one or other enantiomer is not observed, since the approach of the olefin over the stereocentre C atoms provides a means of linking the chiralities of the two species. Various other trajectories have been proposed [15,16,21,22], labelled A-D in figure 1.7, though pathway A is favoured according to Jacobsen, by the sterics of the ligand, channelling the olefin into the axial binding site over the cyclohexane group [15]. Along this trajectory, it is forced into close proximity with either of the H atoms that are bound to the stereocentre C atoms, presenting an enantioselective channel through which the olefin must pass.

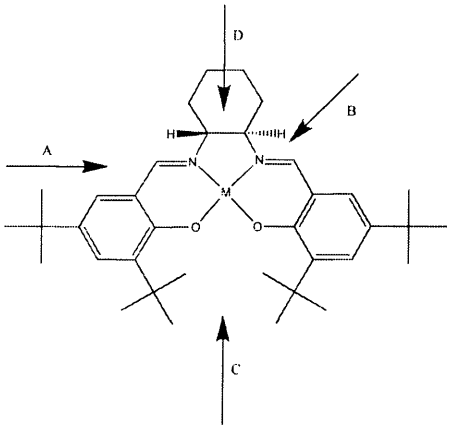

Figure 1.7: *The various proposed olefin attack pathways.*

Besides these steric properties of the ligand, the electronic effects of the catalyst on the ligand are also known to be of great importance in the catalytic process [12]. Enhancements of the yield and enantioselectivity can be achieved by choosing ligands that, as well as playing a steric role in the interaction of the complex and the olefin optimise the electronic environment of the metal centre. Amongst these electronic effects of particular importance is the Jahn-Teller effect, which is particularly relevant to the octahedral geometries adopted by the complexes in catalytic interactions with the axially bound ligand. The Jahn-Teller effect is described in section 1.5.

1.2 Hydrolytic Kinetic Resolution

Where enantiomeric substrates selectively interact with a chiral catalyst, it is possible to selectively alter the reactivities of the enantiomers, allowing the consumption of one, giving optically pure samples of reactant and product with opposite chiral configurations, if the reaction is quenched when maximum purity is reached. This process is known as kinetic resolution, and was discovered in 1899 by Marckwald and McKenzie [23].

This process has been applied in a number of studies [24–28] of epoxides, in which chiral catalysts have been used to bind one enantiomer while the other is hydrolysed, leaving optically pure samples of the epoxide and of the associated diol. With hydrolysis as the means of converting the alternate enantiomer, this process is known as hydrolytic kinetic resolution, HKR. The cobalt salen complex of figure 1.8 is the most popular current catalyst used for preparing enantiomerically pure samples of epoxides and diols.

This technique provides a cheap means of obtaining high purity enantiomer samples, and of controlling the purity required [29, 30].

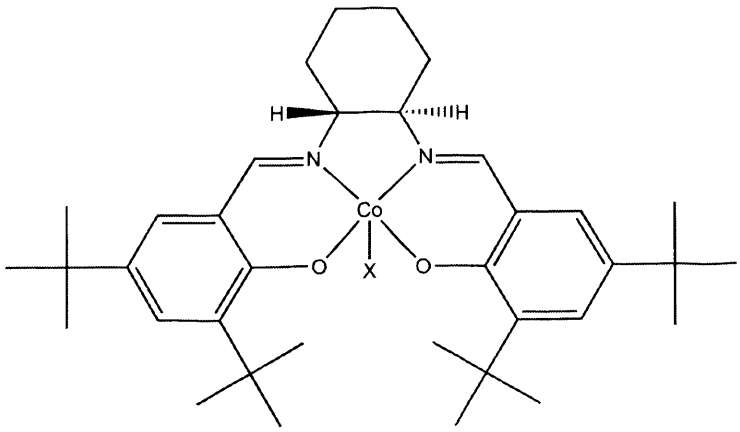

Figure 1.8: *The Co salen compound most commonly used in epoxide HKR.*

1.3 Electron Magnetic Resonance Techniques in Structure Elucidation

As discussed above, electron resonance techniques can be applied to a number of salen based catalyst systems, since many contain paramagnetic transition metal ions. The electron paramagnetic resonance (EPR) technique provides the g-factors, central metal hyperfine interactions, and zero-field splittings, which give detailed information regarding the electronic environment; this is, in many cases, sufficiently sensitive to the nature of the coordinating species and to the binding mechanism to resolve selectivity of binding between enantiomers. It is also possible, using EPR, to study the changes in the electronic environment throughout the catalytic cycle, so pinpointing in some cases the catalytic intermediates.

The subtleties involved in differentiating diastereomeric states can often be demonstrated but not explained using EPR alone, since the perturbation that occurs at the metal centre in switching between enantiomeric interactions is very small. The structures that give rise to such discriminations are also not available through the EPR technique, though they can be probed through analysis of the electron nuclear hyperfine coupling and the nuclear-electric quadrupole interactions of spin-active nuclei in the system (ligand or bound species). A good working model of the mechanism of discrimination is dependent on a knowledge

of such structure relationships, and allows for an improved understanding of the catalytic mechanism.

The electron nuclear double resonance (ENDOR) technique, first reported in 1956 by Feher [31], is able to derive this hyperfine and quadrupole information with much higher spectral resolution than EPR, for reasons discussed in chapter 2, allowing for a thorough picture of the electronic properties (spin and charge densities) of a system to be constructed. It is also possible in an ENDOR experiment to isolate molecular orientations from a frozen solution, thus allowing a complete three-dimensional model of the structure of the system under study to be made. This permits the analysis of systems for which single crystals are not available, and the study of frozen out intermediates along a reaction pathway.

None the less, there have been comparatively few studies that have made use of electron magnetic resonance techniques in determining metal complex-substrate interactions, and in characterising the complex ligands themselves. In those that have been undertaken a range of metals has been used. The manganese salen-type epoxidation catalysts have been investigated by electron magnetic resonance techniques as a means of determining the mechanism of oxo-transfer discussed in section 1.1.2 in a number of studies [32–37]. The effectiveness of the chromium analogue of Jacobsen's catalyst in the epoxidation of *E*-alkenes has made such systems the subject of a similar range of mechanistic EPR studies [38, 39]. Studies of salen complexes of both manganese and chromium are reviewed in reference [40]. The use of vanadium and copper in such spectroscopic studies is discussed at greater length below.

1.3.1 Vanadium

Systems bearing the d^1 VO^{2+} vanadyl ion are among the more extensively studied organometallic complexes in the field of EPR [41–45]. The spin-$\frac{7}{2}$ ^{51}V nucleus has almost 100% abundance and a large nuclear magnetic moment, making it well suited to spectroscopic

studies, both of the biological systems in which it is an important trace element and as an analogue for other first-row transition metal catalysts.

In a number of recent studies, Murphy and co-workers [19, 46, 47] have demonstrated a variety of subtle interaction effects between complexes of VO and their solvents. In the first study [46], the role of strongly coordinating substrates such as pyridine (py) in determining the ratio of *cis*- to *trans*-isomers of bis(acetylacetonato)oxovanadium(IV), $[VO(acac)_2]$, by regulating the equilibrium between them was demonstrated. Figure 1.9 shows the two possible isomers.

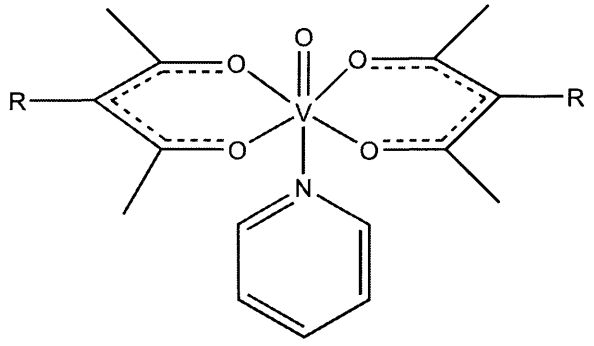

(a) trans

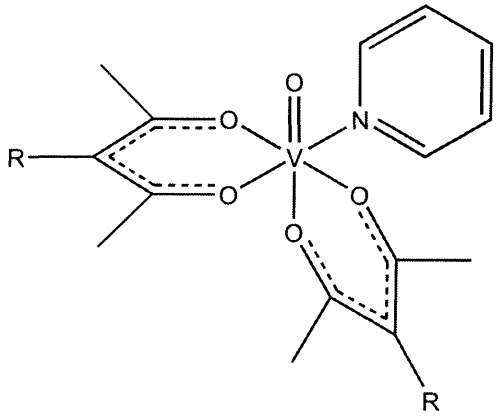

(b) cis

Figure 1.9: *The two possible isomers of $[VO(acac)_2(py)]$, in which the pyridine occupies (a) the axial coordination site, making the two acac ligands occupy trans positions, and (b) an equatorial coordination site, rendering the acac ligands cis. Here, R=H.*

The ENDOR spectra of this solution were interpreted by their differences from the spectra of $[VO(acac)_2]$ in deuterated dichloromethane, for which the distances to the isolated protons in the *R* position of figure 1.9 were found to be 4.40/4.41Å, and to the methyl group protons, 4.32-5.09Å. Simulations which took into account the two possible ligand conformational isomers in the presence of pyridine explain the differing signals in the presence of pyridine. The differences arise from the fact that 60% of the complexes in the solution had the *cis* conformation, suggesting that pyridine favours the equatorial binding site, disrupting the preferred square pyramidal coordination of the complex in a weakly coordinating solvent. These results were supported by density functional theory (DFT) studies of the two isomers, which identified the *cis* conformation as more stable, but only by ~ 3 kJmol^{-1}, explaining the presence of both isomers in frozen solution.

In the second study [47], Murphy *et al.* investigated how the extent to which the VO moiety is raised above the plane of a coordinated salen ligand is affected by coordinating solvent molecules (figure 1.10).

The ENDOR signals that arise from the protons in axial and equatorial positions on the C-C backbone (H^{ax} and H^{eq} in figure 1.10) were identified unambiguously by selective deuteration both in a coordinating solvent (dimethyl formamide, DMF) and a non-coordinating solvent (dichloromethane). The dichloromethane study gave a large degree of inequivalence between the axial proton hyperfine couplings. The values obtained for the two axial positions were $A_{\|}$=3.55 and 4.60MHz, and $A_{\perp}$=-1.65 and -2.75MHz, corresponding to distance of 3.56Å and 3.17Å respectively. The angles formed between the V=O bond and the V-H^{ax} vectors were 60° and 76° respectively. This large discrepancy in the two axial proton signals, implying that the VO moiety occupies a position that is considerably closer (0.39Å) to one than to the other, is consistent with a high degree of pyramidalisation of the moiety above the ligand plane.

In DMF this discrepancy is slightly reduced with the axial protons giving hyperfine couplings of $A_{\|}$=3.35 and 4.30MHz, and $A_{\perp}$=-1.65 and -2.40MHz, corresponding to distances of 3.61Å and 3.27Å respectively, a discrepancy of 0.34Å. The angles also changed, with

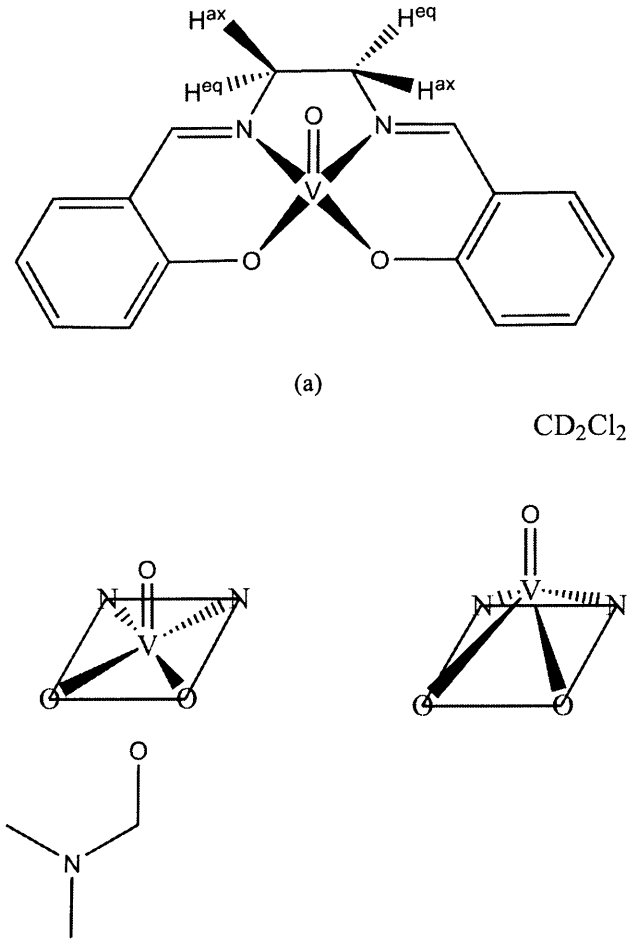

Figure 1.10: *(a) The structure of the [VO(salen)] complex, with axial and equatorial protons (H^{ax} and H^{eq}) labelled. (b) The effect of coordinating (left) vs. non-coordinating (right) solvents on the position of the VO moiety above the ligand pseudo-plane.*

respective values of 80° and 87°. This change indicates a slight pulling of the VO moiety into the ligand plane, as illustrated in figure 1.10 b) by the DMF solvent. Coordination of the DMF was determined by the resolution of proton peaks in the ENDOR spectra of the protic solvent that were absent in the deuterated DMF spectra. This pulling back of the VO, along with the induction/electronic/electrostatic effects of the solvent were resolved in the EPR spectra, with a significant shift in the *g*-tensor values, as listed in table 1.2.

Solvent	g_1	g_2	g_3	g_{iso}
CD_2Cl_2	1.9840	1.9787	1.9524	1.9717
DMF-d_7	1.9810	1.9760	1.9556	1.9709

Table 1.2: *Principal g-tensor components for [VO(salen)] dissolved in CD_2Cl_2 and DMF-d_7 [47].*

These spectroscopic studies were again supported by DFT structural calculations of the two solvent systems, which were found to be in excellent agreement, giving distances and angles for the axial protons of 3.20Å/75° and 3.64Å/57° for the dichloromethane case and 3.48Å/73° and 3.19Å/57° for the DMF case.

In a further study of [VO(salen)] complexes [19], Murphy *et al.* investigated the stereoselective coordination of a chiral epoxide molecule, epoxypropane, to the vanadyl analogue of Jacobsen's catalyst (figure 1.2), [VO(**1**)]. They demonstrated the ability of the ENDOR technique to resolve differences between spectra recorded for the *R,R'*-enantiomer of [VO(**1**)] dissolved in *R- vs. S*-epoxypropane. This implies, by virtue of the differences in coupling constants as well as in peak intensities, differences in the structures of the two complexes in frozen solution. By comparing these spectra to those recorded for *S,S'*-[VO(**1**)] dissolved in both *R*- and *S*-epoxypropane, for which the results of the *R,R'*-complex were mirrored, they demonstrated the preference, at a structural level, for the binding of the 'homochiral' (having the same Cahn-Ingold-Prelog stereochemical assignment) epoxide enantiomer by the complex. This preference was confirmed by DFT calculations on a cut-down model of the complex, which revealed similar geometric dif-

ferences between the homochiral and heterochiral pairings, as well as providing information regarding the spatial positioning of spin-inactive nuclei of the system.

This study revealed the capability of the ENDOR technique, in combination with DFT to provide frozen solution structural information for interacting complexes. It made no mechanistic link between the chirality of the complex and that of the epoxide, and it is with this that chapter 3 of this thesis is primarily concerned.

1.3.2 Copper

Accompanying their description of the angle-selected ENDOR technique, Kreilick *et. al.* [48] included a study of polycrystalline $[Cu(acac)_2]$ [49] (see chapter 2). The powder sample prepared contained approximately 0.5% $[Cu(acac)_2]$ and 99.5% $[Pd(acac)_2]$, arranged in microcrystalline structures as illustrated in figure 1.11.

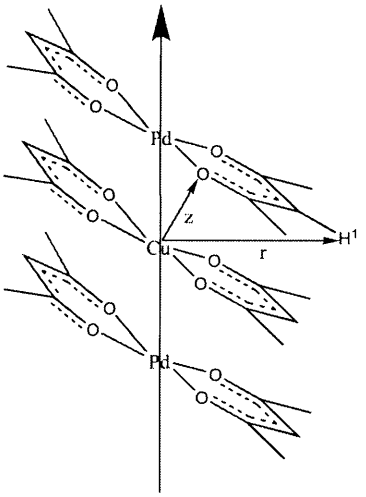

Figure 1.11: *The co-crystalline arrangements of $[Pd(acac)_2]$ and $[Cu(acac)_2]$. The vector linking a copper centre to the isolated proton of a neighbouring $[Pd(acac)_2]$ molecule is labelled r. Also labelled is the molecular z-axis of the $[Cu(acac)_2]$ species, perpendicular to the plane of the molecule.*

The largest coupling they observed in the ENDOR spectra that they recorded was for the extra-molecular methyne proton of neighbouring $[Pd(acac)_2]$ molecules (labelled H^1 in

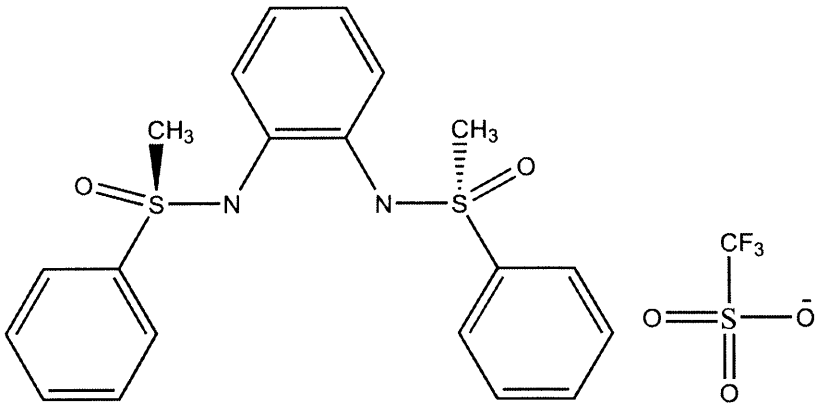

(a) ligand (b) OTf

Figure 1.12: *The structures of ligand* **2** *and the triflate ion, Otf.*

figure 1.11). They recorded spectra for ten successive field values ranging from a value that corresponded to a B-field parallel to the molecular z-axis through several angles intermediate between the z-axis and the $x-y$ plane, and used a least squares procedure to determine a best fit value for $|r|$, for the angle between r and the z-axis, θ and for the isotropic hyperfine coupling, a_{iso}. The values obtained were $r = 3.25$, $\theta = 9.7°$ and $a_{iso} = 0.28$MHz. They thus demonstrated the power of the technique as a means of determining the spacings between molecular species in co-crystals in microcrystalline powder samples.

Extensive studies of Diels-Alder reactions catalysed by a copper(II) catalyst by Bolm *et al.* [50] used a variety of electron magnetic resonance techniques, including hyperfine sublevel correlation spectroscopy (HYSCORE) and pulsed ENDOR to categorise the structural changes of the catalyst that take place during the catalytic cycle. Starting with a complex of [Cu(**2**)$(OTf)_2$], where (**2**) and OTf are as shown in figure 1.12, they detected broad EPR features, implying weak coordination, which became much better resolved on the coordination of the dieneophile *N*-(1-oxoprop-2-en-1-yl)oxazolidin-2-one (figure 1.13).

The parameters resolved for this system, obtained from W-band EPR experiments, of the ^{14}N hyperfine parmaters determined by Davies ENDOR [51], and of the ^{19}F hyperfine in-

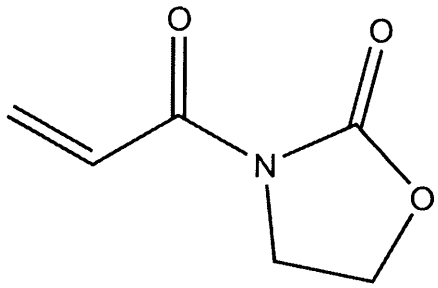

Figure 1.13: *The N-(1-oxoprop-2-en-1-yl)oxazolidin-2-one dieneophile.*

teraction determined by Mims ENDOR [52] were found to correspond to a square planar geometry before coordination of the dieneophile, with the OTf at a distance of ~ 5Å. On coordination, the dieneophile was found to alter the geometry to give a distorted square pyramidal complex, with the OTf ion incorporated into the first coordination sphere of the copper. Since it was known previously [53, 54] that the nature of the counter ion was important in controlling the stereoselectivity, the complex was studied using the same techniques with a range of anions, which revealed radically different coordination geometries for Cl^- and for Br^-, but not for SbF_6^-. This implies that it is the presence of certain anions in the first coordination sphere that is responsible for the stereoselectivity. This links the asymmetry of the coordination sphere to the asymmetry of the coordination of the dieneophile, which leads to an asymmetry in the Diels-Alder process.

These various studies have highlighted the power of electron magnetic resonance techniques in identifying the structures in solution and microcrystalline powders of a range of transition metal complex structures. Several of them have also pointed out the importance of quantum chemical calculations, particularly DFT studies, as a means of providing support for the conclusions drawn on the strength of the spectroscopic studies. It is with the complementary nature of these two techniques as tools for the elucidation of structures in solution that this thesis is concerned.

1.4 Catalysis in Microporous Materials

Microporous materials, including silicate zeolites, silico-alumino-phosphates (SAPOs), and alumino-phosphates (AlPOs) belong to a class of materials which can be prepared and modified to act as heterogeneous catalysts for which a single active catalytic site can be identified, known as single site heterogeneous catalysts, SSHCs [55]. The identity of such sites within the three-dimensional framework of the materials allows for a picture of the various catalytic mechanisms that the given structure participates in. Such mechanistic data can be used to explain the selectivities and catalytic rates that the catalytic system displays, which allows for a systematic improvement of the catalyst. The pore system within the frameworks of such materials allows them to effectively 'sieve' substrates, accounting for high regio-selectivities, while the high surface area of the pores accounts for high catalytic rates.

Catalytic activity can be introduced within the framework by the tethering of an organo-metallic catalytic species. The incorporation of metalloporphyrins, metallosalen and other metallo-molecular complexes within such frameworks has been proposed as a means of preventing dimerisation of the catalyst molecules which inhibits the catalytic activity of the sample. Further heterogeneous catalysis provides a more straightforward means of product separation, and makes for a greater selectivity (by virtue of the narrow framework pores) than the catalyst alone provides. The epoxidation of a range of alkenes was achieved by Jacobs [56] with *cis*-$[Mn(bipyridine)_2]^{2+}$ (figure 1.14) encapsulated within the pores of Zeolite Y, without the decomposition of the peroxide oxidising agent.

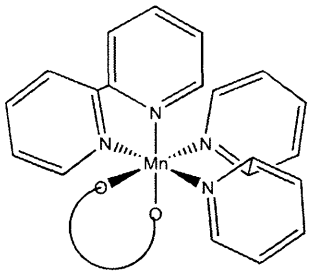

Figure 1.14: *The cis-[Mn(bipyridine)$_2$] complex.*

Herron [57] demonstrated the encapsulation of [Co(salen)] in the zeolite Y pore structure by treating the Co^{II} substituted lattice with the salen ligand. On absorbing pyridine, forming an adduct with the complex, Herron showed that the complex developed a similar affinity for the dioxygen molecule as the same adduct in solution, indicating that the chemistry of the encapsulated species was similar to that of the heterogeneous catalyst.

Alternatively, catalytic activity in zeolite/SAPO/AlPO frameworks can arise from the incorporation of an atomic or ionic species into a framework or extra-framework site. Transition metal ions that are incorporated in this manner, provide easily accessible Brønsted acid sites and redox active centres. The incorporation of metallocene species such as $[Ti(Cp)_2Cl_2]$, where Cp is C_5H_5, and subsequent removal of the Cp and Cl ligands was established by Maschmeyer *et al.* [58] in 1995. They demonstrated the conversion of the titanocene dichloride species into a tripodally bound $Ti^{IV}OH$ active site (figure 1.15) through X-ray absorption spectroscopy supported with DFT calculations.

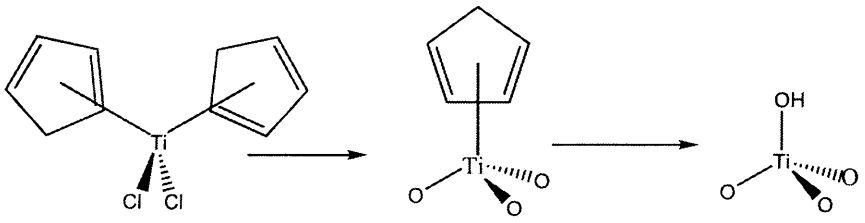

Figure 1.15: *The conversion of $[Ti(Cp)_2Cl_2]$ to a $Ti^{IV}OH$ active site in a mesoporous silicate.*

Similar metallocene species have also been used to incorporate Mo^{VI}, Cr^{VI} and VO^{IV} species in silica materials [59,60].

It is further possible to incorporate transition metal ions on synthesis of the zeolite or AlPO material, to give substituted zeolites and MAlPOs [61]. Having uniformly spaced and dilute metal species, these MAlPO materials are very good examples of SSHCs, and have been produced for a range of metals, including Mg^{II}, Co^{II}, Zn^{II}, and Mn^{II}. They have been applied to the shape-selective conversion of methanol into light olefins, by

the transfer of the acid proton, which loosely attaches to the O atom adjacent to the M^{II} species to balance the charge. There remains some controversy, however, as to how the metal ions are incorporated, whether it is into extra-framework, hydrated sites, or into the tetrahedral framework sites.

Gabelica and Valange [62] have shown that heteroelements that are of a similar size to the phosphorous and aluminium (or silicon) framework species and able to take on a tetrahedral geometry can be incorporated. For Cu^{II} ions however, whose incorporation into such materials has been found to decompose and reduce NO [63], the tetrahedral sites, it has been suggested, represent too compact and distorted a coordination environment. Being subject to the Jahn-Teller effect (section 1.5), however, does allow copper in octahedral environments to elongate one axis, which might, with coordinating water, be expected to allow for smaller perturbations to the lattice structure than a square planar geometry would require.

A recent study by Delabie *et al.* [64] of Cu^{II} ions in mordenite used DFT studies of clusters cut from the framework, to which the Cu^{II} ions were bound in extra framework positions. They based this extra-framework coordination on the fact that the large, electron rich, Cu^{II} ions do not commonly adopt a tetrahedral geometry. They used *g*-tensors calculations at the multiconfigurational perturbation theory level to justify these models, and found good agreement with experiment. The hydrated, charge balanced Cu clusters that they used were able to adopt square planar, trigonal planar or square pyramidal geometries by virtue of being within the pores of the material. On the strength of these results, they concluded that Cu^{II} ions occupy extra framework sites in mordenite. In chapter 4, however, evidence based on DFT calculations both of geometries and of EPR parameters of framework site substituted Cu^{II} ions is presented which supports the idea of such incorporation into the framework of a Cu AlPO.

1.5 The Jahn-Teller Effect

The Jahn-Teller effect is important in the chemistry of many transition metal complex ions, often having a significant impact on their coordination environments, particularly in octahedrally coordinated species. The effect arises from the fact that degeneracies in non-linear molecules lead to instability, as demonstrated by Jahn and Teller [65], and will undergo structural distortion to lift the degeneracy. Octahedral copper(II) complexes, for example, with a d^9 electronic configuration, contain three electrons in degenerate e_g orbitals, giving rise to a degenerate ground state. This degeneracy is lifted by the lengthening (occasionally shortening) of one of the pairs of opposite bonds. This is illustrated in figure 1.16, showing the optimal geometry, with bond lengths labelled, of hexaaqua copper(II).

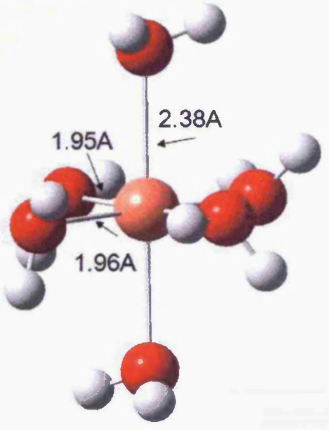

Figure 1.16: *The optimal configuration of hexaaqua copper(II), a typical Jahn-Teller octahedral copper complex. The distortion manifests in an elongation of the Cu-O bonds along the z-axis, and a slight variation in the distances along the x- and y-axes.*

Figure 1.17 illustrates the splitting that occurs most commonly in octahedral copper complexes. The degeneracy between the two d orbitals of e_g symmetry is lifted by raising the energy of the $d_{x^2-y^2}$ orbital, and lowering that of the d_{z^2} orbital, by elongation of the bonds along the z-axis. This elongation also lifts the degeneracy of the three d orbitals of t_{2g} symmetry, raising the energy of the d_{xy} orbital and lowering that of the d_{xz} and d_{yz}

orbitals.

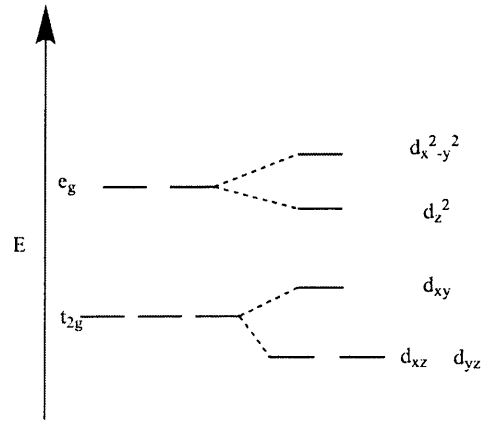

Figure 1.17: *The lifting of the degeneracy of the d-orbitals in an octahedral d^9 copper complex by the Jahn-Teller effect.*

Chapter 2

Theory

2.1 EPR

Electron Paramagnetic Resonance spectroscopy [66] is a powerful technique for probing the chemical environment of open shell systems. The technique makes use of the fact that unpaired electrons can occupy two spin states, whose degeneracy is lifted by their interaction with an external magnetic field. These energy levels are further split by interactions with spin-active nuclei (*e.g.* the single proton of the H-nucleus, which has spin-$\frac{1}{2}$). These energy levels can be probed by irradiating the sample with electromagnetic radiation, sweeping the magnetic field and observing the field values at which absorption takes place due to excitations between levels.

The requirement of an unpaired electron restricts the technique to radical systems, such as organic radicals, in which the electron occupies an isotropic molecular orbital, and so gives rise to an isotropic signal, and open-shell paramagnetic transition metal systems, where the electron normally occupies a molecular orbital which contains a large metal *d*-orbital contribution, and thus gives rise to an anisotropic signal. It is with these transition metal systems that this study is concerned.

Figure 2.1 illustrates the splitting of the electronic energy levels by the magnetic field, the first level splitting to the left of the figure, the levels having energies of $\pm\frac{1}{2}g\mu_B B_0$, where B_0 is the applied magnetic field, g is the electron g-factor, and μ_B is the Bohr Magneton. The splitting which occurs to the right is the splitting of the nuclear energy levels by B_0, giving energy levels of $\pm\frac{1}{2}g_N\mu_N B_0$, where g_N is the nuclear g-factor, and μ_N is the nuclear magneton. The final interaction is between the nucleus and the electron, $\pm\frac{1}{4}ha$, where h is Planck's constant and a is the hyperfine interaction parameter which parameterises the given electron-nuclear interaction. The opposite signs of the charges on the electron and the nuclei mean that they are split by the magnetic field in opposite directions, with opposite signed spins having higher energy levels when exposed to the magnetic field. For this reason, the levels in the upper electron spin manifold move closer together, while those in the lower manifold move further apart. Since only electron spins are excited in the EPR experiment, this means that two EPR excitation energies, as well as the two

NMR excitation energies, differ in magnitude (as labelled EPR1 and EPR2 and NMR1 and NMR2 in figure 2.1), and give rise to the two observed peaks.

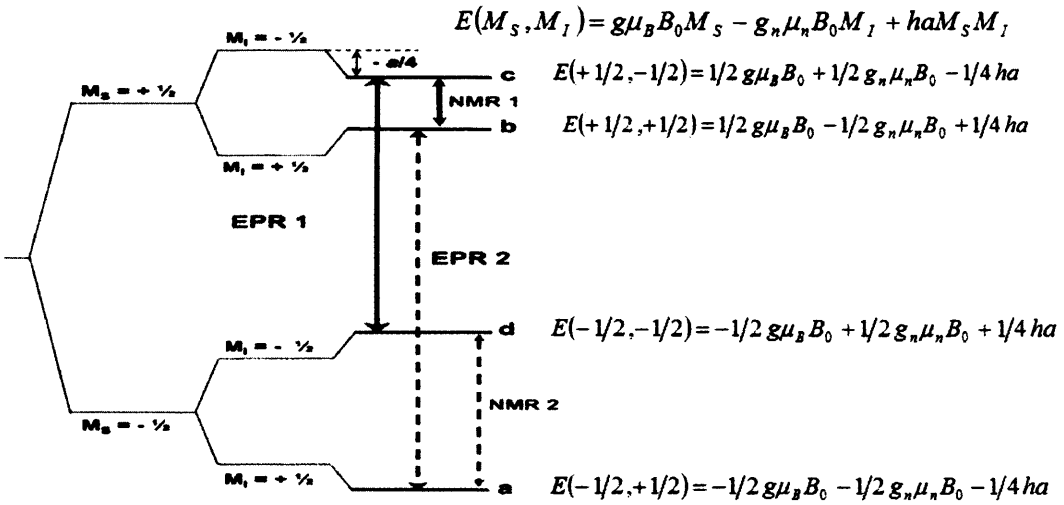

Figure 2.1: *The energy levels of an electron and a single nucleus in a magnetic field. The electronic energy levels are split by the magnetic field, as are the nuclear energy levels, with a further splitting due to the interaction between the two.*

The electronic and nuclear magnetic quantum numbers, M_S and M_I represent the possible projections of the respective spin quantum numbers, S and I onto the magnetic field direction. The energy levels associated with these magnetic quantum numbers are obtained from the spin-Hamiltonian:

$$\hat{H} = \mu_B g B_0 S - \mu_N B_0 g_N I + SAI \tag{2.1}$$

Where S is the electron spin, I is the nuclear spin, g is the g-factor of the system and A is the hyperfine coupling constant of the electron and the nucleus.

The energy levels are:

$$E(M_S, M_I) = g\mu_B B_0 M_S - g_N \mu_N B_0 M_I + haM_I M_S \tag{2.2}$$

which are labelled on figure 2.1.

2.1.1 The g-Factor

The spin of the unpaired electron gives rise to a magnetic moment, μ as well as to a spin angular momentum, L. The ratio of these two values,

$$\gamma_e = \frac{\mu}{L} \tag{2.3}$$

is the magnetogyric ratio, γ_e, which according to classical physics is given by

$$\gamma_e = \frac{q}{2m_e}. \tag{2.4}$$

where m_e is the mass of the electron.

In quantum mechanics, however, this does not hold, since the angular momentum that arises from electron spin is not strictly analogous to the angular momentum of a classical spinning body. The relationship requires a scaling factor, g_e:

$$\gamma_e = \frac{-e}{2m_e} g_e \tag{2.5}$$

g_e is slightly greater than 2, $g_e = 2.0023$ for a free electron [69]. When the electron is subject to magnetic fields other than the externally applied one (such as due to the nuclei or to other electrons), it becomes shielded from the external magnetic field. The shielding parameter $(1 - \sigma)$ is multiplied by the free electron g-factor, g_e to give the g-factor. When the shielding fields are anisotropic, such as in a transition metal d-orbital (or rather a molecular orbital that is dominated by a transition metal d-orbital), due to coupling of the spin and orbital angular momenta, this factor also requires a tensor expression.

2.1.2 Hyperfine Coupling

The interaction of the unpaired electron with spin-active nuclei is known as hyperfine coupling. The factor controlling this interaction appears as the term a in figure 2.1. It consists of two contributions, one isotropic, the Fermi-contact interaction [67], a through

bond term that describes the density of the unpaired electron at the given nucleus, and one anisotropic, which is a magnetic dipole-dipole interaction. The a factor of figure 2.1 becomes, in three dimensions, an A-tensor. The dipole-dipole (anisotropic) contribution is described by the dipole-dipole Hamiltonian:

$$\hat{H}_{DD} = \frac{\mu_0}{2h} g_e \mu_B g_N \mu_N \left[\frac{(3S \cdot r)(r \cdot I)}{|r|^5} - \frac{S \cdot I}{|r|^3} \right] \tag{2.6}$$

where μ_0 is the permeability of free space and r is the vector between the electron and nuclear spins.

On integration over the spatial electron distribution, this becomes:

$$\hat{H}_{DD} = S\hat{T}I \tag{2.7}$$

Where T is the dipolar coupling tensor, whose components are given by:

$$T_{ij} = \frac{1}{2}\alpha_f^2 g_e g_N \mu_B \mu_N \left\langle \psi_0 \right| \frac{3r_i r_j - \delta_{ij}|r|^2}{|r|^5} \left| \psi_0 \right\rangle \tag{2.8}$$

Where $\alpha_f^2 = \frac{\mu_0}{h}$.

This coupling can calculated by expanding $\hat{H}_{DD}$ in powers of $\frac{|r|}{R_k}$, where R_k is the distance between the nuclear centre N and the eth atomic orbital. For $R_k \gtrsim 2.5\mathring{\text{A}}$ this can be approximated as a point dipole using equation 2.9 [68].

$$T = \frac{1}{2}\alpha_f^2 g_e g_N \mu_B \mu_N \sum_{k \neq N} \rho_k (3r_k \cdot r_k - 1)/R_k^3 \tag{2.9}$$

When the unpaired electron is located on a transition metal centre, the spin density of the metal nucleus ρ_M can frequently be taken as unity. This coupling tensor then becomes:

$$T_{ij} = \frac{1}{2}\alpha_f^2 g_e g_N \mu_B \mu_N \left[\frac{3\hat{r}_i\hat{r}_j - \delta_{ij}}{|r|^3}\right] \tag{2.10}$$

Where r is now the vector from the transition metal centre and the (proton) nucleus in question, and $\hat{r}_i$ is the i^{th} component of the unit vector in that direction.

This approximation allows the easy calculation of the distances of the protons of a transition metal complex from the metal centre. The validity of the approximation is limited by requirements of the localisation of the unpaired electron to a spatially small orbital at the metal centre, and of a suitable distance ($|r| \geq 2.5$Å) between the metal centre and the proton under study. Despite these limitations, it has been used in a number of studies [19, 46, 47] to give proton distances generally to within ~ 0.1Å. Application of this approximation thus requires care in ensuring its validity in terms of these limitations, and must be substantiated by some alternative analysis, such as a theoretical geometry calculation.

2.1.3 Simulation of Powder EPR Spectra [70]

A sample EPR spectrum for an anisotropic system is given in figure 2.4. For convenience of locating the peaks, EPR spectra are commonly recorded by taking the derivative of the absorption at each magnetic field value, rather than its magnitude. The expression which describes the spin Hamiltonian in such an anisotropic system, with the incorporation of the quadrupolar moments of any magnetic nuclei, is given in equation 2.11.

$$\hat{H} = \mu_B B_0 g \cdot \hat{S}/h + \sum_i (\hat{S} \cdot A_i \cdot I_i - g_N^i \mu_N^i B_0 \cdot \hat{I}/h + \hat{I} \cdot Q \cdot \hat{I}) \tag{2.11}$$

Where g is the three dimensional g-tensor, A is the A-tensor and Q is the quadrupolar coupling tensor. The sum is over all spin-active nuclei.

The alignment of the magnetic dipoles arising from the electron spins in a powder or solution sample are random and take on all possible directions. If the molecular g-tensor

is taken as the frame of reference, then across the sample the magnetic field vector takes on all possible directions within the frame. The summation of the effects of all of these *B*-field vectors then constitutes the EPR spectrum obtained. Since the magnitude of the field is constant, its effect in any one direction can be described using the angles θ and ϕ, where θ is the angle between the z-axis and the vector from the origin to the current position of the *B*-field vector, and ϕ is the angle between the projection of the *B*-field vector onto the x-y plane and the x-axis, and the net effect on all orientations of the molecule is obtained by integrating over these two angles (see figure 2.2).

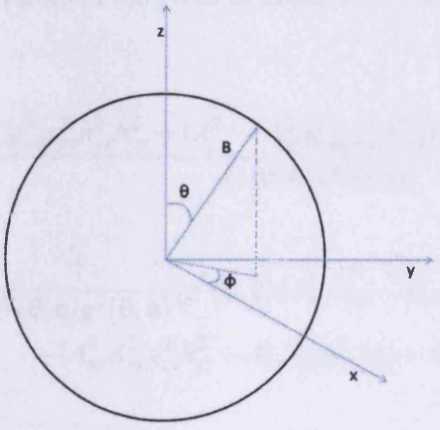

Figure 2.2: *The angles θ and ϕ in the integration of the effect of the B-field over all possible orientations of the molecule in solution. θ is the angle between the B-field vector and the z-axis, ϕ is the angle between the projection of the B-field vector onto the x-y plane and the x-axis.*

The effective g-value in any direction within the frame is given by functions of the direction cosines:

$$h_{xx}^2 = \sin^2\theta\cos^2\phi \tag{2.12}$$

$$h_{yy}^2 = \sin^2\theta\sin^2\phi \tag{2.13}$$

$$h_{zz}^2 = \cos^2\theta \tag{2.14}$$

so that:

$$g^2(\theta,\phi) = g_{xx}^2 h_{xx}^2 + g_{yy}^2 h_{yy}^2 + g_{zz}^2 h_{zz}^2 \tag{2.15}$$

The effective A-value in any direction is given similarly:

$$A^2(\theta,\phi) = \frac{[(A_{xx}g_{xx}h_{xx})^2 + (A_{yy}g_{yy}h_{yy})^2 + (A_{zz}g_{zz}h_{zz})^2]}{g^2(\theta,\phi)} \tag{2.16}$$

First and second order combinations of the A- and g-tensors give the effective first and second order hyperfine values of the given orientation, $K_1(\theta,\phi)$ and $K_2(\theta,\phi)$.

$$K_1(\theta,\phi) = \frac{(A_{xx}^2 - A_{yy}^2)g_{xx}^2 g_{yy}^2 h_{xx}^2 h_{yy}^2 + (A_{yy}^2 - A_{zz}^2)g_{yy}^2 g_{zz}^2 h_{yy}^2 h_{zz}^2 + (A_{xx}^2 - A_{zz}^2)g_{xx}^2 g_{zz}^2 h_{xx}^2 h_{zz}^2}{A^2(\theta,\phi)g^4(\theta,\phi)} \tag{2.17}$$

$$\begin{aligned} K_2(\theta,\phi) = \frac{1}{A^2(\theta,\phi)g^2(\theta,\phi)}[&g^2(\theta,\phi)(A_{xx}^2A_{yy}^2 + A_{xx}^2A_{zz}^2 + A_{yy}^2A_{zz}^2) \\ &-(A_{xx}^2A_{yy}^2g_{zz}^2h_{zz}^2 + A_{xx}^2A_{zz}^2g_{yy}^2h_{yy}^2 + A_{yy}^2A_{zz}^2g_{xx}^2h_{xx}^2)] \end{aligned} \tag{2.18}$$

Applying these to the expressions for the energy levels (equation 2.2) gives, with second order effects incorporated, the following expressions for the two states associated with each value of M_S, and for arbitrary M_I:

$$\begin{aligned} E_1(-\tfrac{1}{2}, M_I) = &-\frac{1}{2}g(\theta,\phi)\mu_B B - \frac{1}{2}M_I A(\theta,\phi) \\ &-\frac{1}{g(\theta,\phi)\mu_B B}[\frac{M_I^2 K_1}{2} + \frac{K_2}{4}(I(I+1) - M_I^2) + \frac{M_I A_{xx}A_{yy}A_{zz}}{4A(\theta,\phi)}] \end{aligned} \tag{2.19}$$

$$\begin{aligned} E_2(\tfrac{1}{2}, M_I) = &\frac{1}{2}g(\theta,\phi)\mu_B B + \frac{1}{2}M_I A(\theta,\phi) \\ &+\frac{1}{g(\theta,\phi)\mu_B B}[\frac{M_I^2 K_1}{2} + \frac{K_2}{4}(I(I+1) - M_I^2) + \frac{M_I A_{xx}A_{yy}A_{zz}}{4A(\theta,\phi)}] \end{aligned} \tag{2.20}$$

The spacing between these energy levels (or spacings, where several nuclei or nuclei with $I > \frac{1}{2}$ give rise to several energy levels) correspond to the frequencies which are absorbed by the sample:

$$h\nu = g(\theta,\phi)\mu_B B + M_I A(\theta,\phi) + \frac{1}{g(\theta,\phi)\mu_B B}[\frac{M_I^2 K_1(\theta,\phi)}{2} + \frac{K_2(\theta,\phi)}{4}(I(I+1) - M_I^2)] \tag{2.21}$$

From this can be determined the resonance frequencies for a given set of input parameters. The standard continuous wave EPR experiment actually involves scanning the magnetic field at a fixed frequency, due to the comparative facility of constructing the electronics for such scanning, since the microwaves used in the experiment must resonate in a fixed sized cavity, and so the resonance magnetic field values are computed from equation 2.21 in simulating such spectra. Onto the peaks are convoluted Gaussian or Lorentzian functions to account for the broadening of the lines.

2.2 ENDOR

Electron Nuclear DOuble Resonance spectroscopy [31] is a technique for probing the interaction between the unpaired electron(s) of a system and the nuclei that have spin $s \geq \frac{1}{2}$. This interaction cannot be investigated *via* EPR spectroscopy, because line-splitting and line-broadening effects give rise to high spectral densities, which makes their resolution very low. Further, the NMR technique is not suitable as the presence of the unpaired electron(s) causes the NMR line-widths to broaden considerably. The solution that the ENDOR technique offers is to detect the NMR signal *via* changes in the intensity of the EPR signal.

The energy levels associated with a paramagnetic species in a magnetic field have populations that obey a Boltzmann distribution, which depends on the energy difference between the two states (equation 2.22).

$$\frac{N_1}{N_2} = \exp\left[-\frac{E_1 - E_2}{kT}\right] \tag{2.22}$$

Where $\frac{N_1}{N_2}$ is the ratio of the populations of levels 1 and 2, $E_1 - E_2$ is the energy differ-

ence between the levels, k is the Boltzmann constant, and T is the temperature of the experiment.

The splitting of the electronic energy levels in a magnetic field are thus given by equation 2.23.

$$\frac{N_1}{N_2} = \exp\left[-\frac{g\mu_B B_0}{kT}\right] \tag{2.23}$$

Which can be approximated at the typical fields of $\sim 10^{-1}T$ and temperatures of $\sim 10K$ by equation 2.24.

$$\frac{N_1}{N_2} \approx 1 - \frac{g\mu_B B_0}{kT} = 1 - \varepsilon \tag{2.24}$$

The differences between the nuclear spin levels can be neglected in this treatment [71], since they are approximately three orders of magnitude smaller, due to the differences between the Bohr and nuclear magnetons. These populations, obtained on placing the sample in a magnetic field, are labelled for a simple $s = \frac{1}{2}$, $I = \frac{1}{2}$ system in figure 2.3 a).

In the ENDOR experiment, one line of the EPR spectrum is saturated by maintaining a steady magnetic field and microwave frequency at the values associated with the chosen EPR transition (figure 2.3 b)). This saturation equalises the populations of the upper and lower electronic energy levels in the lower nuclear spin state, levels A and C, and reduces the intensity of the absorption of the saturating radiation until only a trace signal is observed. When the NMR radio frequencies are scanned, and the NMR transitions, as illustrated in figure 2.3 c) and d), are excited, the population difference between levels A and C are restored, the previously saturated EPR transition is restored, and a signal is observed. The nuclear transition frequencies are thus observed by their effect on the (higher frequency) EPR transition, a process known as quantum transformation, which gives rise to an improvement in resolution of approximately three orders of magnitude. In this way,

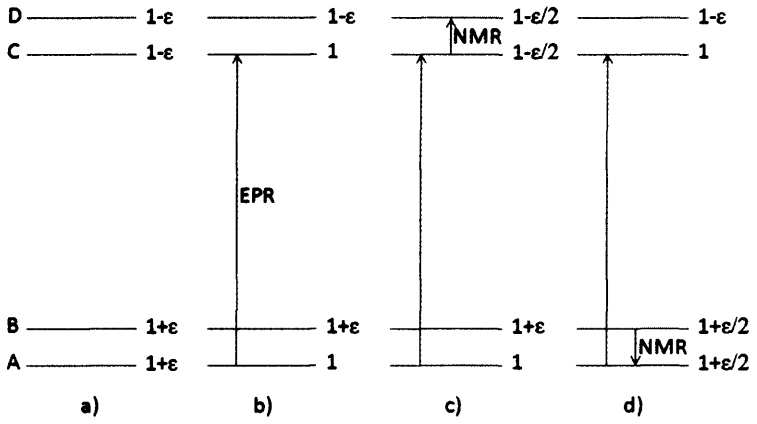

Figure 2.3: *A four level energy diagram, demonstrating the ENDOR experiment. Levels A and B are the nuclear spin levels of the lower electron spin manifold, C and D of the upper electron spin manifold. The relative populations of each level are given for every step in the process, where* $\varepsilon = \frac{g\mu_B B_0}{kT}$. *The steps in the experiment are a) the splitting of the energy levels by the application of a magnetic field, b) the saturation of one of the EPR transitions to equalise level A and C populations, c) the de-saturation of the EPR signal by excitation of the C-D NMR transition, and d) the de-saturation of the EPR signal by excitation of the A-B NMR transition.*

a signal is obtained only for those NMR transitions that are maintained by saturation of the given EPR transition, consisting of two peaks per group of equivalent nuclei, one occurring at high field, one at low field, separated by the hyperfine coupling constant a, and centred on the frequency that would be expected for the particular nucleus to show resonance at, in the absence of the unpaired electron, the nuclear Larmor frequency (equation 2.25).

$$\nu_N = \frac{g_N \mu_N}{\hbar} B \tag{2.25}$$

In powders and solutions [72], the EPR signal is composed, as discussed in section 2.1.3, of signals arising from every possible alignment of the molecule under study with respect to the magnetic field. In transition metal complexes, where the g- and A-tensors are not isotropic, the spectrum contains contributions from all possible linear combinations of the three g-tensor principal components. By saturating an EPR transition that corresponds to one particular principal component and exciting the NMR transitions only in those molecules which have this component of their g-tensor aligned with the B-field, individual components of the hyperfine tensor can be extracted from the ENDOR spectra. This requires the identification of the turning points of the EPR spectrum, in order to choose the line to saturate.

Figure 2.4 illustrates the turning points in an axial transition metal EPR spectrum of $VO(acac)_2$ (for which $g_{xx} = g_{yy}$, $A_{xx} = A_{yy}$), for which the hyperfine coupling parallel to the molecular z-axis, $A_{\|} = A_{zz}$ is greater than that in the x-y plane, $A_{\perp} = A_{xx} = A_{yy}$.

The dashed lines in figure 2.4 label the spectral lines which originate purely from molecules for which the B-field aligns parallel (far left) and perpendicular (right of the centre) to the z-axis of the g-tensor. These are determined with reference to the angular dependency graphs plotted underneath the EPR spectrum, which link the parallel and perpendicular components of each $\delta I = \pm 1$ transition. They are obtained by determining the angular dependence of the resonance magnetic field *via* equation 2.26.

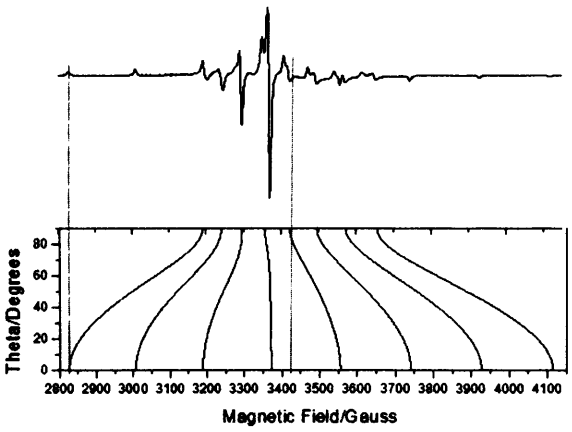

Figure 2.4: *The EPR spectrum of an axial species ($VO(acac)_2$). The dashed lines illustrate lines which originate purely from molecules for which the B-field aligns parallel (far left) and perpendicular (right of the centre) to the z-axis of the g-tensor.*

$$B(\theta) = h\nu - \frac{hIA(\theta)}{g(\theta)\mu_B} \tag{2.26}$$

Where the angle θ is the angle between the z-axis and the B-field, I is the nuclear spin, ν is the static microwave frequency and h is Planck's constant.

Having thus identified lines on the EPR spectrum due to individual transitions, the ENDOR spectra for the perpendicular and parallel directions can be obtained. The alignment of the hyperfine tensor associated with each of the nuclei is not necessarily the same as that of the g-tensor, and the alignment of the B-field with the hyperfine tensor of any given nucleus can give rise to more than a single pair of peaks in either or both of the spectra recorded with the B-field parallel or perpendicular to the molecular z-axis, but to a pair of peaks associated with each.

For molecules of rhombic symmetry, the above discussion must be extended to include three distinct principal values of the g- and A-tensors [70].

2.2.1 Simulation of Powder ENDOR Spectra

The accurate identification of the pairs of peaks, in terms of the hyperfine coupling associated with each, and which nucleus gives rise to each requires, for an axially symmetric EPR system, simultaneous simulation of the parallel and perpendicular ENDOR spectra. The simulation of the spectrum proceeds as follows:

Firstly the resonance frequencies must be calculated. With a knowledge of the g-tensor obtained *via* simulation of the associated EPR spectrum, these can be calculated by equation 2.27.

$$\nu_{\pm} = \left[\sum_{i=1}^{3}\left[\frac{m_s}{g(\theta,\phi)}\left(\sum_{j=1}^{3} g_j h_j A_{ji}\right) - h_i \nu_N\right]^2\right]^{1/2} \tag{2.27}$$

Where $\nu_{\pm}$ refers to the resonances that occur at a frequency of $\frac{a}{2}$ above and below the nuclear Larmor frequency, ν_N, A_{ji} are the components of the A-tensor of the given nucleus, the h_i are the direction cosine functions, and the process is repeated for all values of the electron magnetic quantum number, m_s.

With these frequencies obtained, the spectral peaks can be located on the spectrum. The magnitude of each resonance, however, must be determined by the probabilities of the transition taking place. A more detailed description of this process is given in the discussion of the ENDOR simulation code development, in chapter 5.

2.3 Quantum Chemistry

2.3.1 Molecular Orbitals

The purpose of quantum chemical calculations is to describe the properties of a system (atoms, molecules, crystals, complexes, ions, etc.) that arise from its electronic wavefunc-

tion, Ψ. The wavefunction is a mathematically abstract construction from which all of the properties of the system can be extracted [73], with the electronic wavefunction, insofar as it can be extracted from the nuclear wavefunction (an approximation which holds due to the widely differing masses of the electrons and nuclei), containing the electronic information of the system. Properties are extracted using operators, which isolate the given property, and thus extract it on integration. The most commonly required property of any system is the energy, largely because minimising the energy with respect to the nuclear positions gives the optimum conformation. The energy is obtained *via* the Schrödinger equation [74]:

$$\hat{H}\Psi = E\Psi \tag{2.28}$$

Which is solved for the energy, E, *via*:

$$E = \frac{\int \Psi^{\star} \hat{H} \Psi d\tau}{\int \Psi^{\star} \Psi d\tau} \tag{2.29}$$

for which the integrals are evaluated in volume elements of $d\tau$ over all space.

$\hat{H}$ in equations 2.28 and 2.29 is the Hamiltonian operator, whose form (in atomic units, in which the electron charge and mass, the Planck constant and the Bohr radius, a_0 are defined as unity) is given in equation 2.30:

$$\hat{H} = -\frac{1}{2}\sum_{I=1}^{N}\frac{1}{M_I}\nabla_I^2 + \sum_{I=1}^{N}\sum_{J>I}^{N}\frac{Z_I Z_J}{R_{IJ}} - \frac{1}{2}\sum_{i=1}^{n}\nabla_i^2 + \sum_{i=1}^{n}\sum_{j>i}^{n}\frac{1}{r_{ij}} - \sum_{i=1}^{n}\sum_{I=1}^{N}\frac{Z_I}{r_{iI}} \tag{2.30}$$

where M_I are the nuclear masses, Z_I are the nuclear charges, R_{IJ} is the vector between nucleus I and nucleus J, r_{ij} is the vector between electrons i and j, r_{iI} is the vector between electron i and nucleus I, and ∇^2 is the Laplacian operator. I,J refer to each of the N nuclei, and i,j to each of the n electrons.

The first two terms in equation 2.30 are the nuclear kinetic energy and nuclear-nuclear

repulsion energy respectively, which, under the aforementioned separation of electronic and nuclear wavefunctions can be added after solution of the electronic wavefunction (in fact, the kinetic energy of the nuclei is often neglected, since clamped nuclear geometries are required for the calculation of many properties, including optimum electronic configuration), whose Hamiltonian contains only the remaining three terms, respectively the electronic kinetic energy, the electron-electron repulsion and the electron-nuclear attraction energies (equation 2.31).

$$\hat{H}_{el} = -\frac{1}{2}\sum_{i=1}^{n}\nabla_i^2 + \sum_{i=1}^{n}\sum_{j>i}^{n}\frac{1}{r_{ij}} - \sum_{i=1}^{n}\sum_{I=1}^{N}\frac{Z_I}{r_{iI}} \tag{2.31}$$

A complication to this 3n-dimensional problem arises from the construction of a relativistically invariant version of the Schrödinger equation, or, conceptually, from the requirement of a fourth quantum number to describe the role of electron magnetic moment in atomic spectroscopy, the electron spin. Spin allows two electrons to occupy a single spatial orbital, and so is introduced into the Schrödinger equation *via* two spin functions, $\alpha(\omega)$ and $\beta(\omega)$, of the spin variable ω, which takes values of $\pm\frac{1}{2}$. These functions are orthonormal, *i.e.*

$$\int \alpha^*(\omega)\alpha(\omega)d\omega = \langle\alpha|\alpha\rangle = 1 \tag{2.32}$$

$$\langle\beta|\beta\rangle = 1 \tag{2.33}$$

and

$$\langle\alpha|\beta\rangle = \langle\beta|\alpha\rangle = 0 \tag{2.34}$$

The shorthand notation $\langle\alpha|\alpha\rangle$ is known as Dirac notation [75].

The wavefunction is thus a function of n sets of four co-ordinates, $\underline{x} = \{\underline{r}, \omega\}$:

$$\Psi = \Psi(\underline{x}_1, \underline{x}_2, ..., \underline{x}_n) \tag{2.35}$$

Solution of this many body problem for Ψ requires numerical solution, the simplest form of which was devised by Hartree [76], and later improved by Fock [77]. To account for the anti-symmetric requirement of the wavefunction they pointed out that the sign of Ψ must change on the exchange of two identical particles:

$$\Psi(\underline{x}_1, \underline{x}_2, ..., \underline{x}_i, ..., \underline{x}_j, ...\underline{x}_n) = -\Psi(\underline{x}_1, \underline{x}_2, ..., \underline{x}_j, ..., \underline{x}_i, ...\underline{x}_n) \tag{2.36}$$

The simplest approach to solving this problem is to first construct molecular orbitals as linear combinations of atomic orbitals (LCAO) [78], *i.e.*

$$\psi_i = \sum_{\mu} c_{i\mu}\phi_\mu \tag{2.37}$$

Where $c_{i\mu}$ is the coefficient of atomic orbital ϕ_μ in molecular orbital ψ_i. Molecular spin orbitals, here denoted $\chi(j)$, are the product of spatial orbitals $\phi(j)$ and spin orbitals $\alpha(j)$ or $\beta(j)$, where j is the index of the electron that occupies the given orbital.

These can be combined into the all-electron wavefunction using a simple product (the Hartree product):

$$\Psi(1,2,3,...,n) = \chi_1(1)\chi_2(2)\chi_3(3)...\chi_n(n) \tag{2.38}$$

However this does not satisfy the anti-symmetry requirement of equation 2.36. The simplest means of meeting this requirement is to exploit the properties of the matrix determinants. For example, the determinant for a two electron system is given by equation 2.39:

$$\Psi = \frac{1}{\sqrt{2}} \begin{vmatrix} \chi_1(1) & \chi_2(1) \\ \chi_1(2) & \chi_2(2) \end{vmatrix} \tag{2.39}$$

Which on expansion gives:

$$\Psi = \frac{1}{\sqrt{2}}(\chi_1(1)\chi_2(2) - \chi_2(1)\chi_1(2)) \tag{2.40}$$

Which satisfies the anti-symmetry requirement, since the interchange of two rows of a determinant reverses its sign. The general form of the determinant is given in equation 2.41:

$$\Psi = \frac{1}{\sqrt{n}} \begin{vmatrix} \chi_1(1) & \chi_2(1) & \cdots & \chi_n(1) \\ \chi_1(2) & \chi_2(2) & \cdots & \chi_n(2) \\ \vdots & \vdots & \ddots & \vdots \\ \chi_1(n) & \chi_2(n) & \cdots & \chi_n(n) \end{vmatrix} \tag{2.41}$$

Using this wavefunction in equation 2.29 gives an energy associated with the wavefunction. The coefficients $c_{i\mu}$ can then be optimised in accordance with the variational principle, which states that any adjustment which causes a reduction in the energy is an improvement of the wavefunction as an approximation of the ground-state wavefunction for the given basis set of atomic orbitals. Care must taken to avoid local minima, *e.g.* by providing a sufficiently accurate starting guess. Incorporation of extra atomic basis functions then reduces the energy further, *i.e.* improves the wavefunction, but for a higher computational cost.

In solving equation 2.29, the Hamiltonian (equation 2.31) is divided into one-electron terms (kinetic energy and electron-nuclear attraction), which give rise to integrals involving the coordinates of one electron, and two-electron terms, the electron-electron interaction:

$$\sum_{i=1}^{n} \sum_{j>i}^{n} \frac{1}{r_{ij}} \tag{2.42}$$

Taking as an example the ground-state wavefunction of the hydrogen molecule, the Slater determinant is expanded to give:

$$\Psi = \begin{vmatrix} 1\sigma_g(1)\alpha(1) & 1\sigma_g(1)\beta(1) \\ 1\sigma_g(2)\alpha(2) & 1\sigma_g(2)\beta(2) \end{vmatrix} = [1\sigma_g(1)\alpha(1)1\sigma_g(2)\beta(2) - 1\sigma_g(1)\beta(1)1\sigma_g(2)\alpha(2)] \tag{2.43}$$

Where $1\sigma_g = A(1S_A + 1S_B)$ is the bonding gerade σ molecular orbital, and $1S_A$ and $1S_B$ are s-type functions on nuclei A and B respectively Applying this to the two-electron part of the Hamiltonian, equation 2.42 gives:

$$\begin{aligned} &\int\int d\tau_1 d\tau_2 1\sigma_g(1)1\sigma_g(2)(\tfrac{1}{r_{12}})1\sigma_g(1)1\sigma_g(2) \times \int d\omega_1 \alpha(1)\alpha(1) \int d\omega_2 \beta(2)\beta(2) + \\ &\int\int d\tau_1 d\tau_2 1\sigma_g(1)1\sigma_g(2)(\tfrac{1}{r_{12}})1\sigma_g(1)1\sigma_g(2) \times \int d\omega_2 \alpha(2)\alpha(2) \int d\omega_1 \beta(1)\beta(1) - \\ &\int\int d\tau_1 d\tau_2 1\sigma_g(1)1\sigma_g(2)(\tfrac{1}{r_{12}})1\sigma_g(1)1\sigma_g(2) \times \int d\omega_1 \alpha(1)\beta(1) \int d\omega_2 \alpha(2)\beta(2) - \\ &\int\int d\tau_1 d\tau_2 1\sigma_g(1)1\sigma_g(2)(\tfrac{1}{r_{12}})1\sigma_g(1)1\sigma_g(2) \times \int d\omega_1 \alpha(1)\beta(1) \int d\omega_2 \alpha(2)\beta(2) \\ &= 2 \times \int\int d\tau_1 d\tau_2 1\sigma_g(1)1\sigma_g(1)(\tfrac{1}{r_{12}})1\sigma_g(2)1\sigma_g(2) + 0 \end{aligned} \tag{2.44}$$

Where the orthogonality condition has been used to identify those integrals which give a zero result.

By equations 2.32 to 2.34 the non-zero terms are the first two terms, which represent the repulsion between the regions of electron density associated with each electron. This is the Coulombic repulsion between the two electrons.

The second two terms both equal zero due to the orthogonality of the α and β spin functions. In triplet hydrogen, for which the Slater determinant is:

$$\begin{vmatrix} 1\sigma_g(1)\alpha(1) & 1\sigma_u(1)\alpha(1) \\ 1\sigma_g(2)\alpha(2) & 1\sigma_u(2)\alpha(2) \end{vmatrix} \tag{2.45}$$

these terms persist as:

$$-\int\int d\tau_1 d\tau_2 1\sigma_g(1)1\sigma_u(2)(\tfrac{1}{r_{12}})1\sigma_u(1)1\sigma_g(2) \times \int d\omega_1 \alpha(1)\alpha(1) \int d\omega_2 \alpha(2)\alpha(2)$$
$$-\int\int d\tau_1 d\tau_2 1\sigma_u(1)1\sigma_g(2)(\tfrac{1}{r_{12}})1\sigma_g(1)1\sigma_u(2) \times \int d\omega_1 \alpha(1)\alpha(1) \int d\omega_2 \alpha(2)\alpha(2)$$
$$= -2\int\int d\tau_1 d\tau_2 1\sigma_g(1)1\sigma_u(2)(\tfrac{1}{r_{12}})1\sigma_u(1)1\sigma_g(2) \quad (2.46)$$

This interaction involves the exchange of two electrons, and has no classical analogue. It is known as the exchange interaction and occurs only between electrons of parallel spin, and causes such pairs of electrons to avoid each other, creating an *exchange hole* around each electron.

This treatment of the wavefunction, in which the atomic orbital coefficients are optimised to give the lowest energy wavefunction for which the field produced by and acting on the electrons is self-consistent (SCF treatment), does not correlate electron motions beyond the creation of exchange holes. The empirical cusp in the probability of finding another electron very close to any electron is not accounted for in this simple Hartree-Fock (HF) method. Account of this correlation requires the inclusion of excited state determinants into the ground state wavefunction, with excitations mixed in either perturbatively (Møller-Plesset perturbation theory [79]) or *via* excitation operators (configuration interaction [80] and coupled-cluster [81]). Alternatively, it can be calculated from the electron density using density functional theory.

2.3.2 Basis Set Superposition Error

As mentioned above, the incorporation of extra basis functions in a calculation improves the accuracy of the calculation. This can actually be a problem when calculating the energy of the interaction between two fragments, thanks to what is known as basis set superposition error (BSSE).

The simplest possible means of calculating the energy of the interaction between two fragments A and B is to subtract the energies of each fragment in isolation from that of

the interacting pair:

$$\Delta E_{int} = E^{AB} - E^{A} - E^{B} \tag{2.47}$$

Where ΔE_{int} is the energy of the interaction, E^{AB} is the energy of the interacting pair and E^{A} and E^{B} are the energies of each of the fragments in isolation.

The problem with this procedure is that when the two fragments are combined for the calculation of E^{AB} each is able to make use of the basis functions of the other, so lowering its own energy, in a way that it is unable to in the monomer calculations. This renders the comparison of the pair and individual energies invalid, and the total amount by which the fragments are able to reduce their energies in the pair calculation is called the BSSE. Using superscripts $\{\alpha\}$ and $\{\beta\}$ to denote the basis sets applied to fragments A and B respectively, and $\{\alpha\beta\}$ to denote the total basis incorporating the basis functions of basis α and β, this means that:

$$\Delta E_{int}(R) = E^{\{\alpha\beta\}AB}(R) - E^{\{\alpha\}A}(R) - E^{\{\beta\}B}(R) + BSSE \tag{2.48}$$

where R is the distance between A and B,

The most common means of avoiding the problems that arise from the BSSE is to calculate the energies of each fragment in the basis set of the complete pair, with the electrons and nuclear charges of the other fragment removed, in what is known as the counterpoise (cp) procedure [82].

$$\Delta E_{int}^{cp}(R) = E^{\{\alpha\beta\}AB}(R) - E^{\{\alpha\beta\}A}(R) - E^{\{\alpha\beta\}B}(R) \tag{2.49}$$

where $E^{\{\alpha\beta\}A}(R)$ and $E^{\{\alpha\beta\}B}(R)$ are the respective energies of monomers A and B obtained using the full dimer basis $\{\alpha\beta\}$ at the geometries of each monomer in the complex AB.

BSSE then is estimated as the difference between the corrected and uncorrected interaction energies, $\Delta E_{int}(R) - \Delta E_{int}^{cp}(R)$.

2.3.3 DFT

Density functional theory attempts to calculate the electronic structure of atoms and molecules using, instead of the n-electron, (*i.e.* 3n-dimensional) wavefunction, the 3-dimensional electron density, $\rho(\underline{r})$. The theoretical key to the theory is in the Hohenberg-Kohn theorems [83] which state that the electronic energy (and, indeed, any observable property) of any system is a unique functional of the electron density, (equation 2.50) and that the minimum ground state energy is obtained for the ground state electron density.

$$E[\rho(\underline{r})] = \langle \Psi | \hat{H} | \Psi \rangle \tag{2.50}$$

The actual functional form of the relationship between the energy and the electron density is not provided by the Hohenberg-Kohn theorems, and indeed is not known. The Kohn-Sham theory [84] allows approximations to its form to be made by partitioning the energy into electronic kinetic energy, Coulombic electron-electron repulsion and exchange and correlation energies. The kinetic energy of a system of non-interacting electrons, $T_s[\rho(\underline{r})]$ can be found exactly, and to this system is applied an external potential, $\nu(\underline{r})$, which reproduces the ground state electron density of the system in question (equation 2.51).

$$E[\rho(\underline{r})] = T_s[\rho(\underline{r})] + J[\rho(\underline{r})] + \int \nu(\underline{r})\rho(\underline{r})d\underline{r} + E_{xc}[\rho(\underline{r})] \tag{2.51}$$

The Coulombic energy ($J[\rho(\underline{r})]$) is classical, and easily obtained, leaving the exchange and correlation term, $E_{xc}[\rho(\underline{r})]$. The form of this is unknown, and so must be approximated using functionals which are, in general, fitted to data sets. A large number of functionals is available, to approximate the exchange and correlation energies.

Functionals

The simplest approach to DFT is to assume that the exchange and correlation are functionals only of the electron density, the local spin density approximation (LSDA). More sophisticated methods incorporate some dependence on the gradient of the electron density, $\nabla\rho(\underline{r})$ in the generalised gradient approximation (GGA). A common LSDA expression for the exchange functional is due to Slater [85]:

$$E_x[\rho_\alpha(\underline{r}),\rho_\beta(\underline{r})] = -\frac{3}{2}(\frac{3}{4\pi})^{\frac{1}{3}}\int(\rho_\alpha^{4/3}(\underline{r})+\rho_\beta^{4/3}(\underline{r}))d\underline{r} \tag{2.52}$$

Where ρ_α and ρ_β are the α and β spin densities respectively.

A common LSDA functional for the correlation energy (whose form is more complicated) is due to Vosko, Wilk and Nusair (VWN) [86]:

$$\begin{aligned} E_c[\rho(\underline{r})] = \int\rho(\underline{r})\times\frac{A}{2}\{&\ln\frac{x^2}{X(x)}+\frac{2b}{Q}tan^{-1}\frac{Q}{2x+b}-\frac{bx_0}{X(x)} \\ &[\ln\frac{(x-x_0)^2}{X(x)}+\frac{2(b+2x_0)}{Q}tan^{-1}\frac{Q}{2x+b}]\} \end{aligned} \tag{2.53}$$

Where $x = r_s^{1/2}$, $r_s^3 = \frac{3}{4\pi\rho(\underline{r})}$, $X(x) = x^2+bx+c$, $Q = (4c-b^2)^{1/2}$, with $A = 0.0621814$, $x_0 = -0.409286$, $b = 13.0720$, and $c = 42.7198$. A, b, c and x_0 are parameters which have been adjusted to fit observed properties.

A common GGA functional (incorporating the gradient of the electron density) for the exchange is due to Becke (B88) [87]:

$$E_x[\rho(\underline{r})] = E_x^{LSDA}[\rho(\underline{r})] - b\sum_{\sigma=\alpha,\beta}\int\rho_\sigma^{4/3}\frac{x_\sigma^2}{(1+6bx_\sigma sinh^{-1}x_\sigma)}d\underline{r} \tag{2.54}$$

Where $x_\sigma = \frac{|\nabla\rho_\sigma|}{\rho_\sigma^{4/3}}$, and $E_x^{LSDA}[\rho(\underline{r})]$ is the LSDA exchange functional of Slater (equation 2.52).

Finally, a common GGA correlation functional is due to Lee, Yang and Parr (LYP) [88]:

$$E_c[\rho(\underline{r})] = -a\int \frac{1}{1+d\rho^{-1/3}}\{r + b\rho^{-2/3}[C_F\rho^{5/3} - 2t_W + (\frac{1}{9}t_W + \frac{1}{18}\nabla^2\rho)e^{-cr^{-1/3}}]\}d\underline{r} \tag{2.55}$$

Where $t_W = \sum_{i=1}^{n} \frac{|\nabla\rho_i(\underline{r})|^2}{\nabla\rho_i(\underline{r})} - \frac{1}{8}\nabla^2\rho$, $C_F = \frac{3}{10}(3\pi^2)^{2/3}$, $a = 0.049$, $b = 0.132$, $c = 0.2533$, and $d = 0.349$ are parameters that have been optimised to fit a range of experimental data.

The combination, for example, of these last two functionals to calculate exchange *via* Becke's functional and correlation *via* that of Lee, Yang and Parr is referred to as BLYP. Combinations of any exchange functional with any correlation functional are denoted similarly, using abbreviations based on the authors' surnames.

Hybrid DFT

It is worth noting that the exchange as calculated by the Hartree-Fock (HF) procedure is exact, and reasonably computationally cheap to obtain. For this reason a number of methods exist to incorporate HF exchange into DFT calculations. Most popular of these is the B3LYP functional [89], which uses an empirically parameterised combination of the B88 exchange functional, HF exchange, and the VWN and LYP correlation functionals:

$$E_{xc} = AE_x^{LSDA} + (1-A)E_x^{HF} + B\Delta E_x^{B88} + CE_c^{LYP} + (1-C)E_c^{VWN} \tag{2.56}$$

Other important hybrid functions are the BHandH functional [90] (equation 2.57),

$$E_{xc} = \frac{1}{2}E_x^{LSDA} + \frac{1}{2}E_x^{HF} + E_c^{LYP} \tag{2.57}$$

and the BHandHLYP functional [90] (equation 2.58).

$$E_{xc} = \frac{1}{2}E_x^{LSDA} + \frac{1}{2}E_x^{HF} + \frac{1}{2}\Delta E_x^{B88} + E_c^{LYP} \tag{2.58}$$

Periodic DFT

Solid state crystalline materials consist of infinitely repeating three-dimensional cells. It is naturally impossible to perform any sort of quantum chemical calculation on an infinite number of atoms, and extremely difficult to do so even for a large number (more than approximately 200) of heavy atoms at a DFT level, with current computational limitations. The calculation of solid state properties thus relies on the repeating nature of such structures, by performing the computation on a simple repeating unit (unit cell) of the structure within the field of the infinitely repeating crystal. A restriction that is placed on the calculated wavefunction is that the electron density ($\psi^*\psi$) be repeated for each unit cell of the structure, thus the wavefunction of only one unit cell need be obtained (within the field provided by its infinite images) to determine any observable properties of the crystal.

The flexibility of using the density (the simplest observable property of the wavefunction) allows the wavefunction in any unit cell to be positive or negative, or even imaginary, without affecting this density. This allows a series of states to be built up, of which the lowest energy state is that for which the bonding interaction between neighbouring cells is maximised. States of increasing energy occur in which periodic anti-bonding interactions in each direction gradually increase, to the maximum energy state, that which maximises the anti-bonding interaction between cells. This is represented schematically for the *s* orbitals of a one dimension array of atoms in figure 2.5. The corresponding band of states is also given.

The electronic wavefunction must therefore incorporate a wave-like part to represent the sign of the cell wavefunction in each cell, as well as including the cell wavefunction itself. This gives rise to the Bloch expression for the wavefunction [91] (equation 2.59).

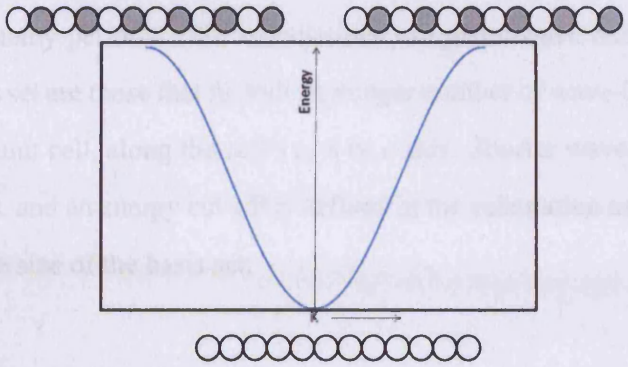

Figure 2.5: *Schematic representation of a linear array of atomic s orbitals, combining all bonding (bottom) and all anti-bonding (top) configurations. The corresponding band of states is also given.*

$$\psi_{j,k}(r) = \exp[ik \cdot r]\chi_j \tag{2.59}$$

Where χ_j is the cell-wavefunction, r is the real space vector and k is a reciprocal space vector. This k-vector links the various states defined by the degree of bonding/anti-bonding between cells, giving the variation in energy across them. Gaining accurate results for the entire system, therefore, requires sampling this vector over a range in the reciprocal space, since contributions to the total properties of the crystal are made by each of the states. This sampling takes place at a set of points in the given k-space, the k-points.

The cell wavefunction can conveniently be expanded as a set of plane-waves using a Fourier transform.

$$\chi_i(r) = \sum_G c_{i,G} \exp[iG \cdot r] \tag{2.60}$$

Where G is the set of three reciprocal lattice vectors, defined by $G \cdot l = 2\pi m$, where l is a linear combination of the lattice vectors of the crystal and m is an integer which defines the periodicity in the direction of the given set of lattice vectors, G.

For this reason, many periodic DFT calculations use plane-wave basis sets. The plane waves in the basis set are those that fit with an integer number of wave-lengths into the box that contains the unit cell, along the cell's a, b or c axis. Shorter wavelengths correspond to higher energies, and an energy cut-off is defined in the calculation as the limiting factor in determining the size of the basis set.

Limitations

Density functional theory is limited in two major ways. The more fundamental is the lack of any theory to systematically improve the performance of the functionals used. Conjectures based on the uniform electron gas and perturbations thereto provide functionals that give the optimum fit to large data sets and perform extremely well for a large variety of systems (at a very reasonable computational cost, when compared to post-HF wave-function methods), but are not rigorously based on theory, and can only be developed by re-parameterisation, or by including further terms based on further conjecture.

The other limitation is the inability of the theory to model long-range dispersion interactions. The local nature of the LDA restricts electron-electron interactions to within small regions of space, thus neglecting dispersion effects, and failing in many cases to predict bound minima for such systems as $\pi - \pi$ bound benzene monomers. Fortuitous cancellation of errors does allow some functionals to model some of these effects, however, and some functionals exist to incorporate dispersion effects either within the functional or as a simple Van der Waals C_6 parameter, with a damping factor to prevent it affecting short-range interactions.

2.4 Distributed Multipole Analysis

The electrostatic field due to any molecular system can be described by multipolar moments at each atomic centre and those that arise from the presence of electron pairs and

non-uniform electron distributions. These multipolar moments can be calculated *via* the distributed multipole analysis theory of Stone [92] as follows.

The theory is based on the fact that the product of two Gaussian functions is a third Gaussian function centred on a point between them:

$$\begin{aligned}\phi(\underline{A}) \times \phi(\underline{B}) &= \exp[-\alpha(\underline{r}-\underline{A})^2]\exp[-\beta(\underline{r}-\underline{B})^2] \\ &= \exp[-(\frac{\alpha\beta}{\alpha+\beta})(\underline{A}-\underline{B})^2]\exp[-(\alpha+\beta)(\underline{r}-\underline{P})^2] \end{aligned} \quad (2.61)$$

Where $\phi(\underline{A})$ and $\phi(\underline{B})$ are Gaussian basis functions with exponents α and β, centred at $\underline{A}$ and $\underline{B}$, and $\underline{P} = \frac{(\alpha\underline{A}+\beta\underline{B})}{(\alpha+\beta)}$ is the centre of the resultant Gaussian function.

If each pair of basis functions in the basis set of a given system are multiplied this way, a set of Gaussian product functions, distributed through space which each represent a portion of the electron density are obtained. The multipole moments of each of these product functions, it can be shown, form a series which terminates, and can be obtained by integrating over all space the product of each of these functions with the appropriate solid harmonic, $R_l^m(\underline{r})$. It is most convenient to relocate those product functions which lie between atoms onto the nearest atomic centres, dividing them as necessary, in which case the series is not guaranteed to terminate, but must be truncated. Summing the series obtained from each pair provides the multipole moments at each atomic position, which can then be used to calculate the electrostatics of the system.

2.5 Electrostatic Interactions

The interaction of two atoms in separate molecules sometimes contains some strictly covalent character, and requires a detailed quantum mechanical description of exchange and correlation effects to accurately model. Often, however, it can be described by a strictly classical electrostatic model, provided multipolar moments up to a convergent order are known.

The first-order contribution to this electrostatic interaction energy is given by the charge-charge term, as described by Coulomb's law:

$$E_{q-q} = \frac{q_1 q_2}{4\pi\varepsilon_0 |\underline{r}_{12}|} \tag{2.62}$$

where q_1 and q_2 are the charges on particles 1 and 2, ε_0 is the permittivity of free space, and $|\underline{r}_{12}|$ is the distance between the two particles.

The next contribution is the charge-dipole term (equation 2.63)

$$E_{q-\mu} = \frac{(\hat{\underline{r}}_{12} \cdot \underline{\mu}_2)q_1 - (\hat{\underline{r}}_{12} \cdot \underline{\mu}_1)q_2}{4\pi\varepsilon_0 |\underline{r}_{12}|^2} \tag{2.63}$$

where $\hat{\underline{r}}_{12} = \frac{\underline{r}_{12}}{|\underline{r}_{12}|}$, and μ_i is the dipole moment at site i.

The next term, the dipole-dipole term given by equation 2.64 is the highest order term considered necessary for this study.

$$E_{\mu-\mu} = \frac{(\underline{\mu}_1 \cdot \underline{\mu}_2) - 3(\underline{\mu}_1 \cdot \hat{\underline{r}}_{12})(\underline{\mu}_2 \cdot \hat{\underline{r}}_{12})}{4\pi\varepsilon_0 |\underline{r}_{12}|^3} \tag{2.64}$$

2.6 Calculating EPR parameters [93]

There are numerous approaches to obtaining EPR parameters from quantum chemical calculations. A common means is to use a second order perturbation to the DFT field, in which approach the g-tensor can be extracted as the second order mixed derivative of the energy, E, with respect to the magnetic field and the electron spin (equation 2.65, and the A-tensor as the derivative of the energy with respect to the electron and nuclear spins (equation 2.66).

$$g_{uv} = \frac{1}{\mu_B} \frac{\partial^2 E}{\partial B_u \partial S_v} \tag{2.65}$$

$$A_{uv}^{N} = \frac{\partial^2 E}{\partial I_u^N \partial S_v} \tag{2.66}$$

Where the indices u and v represent the three Cartesian directions, x, y and z.

The processes by which a DFT calculation can be used to obtain these values are outlined below.

2.6.1 Calculating A-Tensors

The three contributions to the hyperfine couplings are the Fermi contact (isotropic) term, A^{FC}, the spin-dipole (anisotropic) term, A^{SD}, and the spin-orbit coupling contribution, A^{HC-SO}.

The Fermi contact term is given by the spin-density on the given nucleus. It is calculated for nucleus N by equation 2.67

$$A_{uv}^{FC}(N) = \langle S_z \rangle^{-1} \left[\sum_{i}^{occ(\alpha)} \langle \chi_i^{\alpha} | H_{uv}^{FC} | \chi_i^{\alpha} \rangle - \langle \chi_i^{\beta} | H_{uv}^{FC} | \chi_i^{\beta} \rangle \right] \tag{2.67}$$

Where $\langle S_Z \rangle$ is the expectation value of the Z-component of the total spin, χ_i^{α} and χ_i^{β} are the α and β spin-orbitals that result from an electronic structure calculation, u,v represent the Cartesian direction indices, x, y and z, and H_{uv}^{FC} is the derivative with respect to the v component of the magnetic field of the spatial component of the FC Hamiltonian, $\hat{H}_{uv}^{FC}$, whose form is given in equation 2.68

$$\hat{H}_{FC}(N) = \frac{4\pi}{3} \alpha_f^2 g_e g_N \mu_N \mu_B \sum_i S_i \cdot I_N \delta(\underline{r}_{iN}) \tag{2.68}$$

Where α_f is the fine structure constant, S_i is the spin vector of the i^{th} electron, I_N is the spin of nucleus N, and $\underline{r}_{iN}$ is the vector between the unpaired electron and nucleus N.

The point-dipole approximation to the spin-dipole term, the A-tensor, is given in equation 2.10. The approximation that the electron acts as a point dipole, however, is not always valid. The more general expression, for non-localised electrons, is given in equation 2.69.

$$A_{uv}^{SD}(N) = \langle S_z \rangle^{-1} \left[\sum_{i}^{occ(\alpha)} \langle \chi_i^{\alpha} | H_{uv}^{SD} | \chi_i^{\alpha} \rangle - \langle \chi_i^{\beta} | H_{uv}^{SD} | \chi_i^{\beta} \rangle \right] \tag{2.69}$$

The form of the spin-dipole Hamiltonian, $\hat{H}^{SD}$, is given in equation 2.70. The derivative of the spatial component of this Hamiltonian with respect to the v component of the magnetic field gives H_{uv}^{SD}. Note that this contribution is important in obtaining accurate DFT derived hyperfine interaction parameters, but is specifically neglected in the model presented in this thesis for the calculation of ENDOR derived geometric parameters, for which the relationship of equation 2.10 is used.

$$\hat{H}_{SD}(N) = \frac{1}{2}\alpha_f^2 g_e g_N \mu_N \mu_B \sum_i \left[\frac{3(s_i \cdot r_{iN})(r_{iN} \cdot I_N)}{r_{iN}^5} - \frac{s_i \cdot I_N}{r_{iN}^3} \right] \tag{2.70}$$

To first order, the spin-orbit contribution comprises three components, the one electron spin-orbit contribution (HC-SO) and the two electron spin-same-orbit (HC-SSO) and spin-other-orbit (HC-SOO) contributions. These are given in equations 2.71 and 2.72.

$$A_{uv}^{HC-SO}(N) = \langle S_z \rangle^{-1} \left[\sum_{i}^{occ(\alpha)} \langle \chi_i^{\alpha} | H_{uv}^{HC-SO} | \chi_i^{\alpha} \rangle - \langle \chi_i^{\beta} | H_{uv}^{HC-SO} | \chi_i^{\beta} \rangle \right] \tag{2.71}$$

Where again the spatial component of the Hamiltonian $\hat{H}^{HC-SO}$ (equation 2.73) is differentiated with respect to the v component of the magnetic field to give H_{uv}^{HC-SO}.

$$A_{uv}^{HC-SSO}(N)+A_{uv}^{HC-SOO}(N)=\langle S_z\rangle^{-1}[\sum_{i}^{occ(\alpha)}\langle\chi_i^{\alpha}|H_{uv}^{HC-SSO}+H_{uv}^{HC-SOO}|\chi_i^{\alpha}\rangle - \sum_{i}^{occ(\beta)}\langle\chi_i^{\beta}|H_{uv}^{HC-SSO}+H_{uv}^{HC-SOO}|\chi_i^{\beta}\rangle] \quad (2.72)$$

The Hamiltonians $\hat{H}^{HC-SSO}$ and $\hat{H}^{HC-SOO}$, from which H_{uv}^{HC-SSO} and H_{uv}^{HC-SOO} are obtained are given in equations 2.74 and 2.75.

$$\hat{H}_{HC-SO}(N)=\frac{1}{4}\alpha_f^4 g_e g_N \mu_N \mu_B \sum_i \sum_{N'\neq N} \frac{Z_{N'}}{r_{iN'}^3 r_{iN}^3}[(r_{iN}\cdot r_{iN'})((S_i\cdot I_N)-(S_i\cdot r_{iN'})((I_N\cdot r_{iN})] \quad (2.73)$$

Where r_{ij} is the vector between the i^{th} and j^{th} electrons, and N' refers to the coordinates of nuclei other than nucleus N.

$$\hat{H}_{HC-SSO}(N)=\frac{1}{4}\alpha_f^4 g_e g_N \mu_N \mu_B \sum_{i,j}\sum_{N} \frac{1}{r_{ij}^3 r_{iN}^3}[(r_{ij}\cdot r_{iN})((S_i\cdot I_N)-(S_i\cdot r_{iN})((I_N\cdot r_{ij})] \quad (2.74)$$

Where N' refers to all nuclei other than nucleus N.

$$\hat{H}_{HC-SSO}(N)=\frac{1}{4}\alpha_f^4 g_e g_N \mu_N \mu_B \sum_{i,j}\sum_{N} \frac{1}{r_{ij}^3 r_{iN}^3}[(r_{ji}\cdot r_{jN})((S_i\cdot I_N)-(S_i\cdot r_{jN})((I_N\cdot r_{ji})] \quad (2.75)$$

Finally, the second order corrections to the spin-orbit contribution to the hyperfine coupling, the paramagnetic spin-orbit coupling, computes the interaction between nuclear spin and the electron orbit, and requires the application of a paramagnetic nuclear spin-electron orbit Hamiltonian operator to the unoccupied orbitals of the system. This property requires accurate virtual orbitals, and the application of an extra operator at the DFT-SCF stage, and is thus the most computationally demanding contribution to determine. The form of the operator is given in equation 2.76.

$$\hat{H}_N^{PSO}(I) = \alpha_f^2 g_N \mu_B \sum_i \frac{l_{iN}}{r_{iN}^3} \tag{2.76}$$

Where $l_{iN} = r_{iN} \times P_i$ is the angular momentum coupling operator for the motion of electron i with respect to nucleus N. Similar operators for the angular momentum coupling operator for two electron spins (l_{ij}) and for the angular momentum operator for an electron motion with respect to the origin (l_{iO}) are derived *via* similar expressions.

This Hamiltonian is applied to the occupied and virtual orbitals of the calculation according to equation 2.77.

$$A_{uv}^{PSO}(N) = \langle S_z \rangle^{-1} [\sum_i^{occ(\alpha)} \sum_a^{virt(\alpha)} \frac{\langle \chi_i^\alpha | H_u^{SO} | \chi_a^\alpha \rangle \langle \chi_a^\alpha | H_v^{PSO} | \chi_i^\alpha \rangle}{\varepsilon_i^\alpha - \varepsilon_a^\alpha} - \frac{\langle \chi_i^\beta | H_u^{SO} | \chi_a^\beta \rangle \langle \chi_a^\beta | H_v^{PSO} | \chi_i^\beta \rangle}{\varepsilon_i^\beta - \varepsilon_a^\beta}] \tag{2.77}$$

Where ε_i^α is the energy eigenvalue for orbital χ_i^α, etc.

2.6.2 Calculating the g-Tensor

The g-tensor is generally calculated as a correction to the free electron g-value, g_e, *i.e.* $\mathbf{g} = g_e \mathbf{1} + \delta\mathbf{g}$, and it comprises three principal contributions, the orbital Zeeman/spin-orbit coupling, $g_{\mu\nu}^{OZ/SOC}$, a reduced mass correction term, $g_{\mu\nu}^{RMC}$, and a gauge correction, $g_{\mu\nu}^{GC}$. The calculation of the dominant term, $g_{\mu\nu}^{OZ/SOC}$, is computationally demanding as it requires the use of a perturbation operator which acts on the virtual orbitals. The reduced mass correction and gauge correction terms can be computed from the occupied orbitals that result from the SCF-DFT calculation. A thorough treatment of these calculations is given in reference [93].

2.7 Tensor Diagonalisation

The simulation of EPR and ENDOR spectra require details of the A- and g-tensors. The calculations are greatly simplified if they are performed in the frames of reference for which these tensors are diagonal. An important step in generating A-tensor components from structural parameters is therefore the diagonalisation of the A-tensors of the nuclei, and deriving the rotations required to align them to the molecular frames. In this work, this is done using the diagonalisation procedure described below, and by deriving the Euler angles linking the two frames.

2.7.1 Matrix Diagonalisation

The Tensors associated with EPR and ENDOR are represented by 3×3 matrices. The diagonalisation of a 3×3 matrix is a process of finding the eigenvectors and associated eigenvalues of the matrix. Provided Matrix M can be diagonalised, it is done by multiplying the matrix comprised of its eigenvectors written as columns by M, and multiplying the inverse of this matrix of eigenvectors by that product, *i.e.* $A = D^{-1}MD$, where D is the matrix of eigenvectors, and A is the diagonalised matrix. The diagonal components of A are the eigenvalues of M.

The eigenvalues are found by solving the eigenvalue equation 2.78.

$$\begin{vmatrix} M_{xx}-\lambda & M_{xy} & M_{xz} \\ M_{yx} & M_{yy}-\lambda & M_{yz} \\ M_{zx} & M_{zy} & M_{zz}-\lambda \end{vmatrix} = 0 \tag{2.78}$$

Where λ is the eigenvalues. This determinant gives rise to cubic equation 2.79.

$$a\lambda^3 + b\lambda^2 + c\lambda + d = 0 \tag{2.79}$$

Where $a = 1$, $b = -(M_{xx} + M_{yy} + M_{zz})$, $c = -(M_{xy}M_{yx} + M_{yz}M_{zy} + M_{xz}M_{zx} - M_{xx}M_{yy} - M_{yy}M_{zz} - M_{xx}M_{zz})$ and $d = -(M_{xx}M_{yy}M_{zz} + M_{xy}M_{yz}M_{zx} + M_{xz}M_{yx}M_{zy} - M_{xx}M_{yz}M_{zy} - M_{xz}M_{yy}M_{zx} - M_{xy}M_{yx}M_{zz})$.

The cubic equation is solved by first calculating the discriminant, Δ, *via* equation 2.80.

$$\Delta = (\frac{c}{3} - \frac{b^2}{9})^3 + (\frac{cb - 3d}{6} - \frac{b^3}{27})^2 \tag{2.80}$$

The discriminant is used to determine the number of real roots of the equation. If $\Delta < 0$ the equation has 3 distinct, real roots. Otherwise it has imaginary or coincidental roots, and M cannot be diagonalised.

The next step is to define $z = (r^2 - \Delta)^{1/2}$, where $r = \frac{cb-3d}{6} - \frac{b^3}{27}$. Then the angle θ between the solutions is determined: $\theta = \arccos(\frac{r}{|z|})$.

The solutions to the cubic equation are given by equations 2.81

$$\lambda_1 = 2|z|^{1/3}\cos(\frac{\theta}{3}) - \frac{c}{3} \tag{2.81}$$

$$\lambda_2 = -|z|\cos(\frac{\theta}{3}) - \frac{c}{3} - 3^{1/2}|z|\sin(\frac{\theta}{3}) \tag{2.82}$$

$$\lambda_3 = -|z|\cos(\frac{\theta}{3}) - \frac{c}{3} + 3^{1/2}|z|\sin(\frac{\theta}{3}) \tag{2.83}$$

These give the eigenvalues, which are the diagonal elements of the diagonalised matrix, equation 2.84.

$$\begin{bmatrix} \lambda_1 & 0 & 0 \\ 0 & \lambda_2 & 0 \\ 0 & 0 & \lambda_3 \end{bmatrix} \tag{2.84}$$

2.7.2 Euler Angles

The rotation between two arbitrary coordinate frames can be described using three rotation angles, α, β, and γ, the Euler angles. The order in which these rotations are made, and the axis about which they are made requires a convention. In this study α is defined to be around the z-axis of the original frame, β to be around the y-axis of the resulting rotated frame (y') and γ to be around the z-axis of that rotated frame (z'') (figure 2.6).

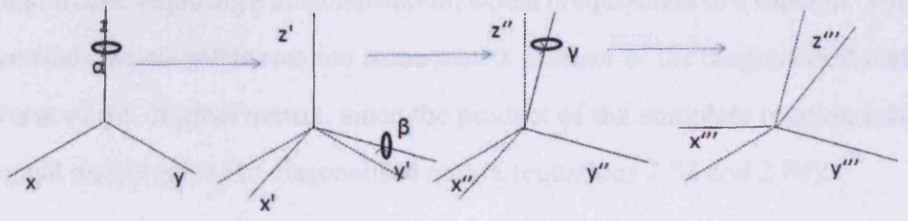

Figure 2.6: *The three Euler angles to rotate one arbitrary frame to another. The z-y-z convention, used in this study, is illustrated.*

Rotation of a vector by angle ψ about the z-axis is given by the rotation matrix of equation 2.85.

$$\begin{pmatrix} x' \\ y' \\ z' \end{pmatrix} = \begin{pmatrix} \cos\psi & -\sin\psi & 0 \\ \sin\psi & \cos\psi & 0 \\ 0 & 0 & 1 \end{pmatrix} \begin{pmatrix} x \\ y \\ z \end{pmatrix} \tag{2.85}$$

Similarly, a rotation about the y-axis by angle ϕ is given by equation 2.86.

$$\begin{pmatrix} x' \\ y' \\ z' \end{pmatrix} = \begin{pmatrix} \cos\phi & 0 & \sin\phi \\ 0 & 1 & 0 \\ -\sin\phi & 0 & \cos\phi \end{pmatrix} \begin{pmatrix} x \\ y \\ z \end{pmatrix} \tag{2.86}$$

Combining these rotations in order gives the rotation matrix for a set of three Euler angles of equation 2.87.

$$\begin{pmatrix} x''' \\ y''' \\ z''' \end{pmatrix} = \begin{pmatrix} c\gamma c\beta c\alpha - s\gamma s\alpha & -c\gamma c\beta s\alpha - s\gamma c\alpha & c\gamma s\beta \\ s\gamma c\beta c\alpha + c\gamma s\alpha & -s\gamma c\beta s\alpha + c\gamma c\alpha & s\gamma s\beta \\ -s\beta c\alpha & s\beta s\alpha & c\beta \end{pmatrix} \begin{pmatrix} x \\ y \\ z \end{pmatrix} \tag{2.87}$$

Where, for brevity, $\cos\alpha$ is denoted $c\alpha$, *etc.* and $\sin\alpha$ is denoted $s\alpha$ *etc.*

This process is necessary for diagonalisation - the A-tensor is not generally diagonal in the molecular frame, requiring a diagonalisation, which is equivalent to a rotation. The matrix that describes the complete rotation is the matrix product of the diagonalised matrix and the inverse of the original matrix, since the product of the complete rotation matrix and the original matrix gives the diagonalised matrix (equations 2.88 and 2.89).

$$D = EM \tag{2.88}$$

Therefore

$$E = DM^{-1} \tag{2.89}$$

Since the diagonalised matrix has been obtained, the Euler angles can be extracted from this product *via* simple trigonometric conversions, provided the appropriate Euler convention is observed in arranging the diagonal components.

2.8 Least Squares Polynomial Fitting

To fit a polynomial of order k to a data set x,y the following procedure is used:

The polynomial is given as $a_0 + a_1x + a_2x^2 + \ldots + a_kx^k$. The difference between the polynomial and the data set is defined by the residual:

$$R^2 = \sum_{i=1}^{N} [y_i - (a_0 + a_1 x_i + a_2 x_i^2 + ... + a_k x_i^k)]^2 \quad (2.90)$$

The objective of the fitting routine is to minimise this residual with respect to the coefficients, $a_0, a_1, a_2, ... a_k$, *i.e.* find the values of these coefficients for which the derivative of the residual with respect to each coefficient is zero, *i.e.*

$$\frac{\partial(R^2)}{\partial a_0} = -2\sum_{i=1}^{N}[y_i - (a_0 + a_1 x_i + a_2 x_i^2 + a_3 x_i^3 + ... + a_k x_i^k)] = 0 \quad (2.91)$$

$$\frac{\partial(R^2)}{\partial a_1} = -2\sum_{i=1}^{N}[y_i - (a_0 + a_1 x_i + a_2 x_i^2 + a_3 x_i^3 + ... + a_k x_i^k)]x = 0 \quad (2.92)$$

$$\frac{\partial(R^2)}{\partial a_2} = -2\sum_{i=1}^{N}[y_i - (a_0 + a_1 x_i + a_2 x_i^2 + a_3 x_i^3 + ... + a_k x_i^k)]x^2 = 0 \quad (2.93)$$

$$\frac{\partial(R^2)}{\partial a_k} = -2\sum_{i=1}^{N}[y_i - (a_0 + a_1 x_i + a_2 x_i^2 + a_3 x_i^3 + ... + a_k x_i^k)]x^k = 0 \quad (2.94)$$

The optimum values for the coefficients are given by the following set of equations:

$$a_0 N + a_1 \sum_{i=1}^{N} x_i + a_2 \sum_{i=1}^{N} x_i^2 + ... + a_k \sum_{i=1}^{N} x_i^k = \sum_{i=1}^{N} y_i \quad (2.95)$$

$$a_0 \sum_{i=1}^{N} x_i + a_1 \sum_{i=1}^{N} x_i^2 + a_2 \sum_{i=1}^{N} x_i^3 + ... + a_k \sum_{i=1}^{N} x_i^{k+1} = \sum_{i=1}^{N} x_i y_i \quad (2.96)$$

$$a_0 \sum_{i=1}^{N} x_i^2 + a_1 \sum_{i=1}^{N} x_i^3 + a_2 \sum_{i=1}^{N} x_i^4 + ... + a_k \sum_{i=1}^{N} x_i^{k+2} = \sum_{i=1}^{N} x_i^2 y_i \quad (2.97)$$

$$a_0 \sum_{i=1}^{N} x_i^k + a_1 \sum_{i=1}^{N} x_i^{k+1} + a_2 \sum_{i=1}^{N} x_i^{k+2} + ... + a_k \sum_{i=1}^{N} x_i^{2k} = \sum_{i=1}^{N} x_i^k y_i \quad (2.98)$$

These sums can be assembled by simply reading in the x and y coordinates of each point in the spectrum, and summing the values of the x-coordinates each raised to the appropriate power, and multiplied by the corresponding y-coordinate where appropriate. This procedure is restricted by the precision of the machine, since each architecture has a maximum size of a floating point number that can be stored in memory, and these sums can reach very large numbers, particularly for the higher orders. This problem can be avoided, at the cost of some accuracy, by incorporating factors to scale and rescale the values of these sums to sizes that can be dealt with. For all of the ENDOR spectra dealt with here, however, and for orders of less than ten, this is not required.

These simultaneous equations can then be solved by Gaussian elimination to obtain the values of $a_0, a_1, a_2, ...a_k$.

Chapter 3

The Role of Weak Interactions in Selective Binding by Metal Salen Complexes

3.1 Introduction

The use of paramagnetic 1st row transition metal species is well established in catalysing important chemical transformations such as alkene oligomerisation, polymerisation, metathesis and oxidation [94]. Low ligand field stabilisation energies permit high rates of ligand exchange in many open-shell systems, which is often augmented for the appropriate ground-state configurations by Jahn-Teller effects, allowing these systems to catalyse transformation reactions with rapid turnovers. Of particular importance are asymmetric transformations, such as the selective generation of chiral products from achiral reactants, or the separation of enantiomers by kinetic resolution [95]. The interactions between the complex and the substrate and/or products in such processes are necessarily weak, making the precise mechanism of the transformations difficult to elucidate. Detailed knowledge of these mechanisms is important in developing ligands with improved selectivity, prompting the use of a variety of methods for probing the structure of the interacting systems in solution. ENDOR spectroscopy and DFT calculations, by virtue of their respective abilities to generate ligand atom-metal ion interactions in frozen glasses and to model the structures and interactions of molecules lend themselves ideally to such studies, and used in combination afford a powerful means of probing otherwise inaccessible (due to their weak nature) interactions.

One of the most important classes among these complexes is that containing chiral *N, N'*-bis-salicylidene-ethylenediamine (salen) derivative ligands [12] (figure 3.1). [96].

These form a class of catalysts which demonstrate useful levels of enantioselectivity for a number of substrates, covering a wide range of reactions [8], referred to by Jacobsen as *"privileged chiral catalysts"*. The (salen) ligand is tetradentate and dianionic, and is pseudo-planar with a distinct molecular z-axis. The vacant coordination sites above and below the ligand plane (or in the case of analogues containing an oxo group, in the position *trans* to the oxo group) are sterically crowded by the protons on the ethylene backbone and by any substituents on the phenyl rings. Metal salen complexes have been applied to a diverse range of reactions, focusing particularly on Mn^{III} for olefin epoxidation and

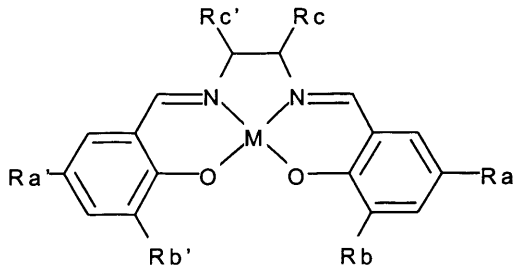

Figure 3.1: *The structure of a metallosalen complex. Selective catalytic activity occurs when Ra and Rb are bulky (e.g. tert-butyl) groups, and when the Rc are not H, giving rise to a chiral complex. In this study, a cyclohexane ring incorporating the two stereocentre C atoms is used.*

later on Cr^{III} and $Co^{II/III}$ for enantioselective epoxide ring opening [95].

The enantio- or diastereoselectivity of these reactions is due in general to either of two possible mechanisms: The introduction of chirality *via* diastereomeric transition states, and the diastereomeric discrimination of one specific enantiomer of the substrate. The latter was only formally observed recently [19] using ENDOR studies of a model chiral *N,N'*-bis(3,5-di-tert-butylsalicylidene)-1,2-diaminocyclohexane-vanadium(IV) oxide ([VO(**1**)]) complex (figure 3.2) to demonstrate differences between the spatial arrangements of bound *R*- and *S*-epoxypropane, although the factors controlling this weak chiral interaction were not explored. In the studies presented here, DFT is used in combination with ENDOR studies to investigate the details of the steric and electrostatic effects on the spatial interactions between a complex consisting of the V=O moiety bound to a salen ligand of figure 3.1 in which R_a and R_b are tertiary butyl groups and R_c is a cyclohexyl group, *R,R*-[VO(**1**)] and a series of epoxide molecules, and between *R,R*-[Cu(**1**)] (figure 3.3) and *R*- and *S*-methylbenzyl amine. These systems show the importance of H-bonding and of $\pi - \pi$ interactions in determining the fine structural details of the interactions that give rise to discriminations in *cis vs. trans* epoxide ring openings and to the enantioselectivity in epoxidation and epoxide ring-opening.

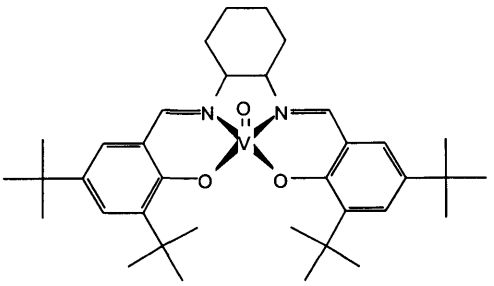

Figure 3.2: *The structure of the* [VO(**1**)] *complex. Significant pyramidalisation occurs, raising the VO moiety above the quasi-planar ligand.*

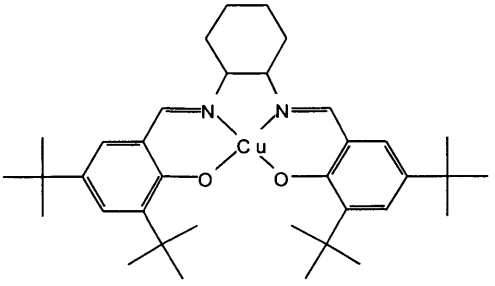

Figure 3.3: *The* [Cu(**1**)] *complex.*

3.2 Structurally Selective Epoxide Binding by a Chiral Vanadyl Salen Complex

Where the ethylene bridge of the salen ligand is substituted, *i.e.* $R_c \neq H$ in figure 3.1, the carbon atoms become stereocentres, and the complex becomes chiral. In the case of [VO(**1**)], this substitution consists of a cyclohexyl group (figure 3.2). Such substituted metallosalen complexes play an important role in asymmetric catalysis of epoxide molecules, in their formation [97, 98], the deracemisation of *meso* epoxides [99] and of epoxy alcohols [100] and in the hydrolytic kinetic resolution [101] and stereospecific polymerisation [102] of racemic epoxides.

The discrimination of stereoisomers by the complex must derive somehow from these stereocentres, but precisely how this is passed on to the interacting epoxide molecule is not well known, and no study has yet supplied any direct link between them and the

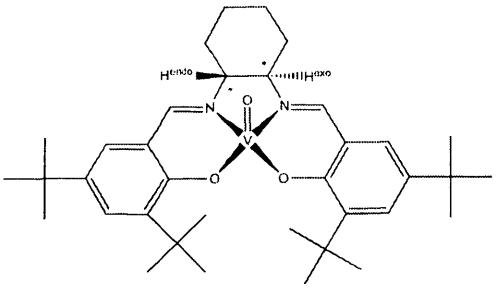

Figure 3.4: *The chiral centres in the* [VO(**1**)] *complex.*

bound epoxide. The mechanism of the interaction in solution of the epoxide and the complex must, through steric and/or electrostatic processes, discriminate between enantiomers. Elucidating this interaction is an important problem in terms of improving the stereospecificity, and one which lends itself to the ENDOR technique. ENDOR has been shown to be able to discriminate between bound enantiomers of epoxypropane [19], and to give structural information on the positions of the epoxide protons in the epoxide ring-opening process. Combining this with DFT calculations, precise information regarding the arrangements of the molecules with respect to the complex can be obtained. This study develops these ideas by using the two techniques in tandem to build up detailed three-dimensional models of the interacting systems and so determine the precise nature of the interaction.

In the epoxide ring opening process the metallosalen complex acts as a Lewis acid in activating the epoxide and the nucleophile. The [VO(*1*)] complex is a much weaker Lewis acid than the catalytically active Cr^{III} and $Co^{II/III}$ versions, and so does not proceed with the ring opening. However, it does bind the epoxide molecules, and so provides a useful spectroscopic probe of a weakend version of the catalytic interaction. It is also known that the unpaired electron of the VO moiety occupies a spatially tight orbital in many environments, thus satisfying the conditions of a simple point-dipole interaction approximation, employed for example in the study of reference [19].

The current study begins with an investigation of the discrimination by [VO(**1**)] of *cis*- and *trans*-2,3-epoxybutane, examining the difference in binding due to *cis/trans* iso-

merism, then moves on to the subtler effects of enantiomeric discrimination in *R*- and *S*-1,2-epoxybutane, in *R*- and *S*-epoxypropane and in *R*- and *S*-chloromethyloxirane and *R*- and *S*-fluoromethyloxirane.

In this study, all spectra were obtained by Damien Murphy, Emma Carter and Robert Farley.

3.2.1 *cis/trans* Isomerism in 2,3-epoxybutane

Differences in reactivity have been observed for *cis- vs. trans-* epoxides and alkenes with [CrCl(**1**)], which specifically deracemises *meso*-epoxides, such as *cis*-**2**, and with [MnCl(**1**)], which specifically catalyses the oxidation of *cis*-alkenes, as well as in similar systems. In the [MnCl(**1**)] catalysed oxidation process, a solid-state observation of an epoxide bound complex has been made [103], but this pre-dissociation intermediate has never been observed in solution.

In this study, using ^{1}H ENDOR spectroscopy of a more weakly binding analogue of this system, [VO(**1**)] binding *cis-* and *trans*-2,3-epoxybutane (*cis*-**2** and *trans*-**2**, figure 3.5), spatial coordinates of the epoxide protons with respect to the vanadium centre have been derived in a frozen solution. From this, it can be determined whether, and to some extent how strongly, the epoxide molecules are bound. DFT modelling has been employed to develop this picture, giving details of the orientation of the epoxide molecule including spectroscopically inactive atoms, and to investigate the electrostatic and steric interactions between the epoxide and complex, thus establishing the importance of H-bonding in the specificity of the binding.

EPR

Continuous wave EPR (*cw*-EPR) spectra were recorded for *rac*-[VO(**1**)] dissolved in *trans*-**2** and in *cis*-**2** (figure 3.6), and simulated with g and ^{51}V tensors of slight rhom-

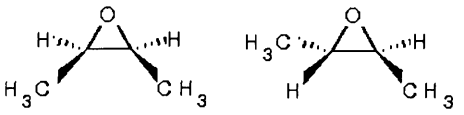

(a) *cis*-**2** (b) *trans*-**2**

Figure 3.5: *The epoxide molecules (a) cis-***2** *(*meso-**2***) and (b) trans-***2** *(*R,R'- *and* S,S'-**2**

bic symmetry. The resulting spin-Hamiltonian parameters are given in table 3.1.

Solvent	g_x	g_y	g_z	A_x/MHz	A_y/MHz	A_z/MHz
	±0.0004	±0.0004	±0.0004	±2 MHz	±2 MHz	±2 MHz
toluene	1.9828	1.9805	1.9525	-172	-161	-487
trans-**2**	1.9828	1.9805	1.9525	-172	-161	-487
cis-**2**	1.9820	1.9805	1.9525	-170	-160	-480

Table 3.1: *EPR spin Hamiltonian parameters for* rac-[VO(**1**)] *dissolved in toluene, trans-***2** *and cis-***2**.

The parameters given in table 3.1 for *trans*-**2** are identical for toluene and *trans*-**2**, (*i.e.* the EPR spectra are identical) indicating a lack of coordination of the *trans*-epoxide to the complex, whereas the parameters for *cis*-**2** are distinct, showing a reduction of $|A_z|$ and of g_x, consistent with the trends observed for axially ligated vanadyl complexes [104]. This implies that, where *trans*-**2** is too bulky to occupy the axial coordination site, *cis*-**2** is able to, so altering the electronic structure and thus the EPR parameters.

Clarification of this selective coordination (of *cis*-**2** over *trans*-**2**) requires structural information of the respective systems, and of the nature of the coordination (in the case of *cis*-**2**). This can be obtained using a combination of ENDOR spectroscopy and DFT calculations.

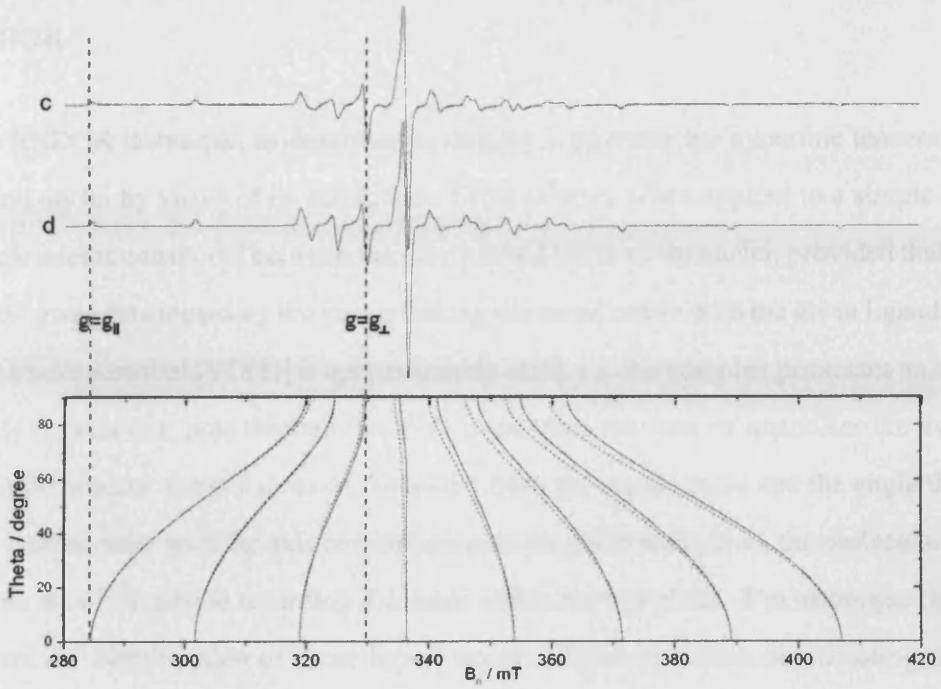

(a) *rac*-VO(**1**) dissolved in *cis*-**2**

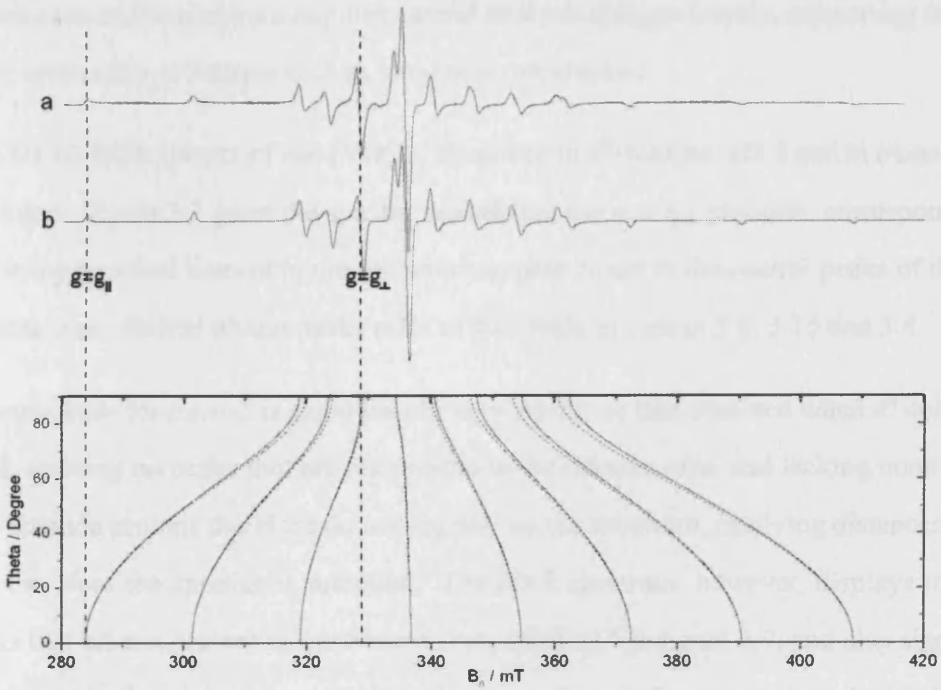

(b) *rac*-VO(**1**) dissolved in *trans*-**2**

Figure 3.6: *X-band (7-12.5 GHz) continuous wave-EPR (cwEPR) spectra (10K) of racemic-*[VO(**1**)] *dissolved in (a) cis-***2**, *and (b) trans-***2**. *The respective simulations are shown above each experimental spectrum, with the angular dependencies below. The solid and dashed lines give the angular dependencies for* $\phi = 0$ *and* $\phi = \frac{\pi}{2}$ *respectively, showing a small rhombic deviation from axial spectra.*

ENDOR

The ENDOR technique, as described in chapter 2, provides the hyperfine tensors for the ligand nuclei by virtue of its resolution. These tensors, when applied to a simple dipole-dipole interaction model between the electron and the relevant nuclei, provided that model holds, gives data regarding the vector linking the metal centre with the given ligand nuclei. The environment of [VO(**1**)] is approximately axial, *i.e.* the complex possesses an approximate C_2 axis that runs through the V=O bond, thus two sets of quantities are available from the spectra, the distances of the nuclei from the metal centre and the angle the linking vectors make with the axis perpendicular to the molecular plane, the molecular z-axis, *i.e.* no data is available regarding the angle within the x-y plane. The technique therefore allows the identification of those ligand nuclei which are within coordinating distance of the metal centre, although unambiguous assignment of which nucleus corresponds to which peak on the spectrum requires careful analysis and, preferably, supporting evidence from some other technique such as structural calculations.

The ^{1}H ENDOR spectra of *rac*-[VO(**1**)] dissolved in d^8-toluene, *cis*-**2** and in *trans*-**2** were recorded. Figure 3.7 gives the spectra recorded at the $g = g_\perp$ position, corresponding to the dashed vertical lines of figure 3.6 which appear closer to the central peaks of the EPR spectra. The labelled proton peaks refer to the labels in figures 3.8, 3.15 and 3.4.

The spectrum for *trans*-**2** is again clearly very similar to that obtained when d^8-toluene is used, showing no peaks that are not present in the toluene case, and lacking none that is. The epoxide protons therefore do not register on the spectrum, implying distances > 5Å, and therefore the epoxide is unbound. The *cis*-**2** spectrum, however, displays multiple peaks that are not present in the toluene case, labelled * in figure 3.7, and also significant distortions to the peaks due to the ligand protons. This indicates, as described below, the coordination of the epoxide molecule to the complex.

In a previous study [19] it was demonstrated using ENDOR and DFT that the largest proton couplings in the [VO(**1**)] complex are due to H^{endo} and H^{exo}, with distances from

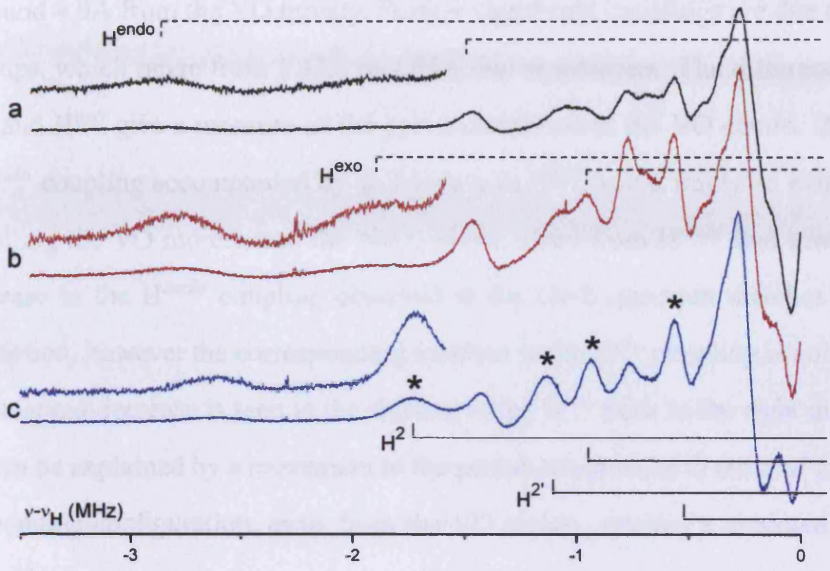

Figure 3.7: *^1H ENDOR spectra (10K) for* rac-[VO(**1**)] *dissolved in a) d^8-toluene, b) trans-***2** *and c) cis-***2**. *The lower frequency sections of the spectra are given as* $\nu - \nu_H$, *recorded at* $g = g_\perp$. *The * mark the epoxide derived peaks in the cis-***2** *case.*

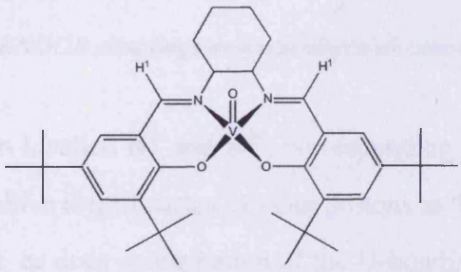

Figure 3.8: *The positions of the H^1 protons.*

the VO moiety of 3.02Å and 3.44Å respectively (the difference in these two distances is due to the pyramidalisation at the V centre towards H^{endo}), and to H^1, each imine proton being around 4.0Å from the VO moiety. Further significant couplings are due to the *tert*-butyl groups, which range from 3.43Å to 4.05Å due to rotamers. The different distances of H^{endo} and H^{exo} give a measure of the pyramidalisation at the VO centre. A decrease in the H^{endo} coupling accompanied by an increase in H^{exo} would imply an axially bound ligand pulling the VO moiety into the N_2O_2 plane, away from H^{endo} and towards H^{exo}. The decrease in the H^{endo} coupling observed in the *cis*-**2** spectrum matches well with this description, however the corresponding increase in the H^{exo} coupling is not observed, instead a marked decrease is seen in the shifting of the H^{exo} peak to the right in figure 3.7 c). This can be explained by a movement of the proton towards the O atom of the epoxide in an H-bonding configuration, away from the VO moiety, causing a torsional distortion in the ligand.

Simulation of the ENDOR peaks arising from the epoxide molecule (* in figure 3.7 c)) gives two distinct couplings, given in table 3.2, suggesting that two epoxide protons lie sufficiently close to the VO to be resolved in the spectrum. A simple point-dipole interaction model gives distances, also given in table 3.2, of 3.26Å and 3.86Å.

	$A_{\|\|}$/MHz	A_{iso}/MHz	A_1/MHz	A_2/MHz	A_3/MHz	r/Å	θ_H/°
H^2	4.47	-0.10	-1.85	-2.80	4.38	3.26	55
$H^{2\prime}$	2.70	-0.10	-1.10	-1.80	2.60	3.86	60

Table 3.2: *^1H ENDOR couplings and calculated distances for H^2 and $H^{2\prime}$.*

These protons have been labelled H^2 and $H^{2\prime}$, corresponding to the labelled protons of figure 3.15, although positive identification of these protons as the nearest to the vanadium requires DFT simulation, as does confirmation of the H-bonding between the epoxide O atom and H^{exo}.

DFT

All of the following DFT calculations were performed using the Gaussian03 [105] suite of programs. Density functional theory, as described in section 2, is unable to model dispersion effects accurately. However, it has been shown [116] that fortuitous cancellation of errors allows accurate geometries to be calculated, despite this shortcoming, provided a judicious choice of functional is made. For this reason, a preliminary study was made to determine which functional would provide the most accurate model for this system.

Choice of Functional

In order to determine the best functional for this system, a small test system was used. The interaction of epoxyethane (figure 3.9) with $CrCl_2O$ was used as such a simple system, and the performance of the BHandHLYP [90], BHandH [90], B3LYP [89], B3PW91 [106] and PBE1PBE [107] functionals, each with a 6-31G(d,p) [108] basis set, were compared for calculated geometries with the MP2 [79] optimised structure, obtained using a cc-pVTZ [109] basis set. Table 3.3 gives the results of these calculations. The optimised geometry is illustrated by figure 3.10.

Figure 3.9: *The epoxyethane molecule.*

From these results it can be seen that the BHandHLYP functional gives results which agree most closely, in terms of dihedral angle and crucially interaction energy, with the high level calculation, and is third best for angles. The B3LYP functional is significantly better than all other functionals for bond lengths, though its failure in other areas, particularly interaction energies, renders it unsuitable here. The BHandHLYP functional is third best among the others for bond lengths by no significant margin. For these reasons, the BHandHLYP functional was chosen.

Choice of Basis

Functional	RMS Δ R /Å	RMS Δθ /°	$\Delta\theta_{dihedral}$ /°	ΔE_{int} /kJ mol^{-1}
BHandHLYP	0.028	3.1	0.6	4.5
BHandH	0.058	2.6	1.2	-33.9
B3LYP	0.014	8.2	0.8	35.7
B3PW91	0.023	3.3	0.9	36.0
PBE1PBE	0.027	2.9	1.2	23.1

Table 3.3: *The RMS deviations of key bond lengths, Δ R, angles, Δθ, and dihedral angles, $\Delta\theta_{dihedral}$ in the $CrCl_2O$+epoxyethane adduct from the MP2/cc-pVTZ geometries as obtained using a variety of functionals with a 6-31G(d,p) basis set. The bond lengths used were those between each of the two Cl atoms and each of the two O atoms and the Cr atom. The angles are the six angles made between each of these four atoms with the Cr atom as the centre. The dihedral angle used is that between one of the epoxide C atoms (the one to the left looking from the epoxide along the O-Cr bond), the epoxide O atom, the Cr and the other O atom. Also given are the differences in the (counterpoise corrected) interaction energies, ΔE_{int} of the bound moieties from the MP2 value of -136.18kJ mol^{-1}.*

The above tests were done using the 6-31G(d,p) basis set, because calculations on the actual systems under study were prohibitively expensive with larger basis sets. The validity of this compromise was tested using basis sets that were enhanced in a variety of ways - extending to triple-ζ (6-311G(d,p) [110]), including diffuse functions (6-31++G(d,p) [111]) and including extra polarisation functions (6-31G(3df,3pd)), as well as the various combinations of these (6-311G(3df,3pd), 6-311++G(d,p), 6-31++G(3df,3pd) and 6-311++G(3df,3pd)), and comparing the optimum geometries and interaction energies to the MP2/cc-pVTZ results, as above. The results of these calculations are given in table 3.4.

As can be seen from table 3.4, extension to a triple-ζ basis offers a marked improvement over the double-ζ basis for calculating interactions energies, and a slight improvement in

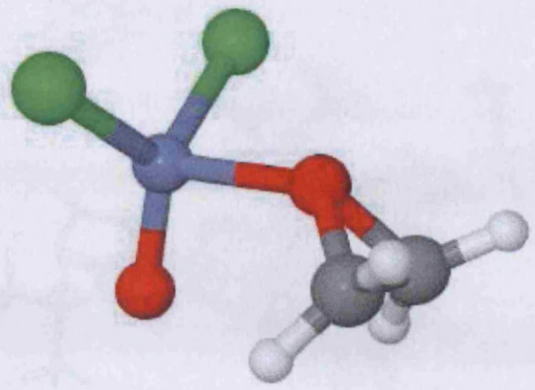

Figure 3.10: *$CrCl_2O$ and epoxyethane, used to find the best functional for modelling complex ion-epoxide interactions*

geometries. The inclusion of diffuse functions and of extra polarisation functions provide less accurate interaction energies, but better configurations. The improvements afforded by all of these basis enhancements are not enough to merit the extra cost, since even convergence of the self-consistent field calculations on the actual test system took significantly more time with any one of them incorporated. These results do show, however, that the 6-31G(d,p) basis set gives geometries to well within 0.1Å and 5°, and energies to within 5kJ mol^{-1} of the MP2/cc-pVTZ values for this test system, and so can be applied with reasonable confidence to the actual systems under study.

Calculations

Both [VO(**1**)] and *trans*-**2** are chiral moieties. However, symmetry is assumed between the mirror image combinations, therefore only *R,R'*-[VO(**1**)] was used. DFT calculations were thus done on the three adducts: *R,R'*-[VO(**1**)]+*R,R'-trans*-**2**, *R,R'*-[VO(**1**)]+*S,S'-trans*-**2**, and *R,R'*-[VO(**1**)]+*cis*-**2**. The initial optimisations were all performed using the ubiquitous B3LYP functional, with structural refinements made using a further optimisation with the selected BHandHLYP functional. The resultant structures of the moieties are given in figure 3.11.

Having optimised the structures, each epoxide molecule was rotated by 90°, 180° and

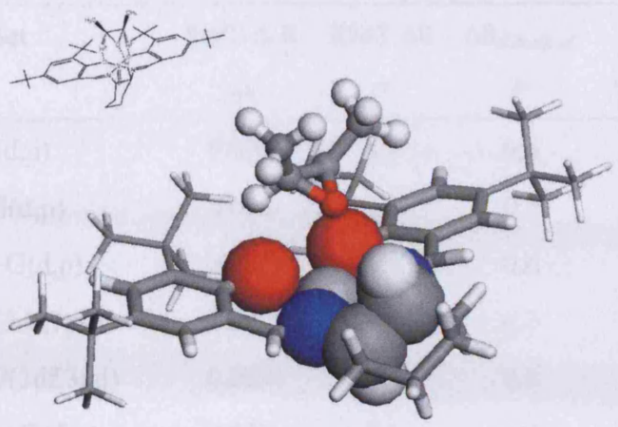

(a)

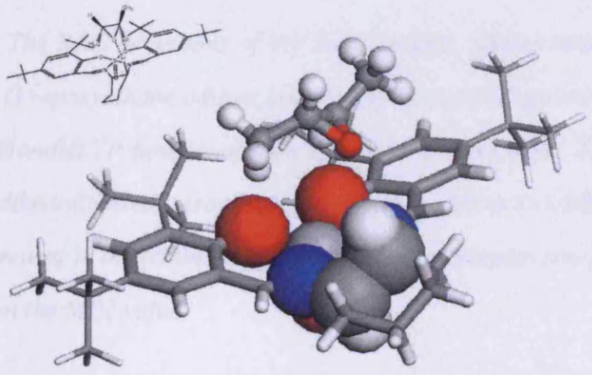

(b)

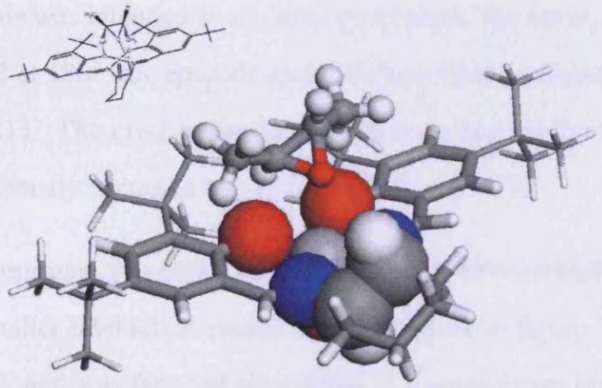

(c)

Figure 3.11: *The optimised structures of (a) R,R'-[VO(**1**)]+cis-**2**, (b) R,R'-[VO(**1**)]+R,R'-trans-**2**, and (c) R,R'-[VO(**1**)]+S,S'-trans-**2***

Basis Set	RMS Δ R /Å	RMS Δθ /°	$\Delta\theta_{dihedral}$ /°	ΔE_{int} /kJ mol^{-1}
6-31G(d,p)	0.028	3.1	0.6	4.5
6-311G(d,p)	0.033	2.5	0.5	-0.3
6-31++G(d,p)	0.026	3.3	0.6	7.9
6-31G(3df,3pd)	0.030	3.4	0.3	10.8
6-311G(3df,3pd)	0.029	2.8	0.8	3.4
6-311++G(d,p)	0.026	3.1	0.4	9.3
6-31++G(3df,3pd)	0.028	3.5	0.2	9.8
6-311++G(3df,3pd)	0.026	3.3	1.3	8.4

Table 3.4: *The RMS deviations of key bond lengths, angles and dihedral angles in the $CrCl_2O$+epoxyethane adduct from the MP2/cc-pVTZ geometries as obtained using the BHandHLYP functional with a variety of basis sets. The bond lengths, angles and dihedrals used were those listed in the caption to table 3.3. Also given are the differences in the (counterpoise corrected) interaction energies of the bound moieties from the MP2 value.*

270° about the dihedral angle formed by one of the O atoms of the N_2O_2 plane, the V atom, the epoxide O atom and one of the C atoms of the epoxide ring, and re-optimised to locate any local minima. Example starting points of these calculations are given for *cis*-**2** in figure 3.12. This was intended as a coarse grid search. However, in each case, with the exception of *cis*-**2** at 180°, the epoxide molecule was found to rotate back to the position given in figure 3.11. The *cis*-**2** molecule flipped over, putting the two methyl groups in the positions previously occupied by H^2 and $H^{2\prime}$ (figure 3.13).

While a stable minimum, this was found by counterpoise corrected calculations, to have a significantly smaller interaction energy to the structure in figure 3.11(a) (-15 kJ mol^{-1} *vs.* -18 kJ mol^{-1}), and was thus not considered as a competitive binding mode given the low temperature of ENDOR experiments.

The further establishment of the structures in figure 3.11 as global minima for the epox-

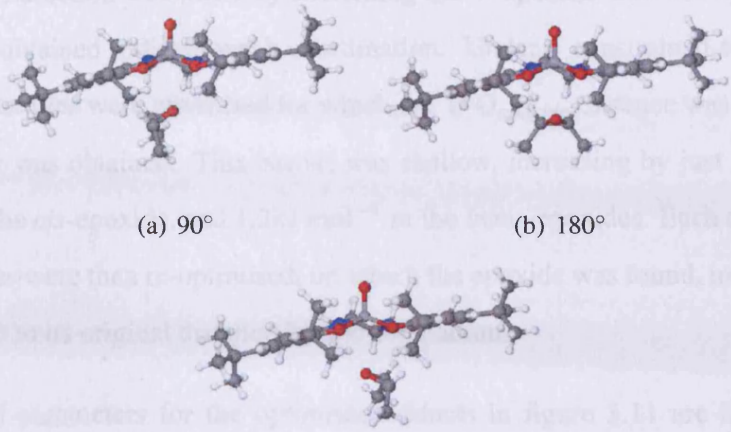

(a) 90° (b) 180°

(c) 270°

Figure 3.12: *The starting geometries of cis-***2** *with R,R'-[VO(***1***)] rotated from the initial optimum geometry of figure 3.11 by (a) 90°, (b) 180° and (c) 270°. (a) and (c) both relaxed to the geometry of figure 3.11, while (b) relaxed to the 'flipped' geometry given in figure 3.13*

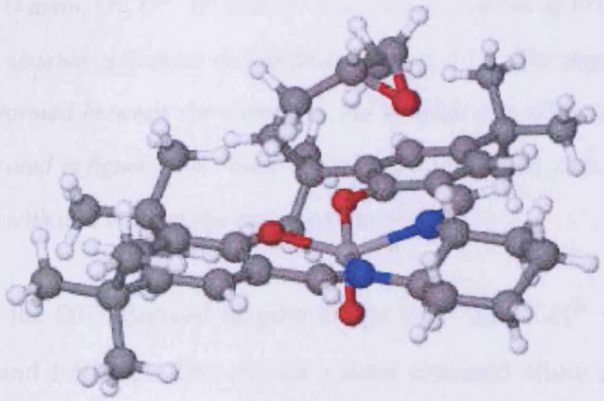

Figure 3.13: *The optimised geometry of the 180° rotated cis-***2** *moiety with [VO(***1***)]. The epoxide has 'flipped' over underneath the N_2O_2 plane, leaving the methyl groups in the positions occupied by H^2 and $H^{2'}$ in figure 3.11(a). This is a high-energy local minimum (see table 3.7).*

ide/complex interaction was made by shortening the V–epoxide distance by 0.5Å, since the distances obtained indicate weak coordination. Under a constrained scan in which successive structures were optimised for which the V–$O_{epoxide}$ distance was shortened by 0.1Å a barrier was obtained. This barrier was shallow, increasing by just 1.7kJ mol−1 over 0.5Å in the *cis*-epoxide, and 1.2kJ mol^{-1} in the *trans*-epoxides. Each of these scan-point structures were then re-optimised, on which the epoxide was found, in each case, to move back out to its original distance from the vanadium.

Key structural parameters for the optimised adducts in figure 3.11 are listed in table 3.5

Epoxide	V–O_{ep} /Å	H^{exo}–O_{ep} /Å	H^2–O^2 /Å	$H^{2\prime}$–$O^{2\prime}$ /Å	O_{ep}–V=O /°	Θ_{plane} /°	Shift Å
cis-**2**	3.50	2.47	2.50	2.90	168	32	0.02
R,R'-trans-**2**	4.16	2.48	2.63	-	160	42	-0.01
S,S'-trans-**2**	4.05	2.36	-	2.58	162	39	0.00

Table 3.5: *Key geometrical features of the (BHandHLYP/6-31g(d,p)) optimised structures of adducts of* [VO(**1**)] *and cis*-**2**, R,R'-trans-**2** *and S,S'-trans*-**2**. O_{ep} *refers to the epoxide O atom,* O^2, $O^{2\prime}$, H^2 *and* $H^{2\prime}$ *refer to the O atoms of [VO(**1**)] and the protons of the epoxide molecules as labelled in figure 3.15. The angle defined by* Θ_{plane} *is that formed between the normal to the epoxide ring plane and the V=O bond, as illustrated in figure 3.14. 'Shift' refers to the difference, in* Å, *between the V–*N_2O_2 *plane with and without the epoxide present.*

Table 3.6 compares the DFT derived lengths of the V-H^2 and V-$H^{2\prime}$ vectors in *cis*-**2** as derived from DFT and ENDOR. The similar values obtained allow a strong degree of confidence in the geometric values listed in table 3.5, as well as positively identifying the appropriate peaks of the ENDOR spectrum as due to H^2 and $H^{2\prime}$.

From table 3.5 it is clear that *cis*-**2** is bound to [VO(**1**)] much more closely. This is evidenced from the shorter spacings between the V atom and the epoxide O atom, O_{ep}, and also from the fact that the V=O shift is greater for *cis*-**2** (in fact, in the case of *R,R'*-**2**

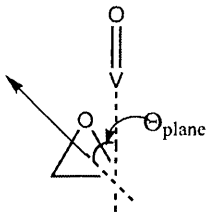

Figure 3.14: Θ_{plane}, *the angle formed between the normal to the plane of the epoxide ring (as defined by the vector product of the two O-C bond vectors) and the V=O bond.*

	R_{ENDOR}/Å	R_{DFT}/Å
H^2	3.26	3.30
$H^{2\prime}$	3.86	3.97

Table 3.6: *The DFT and ENDOR derived distances between the V atom and the H^2 atoms in cis-***2**

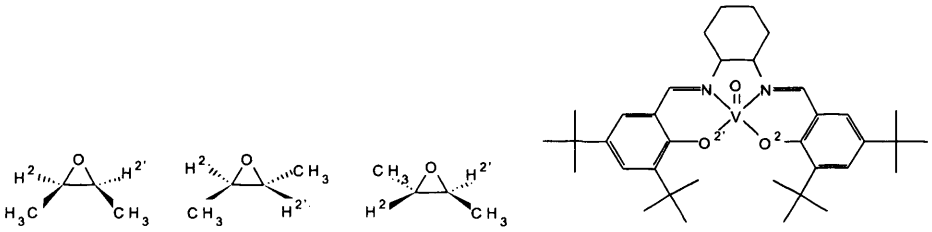

(a) cis-2 (b) RR-2 (c) SS-2 (d) VO(1)

Figure 3.15: *The positions of the H^2 protons and the O^2 atoms*

the epoxide seems to repel slightly the VO moiety, whereas in *S,S'*-**2** the V=O shift is negligible). This V=O shift is defined as the difference between the distances between the average of the coordinates of the atoms in the N_2O_2 plane and the V atom in the coordinating system to the optimised [VO(**1**)] complex with no epoxide.

Also apparent from table 3.5 is that the closest contact between the moieties is between the epoxide O atom and H^{exo}, followed closely by the spacing between the epoxide ring H atoms, H^2, and the O atoms of the N_2O_2 plane, O^2, in H-bonding formation. The two *trans*-**2** isomers are hindered from completing this tripodal H-bonding configuration

by the presence of a methyl group in place of $H^{2\prime}$ in *R,R'-trans*-**2** and of H^2 in *S,S'-trans*-**2**. It should be noted that these methyl groups themselves present protons to the O^2 atoms, at distances of 2.71Å in the *R,R'-trans*-**2** case, and 2.69Å in the *S,S'-trans*-**2** case. As methyl groups, however, they are non-polar, and so unable to form H-bonds with significant strengths.

As well as reducing the number of H-bonds between the moieties, these methyl groups affect the strengths of the remaining two H-bonds, by rotating the molecule with respect to the bound *cis*- epoxide. This was tested by calculating the interaction energies of the moieties, and finding what proportion of those energies is due to electrostatic interactions. These electrostatic contributions were calculated up to dipole-dipole order using the procedure outlined in section 2, from atomic charges and dipole moments calculated using distributed multipole analysis (DMA [92]) obtained with the Gaussian-function DMA program, GDMA, of Stone [112], summed over every pair of atoms between the moieties. These electrostatic energies are given in table 3.7.

Epoxide	Interaction Energy /kJ mol^{-1}	Electrostatic Contribution /kJ mol^{-1}
cis-**2**	-17.6	-17.6
R,R'-trans-**2**	-17.7	-13.0
S,S'-trans-**2**	-17.4	-12.4

Table 3.7: *The (counterpoise corrected) interaction energies of the three adducts, along with the electrostatic contributions to the interaction energies*

Table 3.7 shows similar total interaction strengths for each of the molecules, with significantly smaller electrostatic contributions in the two *trans*-**2** isomers. This would seem to imply stronger electrostatic binding in *cis*-**2**, due to the increased H-bonding in this adduct, with a strengthening charge transfer in the *trans*-**2** interactions. The ENDOR and EPR data demonstrate that the *trans*-**2** molecules coordinate weakly, at great V–O_{ep} distance, and this strengthening effect is not manifest in the V–O_{ep} interaction. The contributions made by each of the suggested H-bonds and of the V–O interactions are given

in table 3.8, which identifies strong V–O interactions and significant H–O interactions, falling in the normal range of weak hydrogen bonds.

Epoxide	V–O_{ep}	H–O_{ep}	O^2–H^2	$O^{2\prime}$–$H^{2\prime}$	$O^{2\prime}$–H^2	O^2–$H^{2\prime}$
cis-**2**	-324.3	-29.0	-29.8	-29.1	-29.8	-24.2
R,R'-trans-**2**	-269.5	-27.1	-28.2	-	-26.1	-
S,S'-trans-**2**	-278.2	-27.3	-	-28.5	-	-24.9

Table 3.8: *The strengths of the V–O_{ep} and suggested H-bonding interactions. Also given are the 'cross' terms, between H^2 and $O^{2\prime}$ and between $H^{2\prime}$ and O^2, which are sizeable due to the shift of the epoxide molecules, each placing one H^2 atom between the O^2 atoms. All interaction energies are in kJ mol^{-1}.*

Epoxide	q(V)/e	q(O_{ep})/e	q(H_{exo})/e	q(O^2)/e	q(H^2)/e	q($O^{2\prime}$)/e	q($H^{2\prime}$)/e
cis-**2**	1.94	-0.41	0.12	-0.73	0.10	-0.73	0.09
R,R'-trans-**2**	1.94	-0.41	0.13	-0.73	0.10	-	-
S,S'-trans-**2**	1.94	-0.41	0.13	-	-	-0.73	0.10

Table 3.9: *The DMA charges on the V, O_ep, H_{endo}, H^2, O^2, $H^{2\prime}$, and $O^{2\prime}$.*

Also apparent from table 3.8 is that the H-bonds that do exist in the *trans*-**2** isomers, as well as the V–O_{ep} interaction are significantly weaker than in the *cis*-**2** case. This is due primarily to the extra distance from the [VO(**1**)] moiety in these adducts, a result of the steric hindrance of the methyl groups to a closer interaction. Variations in the charge-dipole and dipole-dipole contributions to each of these interactions, however, suggests that the alignment of the *cis*- isomer is more favourable in terms of allowing a stronger interaction, especially of the dipole moment associated with the O_{ep} atom, which is supported by the uniformity of the DMA derived charges of table 3.9. Again, the steric influence of the methyl group, this time in rotating slightly the *trans*-**2** isomers with respect to the configuration of *cis*-**2** is detrimental to the interaction.

Conclusions

The importance of these H-bonds identified in the previous section in binding goes a long way towards explaining the selectivity of *cis*-**2** over *trans*-**2** in [VO(**1**)]. The steric hindrance of a methyl group in the position occupied by one of the hydrogen atoms involved in the 3-point H-bonding interaction observed in *cis*-**2** that occurs in *trans*-**2** eliminates an H-bond, and pushes the epoxide away from the [VO(**1**)] moiety, rotating it into a slightly less favourable (in terms of dipole interactions) configuration. These effects combine to explain the selectivity observed in the EPR and ENDOR spectra. The methyl group makes the *trans* interactions much weaker than the *cis* interaction, and so they are not observed experimentally.

3.3 Stereo Selective Epoxide Binding by a Chiral Vanadyl Salen Complex

Introduction

The study of geometric isomerism in 2,3-epoxybutane in section 3.2.1 highlights the importance of hydrogen-bonding in the selectivity of [VO(**1**)] in binding *cis*-2,3-epoxybutane over *trans*-2,3-epoxybutane by [VO(**1**)]. The catalysts for which [VO(**1**)] serves as an analogue, such as [MnCl(**1**)], [CrCl(**1**)] and [Co(**1**)] also show varying degrees of enantioselectivity. The study of section 3.2.1 implicates one of the protons on the cyclohexyl ring, H^{exo}, in the hydrogen bonding mechanism. This is the only proton that appears to be involved attached to a stereocentre, so it seems likely that it is involved in the enantioselectivity process. To investigate this claim, studies have been made [113] using EPR, ENDOR and DFT calculations of *R*- and *S*-1,2-epoxybutane, *R*- and *S*-1,2-epoxypropane, *R*- and *S*-chloromethyloxirane and *R*- and *S*-fluoromethyloxirane (figure 3.16) with *R,R'*- and *S,S'*-[VO(**1**)]. *R*- and *S*-1,2-epoxypropane were investigated in a previous study [19], but are here explored in more detail.

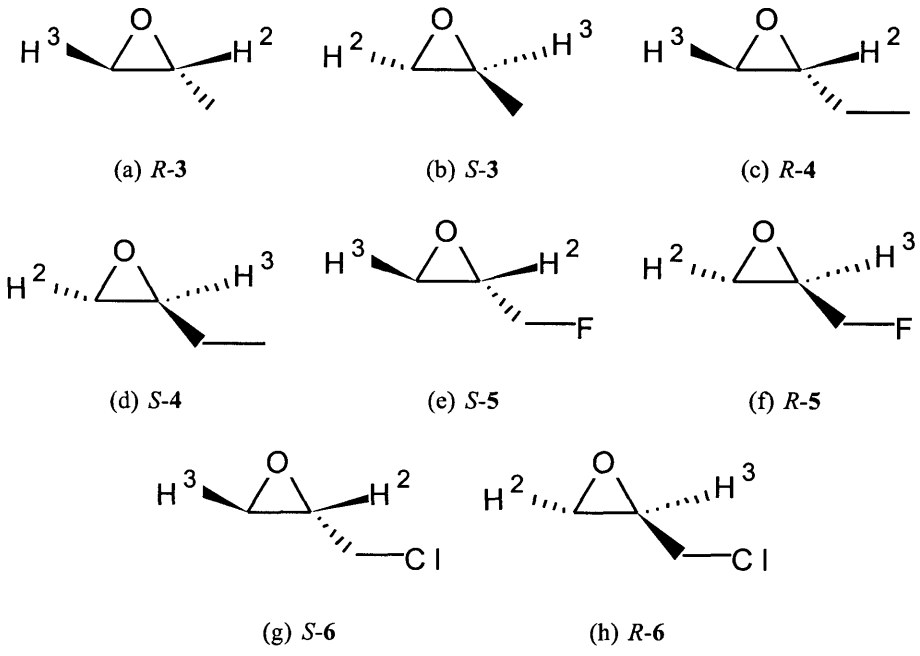

(a) *R*-**3** (b) *S*-**3** (c) *R*-**4**

(d) *S*-**4** (e) *S*-**5** (f) *R*-**5**

(g) *S*-**6** (h) *R*-**6**

Figure 3.16: *The chiral epoxide molecules (a) R-epoxypropane (R-***3***) (b) S-epoxypropane (S-***3***) (c) R-1,2-epoxybutane (R-***4***) (d) S-1,2-epoxybutane (S-***4***) (e) S-fluoromethyloxirane (S-***5***) (f) R-fluoromethyloxirane (R-***5***) (g) S-chloromethyloxirane (S-***6***) (h) R-chloromethyloxirane (R-***6***)*

EPR

EPR spectra were recorded for *R,R'*-[VO(**1**)] and *S,S'*-[VO(**1**)] dissolved in each of the epoxide molecules shown in figure 3.16, as well as for racemic [VO(**1**)] (*rac*-[VO(**1**)]) in *rac*-**3**, *rac*-**4**, *rac*-**5** and *rac*-**6**. Figure 3.17 gives the five spectra for epoxypropane:

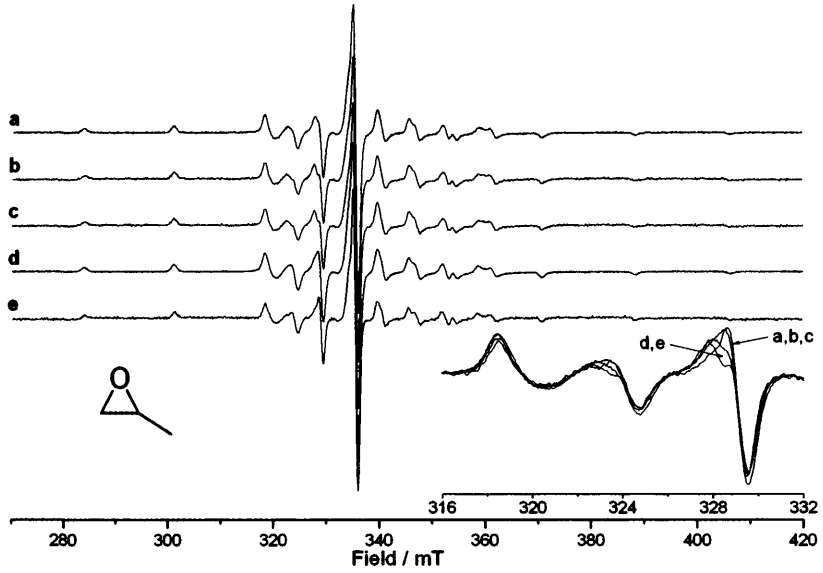

Figure 3.17: *The EPR spectra (10K) of a) rac-[VO(**1**)] dissolved in rac-**3**, enantiomeric pairings b) R,R'-[VO(**1**)] in R-**3** and c) S,S'-[VO(**1**)] in S-**3**, and diastereomeric pairings d) R,R'-[VO(**1**)] in S-**3** and e) S,S'-[VO(**1**)] in R-**3**.*

The close-up section of figure 3.17 makes it clear that the spectra for the enantiomeric pairings (b and c) are very similar, implying identical interactions, and differ from the diastereomeric pairings (d and e), which are likewise very similar to each other. This suggests a significant structural difference between the adducts in each solution. Further, the close similarity of the enantiomeric pairings (b and c) to the racemic combination (a) suggests that in racemic combination the adducts formed are enantiomeric pairings, *i.e.* *R,R'*-[VO(**1**)] forms adducts with *R*-**3**, while *S,S'*-[VO(**1**)] forms adducts with *S*-**3**. The slight differences between the spectra in d) and e) from the spectrum of [VO(**1**)] dissolved in toluene show that these adducts do form, but that the enantiomeric pairings form preferentially.

Similar spectra for chloromethyloxirane are given in figure 3.18. It should be noted that in the case of chloromethyloxirane the enantiomeric assignments are reversed by the priority taken by the carbon atom to which the Cl is bound in the Cahn-Ingold-Prelog assignment. The diastereomeric pairings thus are *R,R'*-[VO(**1**)] in *R*-**3** and *S,S'*-[VO(**1**)] in *S*-**3**.

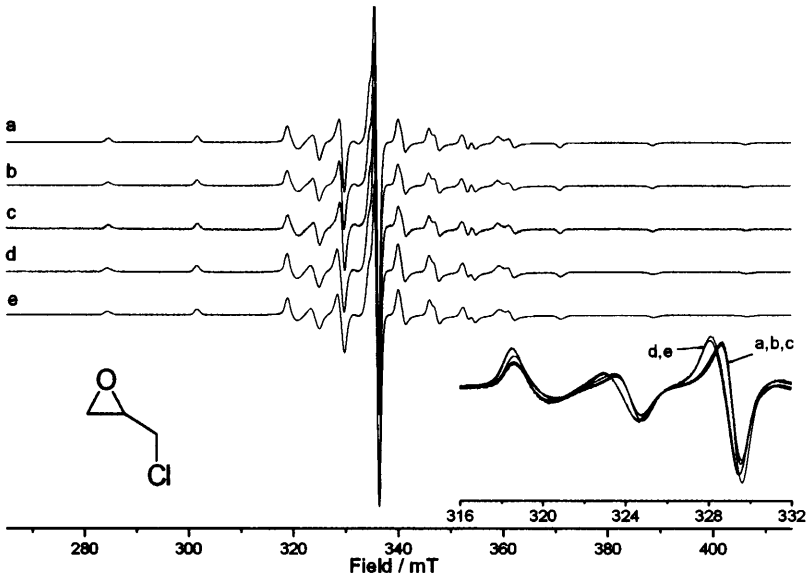

Figure 3.18: *The EPR spectra (10K) of a) rac-[VO(**1**)] dissolved in rac-**6**, enantiomeric pairings b) R,R'-[VO(**1**)] in S-**6** and c) S,S'-[VO(**1**)] in R-**6**, and diastereomeric pairings d) R,R'-[VO(**1**)] in R-**6** and e) S,S'-[VO(**1**)] in S-**6**.*

Again, the identity of a, b and c suggest that, in the racemic combination, specific adducts are formed, this time of *R,R'*-[VO(**1**)] with *S*-**6** and *S,S'*-[VO(**1**)] with *R*-**6**. The diastereomeric pair spectra also differ slightly from that obtained for [VO(**1**)] in toluene. Similar results are obtained for fluoromethyloxirane, in figure 3.19.

Finally, the five spectra associated with 1,2-epoxybutane are given in figure 3.20.

While these spectra differ from that of [VO(**1**)] in toluene, they are essentially identical to each other. This suggests that 1,2-epoxybutane does bind to [VO(**1**)], but without enantioselectivity, suggesting a mechanism that is subtly different to that by which epoxypropane, chloromethyloxirane and fluoromethyloxirane bind. Further investigation of these differences requires that the precise mechanism of each interaction be probed,

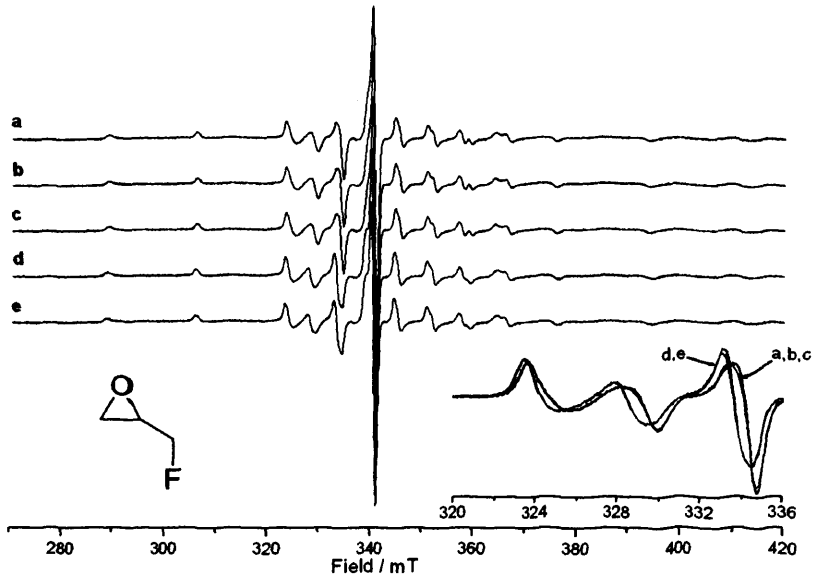

Figure 3.19: *The EPR spectra (10K) of a) rac-[VO(1)] dissolved in rac-5, enantiomeric pairings b) R,R'-[VO(1)] in S-5 and c) S,S'-[VO(1)] in R-5, and diastereomeric pairings d) R,R'-[VO(1)] in R-5 and e) S,S'-[VO(1)] in S-5.*

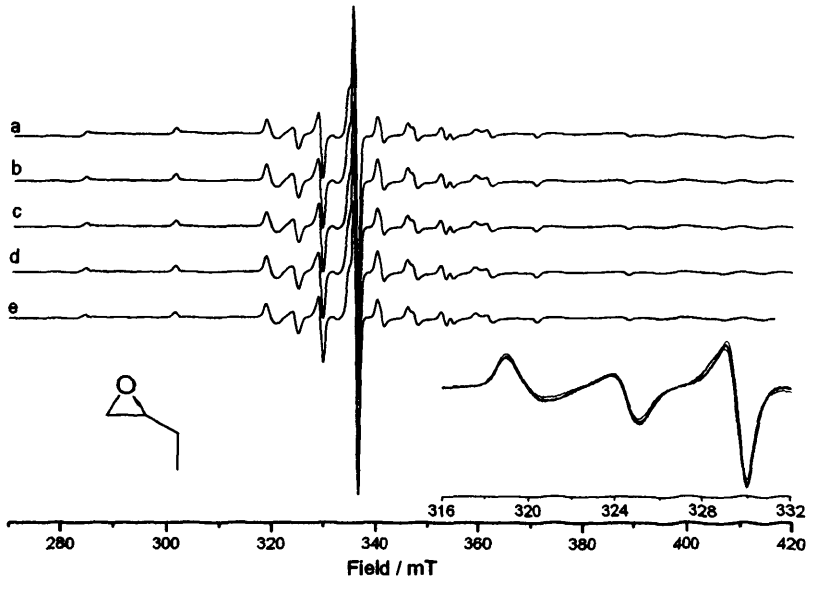

Figure 3.20: *The EPR spectra (10K) of a) rac-[VO(1)] dissolved in rac-4, enantiomeric pairings b) R,R'-[VO(1)] in R-4 and c) S,S'-[VO(1)] in S-4, and diastereomeric pairings d) R,R'-[VO(1)] in S-4 and e) S,S'-[VO(1)] in R-4.*

and this is done, as for the *cis/trans-* isomerism of 2,3-epoxybutane, with a combination of ENDOR and DFT.

3.3.1 ENDOR

More detailed data regarding the precise structure of the interactions between the complex and the epoxide were obtained *via* ENDOR spectra. The spectra of the *rac*-[VO(**1**)] complex in each of the epoxide solvents were recorded and compared to the spectrum obtained with d^8-toluene as the solvent, in which no peaks arising from the solvent are observed. This is illustrated for epoxypropane in figure 3.22, in which are also given the spectra of an analogue of [VO(**1**)] in which all *tert*-butyl groups are replaced by hydrogens in toluene ([VO(**1a**)], figure 3.21), to determine which peaks arise from the protons of the *tert*-butyl groups, and the spectrum of [VO(**1**)] in deuterated d^6-*rac*-epoxypropane, to highlight the effects that the binding of the epoxide has on the couplings due to the other protons, effects which arise largely from the geometric distortions of the complex that occur on binding.

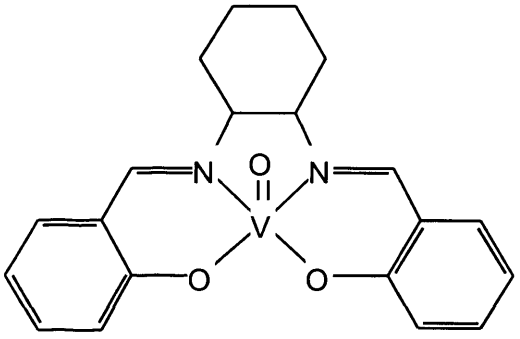

Figure 3.21: *The [VO(**1a**)] molecule*

Slight differences between figure 3.22 a) and figure 3.22 b) are seen with the presence of extra peaks in the latter, with weak couplings, due to the distant *tert*-butyl groups in [VO(**1**)] that are absent from [VO(**1a**)]. The principal differences between figure 3.22 b) and 3.22 c) are the movements of the peaks labelled as arising from H^{exo} out from the centre (due to an increase in the coupling to these protons) and the inwards movement

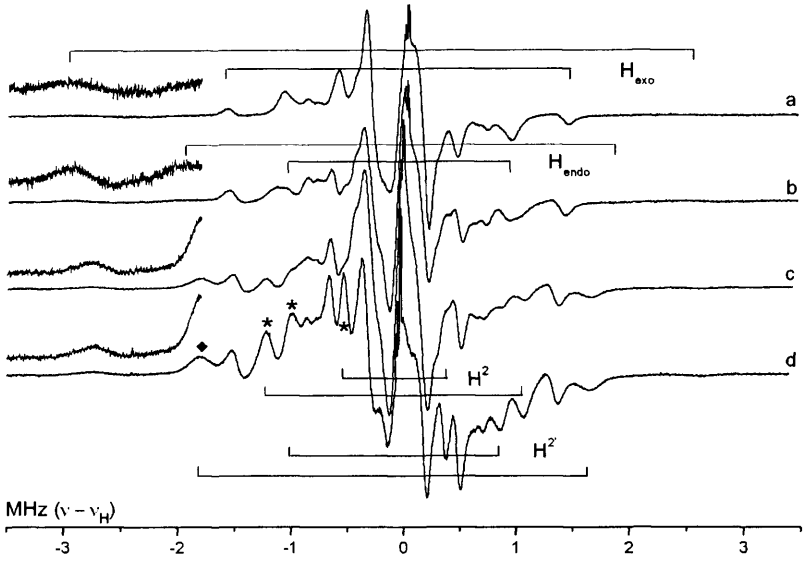

Figure 3.22: *The cw ^1H ENDOR spectra (10K) of a) rac-[VO(**1a**)] dissolved in d^8-toluene/CD_2Cl_2, b) rac-[VO(**1**)] dissolved in d^8-toluene/CD_2Cl_2, c) rac-[VO(**1**)] dissolved in d^6-rac-**3**, and d) rac-[VO(**1**)] dissolved in protic rac-**3**. All spectra were recorded at the position corresponding to $g=g_\perp$.*

(reduction of the coupling) of the peaks due to H^{endo}, which can be explained by a reduction in the pyramidalisation of the VO moiety above the N_2O_2 plane on binding of the epoxide. Finally, the peaks labelled with (*) in figure 3.22 d) are not present in figure 3.22 c), and are therefore necessarily due to the protons of the protic-**3** molecule. A fourth peak arising from protons of the epoxide is masked by the H^{exo} peak, and is labelled (♦).

With these peaks labelled, it was possible to identify the epoxide derived peaks in the ENDOR spectra of each of the homochiral (in which *R,R'*-[VO(**1**] is dissolved in *R*-epoxide, and *vice versa*) and heterochiral (in which *R,R'*-[VO(**1**] is dissolved in *S*-epoxide, and *vice versa*) adducts formed on dissolving *R,R'*-[VO(**1**)] and *S,S'*-[VO(**1**)] in each of the epoxides of figure 3.16. For the epoxypropane case, these are given as recorded at both observer positions $g = g_\perp$ and $g = g_\parallel$, for clarity in figure 3.23.

The opposite pairings (*i.e.* *S,S'*-[VO(**1**)] + *S*-**3** and *S,S'*-[VO(**1**)] + *R*-**3**) produced identical results, confirming the trends observed in the EPR spectra, that homochiral pairings give identical spectra, which are distinct from the heterochiral pairings, which are themselves

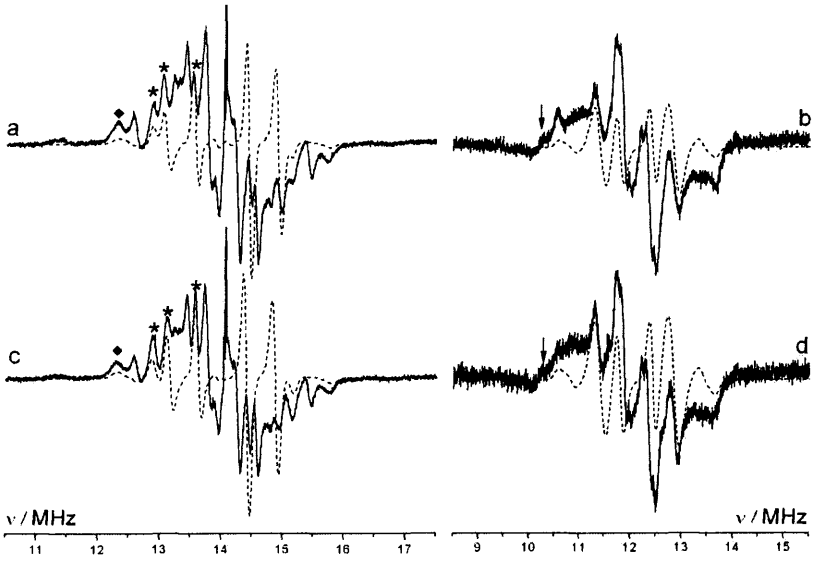

Figure 3.23: *^1H ENDOR spectra (10K) of R,R'-[VO(**1a**)] + R-**3** recorded at the observer positions a) $g = g_\perp$ (328.6mT) and b) $g = g_\parallel$ (288.4mT), and of R,R'-[VO(**1a**)] + S-**3** recorded at the observer positions c) $g = g_\perp$ (328.6mT) and d) $g = g_\parallel$ (288.4mT).*

identical to each other.

Figure 3.24 gives the corresponding spectra for 1,2-epoxybutane.

Unlike the epoxypropane case, the five spectra of figure 3.24 are all identical, though contain peaks that arise from the bound epoxide (labelled * and ♦). This implies that binding occurs, though without enantiomeric discrimination.

The corresponding spectra for chloromethyloxirane and fluoromethyloxirane are given in figures 3.25 and 3.26.

These halogenated cases display the trends observed in the epoxypropane case, namely the identity of the homochiral pairings, their identity to the *racemic* case, and their distinction from the heterochiral cases. This implies again a preferential binding of the homochiral pairings, which is sought out in *racemic* solution.

To obtain further details regarding the precise binding mechanisms, and to support the

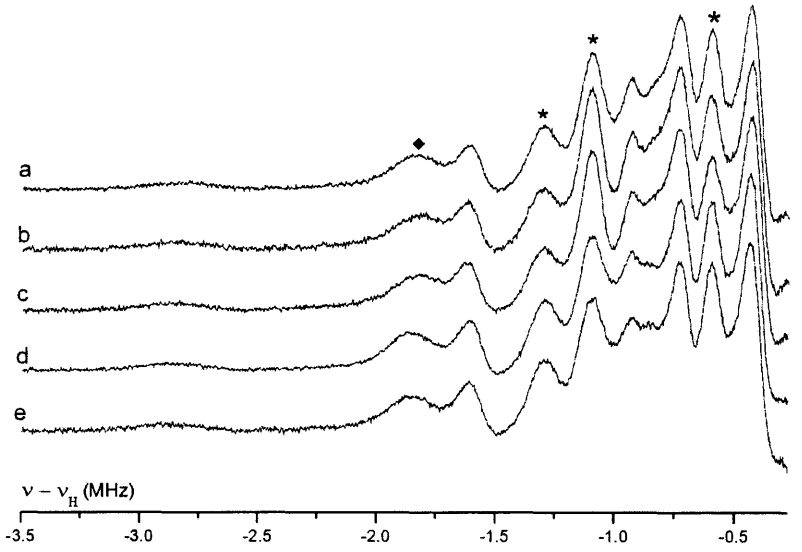

Figure 3.24: *^1H ENDOR spectra (10K) of a) rac-[VO(**1**)] + rac-**4**, b) R,R'-[VO(**1**)] + R-**4**, c) S,S'-[VO(**1**)] + S-**4** d) R,R'-[VO(**1**)] + S-**4** and e) S,S'-[VO(**1**)] + R-**4**. All spectra were recorded at the observer position $g = g_\perp$.*

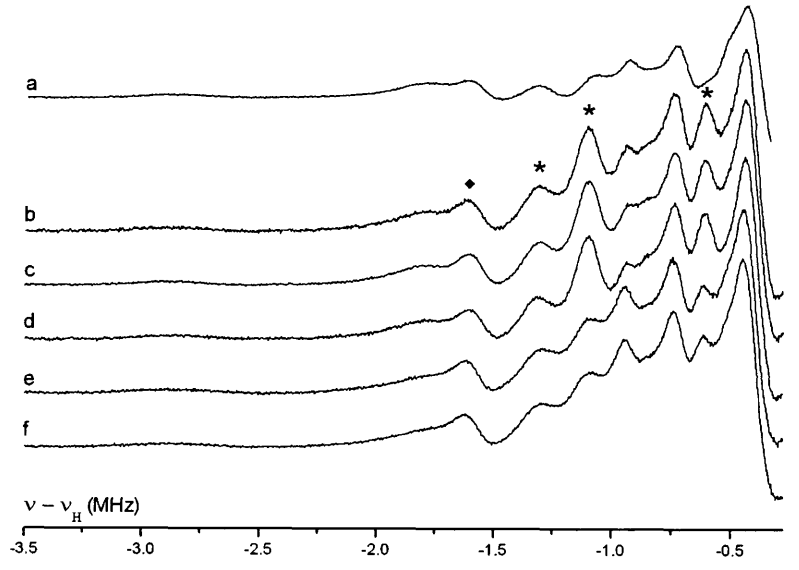

Figure 3.25: *^1H ENDOR spectra (10K) of a) rac-[VO(**1**)] + rac-d^5-**6**, b) rac-[VO(**1**)] + rac-**6**, homochiral pairings c) R,R'-[VO(**1**)] + S-**6**, and d) S,S'-[VO(**1**)] + R-**6**, and heterochiral pairings e) R,R'-[VO(**1**)] + R-**6** and f) S,S'-[VO(**1**)] + S-**6**. All spectra were recorded at the observer position $g = g_\perp$.*

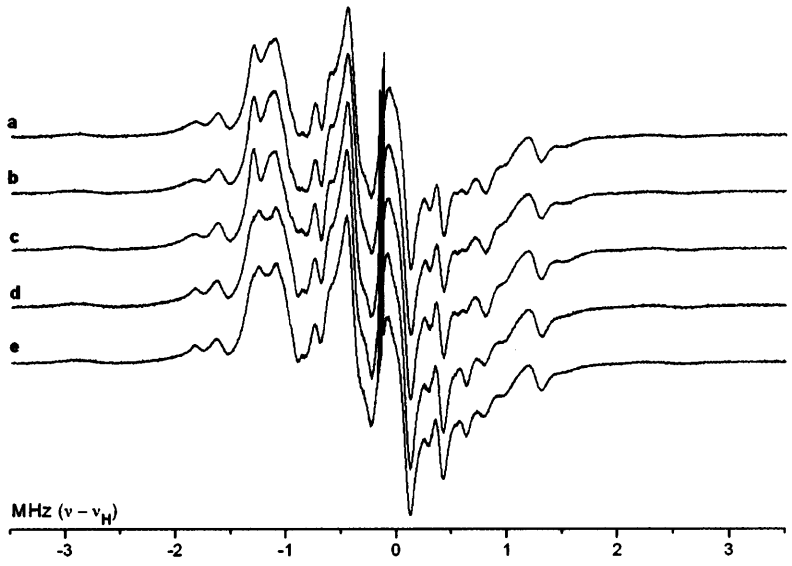

Figure 3.26: ^1H *ENDOR spectra (10K) of a) rac-[VO(***1***)] + rac-***5***, homochiral pairings b) R,R'-[VO(***1***)] + S-***5***, and c) S,S'-[VO(***1***)] + R-***5***, and heterochiral pairings d) R,R'-[VO(***1***)] + R-***5*** and e) S,S'-[VO(***1***)] + S-***5***. All spectra were recorded at the observer position* $g = g_\perp$.

assignment of peaks for these ENDOR data DFT calculations on the system were carried out.

3.3.2 DFT

The DFT calculations on these systems were performed using the BHandHLYP functional with a 6-31G(d,p) basis-set, for reasons given in section 3.2.1. Only *R,R'*-[VO(**1**)] was used in the calculations, since the mirror image adducts were assumed to give identical results. Local minima searches were performed by scanning the dihedral angles between one of the epoxide C atoms, the epoxide O atom, the V atom and one of the O atoms of the N_2O_2 plane in 90° increments, and the V–O_{ep} distance in 0.1Å increments from the optimised geometry to 0.5Å shorter. In each of these cases the structures returned to the optimised configuration that had already been found. Small barriers (<1kJ mol^{-1}) were found for the rotation of the methyl group.

As noted before, the chiral assignment of the halogenated species is opposite to that of the non-halogenated epoxides. For simplicity of discussion, the epoxides will on occasion be referred to using the labels α and β, (*i.e.* α-**3**, β-**3**, etc.) where α refers to that enantiomer for which the substituent is on the same side of the pseudo-plane as H^{exo}, and β to where it occurs on the opposite side. For the *R,R'*-[VO **1**] system studied, this places the substituent always on the same side of the epoxide molecule as H^2 in the α-enantiomer, and as $H^{2'}$ in the β-enantiomer (figure 3.27).

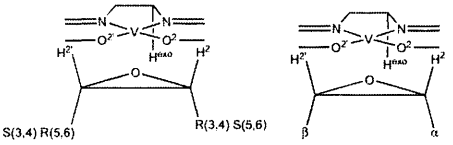

(a) (b)

Figure 3.27: *The α and β enantiomers, labelled with reference to whether the epoxide substituent is on the same or opposite side of the pseudo-plane of the adduct as H^{exo} respectively.*

The optimised geometries of all of the adducts are given in figures 3.29 to 3.31:

The key geometric parameters are given in table 3.10.

Differences in binding can be attributed to three distinct properties (besides chirality) of the epoxide molecules which vary with the functional groups. These are the electronegativity [114] of the substituent, the relative mass of the substituent and the volume of the epoxide. The electronegativity of the epoxide is responsible for inductive effects which affect the electrostatic interactions between the atoms of the epoxide and the complex. The relative mass and molecular volume determine the extent of the steric interactions between the epoxide and the complex. The differing values of each of these three properties for each epoxide are given in table 3.11.

A number of trends are apparent from table 3.10. Firstly, the halogenated epoxides approach much more closely to the V atom than epoxypropane and 1,2-epoxybutane, while the H^{exo}–O_{ep} distances are, in fact, greater in the halogenated species, suggesting that the

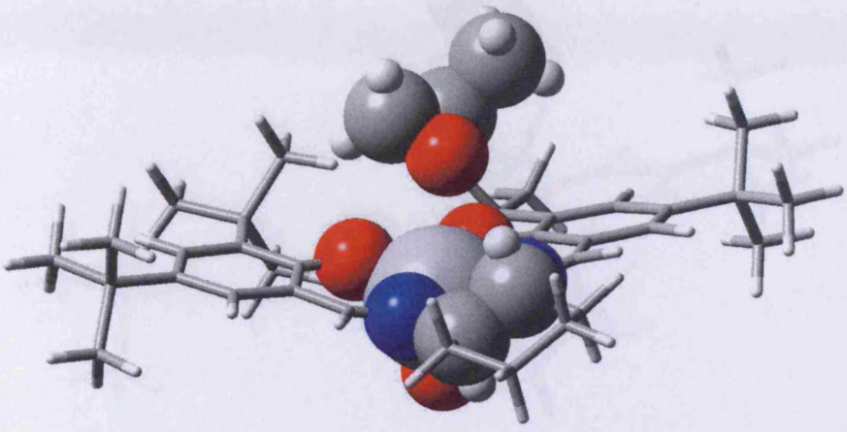

(a) *R*-**3**

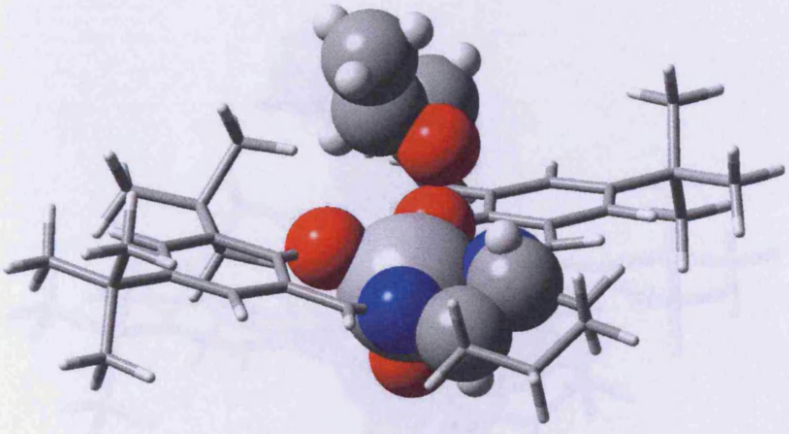

(b) *S*-**3**

Figure 3.28: *The optimised structures of (a) R-epoxypropane (R-***3***) (an* α *configuration) (b) S-epoxypropane (S-***3***) (a* β *configuration).*

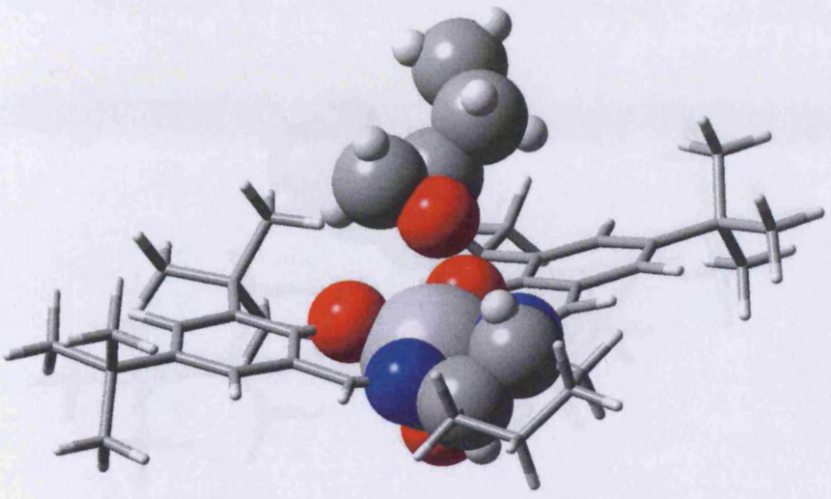

(a) *R*-**4**

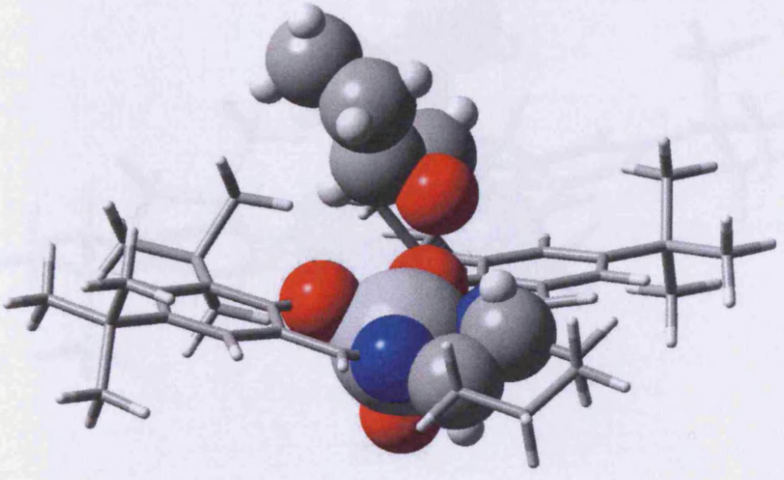

(b) *S*-**4**

Figure 3.29: *The optimised structures of (a) R-1,2-epoxybutane (R-***4***) (an* α *configuration) (b) S-1,2-epoxybutane (S-***4***) (a* β *configuration).*

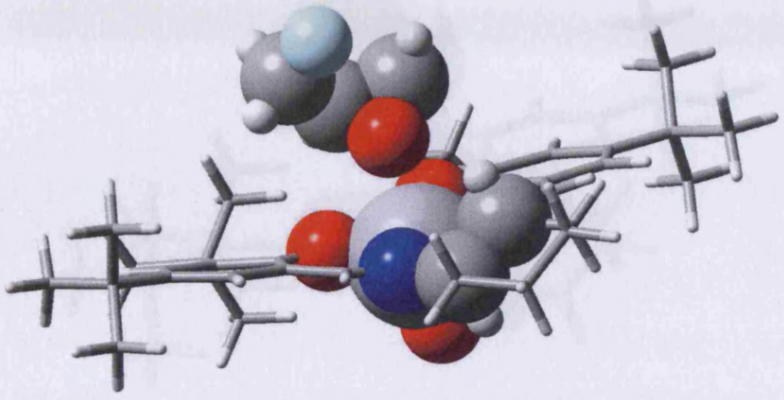

(a) *R*-**5**

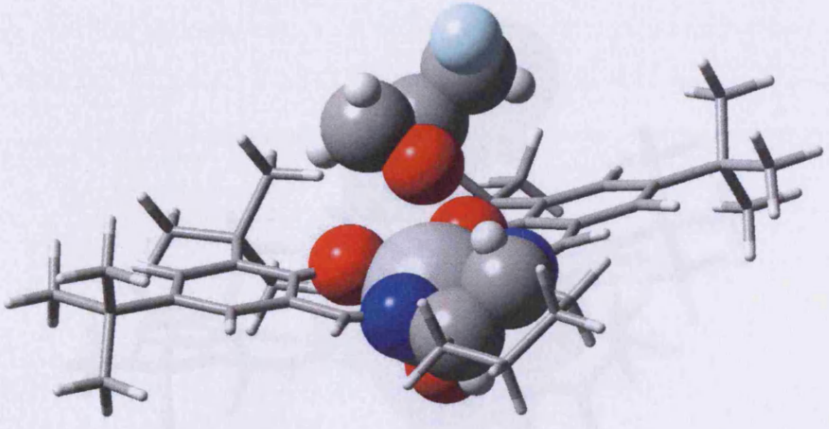

(b) *S*-**5**

Figure 3.30: *The optimised structures of (a) R-fluoromethyloxirane (R-***5***) (a* β *configuration) (b) S-fluoromethyloxirane (S-***5***) (an* α *configuration).*

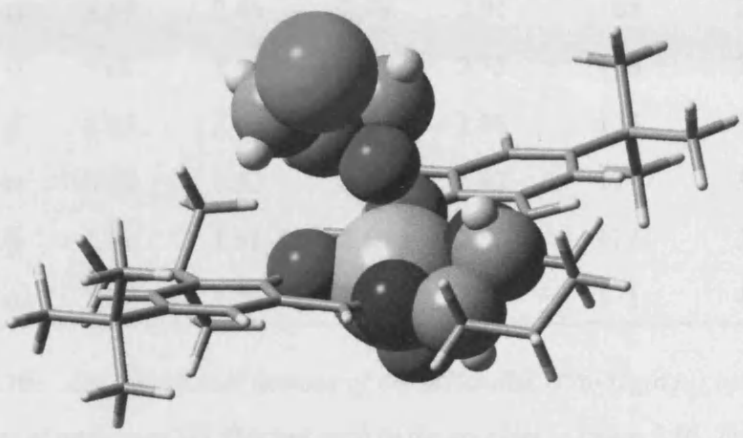

(a) *R*-**6**

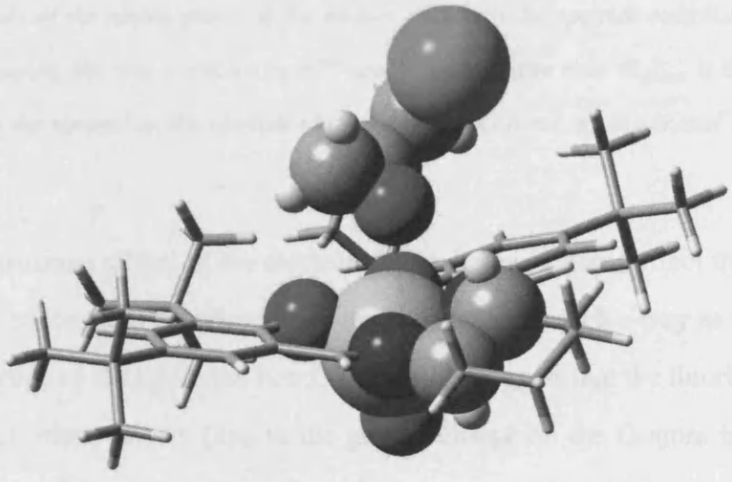

(b) *S*-**6**

Figure 3.31: *The optimised structures of (a) R-chloromethyloxirane (R-***6***) (a* β *configuration) (b) S-chloromethyloxirane (S-***6***) (an* α *configuration).*

Epoxide	α/β	V–O_{ep} /Å	H^{exo}–O_{ep} /Å	H^2–O^2 /Å	H^3–$O^{2\prime}$ /Å	O_{ep}–V=O /°	Θ_{plane} /°	Shift /Å
R-**3**	α	3.50	2.47	2.49	2.97	169	31	0.02
S-**3**	β	3.62	2.45	2.49	2.77	168	26	0.01
R-**4**	α	3.59	2.46	2.49	2.91	168	29	0.01
S-**4**	β	3.66	2.45	2.50	2.75	168	24	0.01
R-**5**	β	2.85	2.62	2.61	2.56	173	39	0.04
S-**5**	α	3.22	2.52	2.45	2.92	171	38	0.09
R-**6**	β	2.90	2.61	2.64	2.53	172	39	0.03
S-**6**	α	3.22	2.54	2.45	2.98	171	40	0.08

Table 3.10: *Key geometrical features of the (BHandHLYP/6-31g(d,p)) optimised structures of adducts of [VO(***1***)] and each of the epoxides in figure 3.16. The properties labelled are described in the caption to table 3.5. The* α/β *assignment refers to the side of the pseudoplane of the adduct on which the epoxide substituent lies,* α *designating the side occupied by* H^{exo} *and* β *the opposite side.* Θ_{plane} *is the angle between the normal to the epoxide ring and the V=O bond, as illustrated in figure 3.14.*

inductive electrostatic effects of the electronegative halogen atoms affect the epoxide in a manner which encourages coordination to the VO moiety in such a way as to pull it away from H^{exo}, disrupting the hydrogen bond. This would suggest that the fluorinated epoxide would approach more closely (due to the greater charge on the O atom induced by the electronegativity of the F atom) than the chlorinated epoxide, which is indeed observed. This effect is what would also be expected to arise from the smaller volume and mass of the fluorine atom, due to the reduced steric hindrance, though the location of the halogen atom away from the vanadyl centre would suggest that this steric effect would be quite weak. This increased attraction is reflected also in the larger extent of the shifting of the VO moiety towards the N_2O_2 plane, and in the slight straightening of the O_{ep}-V=O angle for the halogenated species. Other trends that are observed are due to differences between enantiomers in binding.

Epoxide	Substituent Electronegativity	Molecule Volume /Bohr^{3}mol^{-1}	Substituent Mass /gmol^{-1}
epoxyethane	2.20	384	1.01
epoxypropane	2.40	603	15.04
1,2-epoxybutane	2.43	773	29.06
chloromethyloxirane	3.16	806	35.45
fluoromethyloxirane	3.98	636	19.00

Table 3.11: *The electronegativities, volumes, and masses of the four epoxides in this study, as well as of epoxyethane for comparison. Volumes are derived using a single point volume calculation.*

The presence of any substituent on the epoxide ring tends to pull the epoxide in the direction of the substituent, which is manifest in the shortening of the H^2-O^2 distance in the α-enantiomer and of the H^3-$O^{2\prime}$ distance in the β-enantiomer. The variation in the H^3-$O^{2\prime}$ distance is greater for each of the species, implying that the β-molecules are rotated with respect to the α-molecules about an axis between the V–O_{ep} and H^{exo}–O_{ep} axes, due to the formation of a H-bond between O_{ep} and H^{exo}, as well as being shifted. This effect is likely a result of the increased electronegativity of each substituent with respect to the H atom (table 3.11), causing a withdrawal of electron density from the hydrogen atom bonded to the substituted carbon atom, strengthening the H-bond between that hydrogen atom and the neighbouring oxygen atom of the complex N_2O_2 plane. The greater electronegativity of the halogens than the alkane groups means that this shifting/rotating is more pronounced in the halogenated epoxides.

This shifting is much greater in the halogenated molecules, and is here accompanied by significantly shorter V–O_{ep} distances than in the alkyl cases. Also observed for the halogenated species is a much more significant enantiomeric discrimination, in that the β-enantiomer is, in each case, able to approach much more closely to the V than the enantiomer in the α configuration. Clearly this proximity to the metal centre has a cost in terms

of distorting the ligand geometry, in order to open up a space in which to coordinate. This is met in the halogenated cases by the electron withdrawing effects of the electronegative halogen atoms on the epoxide oxygen atom, greatly increasing attraction to the metal centre. In the alkane substituted cases, the cost of bringing the epoxide close to the metal centre cannot be met by the electrostatics, and instead the H-bond between H^{exo} and O_{ep} limits the proximity of the epoxide to the VO moiety, at the same time allowing the tripodal H-bonding scheme observed in the *cis*-2,3-epoxybutane + [VO(**1**)] adduct. In this case the α-enantiomer is favoured over the β-enantiomer, since the epoxide is shifted towards H^{exo} in the α case, although this effect is less pronounced than in the halogenated cases, in support of the spectroscopic data, to the extent that in the case of 1,2-epoxybutane the enantiomers are not distinguished.

The alkane substituted epoxides, as described above, are unable to get as close to the VO moiety, and so form H-bonds between O_{ep} and H^{exo}. The interaction energies are therefore determined by the relative strengths of these H-bonds and the V-O interaction. The α-enantiomers are able to approach more closely to the V, while the β-enantiomers form slightly shorter H-bonds. Table 3.12 shows that the interaction strengths are greater for the H-bonded β-enantiomers due to non-electrostatic (*i.e.* directional covalent) interactions than for the α-enantiomers, for which the electrostatic interaction energies are greater, but constitute almost the entire interaction strength. The near identity of the electrostatic contributions for *R*- and *S*-**4** explains the lack of discrimination between these enantiomers as demonstrated by the spectroscopic data.

The electrostatic interactions between the V and O_{ep} atoms, along with the three proposed H-bonds in each adduct, are given in table 3.13.

This table strongly supports the notion that the halogenated species form much stronger interactions between V and O_{ep}. Similar values observed for H^{exo}–O_{ep} for halogenated and non-halogenated species suggest that this interaction is less affected by the electrostatics, and the fact that the values are generally smaller than obtained for the H^2–O^2 interactions suggests that this H atom, while only able to form particularly weak H-bonds,

Epoxide	α/β	Interaction Energy /kJ mol^{-1}	Electrostatic Contribution /kJ mol^{-1}
R-**3**	α	-18.6	-18.4
S-**3**	β	-19.1	-17.5
R-**4**	α	-17.1	-17.3
S-**4**	β	-18.5	-17.0
R-**5**	β	-25.3	-22.6
S-**5**	α	-22.3	-31.4
R-**6**	β	-25.8	-24.4
S-**6**	α	-23.5	-31.4

Table 3.12: *The interaction energies of the adducts, along with the electrostatic contributions to the interaction energies, calculated with GDMA.*

serves more to sterically hamper the approach of the epoxide to the V atom.

These calculations explain the far greater enantioselectivity observed for the halogenated than for the non-halogenated species. They also go some way towards explaining the direction of the observed enantioselectivity, *i.e.* that for the non-halogenated molecules, the *R*-enantiomers are preferentially bound by *R,R'*-[VO(**1**)], and *vice versa*, while for the halogenated species it is the *S*-enantiomer that is preferentially bound.

Conclusions

The subtleties of the interplay between sterics and electrostatics in determining the preferred epoxide enantiomer bound by the [VO(**1**)] complex have been investigated and linked to the position of the H^{exo} proton, attached to the stereocentre carbon atom of the cyclohexyl backbone. This proton, which occupies a spatial position that is close to the epoxide molecule, plays two distinct, somewhat opposing roles: it forms an H-bond with the epoxide O atom, and it limits the proximity of the epoxide molecule to the vanadyl centre. The strength of the electrostatic attraction between the epoxide O atom and the V

Epoxide	α/β	V–O_{ep}	H^{exo}–O_{ep}	O^2–H^2	$O^{2\prime}$–H^3	$O^{2\prime}$–H^2	O^2–H^3
R-**3**	α	-320.8	-28.6	-31.0	-28.4	-30.7	-23.1
S-**3**	β	-306.7	-28.1	-27.9	-30.0	-28.2	-25.1
R-**4**	α	-308.5	-28.0	-31.3	-28.3	-31.2	-23.2
S-**4**	β	-299.6	-27.8	-28.1	-30.7	-28.3	-25.9
R-**5**	β	-398.0	-27.6	-33.8	-37.5	-25.7	-35.7
S-**5**	α	-340.4	-27.9	-36.7	-30.0	-35.1	-24.0
R-**6**	β	-398.2	-28.8	-34.1	-38.1	-26.1	-35.8
S-**6**	α	-348.6	-28.9	-37.6	-30.2	-35.7	-24.2

Table 3.13: *The strengths of the V–O_{ep} and suggested H-bonding interactions. Also given are the 'cross' terms, between H^2 and $O^{2\prime}$ and between $H^{2\prime}$ and O^2, which are sizeable due to the shift of the epoxide molecules, each placing one H^2 atom between the O^2 atoms. All energies are in kJ mol^{-1}.*

atom must overcome a barrier to the geometric distortion of the ligand for this means of binding to dominate, and when it does H^{exo} becomes an obstruction, and the enantiomer in which the substituent is positioned such as to avoid steric clashes with this proton is preferentially bound. Where the barrier is not overcome, the formation of an H-bond between H^{exo} and O_{ep} means that electrostatically the enantiomer with the substituent on the same side as H^{exo} is favoured, since the substituent pulls that enantiomer towards H^{exo} by virtue of another H-bond formed between H^2 and O^2. However, in this situation distortion of the complex cancels out this effect, and it is in fact the alternate enantiomer that is favoured.

3.4 Selective Binding of a Chiral Amine Molecule by Chiral Copper Salen Complexes

3.4.1 Introduction

The importance of the formation of weak hydrogen bonds in determining the geometric and enantioselectivity of vanadyl salen complexes in binding epoxide molecules was investigated in the preceding sections. The role such interactions play in determining selectivity demonstrates the importance of weak, outer-sphere interactions in the binding mechanisms of such systems, which must obviously be taken into account when designing novel ligands for improved yields and selectivities, and in extending the range of reactions that can be catalysed by such systems. The need for such novel catalytic systems is driven by the recent explosion of interest in asymmetric catalysis for the production of optically pure compounds for use in the synthesis of natural products, pharmaceutical compounds, fragrances, flavourings and a range of other products. In this section, the importance another type of weak interaction, $\pi - \pi$ interactions, in determining the selectivity of the binding of a chiral amine by another metal salen complex, [Cu(**1**)] is investigated [115].

The amine used in this study is methylbenzylamine, MBA, figure 3.32.

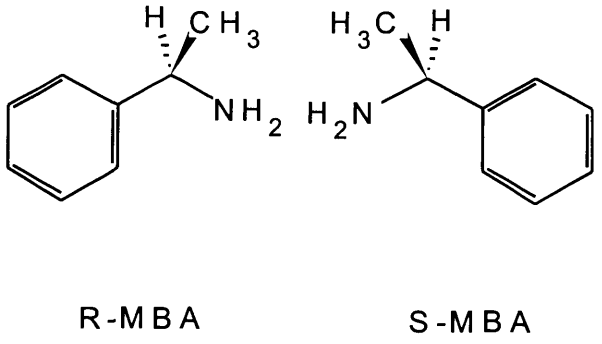

Figure 3.32: *The methylbenzylamine, MBA molecules.*

It was suspected initially that the phenyl ring of the MBA molecule would form a $\pi - \pi$

interaction with the phenyl rings of the salen catalyst. Since the complex used principally in this study, [Cu(**1**)], figure 3.3, has *tert*-butyl groups substituted onto the phenyl rings, it is likely that this $\pi - \pi$ interaction would be hindered. For this reason, the binding of MBA with an alternative complex, in which the *tert*- butyl groups were absent was also investigated. This alternative complex is labelled [Cu(**1a**)], figure 3.33.

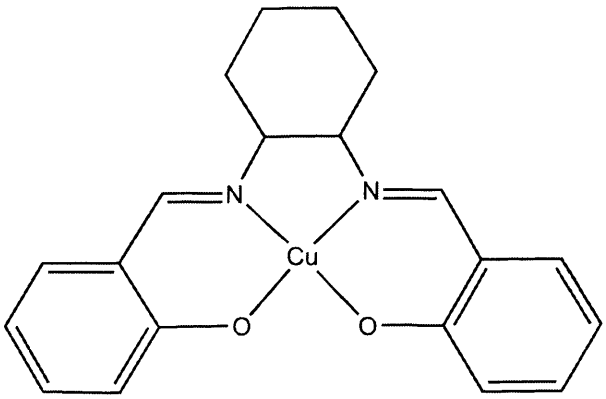

Figure 3.33: *The [Cu(**1a**)] complex.*

The interactions of these two complexes ([Cu(**1**)] and [Cu(**1a**)]) with *R*-MBA and *S*-MBA were investigated using EPR, ENDOR and DFT studies.

3.4.2 EPR

EPR spectra were recorded for *racemic*-MBA + *racemic*-[Cu(**1**)] (figure 3.34 a), *R*-MBA + *R,R'*-[Cu(**1**)] (figure 3.34 b), *S*-MBA + *S,S'*-[Cu(**1**)] (figure 3.34 c), *S*-MBA + *R,R'*-[Cu(**1**)] (figure 3.34 d), and *R*-MBA + *S,S'*-[Cu(**1**)] (figure 3.34 e). These spectra show axially symmetric environments, with good resolution of the hyperfine couplings, and of further superhyperfine splittings. The spectra show subtle differences between the heterochiral cases (d and e) and the homochiral cases (b and c).

All spectra differ from the spectrum of *racemic*-[Cu(**1**)] in toluene (figure 3.35), suggesting binding in all adducts, though the differing signals that arise from the homochiral and heterochiral pairings suggest a difference in the precise mode of binding.

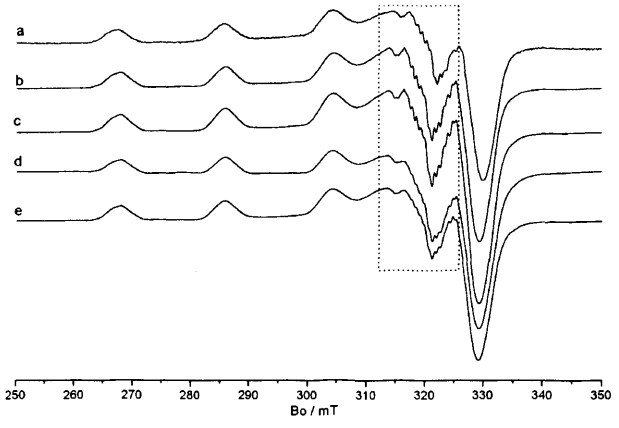

Figure 3.34: *The X-band EPR spectra of a) racemic-MBA + racemic-[Cu(**1**)], b) R-MBA + R,R'-[Cu(**1**)], c) S-MBA + S,S'-[Cu(**1**)] d) S-MBA + R,R'-[Cu(**1**)] and e) R-MBA + S,S'-[Cu(**1**)].*

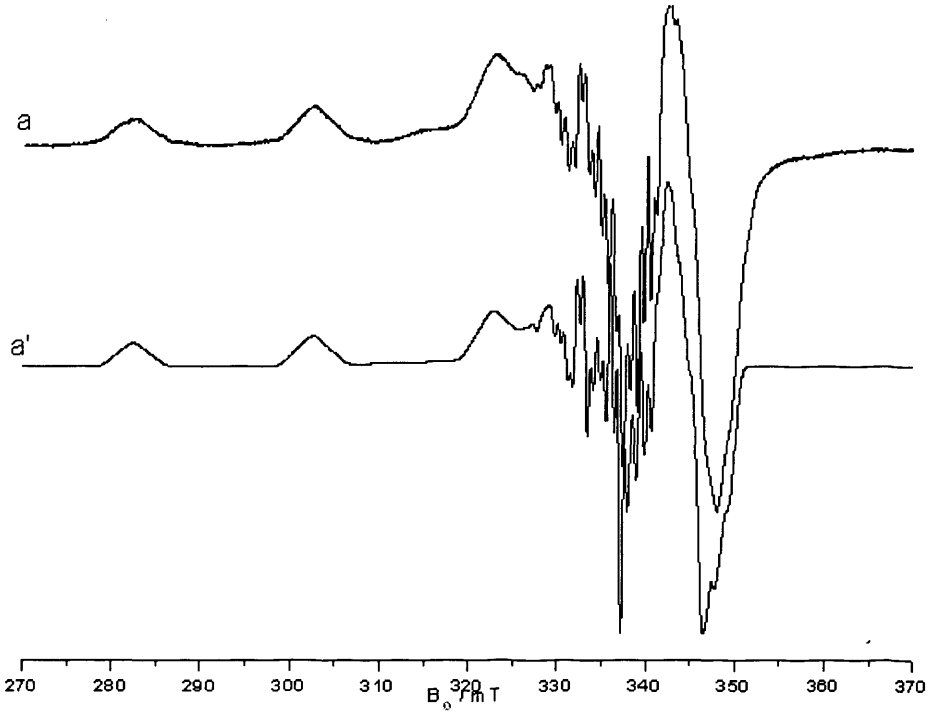

Figure 3.35: *The X-band EPR spectra of racemic-[Cu(**1**)] in toluene.*

The X-band spectra of figure 3.34 appear to demonstrate a greater similarity between the spectra that arise from the homochiral pairings and from the *racemic* combination than between those that arise from the heterochiral pairings and from the *racemic* combination. At higher microwave frequency, however, the W-band spectra show the opposite to be true. Figure 3.36 shows the W-band spectra recorded for *S,S'*-[Cu(**1**)] dissolved in *rac*-MBA, *S*-MBA, *R*-MBA and in toluene. Simulations are given for each case, with the *rac*-MBA solution simulated parameters derived from a combination of the parameters obtained in the simulation of the *R*-MBA and *S*-MBA solutions. By a fitting process, the respective proportions obtained were of 70% *R*-MBA (the heterochiral species) to 30% *S*-MBA (the homochiral species).

Similar results were obtained for [Cu(**1a**)] (figure 3.37), for which the proportion of *R*-MBA to *S*-MBA was found to be 60:40.

These W-band data support the assertion that the enantiomers of MBA are both bound by either enantiomer of [Cu(**1**)] (and of [Cu(**1a**]), in subtly different ways. The preferred coupling (*i.e. more stable binding*), however, as these data make clear is the heterochiral pairings. To investigate possible reasons behind this preference DFT calculations were done for each of the adducts.

3.4.3 DFT

The inability of DFT to accurately model dispersion effect would render it unsuitable for modelling $\pi - \pi$ interactions, however, work by Robertazzi *et al.* [116] on benzene, pyridine and DNA base dimers demonstrated minima on the potential energy surfaces with the BHandH functional. They attributed this ability to qualitatively reproduce geometric details to a fortuitous cancellation of errors within the functional and demonstrated that it applied to a range of $\pi - \pi$ interacting systems, reproducing energies generally to within ± 2 kJ mol^{-1} of the MP2 values. For these reasons, this functional was used with the same 6-31G(d,p) basis set, as for the VO study discussed earlier.

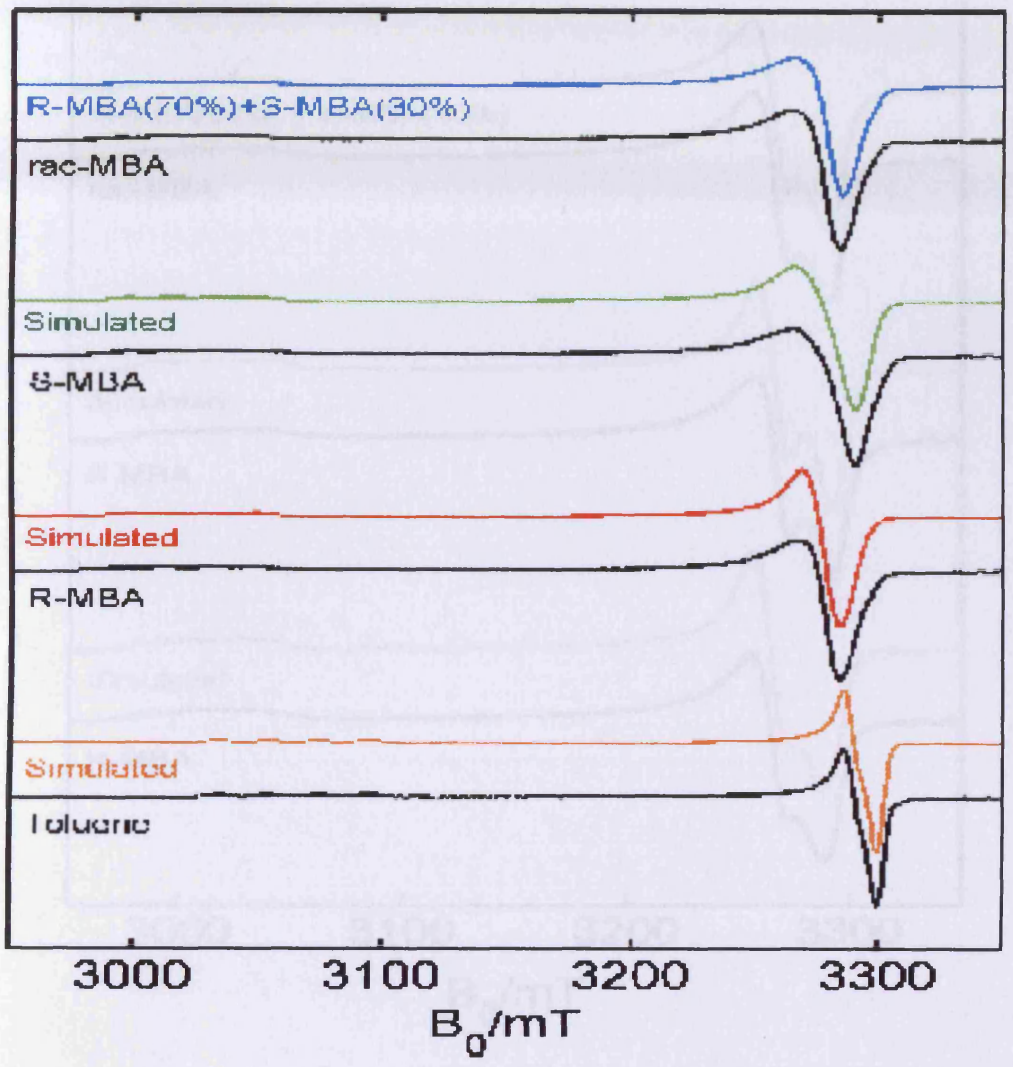

Figure 3.36: *The W-band EPR spectra of S,S'-[Cu(bf 1)] racemic-MBA, S-MBA, R-MBA and toluene, with simulations given above the respective experimental spectra.*

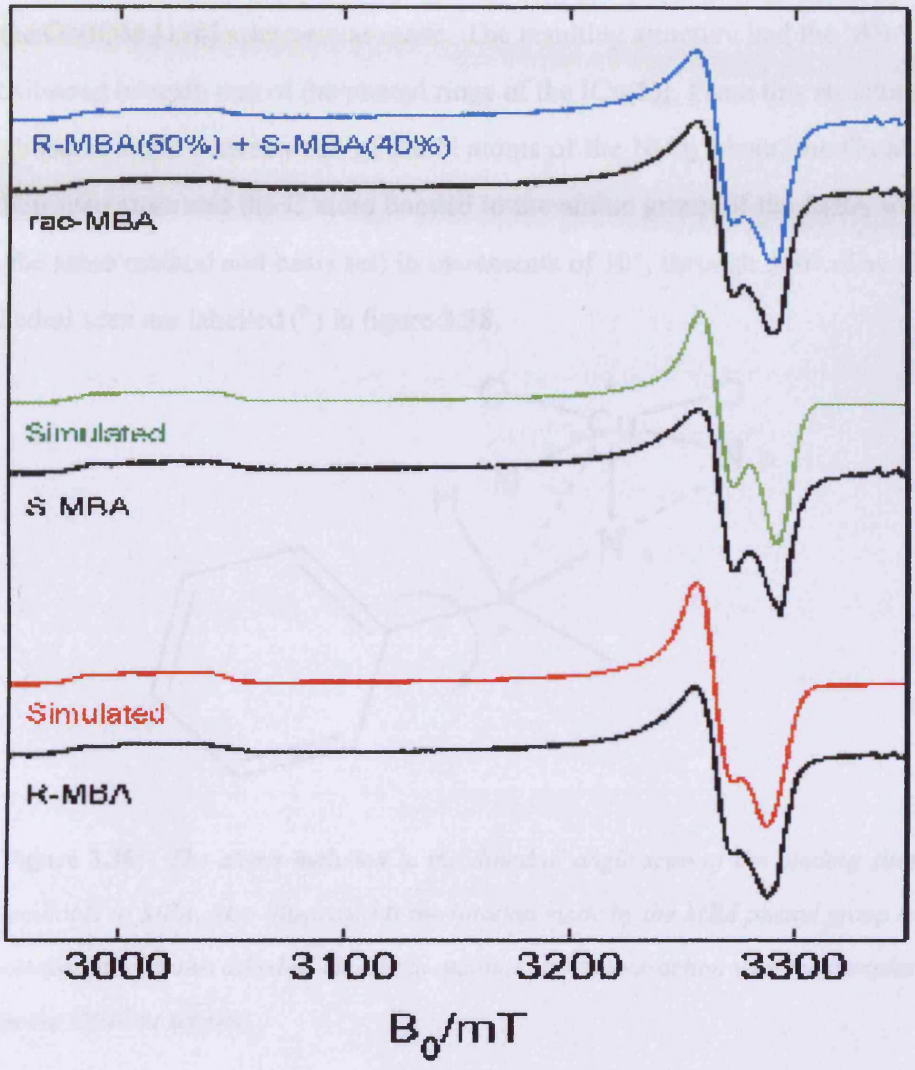

Figure 3.37: *The W-band EPR spectra of S,S'-[Cu(bf 1a)] racemic-MBA, S-MBA, R-MBA and toluene, with simulations given above the respective experimental spectra.*

A preliminary optimisation of *R*-MBA and [Cu(**1**)] using the B3LYP functional with a 6-31G(d,p) basis set on the Cu atom, all three N atoms, both O atoms, the methyl and central C atoms of the MBA, the two imine and two backbone C atoms of the complex, and any H atoms attached, and with the AMBER [117] forcefield on all other atoms, partitioned using the ONIOM [118] scheme was made. The resulting structure had the MBA phenyl ring positioned beneath one of the phenyl rings of the [Cu(**1**)]. From this structure a scan of the dihedral angle between one of the N atoms of the N_2O_2 plane, the Cu atom, the MBA Nitrogen atom and the C atom bonded to the amine group of the MBA was made (using the same method and basis set) in increments of 10°, through 360°. The atoms in this dihedral scan are labelled (*) in figure 3.38.

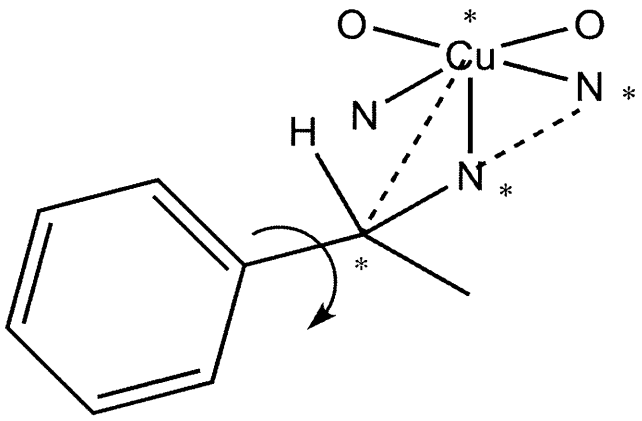

Figure 3.38: *The atoms included in the dihedral angle scan of the binding sites available to MBA. Also illustrated is the rotation made by the MBA phenyl group to compensate for this dihedral change to maintain $\pi - \pi$ interaction with the complex in the ONIOM scheme.*

As the MBA was twisted away from the starting configuration, it was found that the phenyl group rotated by $\sim 20°$ about the bond connecting it to the C atom of the MBA, in order to maintain the $\pi - \pi$ interaction between the phenyl rings, until a threshold angle of 60° greater than the optimum angle was reached, at which point the MBA phenyl ring followed the dihedral change and moved completely to a position beneath the cyclohexyl group of the complex. Further rotation showed a similar distortion, as the MBA phenyl ring remains in the space below the cyclohexyl ring, up to a dihedral angle of 170° greater

than the optimised angle, beyond which point the MBA phenyl ring moved into a position that resembled a $\pi - \pi$ interaction with the other phenyl ring of [Cu(**1**)]. This suggests that the costs of rotating the phenyl group of the MBA is more than compensated by the combined strengths of the $\pi - \pi$ interaction between the MBA and complex phenyl rings and the steric hindrance of the *tert*-butyl groups up to this angle, at which point the sterically uncrowded region below the cyclohexyl ring becomes the favoured position. On further rotation, the MBA is forced into a position in which it is able to form $\pi - \pi$ interactions with the other phenyl ring of the complex. This does not occur, however, until a large, fixed dihedral angle is reached in the scan, implying a lack of symmetry between the $\pi - \pi$ interactions between the MBA and each of the rings. Possible reasons behind this were investigated by performing optimisations of both *R*- and *S*-MBA with [Cu(**1**)] with the optimisations started with the MBA phenyl ring much closer to each of the phenyl rings of [Cu(**1**)] than to the other. These two configurations are labelled side A, when the MBA phenyl ring is placed closer to the [Cu(**1**)] phenyl ring on the left, looking from the Cu centre towards the cyclohexyl group with the MBA beneath the complex plane, and side B with the MBA phenyl ring closer to the right had side phenyl ring of [Cu(**1**)] (see figures 3.39 and 3.40).

Optimisations were thus calculated for each of the following configurations:

1. *R*-MBA + *R,R'*-[Cu(**1**)] with the MBA phenyl ring beneath the complex side A phenyl ring (*R*-1-A)

2. *R*-MBA + *R,R'*-[Cu(**1**)] with the MBA phenyl ring beneath the complex side B phenyl ring (*R*-1-B)

3. *S*-MBA + *R,R'*-[Cu(**1**)] with the MBA phenyl ring beneath the complex side A phenyl ring (*S*-1-A)

4. *S*-MBA + *R,R'*-[Cu(**1**)] with the MBA phenyl ring beneath the complex side B phenyl ring (*S*-1-B)

5. *R*-MBA + *R,R'*-[Cu(**1a**)] with the MBA phenyl ring beneath the complex side A

phenyl ring (*R*-1a-A)

6. *R*-MBA + *R,R'*-[Cu(**1a**)] with the MBA phenyl ring beneath the complex side B phenyl ring (*R*-1a-B)

7. *S*-MBA + *R,R'*-[Cu(**1a**)] with the MBA phenyl ring beneath the complex side A phenyl ring (*S*-1a-A)

8. *S*-MBA + *R,R'*-[Cu(**1a**)] with the MBA phenyl ring beneath the complex side B phenyl ring (*S*-1a-B)

These adducts are shown schematically (without chirality labelling of the MBA) in figures 3.39 and 3.40.

Only the *R,R'* isomer of each of the Cu complexes was studied in these calculations, since it was assumed that the *S,S'* isomers would mirror the results of the *R,R'* isomer. The optimised structures that result from these calculations are given in figures 3.41 to 3.44.

These structures clearly do not all maintain a configuration in which the MBA phenyl ring interacts in a $\pi - \pi$ manner with the appropriate phenyl ring of the copper complex. Steric effects disrupt the $\pi - \pi$ interactions for several of the arrangements, moving the MBA phenyl ring, on optimisation, beneath the cyclohexyl group. To measure the extent to which the rings are maintained in a $\pi - \pi$ interacting configuration three geometric measures have been employed: the distances between the centres of the rings, the minimum distances between the rings, and the angles between the unit normals to the planes of the rings. The centres of the phenyl rings are simply calculated as the average of the coordinates of the C atoms, with the assumption that the rings are regular and planar. This assumption is also applied in the calculation of the angles between the unit normals of the planes, which are defined as the average normalised cross-product of every pair of C-C vectors. The minimum distances are calculated by overlaying a simple triangular grid on the rings, with nine points along each edge (including the two atoms, figure 3.45) and calculating the distance between every pair of these points between the two phenyl

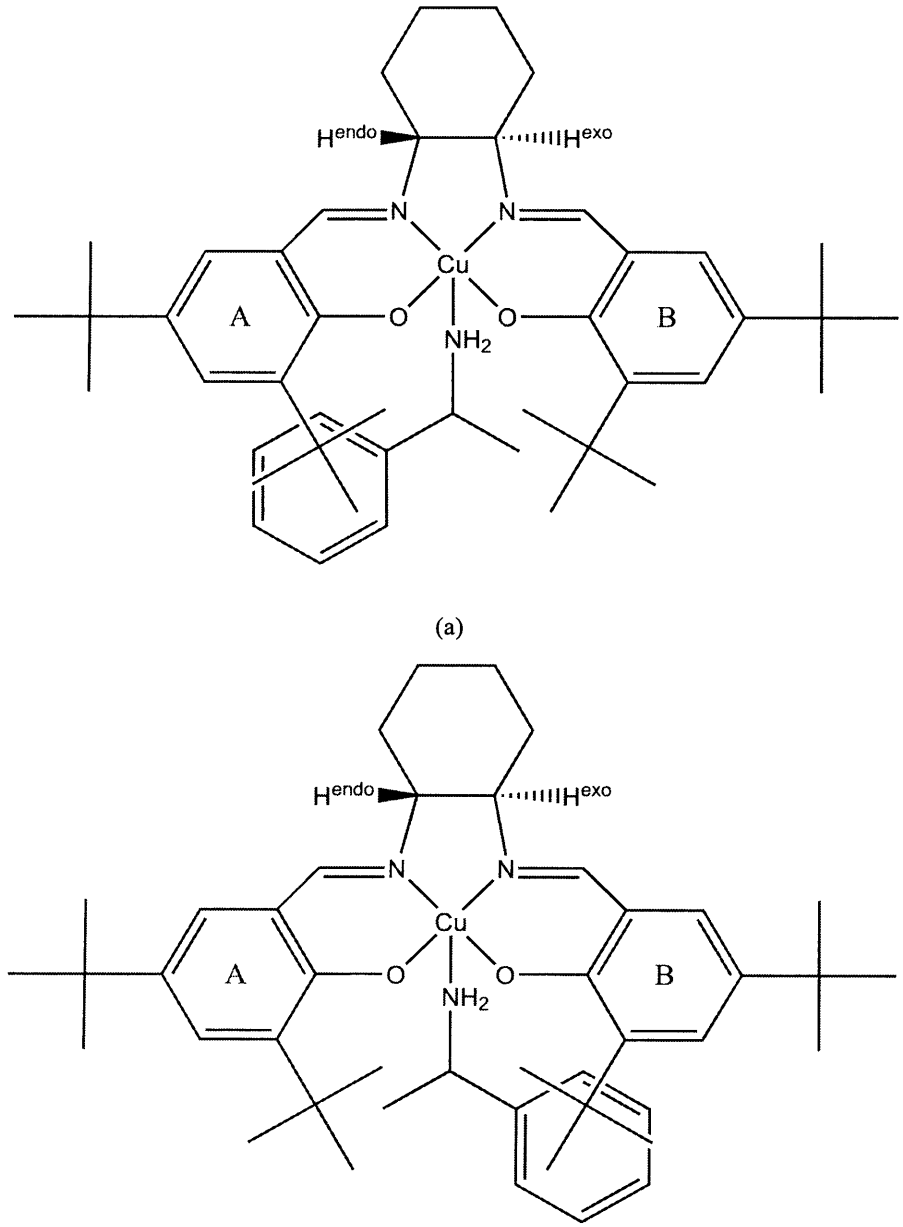

Figure 3.39: *The pre-optimisation configurations of [Cu(**1**)] + MBA in which the MBA phenyl ring is placed closer to a) the complex phenyl ring A and b) the complex phenyl ring B.*

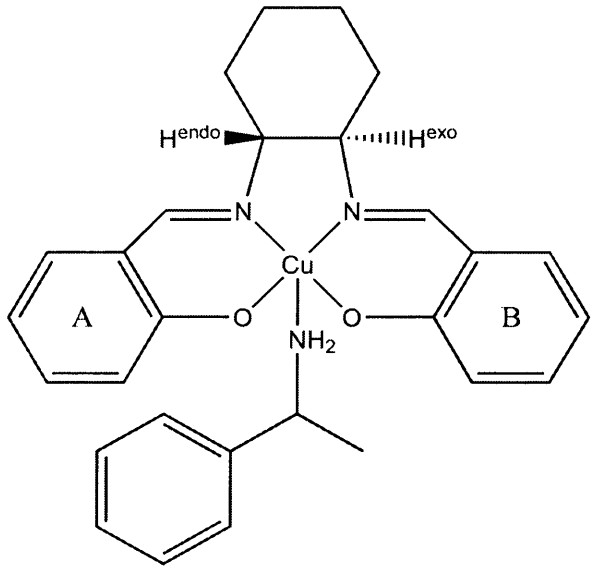

(a)

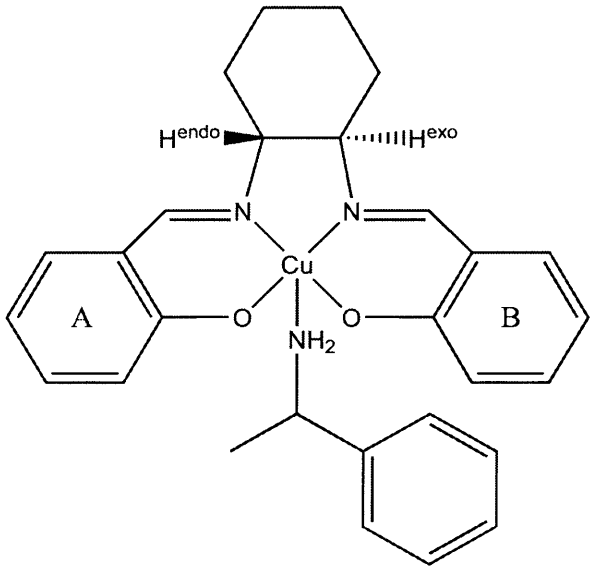

(b)

Figure 3.40: *The pre-optimisation configurations of [Cu(**1a**)] + MBA in which the MBA phenyl ring is placed closer to a) the complex phenyl ring A and b) the complex phenyl ring B.*

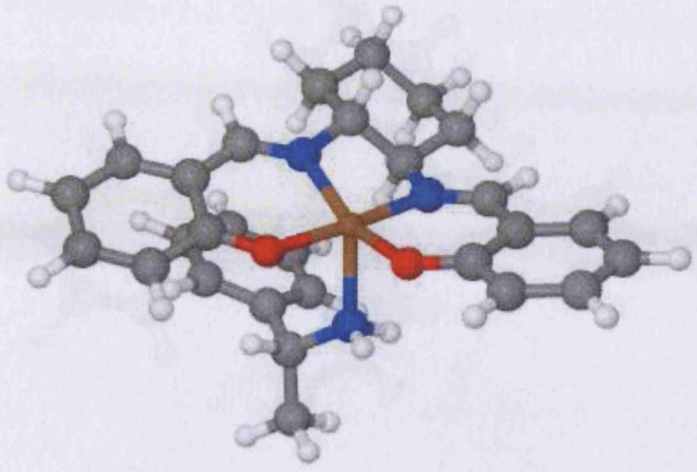

(a) *R*-MBA+Cu(**1a**) Side A

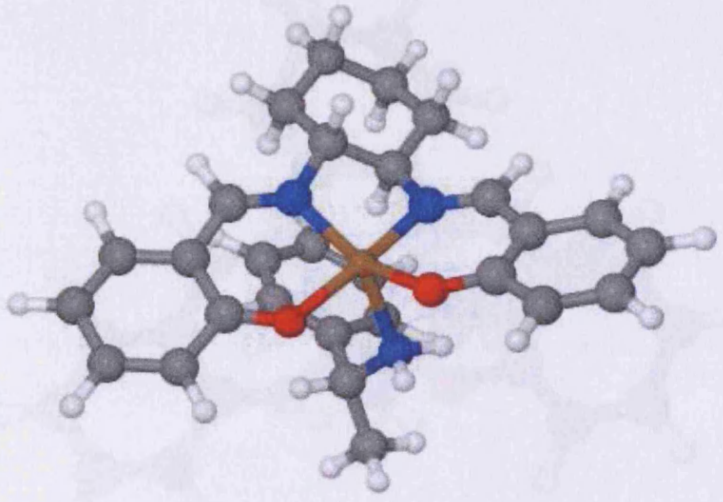

(b) *R*-MBA+Cu(**1a**) Side B

Figure 3.41: *The optimised structures of R-MBA with [Cu(***1a***)], from starting structures in which the MBA phenyl ring was positioned under a) Ring A of the [Cu(***1a***)] and b) Ring B of the [Cu(***1a***)].*

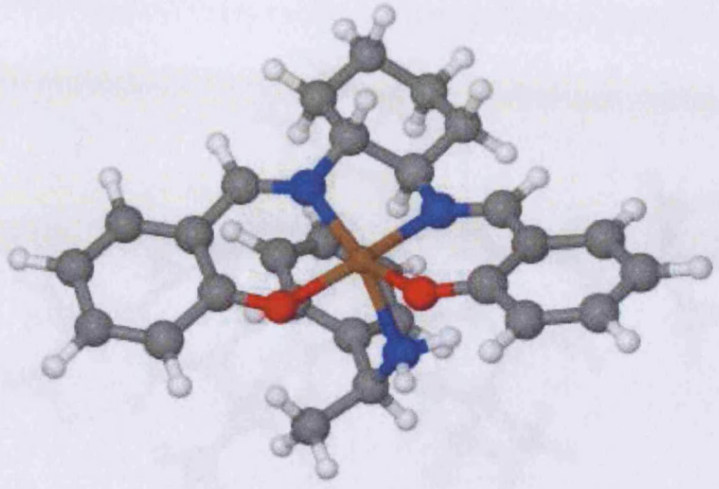

(a) *S*-MBA+Cu(**1a**) Side A

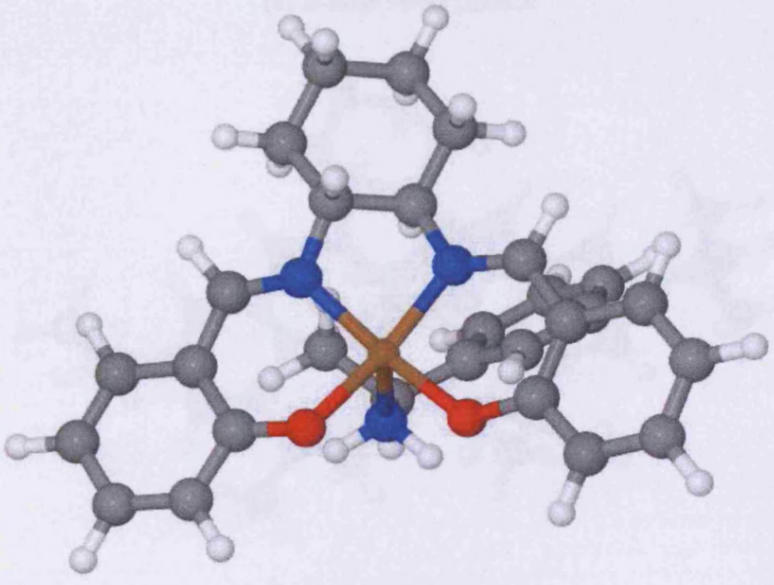

(b) *S*-MBA+Cu(**1a**) Side B

Figure 3.42: *The optimised structures of S-MBA with [Cu(**1a**)], from starting structures in which the MBA phenyl ring was positioned under a) Ring A of the [Cu(**1a**)] and b) Ring B of the [Cu(**1a**)].*

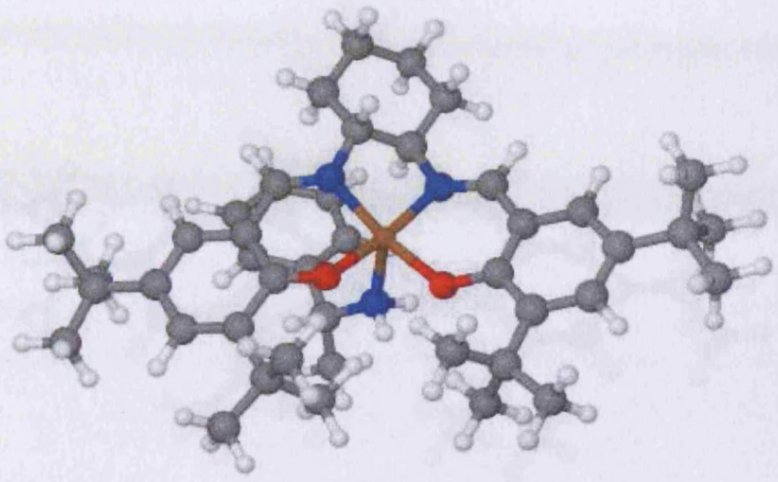

(a) *R*-MBA+Cu(**1**) Side A

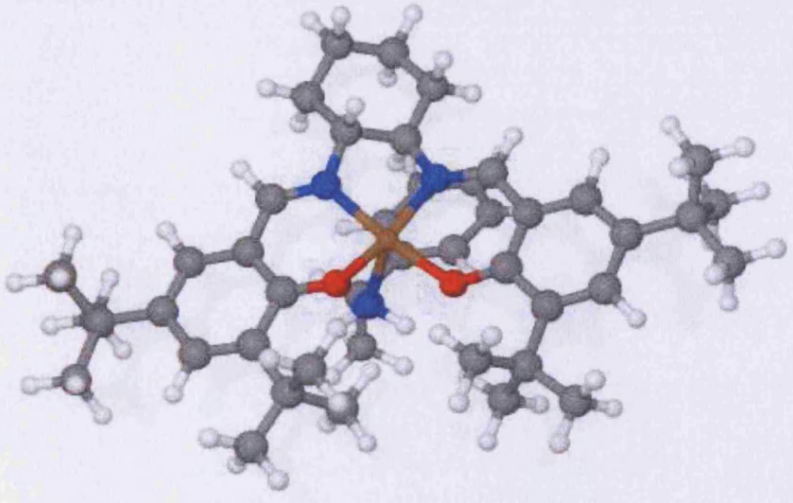

(b) *R*-MBA+Cu(**1**) Side B

Figure 3.43: *The optimised structures of R-MBA with [Cu(**1**)], from starting structures in which the MBA phenyl ring was positioned under a) Ring A of the [Cu(**1**)] and b) Ring B of the [Cu(**1**)].*

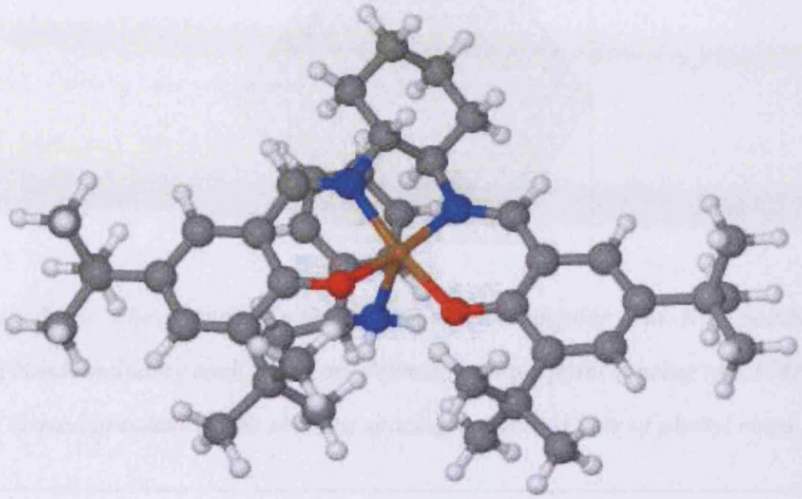

(a) *S*-MBA+Cu(**1**) Side A

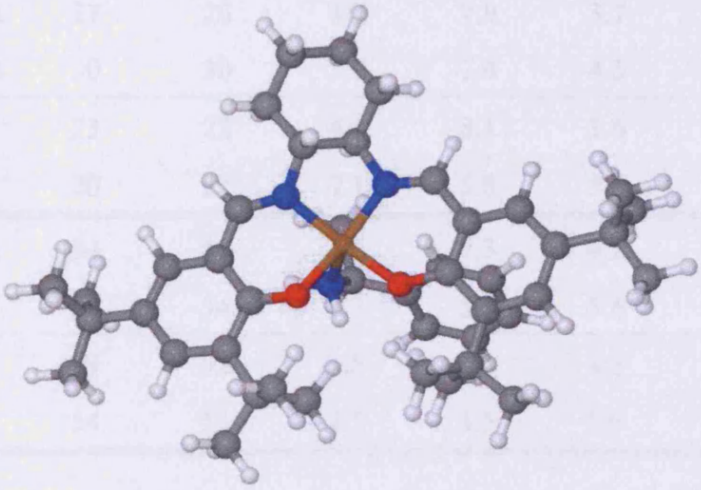

(b) *S*-MBA+Cu(**1**) Side B

Figure 3.44: *The optimised structures of S-MBA with [Cu(**1**)], from starting structures in which the MBA phenyl ring was positioned under a) Ring A of the [Cu(**1**)] and b) Ring B of the [Cu(**1**)].*

rings, thus finding the minimum. The H atoms are not taken to be part of the rings for this calculation. The values obtained for these measurements are given in table 3.14.

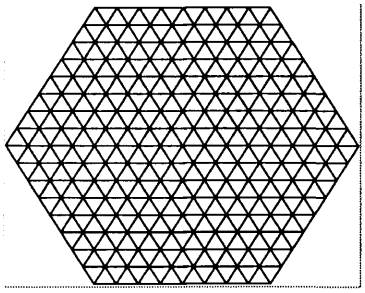

Figure 3.45: *The division of a phenyl ring into a triangular grid. Nine points along each bond (including each atom) are defined, giving a point spacing of 0.174Å. This grid is used to calculate the shortest spacing between a pair of phenyl rings.*

System	$\theta_{\hat{\underline{n}}-\hat{\underline{n}}}(A)$ /°	$\theta_{\hat{\underline{n}}-\hat{\underline{n}}}(B)$ /°	$R_{c-c}(A)$ /Å	$R_{c-c}(B)$ /Å	$R_{min}(A)$ /Å	$R_{min}(B)$ /Å
R-1a-A	27	26	4.7	7.9	3.7	5.8
R-1a-B	30	30	5.7	7.4	4.3	5.5
R-1-A	23	22	4.8	8.1	3.6	6.0
R-1-B	20	22	7.1	5.8	5.0	4.3
S-1a-A	34	35	5.6	7.3	4.2	5.5
S-1a-B	53	54	7.7	5.5	5.6	3.7
S-1-A	38	32	5.8	7.3	4.3	5.6
S-1-B	54	53	7.5	4.5	5.9	3.1

Table 3.14: *The spatial relationships between the centre of the MBA phenyl ring and the complex phenyl rings (A and B) in each of the optimised systems. These are measured in terms of the distance between the centres of the two rings, R_{c-c}, the angle formed between the unit normals to the planes of each of the rings, and the shortest distance between the two rings, based on a hexagonal grid.*

The most evident trend in the data of table 3.14 is that the *S*-MBA molecule remains closer to whichever ring it is initially placed closer to in both the [Cu(**1**)] and [Cu(**1a**)] cases,

while the *R*-MBA molecule only remains close to the 'B' ring of the [Cu(**1**)] complex, showing a tendency to rotate away from phenyl ring B in [Cu(**1a**)], towards phenyl ring A. That the final positions occupied by the *R*-MBA are different when it is placed closer to the two rings of [Cu(**1a**)], *i.e.* that the minimum distance of its phenyl ring from ring A is only 3.7Å when the optimisation is begun with its phenyl ring placed closer to ring A, and is 4.3Å when its phenyl ring is initially placed closer to the complex ring B makes it clear that these two binding modes are distinct. When the MBA ring is initially closer to complex ring B, reference to figure 3.41 shows that the final position is beneath the complex cyclohexane group, towards the 'A' side of that group. This suggests that a stable minimum cannot be located by the MBA in which its phenyl ring is under complex ring B, but that one can under the cyclohexane group before it reaches complex ring A. The confinement of the MBA ring by $\pi - \pi$ interactions is not, therefore, sufficiently strong to overcome the steric crowding at this position.

These positions occupied by the MBA molecules are heavily restricted by three principal factors. In the first place, the Cu-N interaction holds the amine group at a consistent distance from the copper, with a value between 2.2Å and 2.3Å observed for each of the systems. Secondly, steric interactions occur between the MBA methyl group and the *tert*-butyl groups of the complex. When the *R*-MBA molecule is placed closer to ring A of the complex, (figures 3.41 a) and 3.43 a)), the methyl group occupies a region close to the complex N atom that is on the 'B' side of the complex, in a comparatively uncrowded position. When it is placed with its phenyl ring nearer to ring B of the complex, (figures 3.41 b) and 3.43 b)) however, the methyl group occupies a position between (and below) the two complex phenyl rings. This is a crowded region with the presence of *tert*-butyl groups causing a steric clash with the methyl group. The opposite is true for the *S*-enantiomer of MBA, namely that with the phenyl group under complex ring A (figures 3.42 a) and 3.44 a)) its methyl group is between the complex phenyl rings, with it under ring B (figures 3.42 b) and 3.44 b)) its methyl group is in the less crowded region close to the opposite complex N atom. Finally, the H^{exo} proton (as labelled in section 3.2) and the C atom to which it is bonded occupy a region of space close to complex phenyl ring B, making this

ring more crowded generally than ring A.

The positioning of the methyl group leads to the expectation that ring A would be preferred by the *R*-MBA enantiomer, while ring B would be preferred by the *S*-MBA enantiomer for $\pi - \pi$ interactions with the MBA phenyl ring. The positioning of H^{exo} and the attached C atom render ring B generally less preferable to either enantiomer. It is for this reason that the *R*-enantiomer rotates away from ring B in the [Cu(**1a**)] adduct towards the A ring. In the [Cu(**1**)] adduct it also rotates away, but is in fact trapped by the inability of the methyl group to pass the *tert*-butyl groups, and by the inability of the phenyl ring to pass H^{exo}. The *S*-enantiomer is similarly restricted beneath ring A, however the position of H^{exo} some distance from this ring gives the MBA more freedom to shift to minimise the clash between methyl group and the *tert*-butyl groups while maintaining a reasonably small minimum distance between the two rings (4.2Å in the [Cu(**1a**)] adduct and 4.3Å in the [Cu(**1**)] adduct). Beneath complex phenyl ring B the *S*-enantiomer is able to rotate its phenyl ring closer to a T-shaped configuration than to a parallel configuration with the complex phenyl ring B, with angles of 53° and 54° formed between their unit normals in the two complexes (compared to the angles of $\leq 30°$ for the four *R*-systems and of 32-38° for the systems in which the *S*-enantiomer is placed beneath the A ring of either complex). By rotating into this configuration, the *S*-enantiomer is able to form a $\pi - \pi$ interaction with either ring, so overcoming the steric restrictions placed on each ring by the H^{exo}.

These interactions give the (counterpoise corrected) interaction energies in table 3.15. Table 3.16 gives the differences in interaction energies for the systems with the MBA phenyl rings located nearer to phenyl ring A *vs.* phenyl ring B of the appropriate complex.

Negative values in table 3.16 indicate that the configuration in which the MBA phenyl ring is closer to ring A of the complex is more stable than that in which it is closer to ring B. These data show that each of the configurations with each of the enantiomers is strongly bound. They also show that the *R*-MBA enantiomer is, in all of the configura-

	R-MBA	*S*-MBA
System	E_{int}/kJ mol^{-1}	E_{int}/kJ mol^{-1}
1a-A	-92.9	-92.0
1a-B	-91.7	-88.8
1-A	-100.4	-99.1
1-B	-95.6	-84.1

Table 3.15: *The (counterpoise corrected) interaction energies between the MBA and the various complexes, with the MBA phenyl ring initially placed closer to each of the complex phenyl rings.*

System	E_{int} (A) - E_{int} (B)/kJ mol^{-1}
R-1a	-1.2
R-1	-4.8
S-1a	-3.3
S-1	-15.0

Table 3.16: *The (counterpoise corrected) interaction energy differences between the various structures with the MBA placed closer to ring A and to ring B of the relevant complex, E_{int} A - E_{int} B.*

tions, more strongly bound than the *S*-MBA enantiomer. The configurations in which the MBA phenyl ring is placed closer to complex phenyl ring A give almost identical interaction energies for the two enantiomers, indicating that binding in a configuration that allows $\pi - \pi$ interaction with this ring is equally favourable in each. The differences between the two complex ring configurations, however, are significantly smaller for the *R*-enantiomer with each of the complexes than for the *S*-enantiomer, indicating that a competitive mode of binding is available to the *R*-enantiomer, though not in a geometric configuration that favours $\pi - \pi$ interaction with the complex phenyl ring B. The energy difference in the *S*- enantiomer between the A-ring and B-ring configurations limits the importance of this competitive configuration for this enantiomer, particularly for the [Cu(**1**)] complex, for which the greater selectivity is observed in the EPR data. This explains the observed

difference in the EPR signals between the homo- and heterochiral interactions.

3.4.4 Conclusions

EPR investigations of [Cu(**1**)] dissolved in MBA demonstrate that either enantiomer of the MBA will bind to either enantiomer of the complex, but with subtle differences between the homochiral and heterochiral pairings. Further, in *racemic-* combinations, the signal obtained is composed of a linear combination of the pairings, with a 70:30 preference for the heterochiral pairing, with a 60:40 preference observed in the EPR spectra of the less sterically crowded [Cu(**1a**)] complex. Through the use of DFT calculations, on the two complexes, detailed information regarding the precise steric environment that the complex presents to the MBA was obtained, and used to explain these differences in binding modes.

Preliminary DFT studies confirmed the importance of $\pi - \pi$ interactions in determining the binding mode, identifying three potential configurations of the MBA with respect to the complex, namely having the MBA phenyl ring immediately beneath and parallel to either of the complex phenyl ring, and beneath the complex cyclohexane group. The two phenyl rings present the posibility of $\pi - \pi$ interaction as a stabilising influence, while the cyclohexane group presents a less crowded environment, and the exact nature of the binding in each case is a delicate interplay of these two factors.

The principal difference in the mode of binding in the two MBA enantiomers is identified in these calculations as the position of the methyl group of the MBA. Depending on which complex phenyl ring the MBA is placed closest to, the methyl group occupies a position that is either in the sterically crowded region between the complex phenyl rings (occupied by the *tert*-butyl groups), or the more open region close to the cyclohexyl group and to one of the complex N atoms. Since the position of the methyl group is different in each enantiomer, it occupies the crowded region when the MBA is placed under a different ring for each enantiomer. This means that each enantiomer is less crowded

under alternate rings, with *R*-MBA preferring ring A, *S*-MBA preferring ring B. A further consideration is the presence of H^{exo}, which in *R,R'*-[Cu(**1**)] occupies a position closer to ring B than to ring A (by definition of the ring labels), making ring B more crowded, and thus disfavouring ring B for binding. The ability of the *S*-enantiomer in this position to rotate its phenyl ring into a near T-shaped configuration with respect to the phenyl ring B allows it to bind to this ring as well as to ring A, while the *R*-enantiomer binds far less favourably to ring B, showing a far stronger preference for ring A, to the extent of rotating away when it is not sterically prevented from doing so. These geometric and interaction energy data build up a picture which explains the difference in the binding of the two enantiomers in terms of locating discrete sites available for binding of the MBA molecule by $\pi - \pi$ interactions to the complex, with different degrees of preference for each site displayed by each enatiomer.

3.5 Conclusions

Studies have been made to elucidate the precise nature of the interactions between epoxide and aromatic amine molecules with analogues of epoxidation catalysts. In each case, EPR/ENDOR studies have proven sufficiently sensitive to resolve enantiomeric (and geometric) discrimination of the binding, demonstrating preferences for homo-chiral pairings in the interactions of MBA with [Cu(**1**)] and in the interactions of chiral epoxide molecules with [VO(**1**)]. The geometric discrimination of *cis*- over *trans*-2,3-epoxybutane by [VO(**1**)] has also been demonstrated by EPR/ENDOR.

The importance of interactions other than the O/N-Metal centre bond in determining these selectivities has been demonstrated by DFT calculations of the various complex/substrate dimers. In the epoxide cases, the role played by H-bonding between the epoxide ring H atoms and the O atoms of the O_2N_2 plane of [VO(**1**)], and between the epoxide O atom and the H^{exo} atom of [VO(**1**)] was elucidated in calculations of the geometric isomers, *cis*- and *trans*-2,3-epoxybutane, for which the *cis*- isomer was shown to form a tripodal

H-bonding configuration with the [VO(**1**)] complex *via* the three H-bonds mentioned, which the *trans-* isomer was unable to do due to the methyl group in the position that was occupied by one of the H-bond forming H atoms in the *cis-* case. These weak H-bonds, along with the steric hindrance of the methyl group, explain the geometric selectivity of the system, as witnessed by the EPR/ENDOR data.

The role of H-bonds was probed further in an investigation of chiral epoxides, epoxypropane, 1,2-epoxybutane, chloromethyloxirane and fluoromethyloxirane. Selectivity was observed in the EPR/ENDOR experiments, and explained in the DFT calculations with reference to the interaction of the epoxide O atom with the H^{exo} atom. This H^{exo} atom is bonded to a stereocentre C atom, and thus its involvement in the binding mode links the chirality of the complex to the chirality of the epoxide. The precise nature of how this chirality was passed on was found to differ depending on the strength of the interaction between the epoxide O atom and the V centre, as determined by the electronegativity of the substituent on the epoxide. Where this interaction was weaker, H^{exo} was found to act as an anchor, pulling the epoxide towards itself. The selectivity was, in these circumstances, found to be related to the interaction between the epoxide ring H atoms and the O atoms of the N_2O_2 ring, with the epoxide substituent favouring the H-bond that involves the H atom that is bonded to the same C atom as the substituent. Where the interaction between the epoxide O atom and the V centre is stronger, the H^{exo} is found to be an obstruction to the approach of the epoxide to the complex, which is more pronounced when the substituent is on the same side of the epoxide molecule as H^{exo}.

The importance of $\pi - \pi$ interactions was probed for the interaction of methylbenzyl amine with [Cu(**1**)], through reference to a related complex, without *tert*-butyl substituents. In these structures, the link was made between the stereocentre C atoms of the MBA and of the complex by virtue of the crowding that H^{exo} and the stereocentre C atom to which it is bonded cause near to one of the phenyl rings of the Cu complex, and not to the other, and of the steric interaction that occurs between the MBA methyl group and the *tert*-butyl groups of the complex. This leads to a preference for $\pi - \pi$ interaction to occur between the MBA phenyl and that less crowded phenyl ring of the complex. This is tem-

pered by the fact that the methyl group of the MBA clashes sterically with the *tert*-butyl groups of the complex. It was demonstrated that the different enantiomers of MBA were, by virtue of the positioning of their respective methyl groups, hindered by the presence of *tert*-butyl groups on opposing complex phenyl rings. This opposite preference in terms of which complex ring to form a $\pi - \pi$ interaction with leads to the availability of two distinct binding sites for the *S*-MBA enantiomer, with much less distinction between the binding observed in the *R*-enantiomer. Significantly greater differences in interaction energies between the two *S*-enantiomer configurations in each complex are observed, explaining the observed differences in the EPR signals.

The successful implication of H^{exo} in the binding modes of both epoxides and amine leads to the identification of the interaction mechanism by which chirality is conferred in both cases. These two different effects have both been linked, *via* different mechanisms, to the stereocentre C atom, providing different means by which homochiral selectivity is achieved in analogues of catalytically important complexes.

Chapter 4

Incorporation of Copper Ions in an Aluminium Phosphate Material With AEN Topology

4.1 Introduction

The importance of alumino phosphate materials (AlPOs) as catalysts of many reactions depends on the presence of transition metal ions in the structure, acting as Brønsted acid sites or redox active centres [119]. This results in a class of materials that is capable of acting as heterogeneous catalysts. The actual relationship between the host structure and the transition metal ions, particularly whether ions are present in framework or extra-framework sites is a matter of particular interest because it is important in determining the mechanism of the catalytic process.

The incorporation of heteroelements into zeolite frameworks is, according to Gabelica and Vavlange [62], possible provided they are of an appropriate size, and capable of taking on stable tetrahedral geometries. This is restrictive for bulky, electron rich ions such as Co, Fe, Mn and Cu.

This study [120] investigates the incorporation of copper ions into the AlPO-53 framework, whose structure is given in figure 4.1. Hereafter this material is labelled CuIST-2.

The AlPO-53 framework consists of 4-, 6-, and 8-member ring pores and a 2-dimensional 8-member channel system. These pores are illustrated in the Connolly surface in figure 4.2.

Copper(II) is an electron rich d^9 species, which forms Jahn-Teller distorted 6-coordinate octahedral complexes and 4-coordinate square planar complexes. The (distorted) tetrahedral coordination of Cu^{II} complexes is unusual, though several examples possessing strongly chelating ligands forming a tetrahedral environment are known [121–123]. The substitution of Cu^{II} ions into the lattice sites of an aluminium phosphate material would seem to require them to adopt such a tetrahedral coordination. It is therefore generally believed that the catalytic activity of the copper takes place at extra-framework sites, with the copper absorbed in the lattice pores. This study presents spectroscopic and DFT evidence for the incorporation of the Cu^{II} ions into lattice sites.

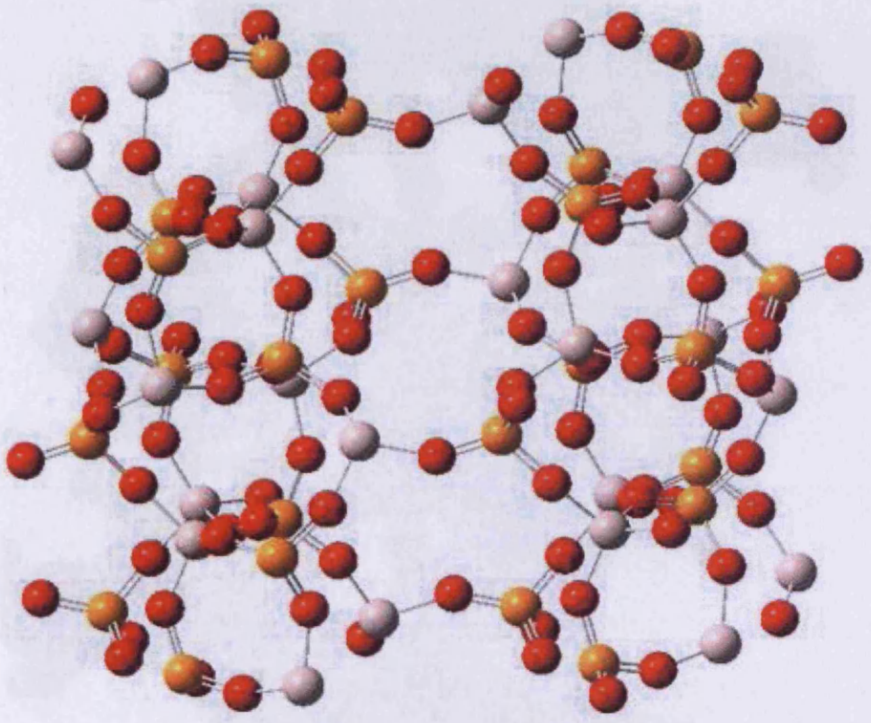

Figure 4.1: *The structure of AlPO-53. In this scheme, oxygen atoms are red, phosphorus atoms are orange and aluminium atoms are pink.*

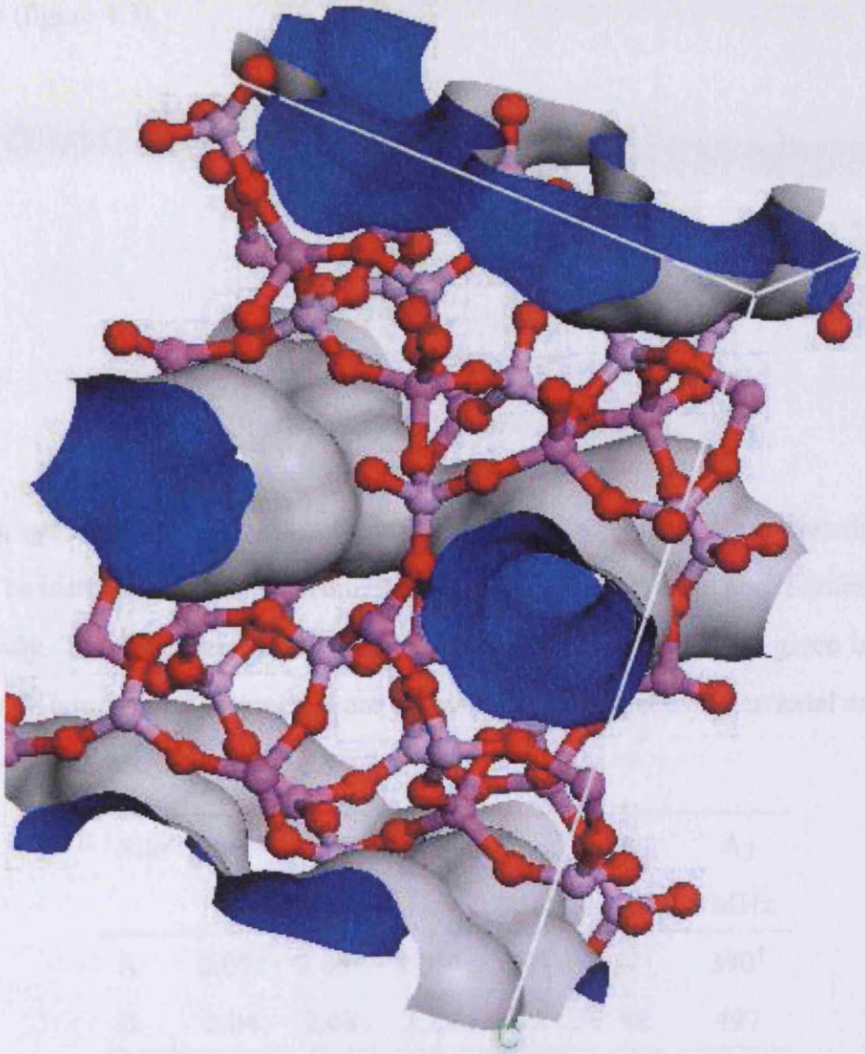

Figure 4.2: *The Connolly surface of AlPO-53, illustrating the 2-dimensional 8-member channel system.*

4.2 Spectroscopic Studies

The spectra of this section were recorded by Damien Murphy.

The synthesis of CuIST-2 involves templating the framework with the methylamine (MA) molecule (figure 4.3).

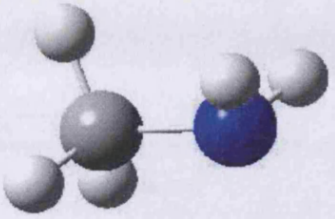

Figure 4.3: *The methylamine (MA) molecule, CH_3NH_2.*

The EPR spectrum of the templated lattice is shown in figure 4.4 a). Two distinct Cu^{II} sites can be identified in this spectrum, labelled A and B, with axial and rhombic g-tensors respectively. The EPR parameters associated with these two sites are given in table 4.1. These spin-Hamiltonian parameters are consistent with respectively an axial environment and a lower symmetry environment.

Site	g_1	g_2	g_3	A_1 /MHz	A_2 /MHz	A_3 /MHz
A	2.05*	2.05*	2.36*	37†	37†	390†
B	2.04	2.08	2.29	43	58	497

Table 4.1: *The EPR parameters for the axial Cu^{II} species (A) and rhombic Cu^{II} (B) species in figure 4.4 a).* * $g_1 = g_2 = g_\perp$, $g_3 = g_\parallel$. † $A_1 = A_2 = A_\perp$, $A_3 = A_\parallel$.

On calcination at 673K, followed by an exposure to air at 300K, the sample gives the EPR signal shown in figure 4.4 b). Again, two distinct sites can be resolved, C and D, though now there is considerable line-broadening due to g- and A-strain that arises from the heterogeneity of the Cu^{II} sites present, rendering the resolution of $A_\perp$ impossible.

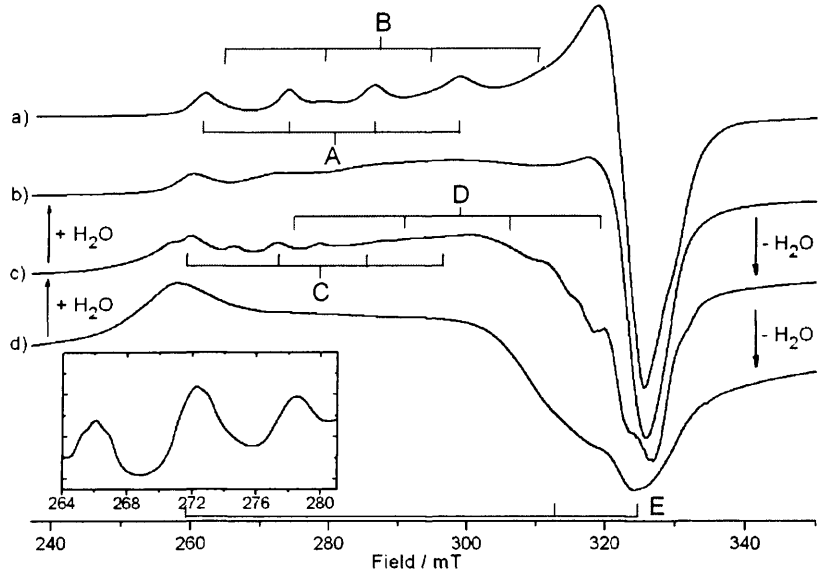

Figure 4.4: *The X-band cw-EPR spectra of CuIST-2 a) with the templating molecule (as synthesised), b) after calcination at 673K and hydration on exposure to air, c) after evacuation at 300K, and d) after evacuation at 500K.*

The parameters that are resolved for the axial environments C and D are given in table 4.2.

Site	$g_{\|}$	$g_{\perp}$	$A_{\|}$/MHz	$A_{\perp}$/MHz
C	2.40	2.07	403	unresolved
D	2.24	2.05	470	unresolved

Table 4.2: *The EPR parameters for the axial Cu^{II} species C and D in figure 4.4 b).*

The sample was then dehydrated by evacuation at 500K. The spectrum that results from this process is given in figure 4.4 d). This spectrum is comprised of the signals that arise from sites C and D with a further rhombic signal arising from a third site, E. The hyperfine splitting in this spectrum cannot be resolved for E nor for sites C and D due to extensive line broadening. The parameters associated with site E are given in table 4.3. The rehydrated sample was then dehydrated at 300K to give the intermediate spectrum of figure 4.4 c), from which can be resolved more easily the remnant signals that arise from sites C and D. A process of rehydrating and dehydrating the sample shows reversibility

on moving between spectra 4.4 b) and 4.4 c).

Site	g_1	g_2	g_3
E	2.06	2.14	2.61

Table 4.3: *The EPR parameters for the rhombic Cu^{II} species E in figure 4.4 c). The A values are not resolved.*

Another observation from the spectra is the resolution of the superhyperfine couplings due to the P atoms. These are recorded for site E, given in the inset of figure 4.4. They can be resolved into two distinct contributions, isotropic contributions of 1.80MHz, arising from a single P nucleus and of 22.5MHz, arising from 3 equivalent P nuclei. These can be interpreted as due to a single P nucleus at some distance from the Cu centre, having, crucially, a weak bonding interaction with the copper, and a group of 3 equivalent much closer, with a much stronger interaction with the copper.

Through the various processes, these spectra show a range of environments that the Cu^{II} ions occupy. These range from a highly symmetric, axial environment (A and C) through a lower symmetry, slightly rhombic environment (B and D) to a very low symmetry environment of unknown coordination (E). This implies that, on removal of the MA and the water, the coordination of the Cu^{II} ions is reduced from 6-coordinate/5-coordinate to some lower coordination. This is consistent with the suggestion that the Cu^{II} ions occupy low symmetry framework sites, with the water and MA, when present, filling the 'empty' vacancies, increasing the coordination and thus increasing the symmetry of the sites.

To support this assertion periodic structural and cluster g-tensor calculations on the structure were carried out.

4.3 DFT

The incorporation of Cu^{II} ions into the framework is more likely to involve the replacement of Al^{III} ions (rather than of P^{V} ions), with the further addition of a single proton to balance the charge discrepancy, giving rise to three symmetrically distinct lattice sites that the copper ions can occupy (figure 4.5).

The steric environments at each of these sites (in terms of the surrounding pore structure) are markedly different providing a possible explanation for the two signals in each of the spectra in figure 4.4.

To study these differences, periodic DFT calculations were carried out using the Vienna Ab Initio Simulation Package, VASP [124] with the PW91 [125] functional and a basis set comprising 201600 plane waves based on an energy cutoff of 300eV on the unsubstituted structure and with a 302400 plane wave basis with a cutoff of 400eV on structures with copper ions substituted into each of the possible sites. A reciprocal space grid comprising $2 \times 2 \times 2$ points in k-space was used in the calculations. A pseudo-potential was applied to each atom to represent the potential due to the core electrons.

Each of the three substitution sites has four surrounding O atoms. Any one of these can be protonated to balance the charge discrepancy that arises from substituting a Cu^{II} ion for an Al^{III} ion, making twelve possible structures. The energies of each of these are given in table 4.4. The labelling of the protonation sites is arbitrary.

The lowest energy structure from table 4.4 is that for the fourth protonation site of the structure with the copper substituted in site 2. Also noted from this table are the lowest energy protonation sites for each of the other copper substitution sites, namely the first protonation site of the structure with the copper in the first substitution site and the fourth protonation of that with the copper in the third substitution site. These three structures were used in all further calculations, for which water and MA molecules were included in the structures. In each of the structures studied the proton sat in an 8-membered ring channel, with the exceptions of the structures with the proton in site 2 with the Cu in the

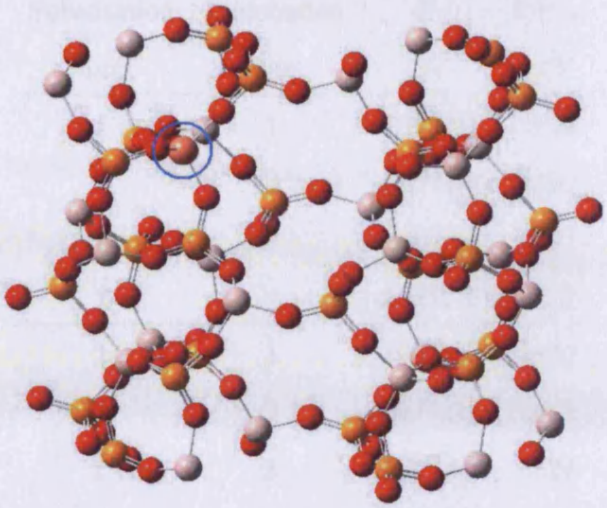

(a) Site 1

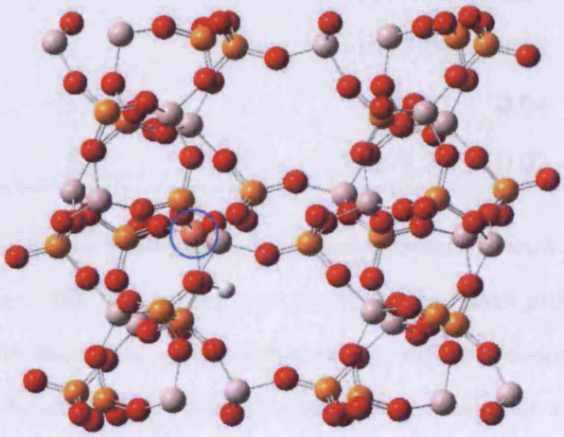

(b) Site 2

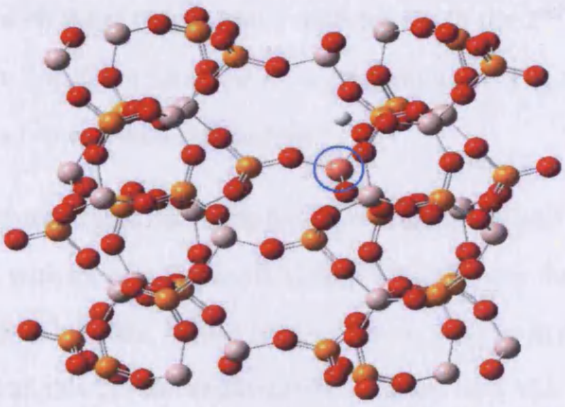

(c) Site 3

Figure 4.5: *The three symmetrically distinct Al sites in AlPO-5 into which copper ions can be incorporated.*

Substitution Site	Protonation Site	E /eV	E-E_{min} /eV
1	1	-1078.02	0.19
1	2	-1077.94	0.27
1	3	-1077.84	0.37
1	4	-1077.75	0.47
2	1	-1078.03	0.18
2	2	-1077.98	0.23
2	3	-1077.95	0.26
2	4	-1078.21	0.00
3	1	-1077.92	0.29
3	2	-1077.94	0.28
3	3	-1078.17	0.04
3	4	-1078.20	0.02

Table 4.4: *The energies of the various substituted structures with each of the various protonations. The lowest energy is found for the fourth protonation site of the structure with the copper substituted in site 2, with an energy of -1078.21eV. The differences between the energies of each structure and this minimum energy structure are also given.*

1^{st} substitution site, with the proton in site 2 with the Cu in the 2^{nd} substitution site, and with the proton in site 2 with the Cu in the 3^{rd} substitution site. For all of these structures, the proton occupied a 6-membered ring hollow.

Further calculations were carried out using the PW91 functional and a basis set containing 302400 plane waves, with an energy cut-off of 400eV to consider the effect of MA and/or water on the framework Cu^{II} ions. With a four coordinate copper in the lattice framework, two extra sites are available for the coordination of water and MA molecules, one axial and one equatorial to the protonated oxygen. Calculations were thus done for each of the molecules in each of these positions, as well as for MA in both, for water in both,

and for MA in one and water in the other. The interaction energies for each of these arrangements are calculated as the difference between the energies of the structures with the coordinated water/MA molecules and the sum of the energies of the structures with no molecules absorbed and of the isolated MA/water molecules, calculated in an equally sized cell. These interaction energies are given in table 4.5.

Small Molecule(s) Coordinated	Site 1 E/kJ mol^{-1}	Site 2 E/kJ mol^{-1}	Site 3 E/kJ mol^{-1}
MA, axial	-86.3	193.4	-43.0
MA, equatorial	31.8	-42.9	-74.2
Water, axial	-60.7	52.4	23.0
Water, equatorial	-22.6	-44.8	-43.1
Two MA	594.5	*	1870.1
Two Water	-103.4	-23.7	-63.1
MA, axial; Water equatorial	-12.9	408.4	*
MA, equatorial; Water axial	47.6	3.7	-98.8

Table 4.5: *The interaction energies of the MA and water in axial and equatorial positions in each of the three substitution sites. Entries marked * show no sign of convergence.*

Despite the fact that site two gives the most negative value for the absorption of a single water molecule in an equatorial position, only sites one and three were considered in further calculations, since the absorption energy for the single equatorial water molecule for site three is very close to that of site two, and because of the trend observed that site one provides the best environment generally for axial coordination, whilst site three is optimum for equatorial coordination. The most negative value overall is that obtained for the absorption of two water molecules into site one. This, however, was not a properly coordinated system, with the equatorial molecule quite remote at 3.62Å, compared to a distance of 2.00Å for the axial water molecule. Site three thus presents the best available space for two water molecules to coordinate. Due to the failure of two MA molecules to

provide a negative interaction energy in any site, they were not considered further.

Figures 4.6 to 4.9 illustrate the coordination of the Cu^{II} centres, showing each Cu^{II} centre along with the surrounding four O atoms, the charge balancing proton and the relevant MA or water molecules cut out from each of the lowest energy optimised structures.

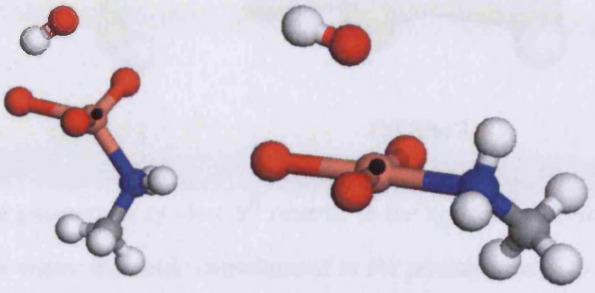

(a) Site 1 (b) Site 3

Figure 4.6: *The geometries of the Cu^{II} centres in the optimised periodic structures, with (a) a single MA molecule coordinated in the position axial to the protonated O atom with the Cu in site 1, and (b) a single MA molecule coordinated in the position equatorial to the protonated O atom with the Cu in site 3. The protonated O atom is shown at the top in each figure.*

The symmetries at the Cu^{II} centres shown in figures 4.6 to 4.9 are, for the cases with two molecules coordinated, 6-coordinate distorted octahedral, for the cases with a single molecule coordinated equatorially (in site 3), 5-coordinate distorted square pyramidal, and for the cases with a single molecule coordinated axially (in site 1), 5-coordinate very distorted square pyramidal with the longer axis within the plane. The bond lengths and angles in these clusters are given in table 4.6. To label each of the coordination sites (including the O atoms of the AlPO structure) the system illustrated in figure 4.10 is used.

The bond lengths of table 4.6 support the idea that the Cu^{II} ions adopt a Jahn-Teller distorted octahedral geometry within the lattice to the greatest extent possible. This is manifest in the fact that the rO_2-Cu and rO_3-Cu distances are, in all cases, shorter than all other bond lengths and similar to each other, and that the rO_1-Cu and rA-Cu distances

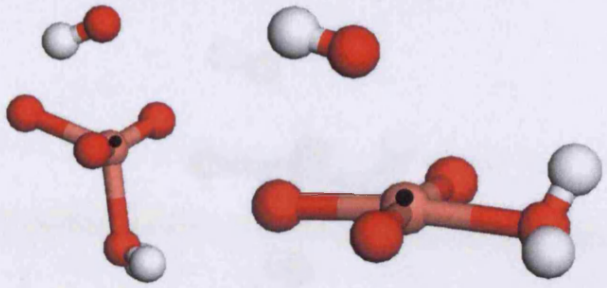

(a) Site 1 (b) Site 3

Figure 4.7: *The geometries of the Cu^{II} centres in the optimised periodic structures, with (a) a single water molecule coordinated in the position axial to the protonated O atom with the Cu in site 1, and (b) a single water molecule coordinated in the position equatorial to the protonated O atom with the Cu in site 3. The protonated O atom is shown at the top in each figure.*

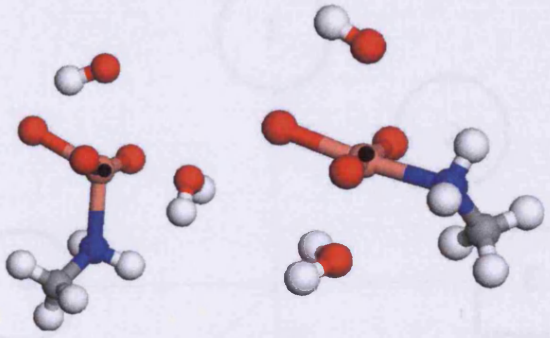

(a) Site 1 (b) Site 3

Figure 4.8: *The geometries of the Cu^{II} centres in the optimised periodic structures, with (a) a water molecule coordinated in the position equatorial, and an MA molecule coordinated in the position axial to the protonated O atom, with the Cu in site 1, and (b) a water molecule coordinated in the position axial, and an MA molecule coordinated in the position equatorial to the protonated O atom with the Cu in site 3. The protonated O atom is shown at the top in each figure.*

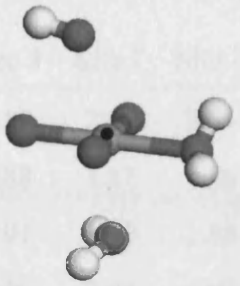

Figure 4.9: *The geometry of the Cu^{II} centre in the optimised periodic structure, with water molecules coordinated in the positions equatorial and axial to the protonated O atom, with the Cu in site 3. The protonated O atom is shown at the top.*

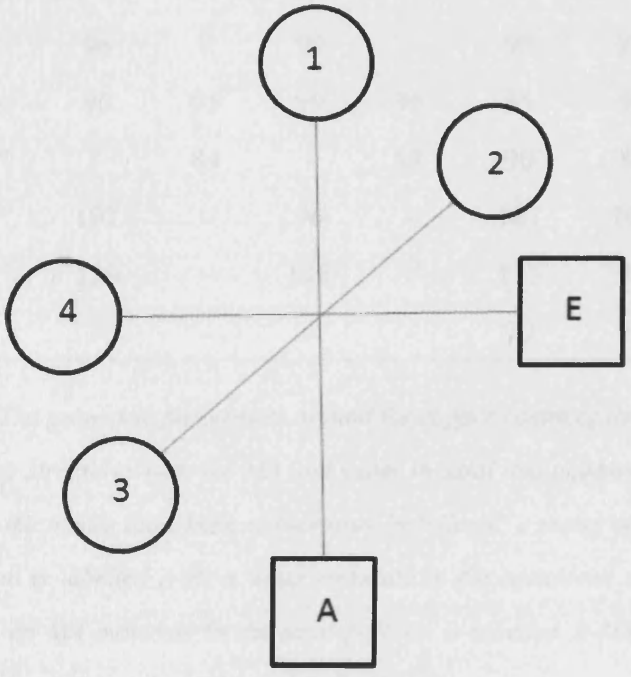

Figure 4.10: *The coordination site labels used in table 4.6.*

	A-MA	E-MA	A-W	E-W	A-MA; E-W	A-W; E-MA	A-W; E-W
	Site 1	Site 3	Site 1	Site 3	Site 1	Site 3	Site 3
rO_1-Cu/Å	2.72	2.59	2.64	2.58	2.68	2.72	2.71
rO_2-Cu/Å	1.91	1.88	1.87	1.86	1.91	1.19	1.87
rO_3-Cu/Å	1.93	1.91	1.90	1.88	1.92	1.94	1.87
rO_4-Cu/Å	2.08	2.00	2.01	1.97	2.14	2.02	2.00
rE-Cu/Å	-	2.05	-	2.11	2.38	2.04	2.12
rA-Cu/Å	2.02	-	2.12	-	2.13	2.54	2.48
O_1-Cu-O_2/°	72	100	74	102	76	97	97
O_1-Cu-O_3/°	84	81	89	81	88	78	77
O_1-Cu-O_4/°	63	79	65	79	62	76	75
O_1-Cu-E/°	-	102	-	109	95	98	107
O_2-Cu-O_4/°	94	91	95	92	88	91	91
O_2-Cu-E/°	-	90	-	85	79	90	86
O_2-Cu-A/°	96	-	99	-	90	83	84
O_3-Cu-O_4/°	96	95	99	96	95	94	96
O_3-Cu-E/°	-	84	-	87	90	84	87
O_3-Cu-A/°	101	-	96	-	107	103	103
O_4-Cu-A/°	130	-	116	-	111	91	94
A-Cu-E/°	-	-	-	-	90	94	85

Table 4.6: *The geometric parameters around the copper centre of the lowest interaction energy structures with the MA and water in axial and equatorial positions. For brevity, the names have been abbreviated as follows: a water molecule in the axial position is labelled A-W, a water molecule in the equatorial position is labelled E-W, an MA molecule in the axial position is labelled A-MA, and an MA molecule in the equatorial position is labelled E-MA.*

are generally longer than the rO_4-Cu and rE-Cu distances. This implies three distinct axis lengths, as would be expected for an octahedral copper complex. The tetrahedral arrange-

ment of the lattice sites makes it more difficult for the angles at the copper centres to reach the 90° expected for an octahedral coordination, and the absence of a sixth coordination in many of the structures allows for the expansion of the angles present. This is manifest more in the site 1 structures, which is likely linked to the fact that the longest bond length in each case is to the protonated oxygen, rendering the axis that includes this O atom the long axis of the complex. The formation of a square-based pyramidal arrangement in which the protonated oxygen is in the axial position is favourable over a square based pyramidal arrangement in which it is equatorial. This means that when only one small molecule is coordinated, it is somewhat preferable that it occurs in the equatorial position.

The geometries of all of these clusters are also consistent with the pattern observed in the phosphorus superhyperfine signals of site E, namely the positioning of one P nucleus at some distance from the Cu centre, and of three equivalent P nuclei much closer to the Cu.

To further qualify these assertions, that the Cu^{II} ions are able to distort the lattice sites into a 5- or 6-coordinate arrangement in the presence of water and MA, while still occupying lattice sites of lower symmetry on dehydration, calculations of the EPR *g*-tensors were made using the ORCA [126] package, using the B3LYP [89] functional and a basis set for which each localised atomic orbital has an individual gauge origin, to deal with the localised paramagnetic current densities that give rise to the magnetic shielding. The IGLO-III [127] basis set was chosen for this, and calculations were done for each of the structures of table 4.5. For these calculations, clusters were cut out from the optimised structures and terminated with H atoms. These clusters consisted in each case of the Cu centre, the neighbouring O atoms (and water/MA molecules as appropriate), the proton, and an O-P-O_4-Al-O_4 chain along each of the four directions associated with the four O atoms (*i.e.* neglecting all but one Al atom along each chain, see figures 4.11 to 4.15) bound to one of each of those groups of O atoms, chosen as the one that lies closest to a straight line along the initial Cu-O vector, and finally the O atoms bound to these Al atoms. When the protons are included, this gives rise to an overall negatively charged

cluster, requiring the inclusion of a single extra P atom and its bound O atoms. This was chosen arbitrarily in each case as one that lies along the chain from the Cu through the protonated O atom (figures 4.11 to 4.15).

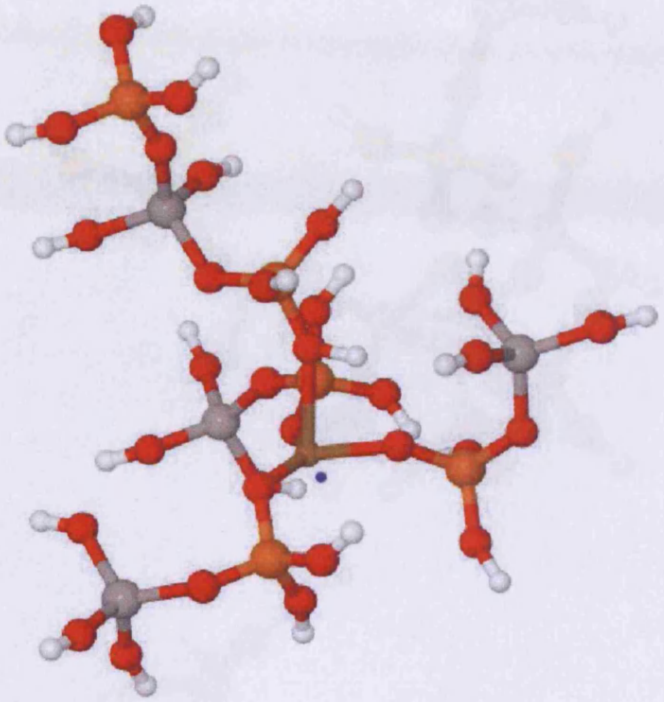

Figure 4.11: *The cluster used in the calculation of the EPR g-tensors with no molecule coordinated.*

The g- and A-tensor values obtained for these calculations are given in table 4.7.

These results do not precisely match the experimentally derived g-tensor values, due to difficulties in calculating accurate g-tensors. They do, however, give trends that can be compared to the experimental values. The key observation from these values is the trend in the values of the parallel component of the g-tensor, g_3. The trends observed for any system as rhombicity is increased are a diverging of the two perpendicular components, g_1 and g_2, and and accompanying marked increase in g_3. This is clearly observed in the value of g_3 derived from the spectra for site E compare to sites A, B, C and D, with a value of 2.61 compared to values ranging from 2.24 to 2.40 for the other sites. This trend is mirrored in the calculated values, with the unabsorbed cluster giving a value of 2.31,

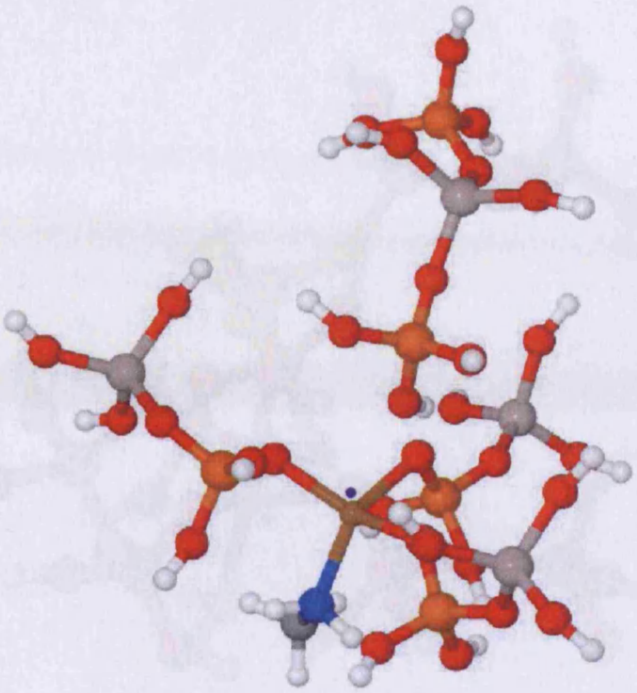

(a)

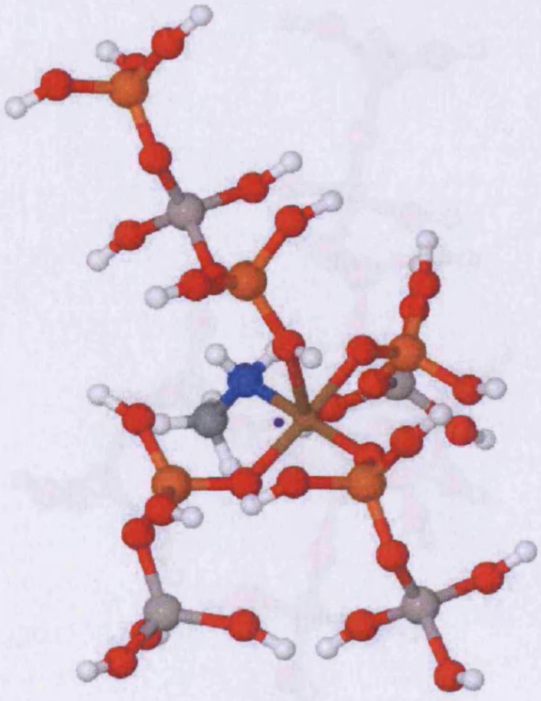

(b)

Figure 4.12: *The clusters used in the calculation of the EPR g-tensors with a single MA molecule coordinated.*

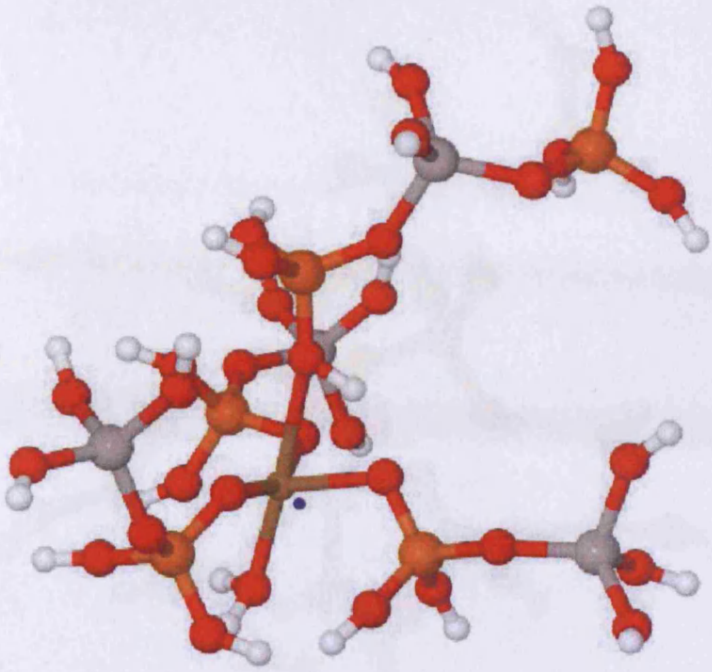

(a)

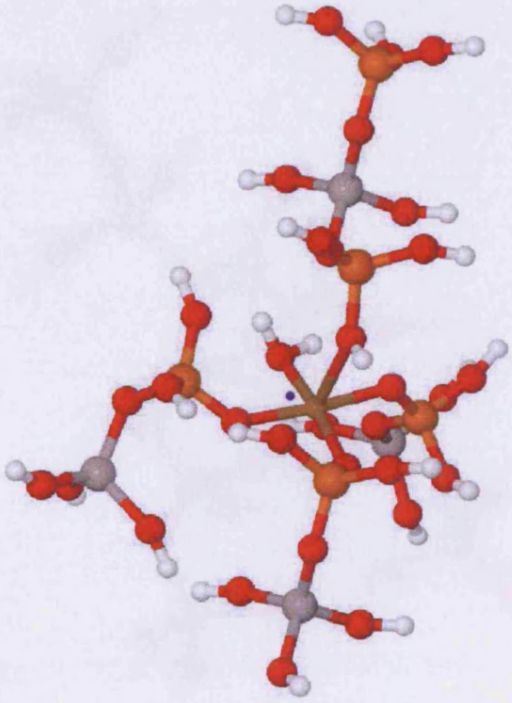

(b)

Figure 4.13: *The clusters used in the calculation of the EPR g-tensors with a single water molecule coordinated.*

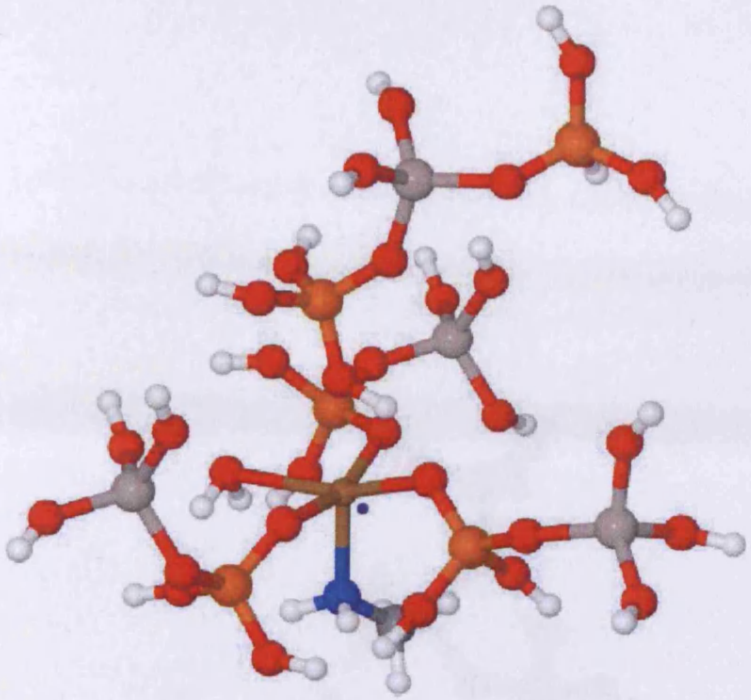

(a)

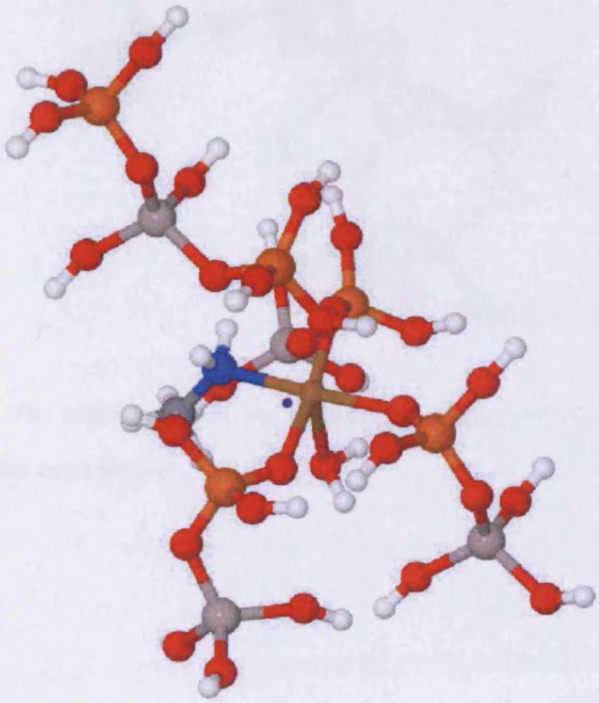

(b)

Figure 4.14: *The clusters used in the calculation of the EPR g-tensors with an MA molecule and a water molecule coordinated.*

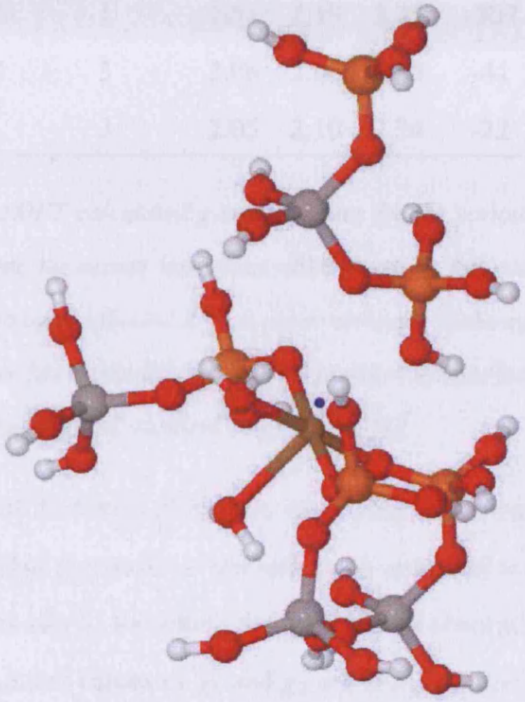

Figure 4.15: *The cluster used in the calculation of the EPR g-tensors with two water molecules coordinated.*

Coordinated Molecule(s)	Substitution Site	g_1	g_2	g_3	A_1 /MHz	A_2 /MHz	A_3 /MHz
None	2	2.06	2.13	2.31	54	299	-487
A-MA	1	2.04	2.11	2.22	104	-148	-728
E-MA	3	2.05	2.06	2.19	-60	-96	-841
A-W	1	2.02	2.18	2.25	-111	422	-455
E-W	3	2.05	2.08	2.23	0	124	-711
A-MA; E-W	1	2.01	2.19	2.22	-307	377	-495
E-MA; A-W	3	2.06	2.06	2.20	-41	-66	-834
A-W; E-W	3	2.05	2.10	2.24	-22	197	-716

Table 4.7: *The DFT calculated g-tensor values for the various structures considered. For brevity, the names have been abbreviated as follows: a water molecule in the axial position is labelled A-W, a water molecule in the equatorial position is labelled E-W, an MA molecule in the axial position is labelled A-MA, and an MA molecule in the equatorial position is labelled E-MA.*

compared to values of 2.19 to 2.25 for the other sites. This reasoning can be extended to explain the calculated g-tensors of the sites with absorbed molecules. In general, the values associated with site 3, for which the preferential absorption occurs in the equatorial position the calculated values of g_1 and g_2 are more similar, and that of g_3 is smaller compared to the values associated with site 1 (for which axial binding is preferred). This implies a higher degree of rhombicity at site 1, associating these clusters with the signals that arise experimentally for sites B and D, with the axial tensors described for site 3 associated with experimental sites A and C. This suggests that the coordination of a molecule (particularly MBA) in the equatorial site renders the g-tensor axial, while axial coordination reduces the rhombicity somewhat, though to a lesser extent. Full octahedral coordination is not necessary for the calculated g-tensor to be fully axial.

The A-tensor values for each of the nearby P nuclei of the plain (unadsorbed) site were also calculated, revealing one small isotropic (through bond) contribution of -0.79MHz

and three much larger, though reasonably diverse, contributions of 9.09MHz, 10.41MHz and 24.07MHz. Within the limitations of the calculation, this trend is consistent with the pattern observed from the spectra.

These data provide a means of explaining the various species observed in the EPR spectra of figure 4.4, as arising from the coordination of water and of MA to Cu^{II} ions absorbed into the various symmetrically distinct framework sites.

4.4 Conclusions

EPR spectra of CuIST-2 give signals that alter slightly on calcination and on dehydration of the sample. Each spectrum is a composite of two or more copper environments, with symmetries that are typical of 5- or 6-coordinate Cu^{II} ions, with a signal arising on dehydration from an environment with lower symmetry. The EPR parameters of these 5- and 6-coordinate sites are not typical of those that arise from hydrated Cu^{II} ions absorbed into extra-framework sites, for which values of $g_{\|}$=2.394 and $g_{\perp}$=2.074 are expected. The parameters of the lower symmetry site are similar to those observed for a 4-coordinate distorted tetrahedral Cu^{II} site in a Cu substituted zeolite [128], for which a $g_{\|}$ value of 2.474 was observed. These data can be explained by the incorporation of Cu^{II} into framework sites, with a distortion of the lattice to provide a coordination that is closer to square planar. The presence of water and MA templating molecules provide a means of filling either or both of the vacant coordination sites, to give 5- or 6-coordinate sites in distorted square-based pyramidal or distorted octahedral arrangements.

Using periodic DFT calculations, the feasibility of these arrangements has been tested. Stable geometries have been obtained *via* these calculations for each of the possible coordination arrangements (4-, 5- and 6-coordinate, with combinations of MA and water molecules filling the vacancies). These have further demonstrated the ability of the Cu^{II} ions to distort the lattice as described to the required distorted tetrahedral/square-based pyramidal/octahedral geometries. *g*-Tensor calculations on clusters cut out from the peri-

odic structures have shown the trends displayed in the EPR spectra, supporting the assertion that these spectra derive from the Cu^{II} ions absorbed into the lattice. The presence of three symmetrically distinct sites into which the Cu^{II} ions can absorb, each having different steric environments explains the presence of different contributions to each of the EPR spectra, since site one preferentially binds in the axial position, site three in the equatorial position, and site two in the equatorial position. The binding of two molecules to give a 6-C environment occurs for two water molecules in site one, and for one MA and one water in site three, with the coordination of two MA molecules requiring too much lattice distortion to accommodate them. It is possible to assign the signals in the EPR spectra as deriving from the absorption of MA and water in site three and of two water molecules in site one giving rise to A, the absorption of two water molecules in site one giving rise to C, the absorption of either one MA or one water in an axial position in site one and in an equatorial position in site three giving rise to B, and the absorption of a water molecule axially in site one, equatorially in site three giving rise to D. E can be assigned to the Cu^{II} ions in site two with no water and no MA absorbed.

Chapter 5

Program to Adjust DFT-Derived Geometries to ENDOR Spectra

5.1 Introduction

ENDOR spectroscopy, as described in chapter 2, is capable of providing information regarding the vectors between each spin-active nucleus (most commonly protons) to the unpaired electron of an open-shell system. The dipolar model which describes this link is dependent on the confinement of the unpaired electron to a spatially restricted orbital and further requires a reasonably accurate pre-conceived geometry, in order to associate the coordinates derived from the various spectra (*e.g.* for an axial system, the parallel and perpendicular spectra) with the same nucleus. DFT provides a computationally reasonable means of obtaining accurate geometries for the transition metal systems for which ENDOR is a useful technique, as well as providing isotropic contributions to the hyperfine interaction.

Conventionally, ENDOR parameters are derived from the spectra by simulation. A code developed in-house exists to simulate ^{1}H ENDOR spectra from an input set of H atom hyperfine parameters and EPR parameters (g-tensor and metal hyperfine parameters), which can then be refined manually to improve the accuracy of the fit at the level of magnetic interaction parameters. The optimal parameters are then interpreted in terms of the geometry of the complex. This manual fitting process can be automated provided a search algorithm is used which is able to search complex parameter spaces without becoming stagnated in local minima.

In this study, a genetic algorithm is used as such a simple yet powerful search tool. The complementary nature of the DFT and ENDOR techniques is here exploited, in using the DFT derived coordinates as the starting parameter set, deriving from the DFT calculation the initial guesses for the hyperfine parameters, and adjusting them to fit to the spectrum, thus optimising the geometry of the protons to fit to the spectra.

The code has been developed with a simple test system, VO(acetylacetonate)$_2$ (VO(acac)$_2$) in deuterated dichloromethane (*i.e.* there are no peaks arising from the solvent). VO(acac)$_2$ is a simple axial system, having indistinguishable x- and y-directions

due to the symmetry of the orbital containing the unpaired electron (figure 5.1).

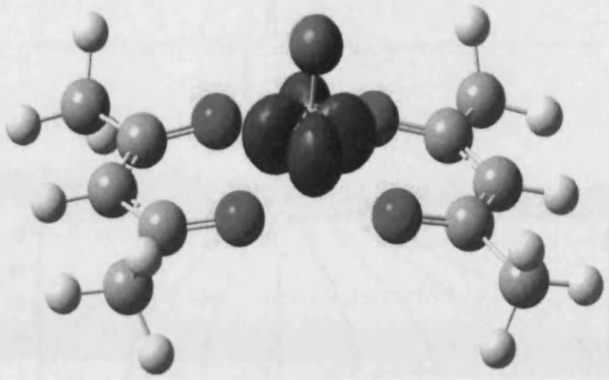

Figure 5.1: *The VO(acac)$_2$ molecule, with the spin-density ($\rho(\alpha) - \rho(\beta)$) shown, as calculated at the B3LYP/6-31g(d,p) level. The electron essentially occupies a $d_{x^2-y^2}$ orbital with some density on the O atom. The complex has a C_2 symmetry axis and a quasi planar ligand, explaining the axial symmetry of the EPR signal.*

The (axial) EPR spectrum of VO(acac)$_2$ is given in figure 5.2.

5.2 Obtaining the Parameter Set

The ENDOR simulation routine requires a complete set of EPR parameters, the *g*-tensor and the metal center *A*-tensor, along with the static *B*-field used, as well as the hyperfine parameters for each spin active nucleus. In addition the Euler angles which rotate each hyperfine frame of reference into that of the *g*-tensor are needed (see chapter 2).

Also required are spectral data such as the linewidths and lineshapes and instrument parameters such as central field and the sweep width. The instrument parameters are obtained from a parameters file associated with the spectrum. The EPR parameters are obtained from the EPR spectrum (*via* simulation), leaving the hyperfine tensors and associated Euler angles, and linewidth and lineshape parameters to be fit to the experimental spectrum. The anisotropic contributions to the *A*-tensor are derived from the DFT derived

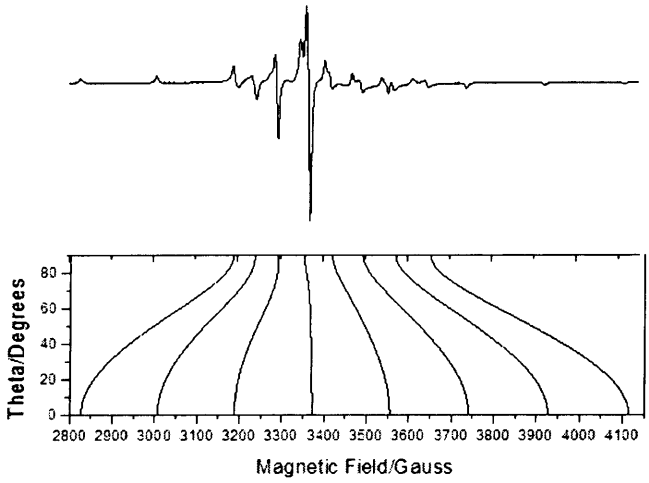

Figure 5.2: *The X-band EPR spectrum of $VO(acac)_2$*

coordinates through the point dipole procedure outlined in section 2.1.2. The localisation of the orbital containing the unpaired electron as shown in figure 5.1, and the proton distances of 4.4Å and 5.1Å for the non-methyl and methyl protons respectively from the vanadium centre, mean that this is a valid approximation for this system.

The isotropic contributions are also obtained from the DFT calculation, as described in section 2.6. Linewidths can be estimated either from a peak-picking routine or can be input by the user. These coordinates, isotropic couplings and spectral parameters are adjusted in the fitting routine to obtain an 'ENDOR structure'.

5.3 Fitting Routine

The fitness criterion by which a given geometry is judged is the sum of the point-by-point squares of the differences between the simulated and experimental spectra:

$$R = 100 \times [\frac{\Sigma_i (y_i^{exp} - y_i^{sim})^2}{\Sigma_i (y_i^{exp})^2}]^{\frac{1}{2}} \tag{5.1}$$

Where y_i^{exp} is the i^{th} experimental spectral absorption point, and y_i^{sim} is the i^{th} simulated spectral absorption point. The process of generating the simulated spectra is discussed in section 5.7.

5.3.1 Pre-conditioning

Equation 5.1 makes it clear that experimental spectral noise will increase the value of R having a negative impact on the calculated fitness of the simulation, so it is desirable to have a spectrum that is as free of noise as possible. For this reason the experimental spectrum is preconditioned to reduce noise. This is achieved by applying a Savitsky-Golay filter [129], which works by moving a window n-data points wide along the x-axis, and using a least squares procedure to fit a polynomial of order m to the data points in between. The value of the polynomial at the central point of the window is assigned to that central point in the smoothed spectrum, and the filter shifts the window along the axis by one data point. The polynomials are fit *via* a set of normalisation factors and coefficients defined in [129], according to equation 5.2.

$$y_i^{smooth} = \frac{1}{(\delta x)^m F} \sum_{i=1}^{n} y_i^{raw} c_i \tag{5.2}$$

Where F is the normalisation for the given window size and order of polynomial, y_i^{raw} is the i^{th} point in the raw experimental spectrum, y_i^{smooth} is the i^{th} point in the smoothed spectrum, δx is the increment along the x (field) axis, and c_i are the associated coefficients.

The effects of this smoothing process are illustrated for a particularly noisy spectrum (of [VO(**1**)]+toluene), in figure 5.3.

Figure 5.3 also displays a non-flat baseline, another spectral artefact (besides noise) that artificially raises the value of the fitness criterion, so hindering the fitting process. A distorted baseline is caused by difficulties in tuning the alignment and opening of the

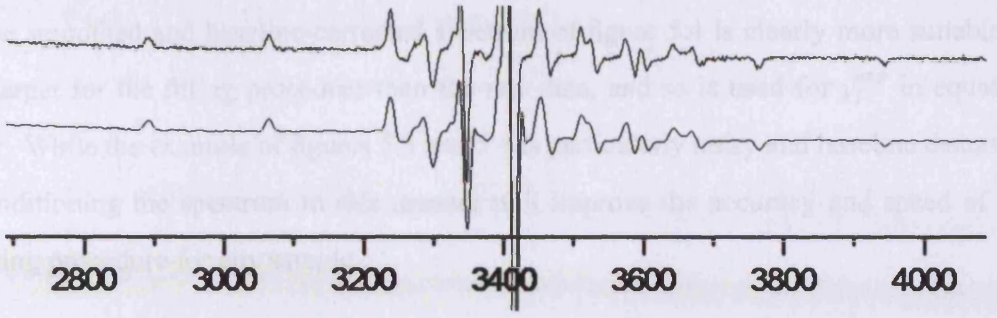

Figure 5.3: *The spectrum of [VO(1)]+toluene (above) with the Savitzky-Golay smoothed spectrum shown below. The smoothing parameters used were for the window width, $n = 25$, and the order of the polynomial $m = 5$.*

resonance cavity of the spectrometer to obtain a symmetric dip at the resonant frequency. This distortion is corrected by fitting a polynomial to the baseline (neglecting the data points of each peak by defining a cut-off magnitude, points whose values are above which are not included in the fit) according to the procedure defined in chapter 2. The polynomial function is then subtracted from each point of the experimental spectrum. The results of this procedure, as applied to the smoothed spectrum of figure 5.3 are given in figure 5.4.

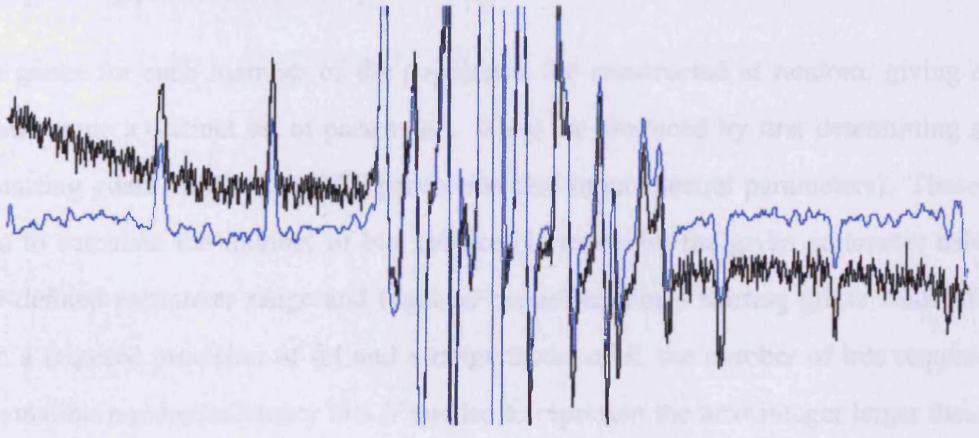

Figure 5.4: *The spectrum of [VO(1)]+toluene (above) with the baseline-corrected spectrum. A polynomial of order $k = 8$ was fit to the raw spectrum, and the smoothing filter has also been applied. The central field has been displayed off scale to allow the effect of the smoothing to be judged.*

The smoothed and baseline-corrected spectrum of figure 5.4 is clearly more suitable as a target for the fitting procedure than the raw data, and so is used for y_i^{exp} in equation 5.1. While the example of figures 5.3 and 5.4 is particularly noisy and baseline distorted, conditioning the spectrum in this manner will improve the accuracy and speed of the fitting procedure for any sample.

5.3.2 Genetic Algorithm

The search routine employed in fitting DFT geometries to the ENDOR spectra is a genetic algorithm [130]. The genetic algorithm uses principles of Darwinian evolution to explore a parameter space, optimising a collection or population of parameter sets using heredity, mating, mutation and selection principles to find multiple function minima (of which, hopefully, one is the global minimum). The parameter sets are represented by chromosomes, individual members of the population, each containing a complete set of parameters which represent genes. These genes are numerical representations of the associated values (in this case, geometric coordinates and spectral parameters), which in this example are represented by binary bit-strings.

The genes for each member of the population are constructed at random, giving each chromosome a distinct set of parameters. They are produced by first determining a set of starting guess values (the DFT geometries and input spectral parameters). These are used to calculate the number of bits required to represent the given parameter using a user-defined parameter range and required precision. For a starting guess value of A_0, with a required precision of δA and a range factor of R, the number of bits required is the smallest number of binary bits N needed to represent the next integer larger than the number X given by equation 5.3.

$$X = \frac{RA_0}{\delta A} \tag{5.3}$$

The genes representing each parameter are concatenated in a prescribed order, and filled

at random with 1s and 0s, illustrated by figure 5.5.

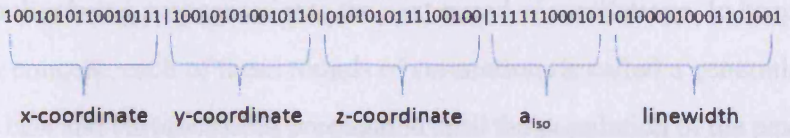

Figure 5.5: *A section from a sample chromosome, representing the shifts from the starting values of the x,y,z coordinates, isotropic hyperfine coupling parameter and line width associated with a single proton. Similar segments associated with each of the other protons are combined with this one, with lineshape data for the whole spectrum included at the end.*

These chromosomes can now be decoded into a complete set of parameters by breaking them back down into sections representing single genes, and applying equation 5.4.

$$A_i = (\sum_{j=1}^{N} \chi_j 2^{N-1-j}) \frac{RA_0}{2^{N-1}} + A_0 - \frac{RA_0}{2} \tag{5.4}$$

where χ_j is the j^{th} binary bit (0 or 1) in the given gene. The incorporation of the A_0 term in equation 5.4 makes it clear that this represents a random shift of the original coordinate, rather than a completely random coordinate. An immediate problem with this scheme is that unequal weighting is given to the coordinates, with a larger number of bits, *i.e.* a larger number of possible values, assigned to the more distant protons (in a coordinate system centred on or near the metal ion, which here is the most commonly used convention), which in fact have the smallest effect on the spectrum. This can be combated using a simple reciprocal factor, though in the $VO(acac)_2$ example this is not done due to the coordinate transformations described in section 5.5 below.

From these decoded parameters a spectrum can be simulated, which is compared to the experimental spectrum and assigned a fitness according to equation 5.1. This process is completed for each chromosome in the population, and a "roulette wheel" is built by assigning each chromosome space on the wheel according to the reciprocal of its fitness (*i.e* those with smaller fitness values, *i.e* better fitness, are assigned a larger space on the

wheel). Random numbers are cast onto the wheel, with the chromosome corresponding to the given number being propagated into the next round of simulations. In keeping with the evolutionary concept, each of these rounds of simulations is called a generation. Random numbers are cast and chromosomes propagated until the population of the next generation equals that of the current generation. By this process, chromosomes with better fitness are statistically represented several times in the next generation, while those having worse fitnesses are eliminated (although they do have a finite probability of persisting).

With the chromosomes reassembled, a weighted random number generator is used to determine how many pairs will be mated (this can be set so that all will be mated if required), then pairs are randomly selected for mating. Mating proceeds by picking a random position along the chromosome (which can occur within a gene) and exchanging all bits occurring after that point in the two chromosomes (figure 5.6)

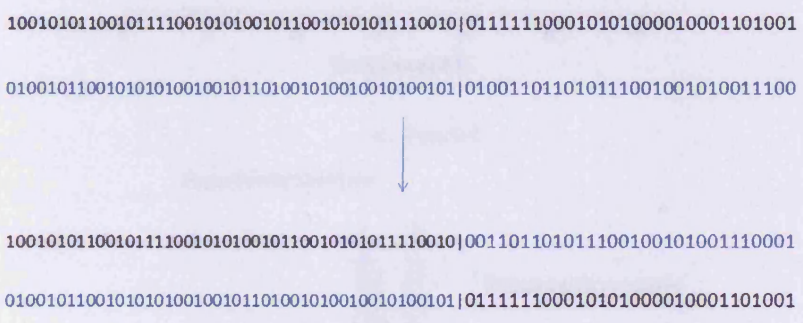

Figure 5.6: *The mating procedure. All bits after the | (included for clarity) are exchanged. The position of this point of exchange is determined by a random number.*

Finally, each bit has a finite probability of mutating (exchanging a 1 for a 0 or *vice versa*). The new population is then decoded and each chromosome analysed by simulating the associated spectrum and evaluating its fitness. This procedure is repeated either for a given number of generations or until the fitness parameter drops below a defined threshold. The parameters optimised this way are output and a geometric representation of the ENDOR coordinates are derived.

5.4 Initial Application

This procedure was applied to the coordinates of the protons of $VO(acac)_2$. The parameters derived from the DFT calculations were used to simulate initial spectra without optimisation using the genetic algorithm, shown along with the experimental spectra in figure 5.7.

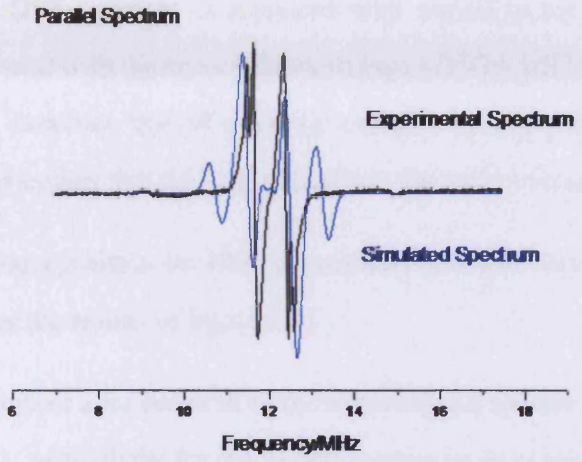

(a) Parallel

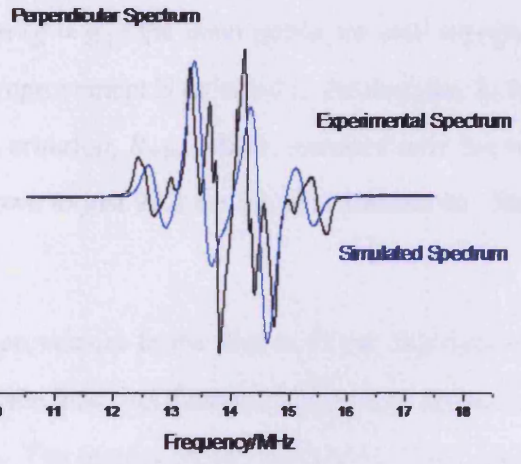

(b) Perpendicular

Figure 5.7: *The initial simulated ENDOR spectra of $VO(acac)_2$, using parameters derived from the DFT calculation, shown against the experimental spectra.*

Clearly these simulations fail to match the experimental spectra. The parallel spectrum

shows simulated peaks outside of the experimental peaks, implying that the z-coordinate of one of the types of proton is too close to the V atom z-coordinate in the simulated geometry. The structure of the perpendicular spectrum does not display enough peaks, suggesting that the linewidths are too large, and the protons too close together, losing the structure of the proton peaks within the broad lines. Neither simulation displays peaks too close to the spectral centre (representing protons that are too far from the electron) implying that the DFT geometry is expanded with respect to the ENDOR geometry, an observation consistent with the known shortcomings of GGA DFT calculations on metals. It is encouraging, however, that all peaks lie close to the experimental spectral regions, which supports the notion that the lack of peaks is due to overbroad lines.

Running the genetic algorithm for 1000 generations on a modest population of 100 chromosomes produces the results of figure 5.8.

These spectra represent a far better fit to the experimental spectra than the initial simulations of figure 5.7, particularly for the parallel spectrum ($g = g_{||}$)for which the outlying peaks have been merged into their appropriate positions on the spectrum, while for the perpendicular spectrum ($g = g_{\perp}$) the inner peaks are well represented, though the outer ones are absent. This improvement is reflected in the decrease in the value of the the lowest value of the fitness criterion, R_{min}, which, summed over the two spectra is 208.4 for the initial spectrum, down to just 92.3 for the final simulation. This decrease is recorded in figure 5.9.

Unfortunately, this improvement in the fitness of the chromosomes obtained using the genetic algorithm gives the final coordinates of the protons shown in figure 5.10, which are not physically feasible. The methyl groups particularly have been distorted immensely, collapsed either towards single positions or into the molecular x-y plane. Clearly it is necessary that the methyl-group rigidity be somehow maintained. Further, as described above, the $VO(acac)_2$ complex has axial symmetry, giving rise to two distinct ENDOR spectra. From these can be derived only two sets of coordinates. For these reasons, a change of coordinates to reduce the number of free variables is required.

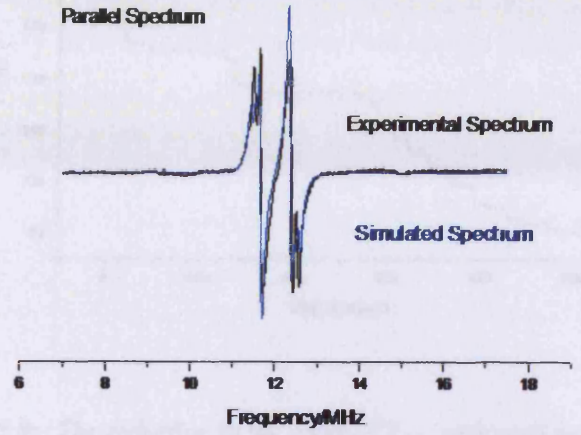

(a) Parallel

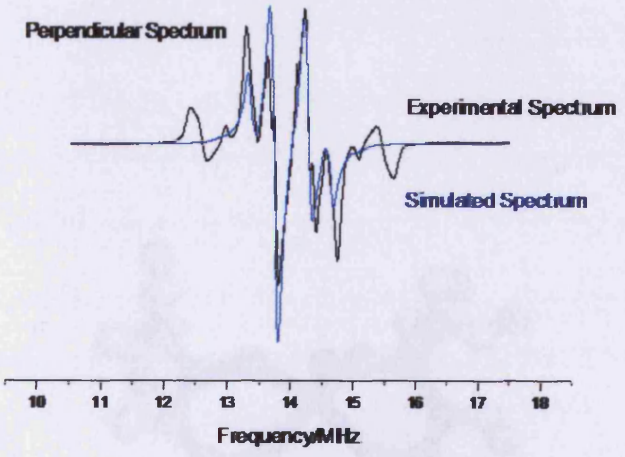

(b) Perpendicular

Figure 5.8: *The final simulated ENDOR spectra of $VO(acac)_2$, after 1000 generations with a population of 100 chromosomes.*

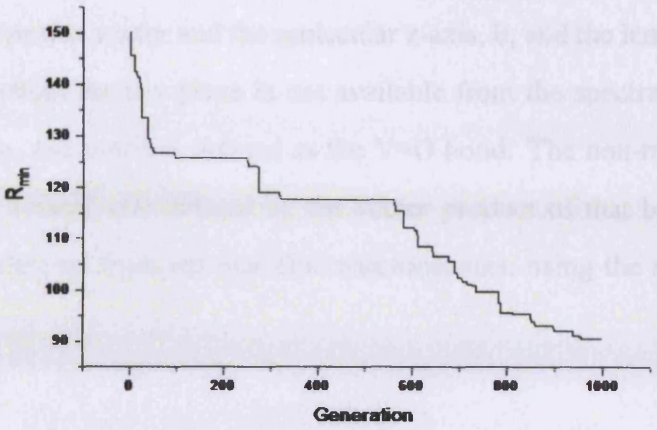

Figure 5.9: *The reduction in the value of R_{min} with each generation.*

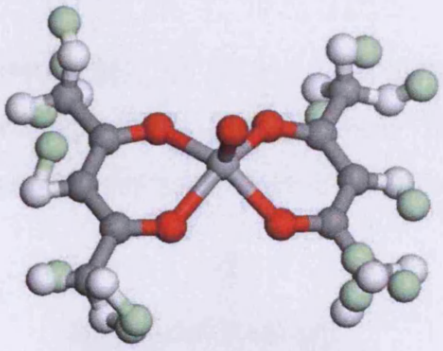

Figure 5.10: *The positions of the protons in the final structure with the lowest value of R (in green) compared to their starting positions (in white). Clearly the final positions are unviable.*

5.5 Change of Coordinates

The coordinates that can be derived from the two spectra are the angle formed by the unpaired electron-proton vector and the molecular z-axis, θ, and the length of that vector, *r*. The position within the x-y plane is not available from the spectra. In the example system, $VO(acac)_2$, the z-axis is defined as the V=O bond. The non-methyl protons are rotated about the normal axis defined by the vector product of that bond and the V–H vector by angles derived from the modified chromosomes, using the rotation matrix of equation 5.5.

$$\begin{pmatrix} x' \\ y' \\ z' \end{pmatrix} = \begin{pmatrix} (1-c\theta)\hat{a}_x^2 + c\theta & (1-c\theta)\hat{a}_x\hat{a}_y - \hat{a}_z s\theta & (1-c\theta)\hat{a}_x\hat{a}_z + \hat{a}_y s\theta \\ (1-c\theta)\hat{a}_x\hat{a}_y + \hat{a}_z s\theta & (1-c\theta)\hat{a}_y^2 + c\theta & (1-c\theta)\hat{a}_y\hat{a}_z - \hat{a}_x s\theta \\ (1-c\theta)\hat{a}_x\hat{a}_z - \hat{a}_y s\theta & (1-c\theta)\hat{a}_y\hat{a}_z + \hat{a}_x s\theta & (1-c\theta)\hat{a}_z^2 + c\theta \end{pmatrix} \begin{pmatrix} x \\ y \\ z \end{pmatrix} \tag{5.5}$$

where $\underline{\hat{a}}$ is the unit normal formed as the cross product of the V–H vector and the molecular z-axis. The trigonometric functions have been abbreviated so that $\cos\theta$ is expressed as $c\theta$, *etc.* and $\sin\theta$ is expressed as $s\theta$, *etc.*

The DFT derived coordinates supply the starting guess values for the angles, and also supply the angle within the x-y plane, ϕ which is not varied. The length of the V–H vector is also lengthened and shortened from its DFT value (figure 5.11).

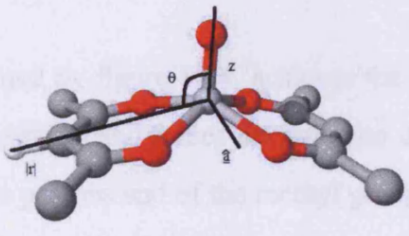

Figure 5.11: *The V–H vector and the z-axis, with the angle θ between them. Also shown is the unit vector product $\underline{\hat{a}}$ of the V–H vector and the z-axis, about which the V–H vector is rotated.*

For methyl groups, a projection is first made of the C-C bond as shown in figure 5.12. This bond connects the methyl group to the molecule, and is extended beyond the C atom to a point P, unit distance from the C atom. A similar rotation and vector expansion then takes place as described above for the individual H atoms, to determine the position of the carbon atom of the methyl group. Point P is then also rotated about the unit normal $\hat{\underline{a}}$ by which the C atom was rotated by the same angle θ. The C-H vectors are also rotated and added onto the new C atom position. Finally, the C-H vectors are rotated by angle χ about the C-P unit vector (figure 5.13).

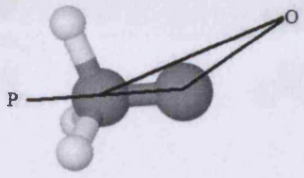

Figure 5.12: *The position of point P, projected along the R-C bond. O is the origin of coordinates.*

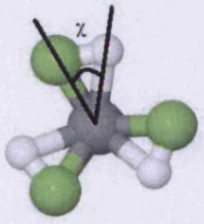

Figure 5.13: *The angle χ by which the methyl group protons are rotated about the C-P unit vector.*

This whole process, illustrated by figure 5.14, achieves the reduction in the number of variables for the genetic algorithm and forces the retention of the methyl group rigidity. First, a rotation of the single protons and of the methyl groups by the angle θ associated with the given proton/methyl group is made about the unit normal associated with each. The vectors are expanded at this point as well. The methyl groups are then rotated about the C-C bond axis, to generate the next structure to be evaluated.

These new x,y,z coordinates are used, as before, to generate the anisotropic A-tensor, and

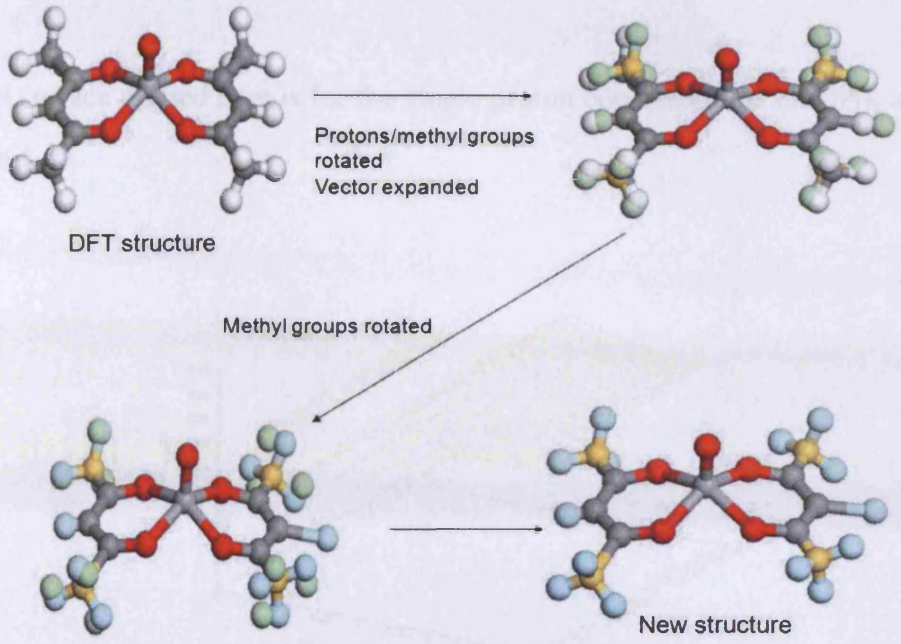

Figure 5.14: *The complete process by which the two-dimensional data (angles and vector lengths) are modified according to the two-dimensional chromosomes.*

so to simulate spectra.

5.6 Two Dimensional Fitting Tests

From figure 5.9 it is clear that the search algorithm is capable of improving the fitness, albeit by incorporating unphysical proton movements. To examine its performance with the more physical coordinate system ($|r|$, θ and χ) surfaces of two dimensions are employed. This restriction of the dimensionality of the parameter space allows simple visualisation of the search progress, as well as providing a simplified test case to which the algorithm is more likely to able to find a reasonable solution in a reasonable timeframe than for the full parameter set. Surfaces are plotted for which the two parameters run along the x and y axes with the fitness value, R, along the z-axis. Note that in each case the remaining H atoms were not included in the spectral simulation.

5.6.1 The Isolated Protons

The first surface plotted here is for the single proton coordinates (θ and $|r|$), and is given in figure 5.15.

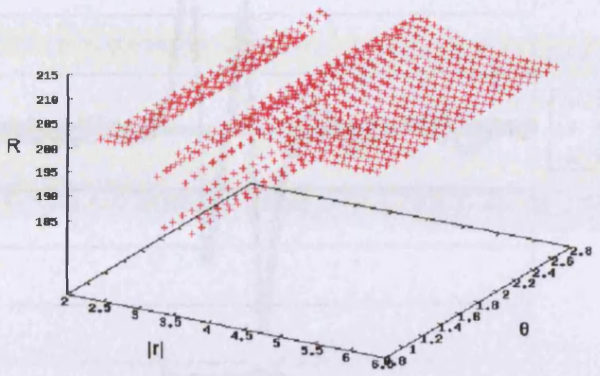

Figure 5.15: *Surface obtained by scanning the proton distance and angle.*

Figure 5.15 makes it clear that the fitness is reasonably insensitive to the angle of the proton, to the extent that variation along this coordinate cannot be discerned, hidden as it is by variation along the distance axis. It does, however, give two distinct valleys along the distance axis, having similar minimum values (187.34 for the valley at 3.35Å, 187.21 for the valley at 3.75Å), giving two viable positions for the proton, well within the error of the spectra assignment. This provides a means of testing the ability of the genetic algorithm to find a global minimum.

Spectra were plotted for the first (smallest r and smallest θ) and last (biggest r and biggest θ) points of this surface, and are given, along with the experimental spectra, in figure 5.16.

The first and last points for the perpendicular spectrum clearly flank the outermost peaks of the experimental spectrum, giving a clear indication that the experimental spectrum effectively lies between them. In the parallel case, both points appear to be outside of the experiment. This suggests the possibility that the proton in question gives rise to a very

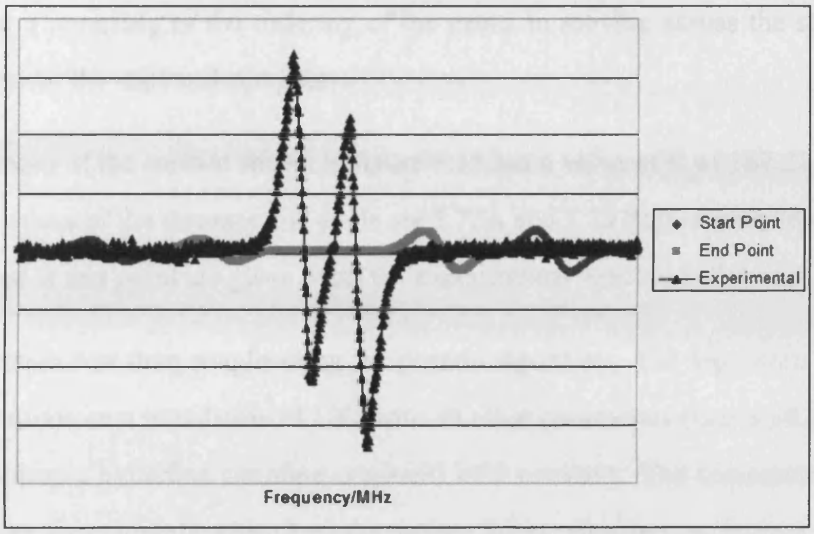

(a) Parallel

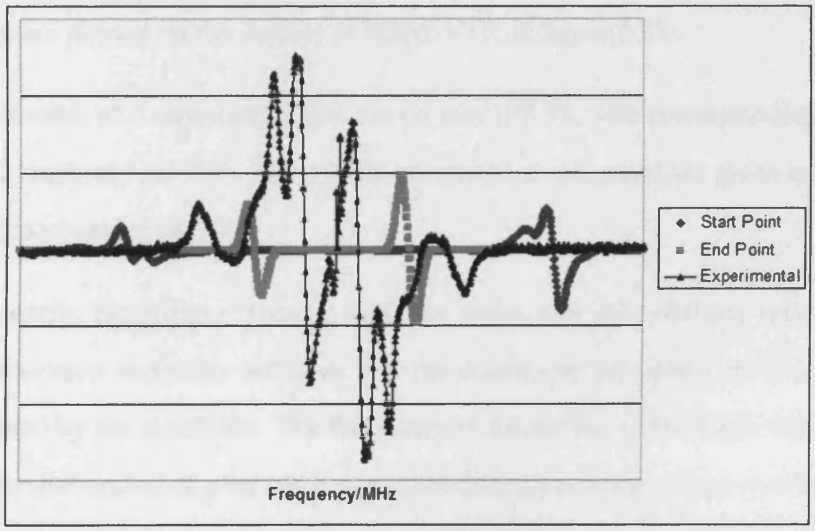

(b) Perpendicular

Figure 5.16: *The first and last points of (a) the parallel and (b) the perpendicular ENDOR spectra for the single proton surface.*

small resonance, barely discernable above the noise. However, on plotting the spectra corresponding to the minimum of the surface (figure 5.17), it becomes apparent that a minimum corresponding to the central spectral features does sit between these points, suggesting a reversing of the ordering of the peaks in moving across the spectral mid-point, between the start and end points.

The minimum of the surface shown in figure 5.15 has a value of R of 187.21. The corresponding values of the distance and angle are 3.75Å and 2.73 Rad respectively. The spectra obtained at this point are given, with the experimental spectra, in figure 5.17.

This minimum was then sought using the genetic algorithm. The algorithm was run for 100 generations on a population of 100, with all other parameters (line-width, line-shape and the isotropic hyperfine coupling constant) held constant. The constraints placed on the variables were slightly wider than the surface limits, allowing the algorithm to search beyond the surface to some extent. The points at which the algorithm reported an improvement are plotted on the surface of figure 5.15, in figure 5.18:

The lowest value of R reported for this search was 187.38, with corresponding distance of 3.78Å and angle of 1.62 Rad. The spectra simulated at this point are given in figure 5.19, with the experimental spectra.

That the genetic algorithm moves, in very few steps, into the extended valley even with so few population members indicates that the search for the optimum V–H distance is accomplished by the algorithm. The flat nature of the surface in the angle direction, however, means that optimising the angle is a more difficult process, which possibly could be neglected, or at least used to determine a very low precision requirement for these angles, since its effect is comparatively small. The initial population finds one or more members in the lower of the two valleys. Since the algorithm only reports improvements in the overall fitness, it never reports any move into the other valley, since each point therein is higher. The reported values are very close to the minimum values of the surface.

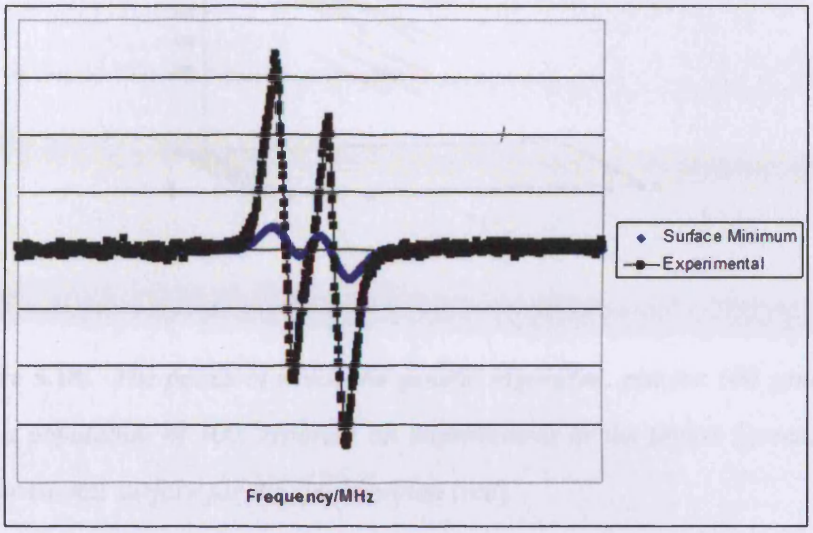

(a) Parallel

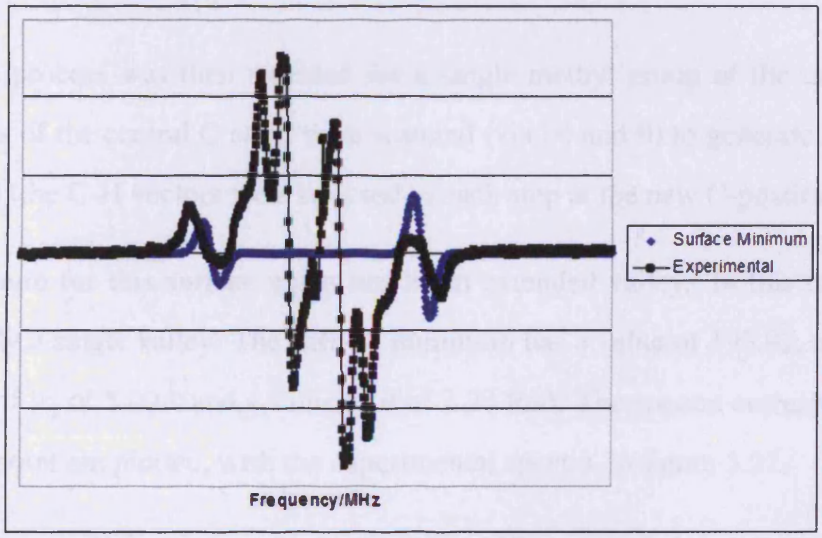

(b) Perpendicular

Figure 5.17: *The surface minimum for (a) the parallel and (b) the perpendicular spectra spectra for the single proton surface.*

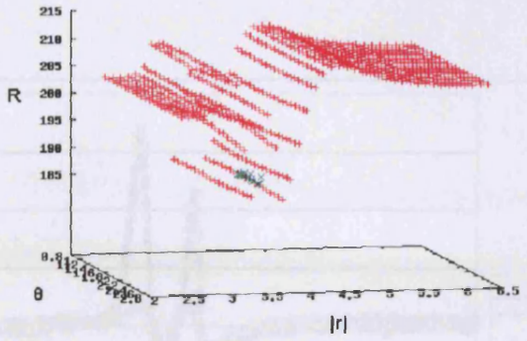

Figure 5.18: *The points at which the genetic algorithm, run for 100 generations with a population of 100, reported an improvement in the fitness (green) on the 2-dimensional surface for the single proton (red).*

5.6.2 The Methyl Groups

The above process was then repeated for a single methyl group of the molecule. The coordinates of the central C atom were scanned (via $|r|$ and θ) to generate the surface in figure 5.20 (the C-H vectors were restored in each step at the new C-postion).

The minimum for this surface again lies in an extended valley. In this case, however, there is only a single valley. The surface minimum has a value of 193.92, corresponding to a value of $|r|$ of 5.00Å and a value of θ of 2.28 Rad. The spectra corresponding to the minimum point are plotted, with the experimental spectra, in figure 5.21.

Of these, the parallel spectrum is the better fit. The methyl group, however, produces two peaks, which are not resolved in the experiment. This is likely due to the ability of the methyl group to rotate, giving rise to a range of proton positions, which cause a line broadening representing smeared out proton positions in the methyl groups. The perpendicular spectrum is not so well represented, with one outside peak on each side (not the one due to the single proton) neglected. The peaks of the inner region are also out of place, with large simulated peaks overlaying relatively minor experimental resonances.

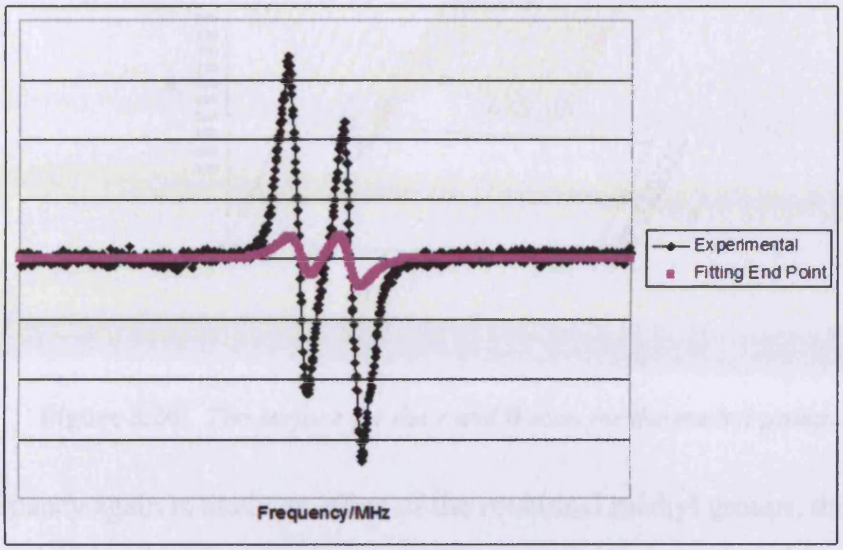

(a) Parallel

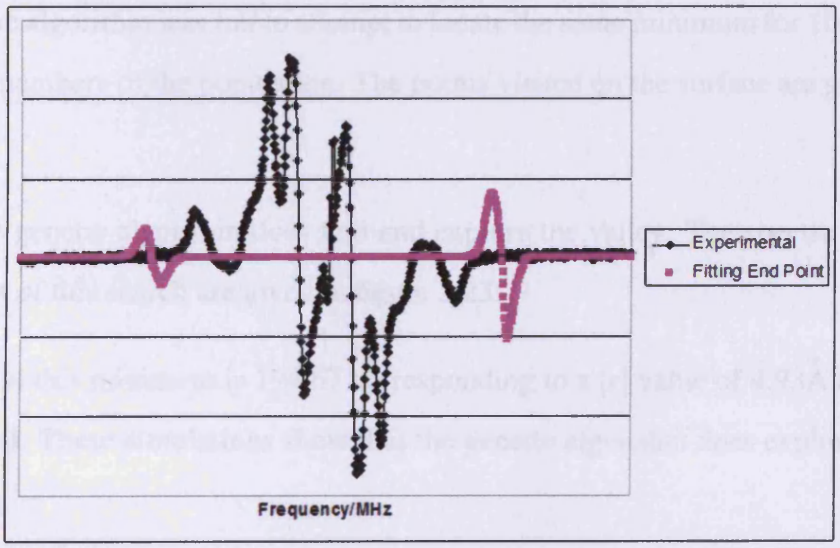

(b) Perpendicular

Figure 5.19: *The (a) parallel and (b) perpendicular ENDOR spectra corresponding to the lowest value of R found by the genetic algorithm for the single proton on carbon 2 of the acac ligand.*

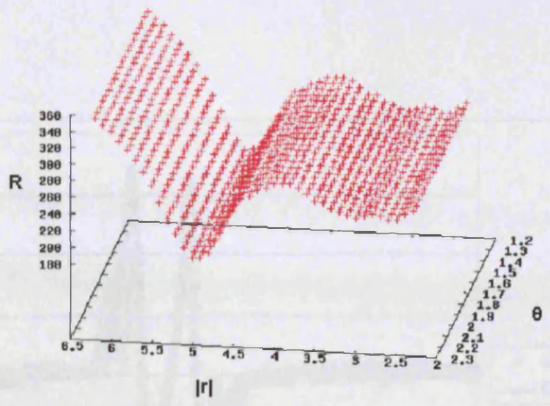

Figure 5.20: *The surface for the r and θ scan for the methyl group.*

This discrepancy again is likely an effect of the rotational methyl groups, this time due to resonances in regions not reached by the stationary protons.

The genetic algorithm was run to attempt to locate the same minimum for 100 generations with 100 members of the population. The points visited on the surface are given in figure 5.22.

Again, the genetic algorithm does find and explore the valley. The spectra for the minimum point of this search are given in figure 5.23:

The value at this minimum is 194.67 corresponding to a $|r|$ value of 4.93Å and a θ value of 2.07 Rad. These simulations show that the genetic algorithm does explore the surface adequately.

The methyl group is rotational, which of course is true of any single bond, but in the case of methyl groups it gives rise to a range of proton positions. The most stable rotation, however, will dominate the spectrum at the low temperatures (typically 10K) of the ENDOR experiment, and this most stable rotation can be determined as a parameter in the fitting routine. A scan was thus made of $|r|$ and χ, the rotational angle of the methyl group. The resulting surface is given in figure 5.24

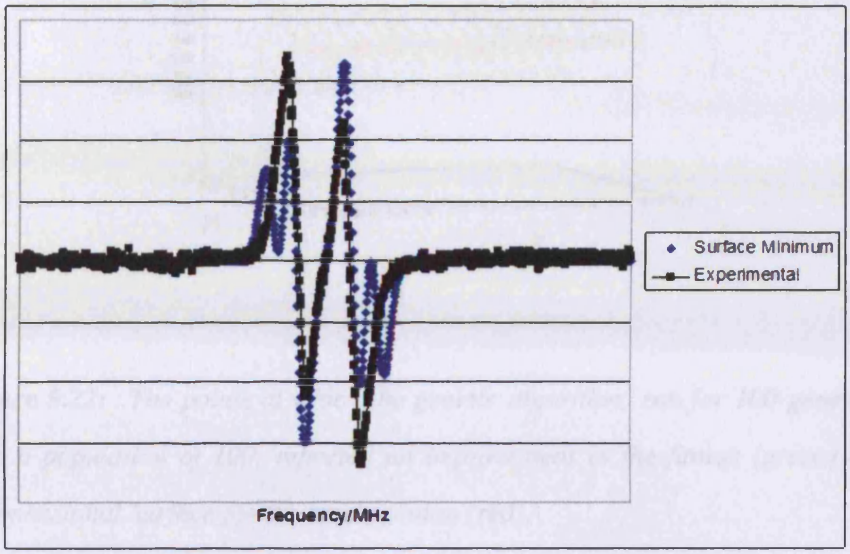

(a) Parallel

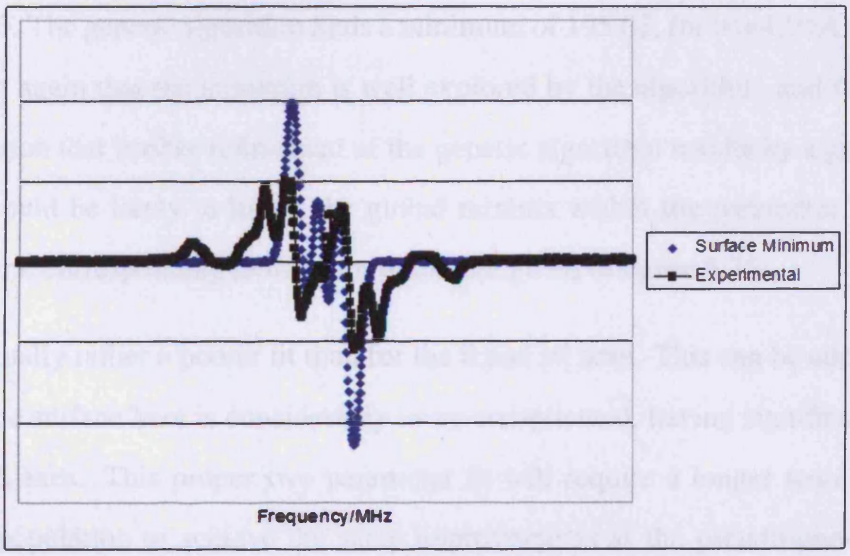

(b) Perpendicular

Figure 5.21: *The surface minimum for (a) the parallel and (b) the perpendicular ENDOR spectra for the single methyl surface for r and theta.*

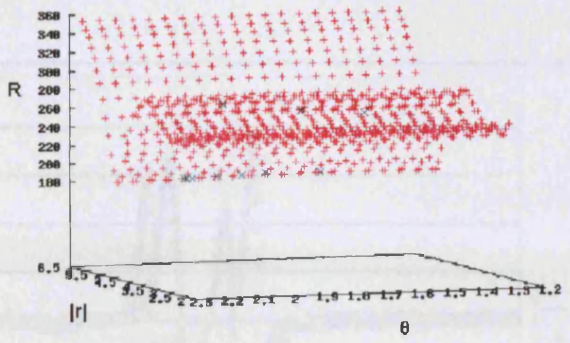

Figure 5.22: *The points at which the genetic algorithm, run for 100 generations with a population of 100, reported an improvement in the fitness (green) on the 2-dimensional surface for the single proton (red).*

This surface shows variation in both directions, implying that χ is a more important variable than θ. The genetic algorithm finds a minimum of 195.03, for $|r|$=4.93Å and χ=0.21^c, suggesting again that the minimum is well explored by the algorithm, and further crediting the notion that further refinement of the genetic algorithm results by a gradient based method would be likely to locate the global minima within the parameter ranges. The final spectra, corresponding to this minimum, are given in figure 5.25.

This is actually rather a poorer fit than for the θ and $|r|$ scan. This can be attributed to the fact that the surface here is considerably more complicated, having significant variations along both axes. This proper two parameter fit will require a longer search time, with a greater population to achieve the same improvements as the pseudo-one-dimensional search of the θ and $|r|$ scan. It does, however, explore the correct region of the surface, demonstrating qualitatively the abilities of the genetic algorithm to locate minima.

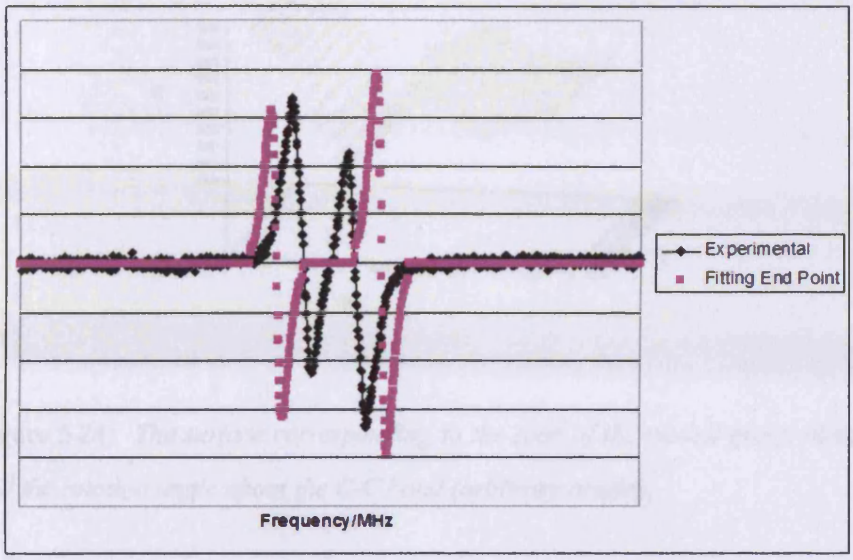

(a) Parallel

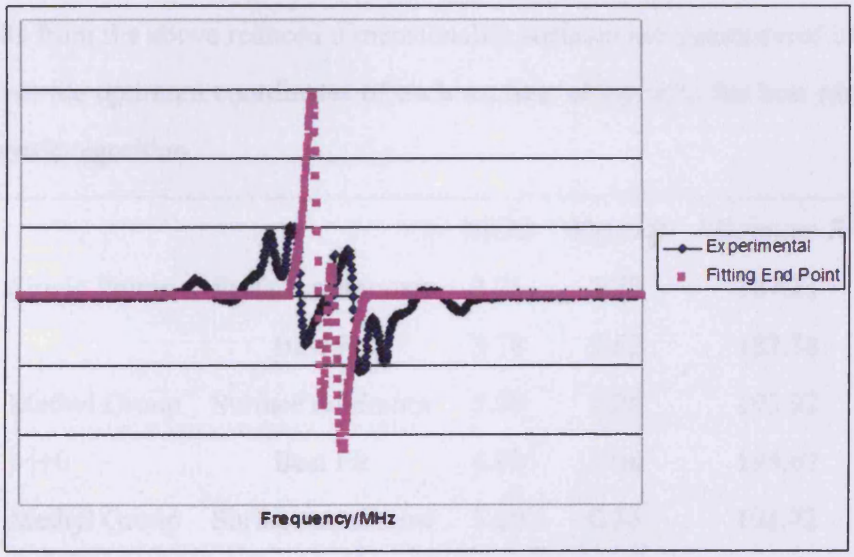

(b) Perpendicular

Figure 5.23: *The (a) parallel and (b) perpendicular ENDOR spectra corresponding to the lowest value of R found by the genetic algorithm for a scan of the $|r|$ and θ of single methyl group.*

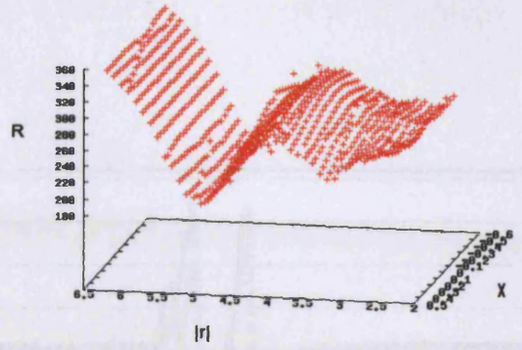

Figure 5.24: *The surface corresponding to the scan of the methyl group distance and the rotation angle about the C-C bond (arbitrary origin).*

5.6.3 Summary

The results from the above reduced dimensionality surfaces are summarised in table 5.1, which gives the optimum coordinates of each surface, along with the best results found by the genetic algorithm.

		$\|r\|$(Å)	θ/χ(rad)	Minimum R^2
Single Proton	Surface minimum	3.75	2.73	187.21
	Best Fit	3.78	1.62	187.38
Methyl Group	Surface minimum	5.00	2.28	193.92
$\|r\|+\theta$	Best Fit	4.93	2.06	194.67
Methyl Group	Surface minimum	5.00	0.16	191.72
$\|r\|+\chi$	Best Fit	4.93	0.21	195.03

Table 5.1: *The coordinates and R^2 values for the surface minima, and the corresponding best fit values of the genetic algorithm search.*

These data make clear that the genetic algorithm has managed in all cases to locate the vicinity of the minimum. The values of the fitness parameter are all still large, but this arises in part from the absence of the single protons in the methyl group simulations and

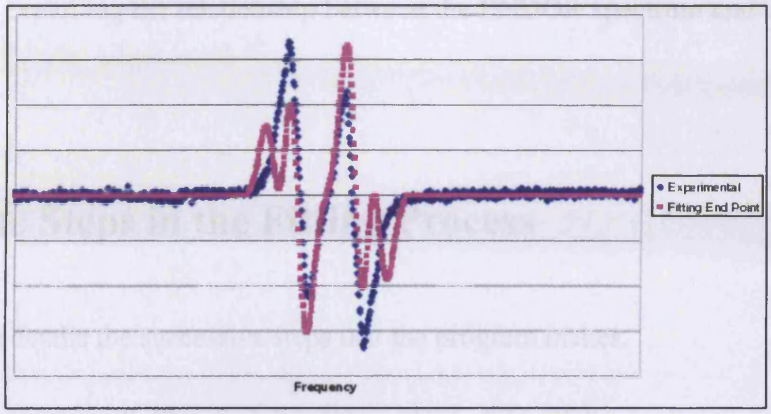

(a) Parallel

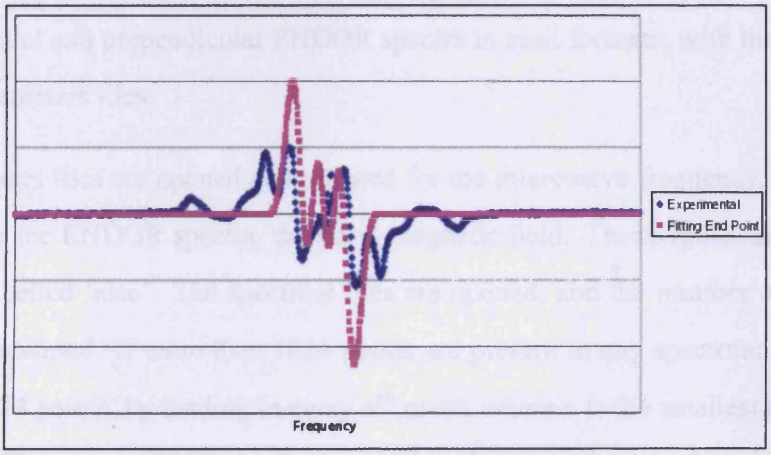

(b) Perpendicular

Figure 5.25: *The (a) parallel and (b) perpendicular ENDOR spectra corresponding to the lowest value of R found by the genetic algorithm for the values of* χ *and* $|r|$ *for a single methyl group.*

vice versa, and in part from the residual error that is expected from the noise of the spectra, and the approximations made in the simulations. This is an encouraging indication of the ability of the genetic algorithm to search these surfaces, and, subsequent to further developments, it is expected to provide a powerful tool for automating the simulation process, by exploiting the relationship between the ENDOR spectrum and the molecular structure.

5.7 The Steps in the Fitting Process

This section details the successive steps that the program makes.

The program is run with files containing the output of the DFT calculation, which must be in G03 format, the EPR spectrum in ascii format, the associated spectrometer parameters, and the parallel and perpendicular ENDOR spectra in ascii formats, with their associated spectral parameters files.

The parameters files are opened and scanned for the microwave frequency, the temperature, and for the ENDOR spectra, the static magnetic field. These values are stored in a structure, labelled 'elec'. The spectrum files are opened, and the number of data points in each are counted. If more than 1024 points are present in any spectrum file, they are scaled to 1024 points, by reading in every n^{th} point, where n is the smallest integer larger than $\frac{N_{points}}{1024}$. This value of 1024 is chosen to allow fast convolution of the peaks onto the simulated spectrum, without significantly affecting the resolution of the spectra. It can be adjusted for particularly crowded spectra. The spectra are then preconditioned according to the process detailed in section 5.3.1. At this point, the experimental spectra are also squared, and subsequently integrated. This provides a scale factor, in equation 5.6.

$$\sigma = [\sum_{i=1}^{N_{points}} y_i^2 \delta x]^{1/2} \tag{5.6}$$

A similar integration is then performed for the simulated spectra (as they are generated),

and each simulated spectral point is multiplied by the ratio $\frac{\sigma_{exp}}{\sigma_{sim}}$ to give a fair comparison in determining fitness, since the units of absorption are arbitrary.

Next the G03 output file is opened, and the atom types and coordinates are read in. They are assigned to a temporary structure labelled 'data', to which is added isotropic hyperfine coupling calculated in the DFT calculation, and the spin and nuclear *g* factor of the given nucleus, found by comparing the atom type to a look-up table, which holds the spins and nuclear *g* factors for many common ENDOR nuclei. This functionality is not yet fully exploited, as the simulation and fitting routines currently only deal with protons. The atom neighbours that are bonded to each atom are determined using a look-up table of standard bond lengths for pairs of atom types. Finally, the program recognises the metal atom in the file, whose coordinates it assigns to the electron spin centre. If several metal atoms are encountered, the program prompts for the user to input which atom corresponds to the spin centre.

A methyl group search routine then locates the methyl groups present, by picking out the C atoms whose neighbour set consists of three H atoms. The fourth neighbour of each methyl C atom is also stored, and used to locate the vector about which the methyl H atoms can rotate, namely the bond between the C atom and this fourth neighbour. The coordinates of each of these five atom are recorded in an array of structures labelled 'meths'. To this structure are added the magnitudes of the distances between the spin centre (metal centre) and the C atoms of the methyl groups and the vectors that link the central methyl C atoms to each of the H atoms. The program then prompts the user to define a molecular z-axis, since this is required to define the angle ω between the z-axis and the metal-methyl vector, and also the unit normal cross product vector of these two vectors, which forms the axis about which the methyl group vector is rotated in the search. It is not yet possible for the program to define a molecular z-axis through a least squares plane calculation routine, although this would be a useful addition. The angles χ by which the methyl groups are rotated about the C-other atom bond are not stored, since these are not defined absolutely - the search routine relocates the methyl group and then performs a rotation by the prescribed value of χ that emerges from the given chromosome.

Every H atom (including those already associated with a methyl group) is then assigned to an array of structures labelled 'nuc', which stores the nuclear coordinates. The vectors linking each H atom to the electron centre are then computed and used to calculate the spin-dipole contribution to the A-tensor associated with the given H atom *via* the point dipole procedure. Each of these A-tensors is diagonalised by the procedure outlined in chapter 2, with the diagonal components (the principal values) stored in the 'nuc' array. The Euler angles are calculated from the product of the diagonalised matrix and the inverted A-tensor, *via* the procedure outlined in chapter 2. The nuclear g-factors are also passed into the 'nuc' array. Finally, the hyperfine standard deviation is determined by the user, and the linewidth associated with each H atom for each ENDOR spectrum can be either user input or estimated from the spectrum using a simple peak-picking routine.

At this point, the user is prompted for the EPR parameters, the principal values of the g-tensor and of the metal centre A-tensor. These are appended to the 'elec' structure, along with user input EPR linewidths. Refinement of these parameters can be made using a preliminary (EPR) genetic algorithm, although the simulation routines are to low order, and the use of pre-simulated parameters is recommended.

Finally, the remaining spectral parameters, the number of H atoms, the frequency range and increment, the range and increment of the angle θ used in the integration, and the hyperfine distribution factor and increment are stored in a structure labelled 'spec'. These parameters are written into the code, and can only currently be adjusted by the user if the code is subsequently re-compiled. This is done because the chosen values have been found to allow simulation with reasonable resolution to take place in a time-frame that is reasonable in light of the genetic algorithm process, however it may prove necessary to increase the flexibility of the code by prompting the user for input of these parameters.

Having established a complete set of parameters, stored in four structures, 'elec', containing the parameters associated with the EPR response, 'nuc', containing parameters associated with the NMR/ENDOR response, 'meths', containing data related to the ge-

ometries of any methyl groups present in the system under study, and 'spec' containing spectrometer parameters, the simulation of the ENDOR spectrum can commence.

The functions to simulate the ENDOR spectrum were written by Robert Farley. The procedure that they follow is as follows.

The routine runs loops over several variables. The first of these is the number of EPR metal centre-electron splittings. For the spin-$\frac{7}{2}$ ^{51}V metal centre of the VO(acac)$_2$ example, this totals eight transitions, for the metal nuclear states $[-\frac{7}{2}, -\frac{5}{2}, -\frac{3}{2}, -\frac{1}{2}, \frac{1}{2}, \frac{3}{2}, \frac{5}{2}, \frac{7}{2}]$. The next loop in is over the number of H atoms. The Larmor frequency of each H atom is calculated *via* equation 5.7.

$$\nu_N = \frac{g_N \mu_N}{h} B_S \tag{5.7}$$

Where B_S is the static B-field of the ENDOR experiment.

Next account is taken where necessary of a thermal distribution of positions of each H atom. This is done *via* the prescribed hyperfine standard deviation, σ_{HC}, and the size of the increment required, δ_{HC}, along with the number of hyperfine increments required, N. The range in each of the values of the A-tensor are set by the dipolar contribution to the parallel component of the A-tensor, $A_{\parallel}^{dip}$, ranging from $A = A_{\parallel}^{dip} - \frac{1}{2}\frac{\sigma_{HC}N}{\delta_{HC}}$ to $A = A_{\parallel}^{dip} + \frac{1}{2}\frac{\sigma_{HC}N}{\delta_{HC}}$. The various A_i values that occur for each increment are then applied in equation 5.8 for the diagonalised A-tensor associated with the given incremental step.

$$A_i = \begin{bmatrix} a_{iso} - \frac{A_i}{2} & 0 & 0 \\ 0 & a_{iso} - \frac{A_i}{2} & 0 \\ 0 & 0 & a_{iso} + A_i \end{bmatrix} \tag{5.8}$$

This diagonal matrix is rotated into the g-frame by the Euler matrix derived on computing the dipolar hyperfine interaction matrix from the coordinates of the given H atom.

The intensity of the absorption associated with each position is determined by its proba-

bility. This information is contained within the standard deviation, σ_{HC}, and is given *via* the Gaussian function of equation 5.9.

$$I_{HC} = \frac{1}{\sqrt{2\pi}\sigma_{HC}} \exp\left[-\frac{1}{2N}\left(\frac{a_i - a_{\parallel}^{dip}}{\sigma_{HC}}\right)^2\right] \tag{5.9}$$

The code then loops over the values of θ and ϕ. For many essentially axial systems a slight rhombicity is observed, which is often not sufficient to determine the x,y coordinates of the species, but does merit a coarse grid integration over ϕ as well as over θ. First the directional cosine functions $h(\theta,\phi)$ are calculated.

$$h_{xx}^2 = sin^2\theta cos^2\phi \tag{5.10}$$

$$h_{yy}^2 = sin^2\theta sin^2\phi \tag{5.11}$$

$$h_{zz}^2 = cos^2\theta \tag{5.12}$$

Then, using these, the effective g-value for this orientation is determined.

$$g^2(\theta,\phi) = g_{xx}^2 h_{xx}^2 + g_{yy}^2 h_{yy}^2 + g_{zz}^2 h_{zz}^2 \tag{5.13}$$

The EPR linewidth, w, is also determined for the given orientation:

$$w^2(\theta,\phi) = w_{xx}^2 h_{xx}^2 + w_{yy}^2 h_{yy}^2 + w_{zz}^2 h_{zz}^2 \tag{5.14}$$

For each H atom, the $A(\theta,\phi)$ is calculated, along with the first and second order effective hyperfine values, $K_1(\theta,\phi)$ and $K_2(\theta,\phi)$

$$A^2(\theta,\phi) = [(A_{xx}g_{xx}h_{xx})^2 + (A_{yy}g_{yy}h_{yy})^2 + (A_{zz}g_{zz}h_{zz})^2]g^2(\theta,\phi) \tag{5.15}$$

$$K_1(\theta,\phi) = \frac{(A_{xx}^2 - A_{yy}^2)g_{xx}^2 g_{yy}^2 h_{xx}^2 h_{yy}^2 + (A_{yy}^2 - A_{zz}^2)g_{yy}^2 g_{zz}^2 h_{yy}^2 h_{zz}^2 + (A_{xx}^2 - A_{zz}^2)g_{xx}^2 g_{zz}^2 h_{xx}^2 h_{zz}^2}{A^2(\theta,\phi)g^4(\theta,\phi)} \tag{5.16}$$

$$\begin{aligned} K_2(\theta,\phi) = \frac{1}{A^2(\theta,\phi)g^2(\theta,\phi)}[g^2(\theta,\phi)(A_{xx}^2 A_{yy}^2 + A_{xx}^2 A_{zz}^2 + A_{yy}^2 A_{zz}^2) \\ -(A_{xx}^2 A_{yy}^2 g_{zz}^2 h_{zz}^2 + A_{xx}^2 A_{zz}^2 g_{yy}^2 h_{yy}^2 + A_{yy}^2 A_{zz}^2 g_{xx}^2 h_{xx}^2)] \end{aligned} \tag{5.17}$$

These are then used to calculate the resonant field and intensity of the EPR transition associated with the given orientation and nuclear spin-state.

The resonant field is given by equation 5.18.

$$B_R = \frac{hm_I A(\theta,\phi)}{g(\theta,\phi)mu_B} - \frac{g(\theta,\phi)}{\nu}[(S(S+1) - m_I^2)(\frac{K_2(\theta,\phi)}{4}) + (\frac{m_I^2 h}{2})] + \frac{h\nu}{g(\theta,\phi)\mu_B} \tag{5.18}$$

Where ν is the (fixed) saturating microwave frequency.

The intensity of the transition at this orientation is given by equation 5.19.

$$I_{EPR} = \frac{h}{g(\theta,\phi)w(\theta,\phi)\mu_B\sqrt{2\pi}} \exp[-\frac{1}{2}(\frac{B_R - B_s}{w(\theta,\phi)})^2] \tag{5.19}$$

Where B_s is the static magnetic field of the experiment.

Next the hyperfine enhancement factor for the given nucleus (and orientation) is computed from the transition probabilities. This process begins with the establishment of a rotation matrix E associated with the given orientation, θ,ϕ:

$$E = \begin{bmatrix} \cos(\theta) & \sin(\theta) & 0 \\ -\sin(\theta)\cos(\phi+\frac{\pi}{2}) & \cos(\theta)\cos(\phi+\frac{\pi}{2}) & \sin(\phi+\frac{\pi}{2}) \\ \sin(\theta)\sin(\phi+\frac{\pi}{2}) & -cos(\theta)\sin(\phi+\frac{\pi}{2}) & \cos(\phi+\frac{\pi}{2}) \end{bmatrix} \tag{5.20}$$

The transpose of this matrix is labelled E^T.

This is used in the calculation of the projection of the g-tensor at the given angle. This is labelled g_{fac}, and is calculated *via* equation 5.21.

$$g_{fac} = (\sum_{i=1}^{3} E_{i3}^T \sum_{j=1}^{3} G_{ij} \sum_{k=1}^{3} G_{jk} E_{k3})^{1/2} \tag{5.21}$$

Where G is the matrix representation of the g-tensor. When this is diagonalised, equation 5.21 simplifies to equation 5.22.

$$g_{fac} = E_{13}^T G_{11}^2 E_{13} + E_{23}^T G_{22}^2 E_{23} + E_{33}^T G_{33}^2 E_{33} \tag{5.22}$$

Here, a subscript of 3 corresponds to the z-direction of the laboratory frame, along which the B-field is aligned. The radio-frequency irradiation is perpendicular to the B-field, and is chosen to represent the x-axis, represented by a subscript 1.

Next, a matrix product of the G- and A-matrices is computed, L.

$$L = GA \tag{5.23}$$

This is modified by multiplying by $\frac{m_s}{g_{fac}}$, and subtracting the nuclear Larmor frequency from each component to give the C-matrix.

$$C_{ij} = \frac{m_s}{g_{fac}} L_{ij} - \nu_N \tag{5.24}$$

The zeroth order ENDOR transition probability, w_0 can be found from equation 5.25.

$$w_0 = 1 - \left(\frac{(\Sigma_{i=1}^3 R_{i1}^T \Sigma_{j=1}^3 C_{ij}^T R_{j3})^2}{\Sigma_{i=1}^3 R_{i3}^T \Sigma_{j=1}^3 C_{ij} \Sigma_{k=1}^3 C_{jk}^T R_{k3}} \right) \tag{5.25}$$

The first order transition probability, w_1 comprises 4 contributions, w_1A, w_1B, w_1C, and w_1D. These are listed in equations 5.26 to 5.29.

$$w_1A = \sum_{i=1}^{3} R_{i1}^T \sum_{j=1}^{3} C_{ij} \sum_{k=1}^{3} C_{jk}^T R_{k1} \tag{5.26}$$

$$w_1B = (\sum_{i=1}^{3} R_{i1}^T \sum_{j=1}^{3} C_{ij} R_{j3})^2 \tag{5.27}$$

$$w_1C = (\sum_{i=1}^{3} R_{i1}^T \sum_{j=1}^{3} C_{ij} R_{j3} - \frac{\nu_N}{g_{fac}} \sum_{i=1}^{3} R_{i1}^T \sum_{j=1}^{3} G_{ij} \sum_{k=1}^{3} G_{jk} R_{k3})^2 \tag{5.28}$$

$$w_1D = (\sum_{i=1}^{3} R_{i1}^T \sum_{j=1}^{3} C_{ij} R_{j3} - \frac{\nu_N}{g_{fac}^2} (\sum_{i=1}^{3} R_{i1}^T \sum_{j=1}^{3} G_{ij} \sum_{k=1}^{3} G_{jk} R_{k3})(\sum_{i=1}^{3} R_{i3}^T \sum_{j=1}^{3} C_{ij}^T R_{j3})) \times \frac{\Sigma_{i=1}^{3} R_{i3}^T \Sigma_{j=1}^{3} C_{ij}^T R_{j3}}{\Sigma_{i=1}^{3} R_{i3}^T \Sigma_{j=1}^{3} C_{ij} \Sigma_{k=1}^{3} C_{jk}^T R_{k3}} \tag{5.29}$$

w_1 then is given by equation 5.30

$$w_1 = \frac{w_1A - w_1B + w_1C - w_1D}{\nu_N^2} \tag{5.30}$$

These transition probabilities lead to the expression for the hyperfine enhancement factor:

$$F_{HC} = |\frac{w_0}{w_1}|^{1/2} \tag{5.31}$$

The final required value in forming the spectrum is the ENDOR resonance frequency, ν_R. This is derived from the A- and g-values, with the directional cosine functions *via* equation 5.32.

$$\nu_R = \left[\sum_{i=1}^{3} \left(\frac{m_s}{g(\theta,\phi)} \sum_{j=1}^{3} g_j h_j A_{ji} - h_i \nu_N \right)^2 \right]^{1/2} \tag{5.32}$$

Finally, with a knowledge of the position of the resonance, the intensity of the transition, the distribution of the nuclear positions and the intensity of the EPR transition giving rise to the ENDOR spectrum, a first derivative Gaussian spectral line can be convoluted onto the spectrum, according to equation 5.33.

$$y_i = I_{EPR} I_{HC} F_{HC} \frac{x_i - \nu_R}{\sqrt{2\pi w^3(\theta,\phi)}} \left(\frac{\nu_R}{\nu_N} \right)^2 \exp[-2 \frac{x_i - \nu_R}{w^2(\theta,\phi)}] \tag{5.33}$$

Where y_i is the i^{th} simulated absorption point and x_i is the i^{th} simulated spectrum frequency point. Optionally this can be mixed by a factor *ls* which is included as a parameter to fit, with a Lorentzian function. The final spectrum is built up as a sum of contributions to the set of N absorption points. It is then squared and integrated to provide the scaling factor, and scaled appropriately, to give the same integration of the square of the spectrum as the experimental spectrum.

The fitness of the spectrum is then judged by application of equation 5.1. At this point, the genetic algorithm begins. The lengths of the binary bit-strings are calculated in accordance with equation 5.3, to generate a segmented set of a defined number, N_{chr}, of chromosomes, segmented according to the various parameters represented by the chromosome. The decoding of the chromosomes, which are initially filled at random with 1s and 0s, requires that the original parameters be available, since the chromosomes store adjustments to be made to the DFT coordinates, rather than their absolute values. The decoding of the randomly filled chromosomes takes place in this manner, with methyl groups revealed first, and relocated, rotated and expanded accordingly. The remaining H atom coordinates are then extracted, along with the isotropic coupling constants associated with each proton, and its linewidth. The Cartesian coordinates are obtained for each H atom and from each set of coordinates a dipolar A-tensor is constructed. These are then used to simulate the ENDOR spectra associated with the given randomly derived

structure, in accordance with the simulation process outlined above. The fitness of each simulated spectrum is then evaluated by equation 5.1. The coordinates associated with the structure giving the lowest fitness, if this value is lower than that of the original structure, are stored, and replaced as better fitness values are obtained. They are also written to a coordinates file which documents the geometric changes that take place during the structural adaptation. The stochastic nature of the search routine means that these changes are not systematic.

The reciprocals of the fitness values are then used to define a space between 0 and 1 occupied by each chromosome, with the total population occupying all the space between 0 and 1. Random numbers are then cast between 0 and 1 N_{chr} times, until the population is restored. Each cast adds the chromosome that corresponds to the number obtained to the next generation population.

Pairs of chromosomes are then picked for mating as described above, and each bit is considered in turn for mutation with an adjustable probability of mutation occurring. A proportion of the population is also replaced by completely new (random) chromosomes. The new population of chromosomes is then decoded and the corresponding spectra simulated, with the process repeated for a defined number, N_{gen}, of generations. The code checks for stagnation of the population (*i.e.* no improvement made after a certain number of generations), and resets the entire population (refilling each chromosome with 1s and 0s) if it is encountered. The loop can be broken before N_{gen} generations have been cycled through if the fitness of the best member is better than an input minimum. When this happens, or N_{gen} is reached, the code writes out the final geometries and spectra, as well as placing the contents of the four structures/arrays of structures, 'elec', 'spec', 'nuc' and 'meths', with the coordinates of the 'meths' and 'nuc' arrays substituted for the current best structure, along with all the data points to a binary format file, from which the code can restart if the final fit is deemed unsatisfactory. This restart will take as the starting point geometry the best geometry reached in the previous run. This is also the geometry that will be used as the reference in moving the H atom coordinates according to the chromosomes. The code displays the best value of the fitness criterion achieved to date after

evaluating the fitness of each generation.

5.8 Conclusions

The extension of an ENDOR simulation code to incorporate a genetic algorithm fitting routine has been made for axially symmetric spin $\frac{1}{2}$ transition metal complexes. The parameters of the fitting routine are the geometric coordinates of the H atoms of the molecule, with a rigid body treatment of the methyl groups, exploiting the fact that the spin-dipole contribution to the hyperfine coupling can be described for many systems using a simple point dipole interaction model to extract geometric parameters from the ENDOR spectra while simultaneously automating the fitting procedure. This geometric optimisation refines the DFT geometry to match the geometry that is derived from the ENDOR spectra, within the confines of the point-dipole model (the 'ENDOR geometry').

The treatment of axially symmetric systems requires a reduction in the dimensionality of the search algorithm from the three Cartesian directions to two dimensions. Unique ENDOR spectra can only be recorded for two molecular frame positions, parallel and perpendicular to the molecular z-axis. Each spectrum supplies one unique coordinate per nucleus, thus necessitating the reduction in dimensionality. The two coordinates that have been chosen are the angle between the z-axis and the vector linking the nucleus in question to the electron centre and the magnitude of this electron-nucleus vector. The coordinates used for methyl groups, treated as rigid bodies, are the angle and magnitude of the vector linking the central C atom to the electron centre, the rotation of the H atoms about the C-other atom bond, and the lengths of the C-H vectors. By making this coordinate shift, the application of this process to a simple sample axial system has achieved significant improvement, improving the fitness in some cases by more than 35%. Schematic reduction of the dimensionality to incorporate just two of the coordinates allows a visualisation of the progress made by the code, and this has revealed its ability to rapidly locate

and search the areas surrounding minima. It has also revealed a large discrepancy in the dependency of the fitness of the angle and the magnitude of the electron-nuclear vector, with the magnitude of the vector, $|r|$ having a far greater importance. This gives rise to flat-bottomed valleys, which the code easily locates, but struggles to find the minimum within. This difficulty can be overcome by fine-tuning the ranges and precision required to for each coordinate, which is left to the user.

The program has shown itself capable of dealing with an axial system containing only H atoms as spin-active nuclei, and for which the molecular z-axis has been defined. It has also demonstrated its ability to locate the regions of minima, but not to search those regions in a thorough manner (which limitation is inherent, due to the stochastic nature of the genetic algorithm). With a view to improving upon these limitations, a number of potential improvements can be made to the code. These include the incorporation of quadrupolar couplings in the ENDOR simulation routines to allow the simulation of nuclei of $I \geq 1$, such as ^{14}N, a routine to define the symmetry and plane of the molecule, to automate the process of defining the molecular z-axis, the extension of the program to handle ENDOR systems of rhombic symmetry, for which three unique spectra are available to determine the three coordinates of each atom, and a numerical gradient following search algorithm to systematically search for the parameter surface minimum once the region of the minimum has been reached. This last refinement, the use of numerical gradients to calculate the steepest descent, would be unable to deal with the multiple-minima of the parameter surface if it were employed as the primary search method, but as a means of refining the optimum points located by the GA, it lends itself ideally.

A further consideration for future developments is the incorporation of fully rotational methyl groups. The ENDOR experiment take place in frozen solution, typically at around 10K. An energy barrier to the rotation of a methyl group in $VO(acac)_2$ of 2.6 kJ mol^{-1} as calculated at the B3LYP/6-31G(d,p) level is not entirely frozen out, and a corresponding distribution of coordinates is expected. The probabilities of the various positions are straightforward to calculate, obeying a Boltzmann distribution. The actual coordinates of the atoms are not so simple to determine, and would require a simple sine-function

approximation.

With some or all of these extra features included the code will represent a means of obtaining both hyperfine and the associated geometric parameters for a given system simultaneously, and in an automatic manner. Currently, this has been shown to be possible for axial ^{1}H-ENDOR systems.

Chapter 6

Conclusions

In this study, a range of transition metal complexes of catalytic significance have been investigated by EPR/ENDOR spectroscopy and by DFT. The aim of these investigations was to elucidate detailed structural information regarding the interactions of the transition metal ions and their environments, both in homogeneous processes (the catalytic interaction between transition metal salen derivative complexes and epoxide/amine molecules) and heterogeneous processes (the incorporation of Cu^{II} ions into an alumino-phosphate material framework).

6.1 Homogeneous Catalysts

6.1.1 Epoxide Studies

Geometric Epoxides

Homogeneous asymmetric epoxidation catalysis has been well studied in recent years. The use of salen derived ligands is well known to give high selectivities, but the precise mechanism by which chirality is conferred to the epoxide molecule is not well understood. In this study the selective binding of geometric isomers of 2,3-epoxybutane by a vanadyl analogue of the experimentally selective Cr and Mn salen catalysts. The model of this selective interaction is developed through a large set of spectroscopic and theoretical data. In the first place, the EPR spectra recorded for the complex dissolved in the *cis*-epoxide differ significantly from those recorded for the *trans*-isomers. These differences demonstrate a conclusive difference in binding between the two species, which, in combination with the fact that the complex in a solution of the *trans*-isomers give a signal that is identical to that recorded in a toluene solution (which is known to show no interaction with the complex) makes it clear that the selectivity displayed by the vanadyl analogue mirrors that of the catalytically active versions, and further that it is a difference in the binding mode that leads to such discrimination, rather than in the mode of attack. As a species which is spectroscopically active, and which results in well understood ENDOR

patterns, the vanadyl analogue, in demonstrating these differences in binding, lends itself to further, more detailed, studies of the precise mechanism of selectivity.

To probe these subtle differences in binding, further spectroscopic studies in the form of ENDOR investigations were made. The resolution of peaks in the *cis*-epoxide solution, whose absence is noted in the *trans*-epoxide case suggests that the *cis*-isomer is held much more closely to the vanadium centre than the *trans*-isomers, as these peaks must arise from the epoxide molecule itself. Further changes in the signals arising from the protons of the cyclohexane backbone, H^{exo} and H^{endo}, observed in the *cis*-isomer, imply a perturbation in the extent to which the VO moiety sits above the N_2O_2 plane of the complex, providing further evidence for the coordination of this isomer, and not of the *trans*-epoxide.

The ENDOR technique allows for the quantification of the distances of the resolved proton peaks, H^2 and $H^{2\prime}$, which it places, within the limitations of the point-dipole interaction approximation (see section 2.1.2), at 3.3Å and 3.9Å respectively. It is further capable of defining the angle formed by the molecular z-axis (the V=O bond) and the vector linking the V centre to each proton, for which values of 55° and 60° are obtained. The lack of information in this spectroscopically axial system relating to the $x-y$ plane, however, requires more detailed geometric studies in order to ascertain more accurate mechanistic information regarding the differences in binding. Difficulties in obtaining crystals, and the need to model the solution (or frozen glass) rather than solid state interactions rule out x-ray crystallography as a means to do this, and so theoretical calculations represent the best method of obtaining this geometric information.

Modelling systems of this size requires a degree of compromise in the sophistication of the quantum chemical technique used, and the particular difficulties of representing the various electronic configurations of transition metal ions mean that DFT is the method of choice in such studies. The local nature of the approximations used in the LDA DFT technique means that particular care must be paid in the selection of a functional and basis set that are able to model the middle-range interactions of binding interactions such

as these. For this reason, a study of a similar, but smaller, interacting system, $CrCl_2O$ + epoxyethane, was used to select the BHandHLYP functional, which gave the best interaction geometries and energy compared to a more sophisticated technique (MP2). There is still some difficulty in representing the dispersion contributions to the H-bonding which was shown in these calculations to be important in determining the details of the interaction, however, agreement with the ENDOR data regarding the distances from the vanadium centre to protons H^2 and $H^{2\prime}$ to within 0.1Å provides reasonable confidence in the accuracy of the model.

This model was built *via* a process of investigating various configurations of each epoxide molecule and complex combination. A preliminary rotation of the epoxide beneath the complex plane, by performing direct optimisation of the system with the epoxide rotated in increments of 90° from the initial (optimised) geometry returned the epoxide to the initial configuration (or else flipped it over into a configuration with a substantially lower interaction energy), leading to a large degree of confidence in the preference of the system for this arrangement, although no energy barrier to rotation was obtained through this process. Pushing the *cis*-epoxide molecule towards the vanadium centre provided a shallow sloping energy barrier, with a cost of less than 2 kJ mol^{-1} to pushing the epoxide 0.5Å closer to the vanadium.

With this confidence that the geometries obtained corresponded to the minima for the interaction of the epoxide with the complex within the limitations of the DFT method used, and with the support of the ENDOR geometric data, detailed information of the nature of the interaction was obtained. Using a multipole analysis, three hydrogen bonds were implicated in the binding mode (see figure 3.11). The disruption to this three-point interaction caused by one of the methyl groups of the *trans*-isomers gives an explanation for the discrimination observed in the EPR spectra based purely on the binding interaction, with multipolar contributions to the interaction energies that further imply this hydrogen binding difference as the cause of the selectivity.

Chiral Epoxides

The geometric epoxide study, in isolating a three-point hydrogen bonding interaction as a cause of discrimination implicates for the first time a hydrogen atom (H^{exo}) attached to a stereocentre carbon atom. The real catalytic systems for which this vanadyl case serves as an analogue show chiral selectivity in addition to geometric selectivity, thus this study was extended to a series of four chiral epoxides, epoxypropane, 1,2-epoxybutane, fluoromethyloxirane and chloromethyloxirane.

The EPR/ENDOR studies demonstrated the ability of the vanadyl complex to resolve the enantiomers of three of these epoxides (1,2-epoxybutane, being the exception), with reversed selectivities (when the change in absolute stereochemistry that results from the priority of the halogen atoms in the Cahn-Ingold-Prelog rules is taken into account) for the halogenated species with respect to epoxypropane. DFT studies probed the more subtle details of the enantiomeric discrimination. A similar process of analysing various configurations to that used in the geometric isomerism study lead to a substantial degree of confidence that the geometries were obtained were minima for the complexing interaction.

These calculations again demonstrated a three-point hydrogen bonding interaction. The selectivity observed can be related to this mode using steric and inductive arguments. The importance of the H^{exo} atom in these interactions varies, however, with the epoxide species. The bulk of the 2,3-epoxybutane ethyl group prevents an approach to the vanadium centre that is sufficiently close to allow this hydrogen bonding interaction to significantly affect the precise positioning of the epoxide molecule. The epoxypropane molecule appears essentially to be anchored to the H^{exo} atom, drawn somewhat to the side of the complex it is on, affecting the steric interaction of the methyl group with the *tert*-butyl groups of the complex. In each halogenated case, however, the H^{exo} atom serves as a significant barrier to the approach of the epoxide oxygen atom to the vanadium centre, favoured by the inductive effects of the halogen atom itself. The clash between the H^{exo} atom and the epoxide halogenoethyl group explains the reversal in selectivity

observed.

These studies provide an explanation for the selectivities observed, with DFT data providing subtle details that are entirely consistent with the ENDOR and EPR data, whose precise nature cannot be probed by either technique. Used in combination, these analyses have, in this study, been used to describe the importance of the stereocentre carbon atom (through its proton, H^{exo}) in the enantioselectivity of an analogue of the epoxidation catalysts. The validity of the vanadyl complex as an analogue is demonstrated by its own selectivity in binding, as evidenced in the EPR data, thus this selectivity mechanism can be extrapolated to the real catalytic systems with some confidence.

Further Studies

This work presents the possibility of a number of further studies to more deeply probe the role of H^{exo} in determining the selectivity. Replacement of the cyclohexane group, for instance with an achiral phenyl group would allow investigation of the nature of the interaction in the absence of H^{exo}, to compare the steric hindrance effects of the halogenated and non-halogenated epoxide interactions in the absence of this hindering/anchoring proton. Selective *tert*-butylation of the salen ligand phenyl rings would highlight the importance of the steric influence of the *tert*-butyl groups in limiting the space available for epoxide coordination, which may play a role in promoting the importance of the H^{exo} hindrance and anchoring.

6.1.2 Aryl Amine Studies

A further study was made of the interaction of an aryl amine, methylbenzyl amine, with a copper analogue of the same catalytic salen complexes. The EPR/ENDOR studies demonstrated a preferential binding of the heterochiral pairing, but also that the homochiral pairings did show some binding. This subtle discrimination was probed by DFT calculations.

Preliminary investigations using a forcefield to represent the phenyl groups both of the complex and of the amine showed a strong preference for $\pi - \pi$ interactions, with the molecule showing a preference for rotating the bond connecting the phenyl group to breaking the $\pi - \pi$ interaction. This lead to the requirement of accurate modelling of the dispersion effects that make up $\pi - \pi$ interactions, and for this reason a functional was selected which had been shown in a previous study [116] to reproduce the minima observed in benzene and DNA base pair dimers at the MP2 level. Using this functional, a similar, though weakened, preference for $\pi - \pi$ interaction was observed. A further steric interaction between the methyl group of the amine and the *tert*-butyl groups of the complex leads to three possible coordination configurations for each of the amine enantiomers, in which the phenyl ring of the amine is positioned beneath either of the complex phenyl rings or beneath the cyclohexane ring.

These three configurations were probed in the DFT studies by arranging the system in the first two configurations and allowing it to optimise. The breaking of the $\pi - \pi$ interactions in favour of coordination near the cyclohexane ring demonstrates the importance of the interplay between the $\pi - \pi$ interaction and the steric clash of the *tert*-butyl groups, which was further investigated by removing the *tert*-butyl groups. Since this interaction is subtle, and DFT is unable to precisely model the dispersion effects which make up $\pi - \pi$ interactions, it is difficult to say without a more sophisticated (and correspondingly expensive) calculation whether the balance between these two conflicting effects (the $\pi - \pi$ interaction and the steric effect of the methyl group) is accurately modelled. However, by allowing the system the comparative freedom from steric hindrance of removing the *tert*-butyl groups the importance of the position of the H^{exo} proton as a further steric factor, this time affecting the position of the phenyl ring itself, was highlighted. Whilst this does not allow a conclusive link between the the H^{exo} position and the direction of the selectivity to be drawn it does, for the first time, implicate the involvement of that proton in the selectivity in some way.

Further Studies

Further studies to probe the precise means by which the H^{exo} atom determines the selectivity would require a more sophisticated modelling procedure, which could more accurately model the dispersion effects of the $\pi - \pi$ interaction. The interaction between the amine nitrogen atom and the copper centre is crucial in determining the distance between the two fragments, which is significantly shorter than in the epoxide study reported here, due to a stronger interaction with the metal centre. This coordination in turn determines the importance of steric interactions. Any technique used must thus be able also to accurately reproduce this interaction.

Further studies at a similar theoretical level involving selective *tert*-butylation, the use of bulky non-aromatic amines, aromatic epoxides or alternative salen analogues might build up, in conjuction with the corresponding EPR/ENDOR studies, a broader picture from which more conclusive evidence may be abstracted in determining this interaction.

6.2 Framework Copper Incorporation in an AlPO Material

This study involved the investigation of an alumino-phosphate material with copper ions incorporated. The substitution of Cu^{II} ions into lattice sites of such materials is controversial, since the low symmetry tetrahedral environment is not common for Cu^{II} ions, although examples of tetrahedral copper centres do exist [121–123] and the incorporation of suitably sized heteroelements in zeolitic frameworks is known to be a possibility [62]. A previous study [64] of a copper-incorporated AlPO framework system provided some evidence for the non-framework incorporation of hydrated copper species. In this study EPR signals arising from Cu^{II} ions in an AlPO material, CuIST-2, altered on dehydration and subsequent calcination in a manner which indicated a reduction in the symmetry of the copper environment.

This reduction in symmetry was interpreted as the reduction in the coordination number of the copper as the water and templating amine molecule is removed from the system. Calcination leads to a completely rhombic signal ($g_3 = 2.61$, $g_2 = 2.14$ and $g_1 = 2.06$), along with two axial signals which persist from before calcination with some distortion, and whose intensity is weakened. This implies the presence of five copper environments, one of which is of very low symmetry and coordination, the remaining four showing reasonably typical copper signals, with the axial symmetry common in Jahn-Teller distorted copper ions. If the copper is able to take the low symmetry, this is most likely to be in order to incorporate into the lattice framework. In order to substantiate this assertion DFT studies of the substituted framework were carried out.

Stable geometries were obtained by periodic DFT calculations of an infinite framework with copper ions (and charge-balancing protons) substituted for each of the three symmetrically distinct aluminium atoms, giving a four-coordinate copper centre. The most stable of these had a distorted trigonal pyramidal arrangement, in which the protonated oxygen atom is at the apex, and the three equatorial oxygen atoms are distorted towards a 'T'-shaped arrangement. Essentially, the tetrahedral lattice is distorted by the Cu^{II} ions towards an octahedral arrangement with two 'missing' coordinating species. These vacant coordination sites open to different channels of the lattice in the three different sites. Further calculations in which the water and templating methyl amine molecule were incorporated in these sites gave favourable interaction energies in the axial coordination position of one site and the equatorial position of another, with a compromise made on the coordination of two water molecules or one water and one methyl amine molecule.

These geometries adopted by the copper ions can explain the five EPR signals observed. The four approximately axial signals can be explained by those ions whose vacant coordination sites are occupied by the water and methyl amine molecules, with slight rhombicity arising, particularly in signal B, and possibly D, through the difficulty in distorting the three equatorial oxygen atoms of the tetrahedral lattice into an exact square planar (with the coordinating species) arrangement, and to the possible presence of nitrogen in that fourth coordination site in place of oxygen. Five coordinate structures might also be

expected to show further increased rhombicity, as the absence of the second axial species might provide more space for distortion of the equatorial plane. The lower symmetry structure is explained by the trigonal pyramidal four coordinate species obtained with no coordination.

The ability to accurately derive *g*-tensors from theoretical calculations would allow the importance of these three factors promoting rhombicity to be quantified, by identifying which signal (A-D) arises from which coordination environment. This is not possible due to difficulties in extracting second-order parameters from the density functional calculation. As discussed in the homogeneous catalysis studies, more sophisticated methods are not available for such systems, and so it is important to identify trends in the *g*-tensor values obtained from the cluster calculations, particularly in the $g_{||}$ values. That the calculated values show approximately axial tensors for those clusters with just an equatorially coordinated molecule, slightly rhombic tensors with an axially coordinated molecule, and a very rhombic tensor with no molecule coordinated points to links between the equatorially coordinated species and signals A and C, between the axially coordinated species, and/or 6-coordinate species and signals B and D, and between the 4-coordinate species and signal E. This further suggests that the principal factor affecting the rhombicity is the geometric distortion at the copper site, rather than the coordination number or the presence of nitrogen.

6.2.1 Further Studies

Further investigation of this or alternative substituted systems might proceed either *via* the acquisition of data related to alternative systems with a view to building up a set of data relating to several framework systems. Alternatively, more detailed *g*-tensor calculations, perhaps initially on smaller clusters, might provide closer agreement with experiment, although difficulties with such calculations would mean that highly accurate calculations would probably require what is currently an unrealistic level of sophistication. More detailed structural investigation might provide a clearer picture of the coordination envi-

ronment, and of the precise extent of the strain placed on the lattice by the incorporation of Cu^{II} ions.

However, the positive identification of the five EPR signals with framework-incorporated Cu^{II} ions with various degrees of coordination allows, even without such further investigation, a high degree of confidence in the assertion that the copper ions do occupy framework sites.

6.3 ENDOR Simulation

The transition metal complex studies discussed above illustrate the importance of ENDOR as a means of extracting geometric data from solution state systems. The accurate elucidation of the ENDOR spectral parameters requires spectral simulation, for which a number of programs are available. Of these very few contain any fitting routines, most requiring a fitting 'by hand' procedure. For this reason, the existing in-house code was developed in this project to incorporate a genetic algorithm search routine.

The importance of some substantiating evidence as provided by DFT in many such ENDOR studies is demonstrated here by the necessity of the calculations carried out for elucidating the more subtle aspects of the coordination of the epoxides and of the MBA. This complementary nature of the DFT and ENDOR techniques has been exploited and expanded in the development of the fitting routines, to adjust DFT derived structural parameters to fit to the ENDOR spectra. This is done *via* the calculation of hyperfine parameters by means of a simple point-dipole model, which provides a very good approximation to the positions of the protons in many transition metal systems [19,46,47], provided the unpaired electron is sufficiently restricted to a spatially tight orbital on the transition metal itself, and the protons in question are sufficiently remote ($r \gtrsim 2.5\text{Å}$) from the transition metal centre. By this process precise geometric parameters are derived from the ENDOR spectra.

Certain refinements to the routines, including the treatment of methyl groups as rigid bodies and the reduction of the coordinate set, have allowed the code to locate regions close to the minima in reduced dimensionality (two-dimensional) tests of the fitting with a sample axially symmetric system, $[VO(acac)_2]$. The surfaces used in these tests have, by virtue of the reduced dimensionality and of the simplicity of the system studied, in which essentially only two largely distinct proton environments are observed have meant that the genetic algorithm used has not been the optimum search routine, since the surfaces studied have not been troubled by local minima. More generally, however, ENDOR spectra for more complicated systems would suffer from local minimum effects, since the matching of a pair of peaks in each of the positions (parallel and perpendicular, or, in the rhombic case, x, y, and z) is not so straightforward. While the code as it stands is not able to investigate such surfaces, it is in principal sufficiently robust a search routine to do so.

6.3.1 Further Studies

In order to model more challenging systems, such as the salen complex interactions described above, a number of refinements are required. In the first place, some fine-tuning of the treatment of methyl-groups to allow for thermal rotations would give better fitness. Also, whilst the genetic algorithm parameters have been tuned to the $[VO(acac)_2]$ system, a more general parameter set, tuned to a large range of complexes is required to make the program universal. Likely difficulties with the time required to search all of the local minima that would arise in a system with many proton environments could be addressed by searching within each local minimum more thoroughly with a gradient following algorithm, freeing the genetic algorithm to search over a more coarse grid. Finally, the inclusion of quadrupolar simulation to the code would be required to extend the studies to nitrogen ENDOR.

Bibliography

(1) Murphy, D.M.; Fallis, I.A.; Willock, D.J.; Landon, J.; Carter, E.; Vinck, E. *Angew. Chem. Int. Ed.* **2008**, *120*, 1436.

(2) Smith, G.J. *Synthesis* **1984**, *8*, 629.

(3) Besse, P.; Veschambre, H. *Tetrahedron* **1994**, *50*, 8885.

(4) Prileschjew, N. *Ber. Dtsch. Chem. Ges.* **1909**, *42*, 4811.

(5) Swern, D. *J. Am. Chem. Soc.* **1948**, *70*, 1235.

(6) Noyori, R. *Angew. Chem. Int. Ed.* **2002**, *41*, 2008.

(7) Heitbaum, M.; Glorius, F.; Escher, I. *Angew. Chem. Int. Ed.* **2006**, *45*, 4732.

(8) Jacobsen, E.N.; *Acc. Chem. Res.* **2000**, *33*, 421.

(9) Katsuki, T,; Sharpless, K.B. *J. Am. Chem. Soc* **1980**, *102*, 5974.

(10) Xia, Q.H.; Ge, H.Q.; Ye, C.P.; Liu, Z.M.; Su, K.X. *Chem. Rev.* **2005**, *105*, 1603.

(11) Movassaghi, M.; Jacobsen, E.N. *Science* **2002**, *298*, 1904.

(12) Yoon, T. P.; Jacobsen, E. N. *Science* **2003**, *299*, 1691.

(13) Pfeiffer, P.; Breith, E.; Lübbe, E.; Tsumaki, T. *Justus Liebig's Annalen der Chemie* **1933**, *503*, 84.

(14) Schurig, V.; Betschinger, F. *Chem. Rev.* **1992**, *92*, 873.

(15) Zhang, W.; Loebach, J.L.; Wilson, S.R.; Jacobsen, E.N. *J. Am. Chem. Soc* **1990**, *112*, 2801.

(16) Jacobsen, E.N.; Zhang, W.; Muci, A.R.; Ecker, J.R.; Deng, L. *J. Am. Chem. Soc* **1991**, *113*, 7063.

(17) Norrby, P.O.; Linde, C.; Åkermark, B. *J. Am. Chem. Soc* **1995**, *117*, 11035.

(18) Hamada, T.; Fukuda, T.; Imanishi, H.; Katsuki, T. *Tetrahedron* **1996**, *52*, 515.

(19) Fallis, I. A.; Murphy, D. M.; Willock, D. J.; Tucker, R. J.; Farley, R. D.; Jenkins, R.; Strevens, R.; *J. Am. Chem. Soc.* **2004**, *126*, 15660.

(20) Pospisil, P. J.; Carsten, D. H.; Jacobsen, E. N. *Chem. Eur. J.* **1996**, *2*, 974.

(21) Hashihayata, T.; Ito, Y.; Katsuki, T. *Tetrahedron* **1997**, *53*, 9541.

(22) Strassner, T.; Houk, K.N. *Organic Lett.* **1999**, *1*, 419.

(23) Marckwald, W.; McKenzie, A. *Ber. Dtsch. Chem. Ges.* **1900**, *33*, 208.

(24) Larrow, J.F.; Jaconsen, E.N. *Topics in Organometallic Chemistry* R.D. Larsen, ed.; Springer-Verlag; Heidelberg; **2003**.o

(25) Schaus, S.E.; Brandes, B.D.; Larrow, J.F.; Tokunaga, M.; Hansen, K.B.; Gould, A.E.; Furrow, M.E.; Jacobsen, E.N. *J. Am. Chem. Soc.* **2002**, *124*, 1307.

(26) Larrow, J.F.; Hemberger, K.E.; Jasmin, S.; Kabir, H.; Movel, P. *Tetrahedron Asymmetry* **2003**, *14*, 834.

(27) White, D.E.; Jacobsen, E.N. *Tetrahedron Asymmetry* **2003**, *14*, 3633.

(28) Kim, G.J.; Lee, H.; Kim, S.J. *Tetrahedron Lett.* **2003**, *44*, 5005.

(29) Kolb, H.C.; VanNieuwenhze, M.S.; Sharpless, K.B. *Chem. Rev.* **1994**, *94*, 2483.

(30) Nielsen, L.P.C.; Stevenson, C.P.; Blackmond, D.G.; Jacobsen, E.N. *J. Am. Chem. Soc.* **2004**, *126*, 1360.

(31) Feher, G. *Phys. Rev.* **1956**, *103*, 834.

(32) Bryliakov, K.P.; Babushkin, D.E.; Talsi, E.P. *J. Mol. Catal. A.* **2000**, *158*, 19.

(33) Bryliakov, K.P.; Kholdeeva, O.A.; Vaninam, M.P.; Talsi, E.P. *J. Mol. Catal. A.* **2002**, *178*, 47.

(34) Hseih, W.Y.; Pecoraro, V.L. *Inorg. Chim. Acta.* **2002**, *341*, 113.

(35) Guilherme, L.R.; Dreschel, S.M.; Tavares, F.; da Cunha, C.J.; Castaman, S.T.; Nakagaki, S.; Vencato, I.; Bortoluzzi, A.J. *J. Mol. Catal. A.* **2007**, *269*, 22.

(36) de Boer, J.W.; Browne, W.R.; Brinksma, J.; Alsters, P.L.; Hage, R.; Feringa, B.L. *Inorg. Chem.* **2007**, *46*, 6353.

(37) Pui, A. *J. Coord. Chem.* **2007**, *60*, 709.

(38) Bryliakov, K.P.; Lobanova, M.V.; Talsi, E.P. *J. Chem. Soc. Dalton Trans.* **2002**, 2263.

(39) Bryliakov, K.P.; Talsi, E.P. *Inorg. Chem.* **2003**, *42*, 7258.

(40) McGarrigle, E.M.; Gilheany, D.G. *Chem. Rev.* **2005**, *105*, 1563.

(41) Atherton, N.M.; Shackleton, J.F. *Mol. Phys.* **1980**, *39*, 1471.

(42) Smith, T.S.; LoBrutto, R.; Percoraro, V.L. *Coord. Chem. Rev.* **2002**, *228*, 1.

(43) Poeppl, A.; Mankiandan, P.; Koehler, K.; Maas, P.; Strauch, P.; Boettcher, R.; Goldfarb, D. *J. Am. Chem. Soc.* **2001**, *123*, 4577.

(44) Ploutarch, B.N.; Dave, P.C.; Goldfarb, D. *J. Magn. Reson.* **2002**, *158*, 126.

(45) Chatterjee, P.B.; Bjattacharaya, S.; Audhya, A.; Choi, K-Y.; Endo, A.; Chaudhury, M. *Inorg. Chem.* **2008**, *47*, 4891.

(46) Murphy, D.M.; Fallis, I.A.; Farley, R.D.; Tucker, R.J.; Avery, K.L.; Willock, D.J. *Phys. Chem. Chem. Phys.* **2002**, *4*, 4937.

(47) Tucker, R.J.; Fallis, I.A.; Farley, R.D.; Murphy, D.M.; Willock, D.J. *Chem. Phys. Lett.* **2003**, *380*, 758.

(48) Henderson, T.A.; Hurst, G.C.; Kreilick, R.W. *J. Am. Chem. Soc.* **1985**, *107*, 7294.

(49) Henderson, T.A.; Hurst, G.C.; Kreilick, R.W. *J. Am. Chem. Soc.* **1985**, *107*, 7299.

(50) Bolm, C.; Martin, M.; Gescheidt, G.; Palivan, C.; Neschadin, D.; Bertagnoli, H.; Feth, M.; Schweiger, A.; Mitrikas, G.; Harmer, J. *J. Am. Chem. Soc.* **2003**, *125*, 6222.

(51) Davies, E.R. *Phys. Lett. A.* **1974**, *47*, 1.

(52) Mims, W.B. *Proc. R. Soc. London, Ser. A* **1965**, *283*, 452.

(53) Thorhauge, J.; Roberson, M.; Hazell, R.G.; Jørgensen, K.A. *Chem. Eur. J.* **2002**, *8*, 1888.

(54) Evans, D.A.; Johnson, J.S.; Olhava, E.J. *J. Am. Chem. Soc.* **2000**, *122*, 1635.

(55) Thomas, J.M.; Raja, R.; Lewis, D.W *Angew. Chem. Int. Ed.* **2005**, *44*, 6456.

(56) Knops-Gerrits, P.P.; Devos, D.; Thibault-Starzyk, F.; Jacobs, P.A. *Nature* **1994**, *369*, 543.

(57) Herron, N. *Inorg. Chem.* **1986**, *25*, 4714.

(58) Maschmeyer, T.; Rey, F.; Sankar, G.; Thomas, J.M. *Nature* **1995**, *378*, 159.

(59) Shannon, I.J.; Maschmeyer, T.; Oldroyd, R.D.; Sankar, G.; Thomas, J.M.; Pernot, H.; Balikdjian, J.P.; Che, M. *J. Chem. Soc. Faraday Trans.* **1998**, *94*, 1495.

(60) Thomas, J.M.; Raja, R. *Stud. Surf. Sci. Catal.* **2004**, *148*, 163.

(61) Thomas, J.M. *Angew. Chem. Int. Ed.* **1988**, *27*, 1673.

(62) Gabelica, Z.; Valange, S. *Micro. Meso. Materials* **1999**, *30*, 57.

(63) Iwamoto, M.; Furukawa, H.; Mine, Y.; Uemura, F.; Mikuriya, S.; Kagawa, S. *J. Chem. Soc. Chem. Commun.* **1986**, 1273.

(64) Delabie, A.; Pierloot, K.; Groonthaert, M.H.; Weckhuysen, B.M.; Schoonheydt, R.A. *Phys. Chem. Chem. Phys* **2001**, *4*, 134.

(65) Jahn, H.A.; Teller, E. *Proc. Royal Soc. London A* **1937**, *161*, 220.

(66) Zavoisky, E. *Journal of Physics USSR* **1944**, *9*, 245.

(67) Fermi, E. *Z. Phys.* **1930**, *60*, 320.

(68) Schweiger, A.; Jeschke, G. *Principles of pulse electron paramagnetic resonance* Oxford UK: Oxford University Press, 2001.

(69) Odom, B.; Hanneke, D.; D'Urso, B.; Gabrielse, G. *Phys. Rev. Lett.* **2006**, *97*, 3.

(70) Mabbs, F.E.; Collison, D. *Electron paramagnetic resonance of d transition metal compounds* Amsterdam; London: Elsevier, 1992.

(71) Murphy, D.M.; Farley, R.D. *Chem. Soc. Rev.* **2006**, *35*, 249.

(72) Hyde, J.S.; Maki, A.H. *J. Chem. Phys* **1964**, *40*, 3117.

(73) Born, M. *Z. Phys.* **1926**, *37*, 862.

(74) Schrödinger, E. *Phys. Rev.* **1926**, *28*, 1049.

(75) Dirac, P.A.M. *The principles of quantum mechanics* 4th Edit. Oxford UK: Oxford University Press, 1982.

(76) Hartree, D.R. *Proc. Cam. Phil. Soc.* **1928**, *24*, 89.

(77) Fock, V. *Z. Phys.* **1930**, *61*, 126.

(78) Lennard-Jones, J.E. *Trans. Faraday Soc.* **1929**, *25*, 668.

(79) Head-Gordon, M,; Pople, J.A.; Frisch, M.J. *Chem. Phys. Lett* **1988**, *153*, 503;

Frisch, M.J; Head-Gordon, M.; Pople, J.A. *Chem. Phys. Lett* **1990**, *166*, 275; Frisch, M.J; Head-Gordon, M.; Pople, J.A. *Chem. Phys. Lett* **1990**, *166*, 281; Head-Gordon, M.; Head-Gordon, T. *Chem. Phys. Lett* **1994**, *220*, 122; Saebo, S.; Almlof, J. *Chem. Phys. Lett* **1989**, *154*, 83;

(80) Foresman, J.B.; Head-Gordon, M.; Pople, J.A.; Frisch, M.J. *J. Phys. Chem.* **1992**, *96*, 135.

(81) Pople, J.A.; Krishnan, R.; Schlegel, H.B.; Binkley, J.S. *Int. J. Quant. Chem.* **1978**, *14*, 545.

(82) Boys, S.F.; Bernardi, S. *Mol. Phys.* **1970**, *19*, 553.

(83) Hohenberg, P.; Kohn, W. *Phys. Rev.* **1964**, *136*, B864.

(84) Kohn, W.; Sham, L.J. *Phys. Rev.* **1965**, *140*, A1133.

(85) Slater, J.C. *Quantum Theory of Molecules and Solids Volume 4: The Self-Consistent Field for Molecules and Solids* **1974** New York, McGraw-Hill.

(86) Vosko, S.H.; Wilk, L.; Nusair, M. *Canadian J. Phys.* **1980**, *58*, 1200.

(87) Becke, A.D. *Phys. Rev. A* **1988**, *38*, 3098.

(88) Lee, C.; Yang, W.; Parr, R.G. *Phys. Rev. B.* **1988**, *37*, 785.

(89) Becke, A.D. *J. Chem. Phys* **1993**, *98*, 5648; Lee, C.; Yang, W.; Parr, R.G. *Phys. Rev. B* **1988**, *37*, 785.

(90) Becke, A.D. *Phys. Rev.* **1988**, *38*, 3098.

(91) Bloch, F. *Z. Phys.* **1926**, *52*, 555.

(92) Stone, A.J. *Chem. Phys. Lett.* **1981**, *83*, 233; Stone, A.J.; Alderton, M. *Mol. Phys.* **1985**, *56*, 1047.

(93) Neese, F. *Magn. Reson. Chem.* **2004**, *42*, S187.

(94) Knowles, S. *Angew. Chem. Int. Ed* **2002**, *41*, 1999.

(95) Jacobsen, E. N.; Pfaltz, A.; Yamamoto, H.; Eds. *Comprehensive Asymmetric Catalysis* Vol. 1-3, Springer: New York, 1999.

(96) Bölm, C.; Martin, M.; Gescheidt, G.; Palivan, C.; Neschadin, D.; Bertagnolli, H.; Feth, M.; Schweiger, A.; Mitrikas, G.; Harmer, J. *J. Am. Chem. Soc* **2003**, *125*, 6222.

(97) Palucki, M.; Finney, N. S.; Pospisil, P. J.; Guler, M. L; Ishida, T.; Jacobsen, E. N. *J. Am. Chem. Soc.* **1998**, *120*, 948.

(98) McGarrigle, E. M.; Gilheany, E. G. *Chem. Rev.* **2005**, *105*, 1563.

(99) Martinez, L. E.; Leighton, J. L.; Carsten, D. H.; Jacobsen, E. N. *J. Am. Chem. Soc* **1995**, *117*, 5897.

(100) Wu, M. H.; Hansen, K. B.; Jacobsen, E. N. *Angew. Chem. Int. Ed.* **1999**, *38*, 2012.

(101) Tokunaga, M.; Larrow, J. F.; Kakiuchi, F.; Jacobsen, E. N. *Science* **1997**, *277*, 936.

(102) Peretti, K. L.; Ajiro, H.; Cohen, C. T.; Lobkovsky, E. B.; Coates, G. W. *J. Am. Chem. Soc.* **2005**, *127*, 11566.

(103) Hashihayata, T.; Punniyamurthy, T.; Irie, R.; Katsuki, T.; Akita, M.; Moro-oka, Y. *Tetrahedron* **1999**, *55*, 14599.

(104) Kirste, B.; van Willigen, H. *J. Phys. Chem.* **1982**, *86*, 2743.

(105) Frisch, M. J.; Trucks, G. W.; Schlegel, H. B.; Scuseria, G. E.; Robb, M. A.; Cheeseman, J. R.; Montgomery, J. A.; Vreven, T.; Kudin, K. N.; Burant, J. C.; Millam, J. M.; Iyengar, S. S.; Tomasi, J.; Barone, V.; Mennucci, B.; Cossi, M.; Scalmani, G.; Rega, N.; Petersson, G. A.; Nakatsuji, H.; Hada, M.; Ehara, M.; Toyota, K.; Fukuda, R.; Hasegawa, J.; Ishida, M.; Nakajima, T.; Honda, Y.; Kitao, O.; Nakai, H.; Klene, M.; Li, X.; Knox, J. E.; Hratchian, H. P.; Cross, J. B.; Adamo, C.; Jaramillo, J.; Gomperts, R.; Stratmann, R. E.; Yazyev, O.; Austin, A. J.; Cammi,

R.; Pomelli, C.; Ochterski, J. W.; Ayala, P. Y.; Morokuma, K.; Voth, G. A.; Salvador, P.; Dannenberg, J. J.; Zakrzewski, V. G.; Dapprich, S.; Daniels, A. D.; Strain, M. C.; Farkas, O.; Malick, D. K.; Rabuck., A. D.; Raghavachari, K.; Foresman, J. B.; Ortiz, J. V.; Cui, Q.; Baboul, A. G.; Clifford, S.; Cioslowski, J.; Stefanov, B. B.; Liu, G.; Liashenko, A.; Piskorz, P.; Komaromi, I.; Martin, R. L.; Fox, D. J.; Keith, T.; Al-Laham, M. A.; Peng, C. Y.; Nanayakkara, A.; Challacombe, M.; Gill, P. M. W.; Johnson, B.; Chen, W.; Wong, M. W.; Gonzalez, C.; Pople, J. A. *Gaussian 03, Revision B.03* Gaussian, Inc: Pittsburg, PA, 2003.

(106) Burke, K.; Perdew, J.P.; Wang, Y. *Electronic Density Theory: Recent Progress and New Directions* Ed. Dobson, J.F; Vignale, G.; Das M.P (Plenum, **1998**)

(107) Perdew, J.P.; Burke, K.; Ernzerhof, M. *Phys. Rev. Lett.* **1996**, *77*, 3865.

(108) Ditchfield, R.; Hehre, W.J.; Pople, J.A. *J. Chem. Phys* **1971**, *54*, 724.

(109) Kendall, R.A.; Dunning Jr. T.H.; Harrison, R.J. *J. Chem. Phys.* **1992**, *96*, 6796.

(110) McLean, A.D.; Chandler, G.S. *J. Chem. Phys* **1980**, *72*, 5639.

(111) Clark, T.; Chandrasekhar, J.; Spitznagel, G.W.; Schleyer, P.v.R. *J. Comp. Chem* **1983**, *4*, 294.

(112) Stone, A.J. *J. Chem. Theory Comput.* **2005**, *1*, 1128.

(113) Murphy, D.M.; Fallis, I.A.; Willock, D.J.; Landon, J.; Carter, E.; van Doorslaer, S.; Vinck, E. *In Preparation.*

(114) Pauling, L. *J. Am. Chem. Soc* **1932**, *54*, 3570.

(115) Murphy, D.M.; Fallis, I.A.; Willock, D.J.; Landon, J.; Carter, E.; van Doorslaer, S.; Vinck, E. *In Preparation.*

(116) Waller, M.P.; Robertazzi, A.; Platts, J.A.; Hibbs, D.E.; Williams, P.A. *J. Comp. Chem.* **2005**, *27*, 491.

(117) Cornell, W.D.; Cieplak, P.; Bayly, C.I.; Gould, I.R.; Merz Jr., K.M.; Ferguson, D.M.; Spellmeyer, D.C.; Fox, T.; Caldwell, J.W.; Kollman, P.A. *J. Am. Chem. Soc.* **1995**, *117*, 5179.

(118) Maseras, F.; Morokum, K. *J. Comp. Chem.* **1995**, *16*, 1170.

(119) Thomas, J.M. *Angew. Chem. Int. Ed.* **1994**, *33*, 913.

(120) Murphy, D.M.; Gabelica, Z.; Ribeiro, M.F.; Fernandes, A.; Loureno, J.P.; Valange, S.; Louati, A.; Willock, D.J.; Landon, J.; Fallis I.A.; van Doorslaer, S. *In Preparation.*

(121) Baumann, F.; Livoreil, A.; Kaim, W.; Sauvage, J-P. *Chem. Comm.* **1997**, *1*, 35.

(122) Funahashi, Y.; Nakaya, K.; Hirota,S.; Yamauchi, O. *Chem. Lett.* **2000**, *10*, 1172.

(123) Wansapura, C.M.; Juyoung, C.; Simpson, J.L.; Szymanski, D.; Eaton, G.R.; Eaton, S.S.; Fox, S. *J. Coord. Chem.* **2003**, *56*, 975.

(124) Kresse, G.; Furthmüller, J. *Phys. Rev. B.* **1996**, *54*, 11169.

(125) Perdew, J.P.; Burke, K.; Wang, Y. *Phys. Rev. B.* **1996**, *54*, 16533.

(126) Neese, F. *ORCA, an ab initio density functional and semiempirical program package, version 2.4, revision 45* **2003**

(127) Kutzelnigg, W.; Fleischer, U.; Schindler, M. *The IGLO Method: Ab Initio Calculation and Interpretation of NMR Chemical Shifts and Magnetic Susceptibilities, Springer-Verlag, Heidelberg* **1990**, *23*.

(128) Munoz, T.; Prakash, A.M.; Kevan, L.; Balkus, K.J. *J. Phys. Chem.* **1998**, *102*, 1379.

(129) Savitzky, A.; Golay, M.J.E *Anal. Chem.* **1964**, *36*, 1627.

(130) Fraser, A. *Aust. J. Biol. Sci* **1957**, *10*, 484.